UNIVERSITY OF SOUTHAMPTON

Faculty of Engineering and Physical Sciences
School of Engineering

Resolvent-Based Models for Nonlinear Solutions of Wall-Bounded Flows and Statistical Estimation of Chaotic Systems

by

Thomas Burton
MEng
ORCiD: 0000-0001-7998-2278

A thesis for the degree of
Doctor of Philosophy

June 2025

University of Southampton

Abstract

Faculty of Engineering and Physical Sciences
School of Engineering

Doctor of Philosophy

Resolvent-Based Models for Nonlinear Solutions of Wall-Bounded Flows and Statistical Estimation of Chaotic Systems

by Thomas Burton

This thesis explores turbulence from a dynamical systems perspective, focusing on the development of resolvent-based models for both nonlinear solutions and the statistical estimation of chaotic systems. By leveraging the concept of Exact Coherent Structures (ECSs), postulated to serve as invariant skeletons within turbulent flows, the work aims to systematically reduce the complexity of turbulence representation while retaining essential dynamical features. Resolvent analysis, a modal decomposition technique, is employed to construct low-dimensional subspaces that capture the dominant dynamics of wall-bounded turbulent flows, such as rotating Couette flow.

The thesis introduces a novel variational optimisation methodology that operates within these resolvent subspaces to compute invariant solutions of the Navier-Stokes equations in wall-bounded domains. This approach is shown to retain the robustness of the underlying optimisation algorithm while improving computational performance through dimensionality reduction of the resolvent-based subspace. The method is demonstrated for equilibrium and periodic solutions on the rotating Couette flow. Furthermore, the work extends these models to construct large period state-space loops, termed *quasi-trajectories*, which approximate the statistics of solutions on chaotic attractors without requiring exact solutions to the governing equations. This concept is validated using the Lorenz system.

Key results include the discovery of equilibrium and periodic solutions for rotating Couette flow, the application of resolvent modes for low-dimensional modelling, and the statistical validation of quasi-trajectories against direct numerical simulations. These findings represent a step towards “closing the loop” in resolvent analysis, bridging the gap between kinematic modes and practical turbulence modelling. This work opens new avenues for efficient computation and control of turbulent flows and provides a foundation for further exploration of chaotic systems using dynamical systems theory.

Contents

List of Figures vii

Declaration of Authorship xiii

Research Outputs xv

Acknowledgements xvii

1 Introduction 1
- 1.1 Invariant Skeletons of Chaotic Motion . . . 3
  - 1.1.1 Approximating Chaos With Large Orbits . . . 6
- 1.2 Modal Projections of ECSs . . . 8
- 1.3 Variational Optimisation for Fluid Dynamics . . . 11
- 1.4 Quasi-Trajectories and Statistical Estimates . . . 12
- 1.5 Thesis Aims and Objectives . . . 14
- 1.6 Chapter Structure . . . 15

2 Numerical Methods for Finding ECSs and Modal Analysis 19
- 2.1 Numerical Method for Finding Invariant Solutions . . . 19
  - 2.1.1 Shooting Methods . . . 22
  - 2.1.2 Global Methods . . . 25
- 2.2 Modal Analysis Techniques . . . 31
  - 2.2.1 Data-Based vs. Operator-Based Methods . . . 31
  - 2.2.2 SPOD . . . 32
  - 2.2.3 Resolvent Analysis . . . 36
- 2.3 Summary of the Gaps in the Literature . . . 41

3 Variational Optimiser 43
- 3.1 Optimisation Problem for the Navier-Stokes Equations . . . 43
- 3.2 Equivalence of Adjoint Dynamics and Gradient-Based Optimisation . . . 47
- 3.3 Residual Gradient Derivation . . . 50
  - 3.3.1 Residual Constraint Implications . . . 56
  - 3.3.2 Period Gradient . . . 58
- 3.4 DAE Formulation of Gradient-Based Variational Optimisation . . . 59
- 3.5 Galerkin Projection . . . 61
- 3.6 Summary . . . 67

4 Rotating Couette Flow and Resolvent Analysis 69

- 4.1 Rotating Plane Couette Flow . . . 69
  - 4.1.1 Flow Geometry and Governing Equations . . . 71
  - 4.1.2 Streamwise Independence and the Rayleigh-Bénard Analogy . . . 72
  - 4.1.3 Bifurcations and Transitions of RPCF . . . 73
- 4.2 Characteristics of 2D3C RPCF . . . 73
  - 4.2.1 Computational Grid . . . 74
  - 4.2.2 Velocity Statistics . . . 75
  - 4.2.3 Spectral Analysis . . . 77
  - 4.2.4 Dominant Turbulent Structures and SPOD . . . 81
    - 4.2.4.1 SPOD Methodology . . . 83
    - 4.2.4.2 SPOD Analysis . . . 84
- 4.3 Resolvent Analysis . . . 87
  - 4.3.1 Deriving Resolvent Modes . . . 87
  - 4.3.2 Efficacy of Resolvent Modes . . . 92
- 4.4 Summary . . . 95

5 Statistical Estimation of the Lorenz System 97

- 5.1 Low-Dimensional Optimisation . . . 98
  - 5.1.1 Problem Definition and Residual Gradient . . . 98
  - 5.1.2 Dimensionality Reduction . . . 100
- 5.2 Resolvent Analysis of the Lorenz System . . . 101
  - 5.2.1 Numerical Details . . . 106
- 5.3 Optimising for UPOs . . . 108
- 5.4 Quasi-Trajectories . . . 110
  - 5.4.1 Statistics of Quasi-Trajectories . . . 110
  - 5.4.2 Time Cost of Computing Quasi-Trajectories . . . 119
- 5.5 Summary . . . 120

6 Search and Analysis of Invariant Solutions of RPCF 123

- 6.1 Numerical Details of Optimisation on RPCF . . . 123
- 6.2 Exact Nonlinear Solutions . . . 126
  - 6.2.1 Equilibria . . . 126
  - 6.2.2 Periodic Orbits . . . 131
- 6.3 Effect of Mode Truncation . . . 137
  - 6.3.1 Cost of Computing Solutions . . . 142
- 6.4 Summary . . . 143

7 Conclusions 145

- 7.1 Summary of the Analysis and Limitations . . . 147
- 7.2 Further Work . . . 149
  - 7.2.1 Pre-Conditioning Due to Low-Order Models . . . 149
  - 7.2.2 Quasi-Trajectories of Chaotic Flows . . . 150
  - 7.2.3 Sensitivity Analysis of Quasi-Trajectories . . . 151
  - 7.2.4 Hybrid-Solver . . . 151

References 153

List of Figures

1.1 Approximation of a smooth state-space with the linearised dynamics around a set of invariant (periodic) solutions, obtained from Artuso et al. (1990). 4
1.2 State-space cartoon denoting evolution of wall-bounded turbulent flow along with ECSs that characterise the local topology, obtained from Graham and Floryan (2021) 5
1.3 Turbulent snapshot (left) and relative periodic orbit (right) for Taylor-Couette flow at an instant where they are close to each other, followed by a finite time shadowing. The velocity fields of each flow are visualised using two isosurfaces of the azimuthal velocity, one being a positive value (red) and the other being a negative value (blue). Obtained from Krygier et al. (2021). 6
1.4 A sample of four UPOs for the Lorenz system of varying length, showing the repeated patterns in the longer UPOs observed in the shorter UPOs. Obtained from Dong (2018) 7
1.5 Panel (a): A long UPO for the Lorenz system projected onto the x-z plane. Panel (b): time series of the z-component of the state. Panel (c): probability distribution of the z-component of the state compared to the distribution obtained from a time-stepping simulation of the equations. Obtained from Lasagna (2018). 8
1.6 Summary of a POD analysis on a cylinder. Panel (a): snapshot of the analysed flow field. Panel (b): sample of the first eight modes obtained from the analysis. Panel (c): relative proportion of the kinetic energy (ratio of eigenvalues) of each mode. Obtained from Taira et al. (2020). . . 9
1.7 Left: true chaotic trajectory and a trajectory obtained through a numerical (time-stepping) algorithm, showing they initially shadow each other before diverging due to accumulation of numerical and computation errors. Right: the numerical trajectory being shadowed for all time by a nearby chaotic trajectory. 13

2.1 First, second, and third iterates of the logistic map, defined by the function $x_{n+1} = f(x_n) = rx_n(1 - x_n)$, with a parameter value of $r = 4$ which is known to chaotic. Fixed points are defined by the intersection of the resulting curve with the straight line. The number of intersections grows exponentially with the period of the possible orbits. 20
2.2 Number of detected UPOs of specific cycle length (defined relative to a given Poincaré section) for the Lorenz system, obtained from Saiki and Yamada (2009) 21

2.3 Panel (a): inverse time evolution of the logistic map with $r = 4$ approaching a period-2 cycle. Panel (b): forward evolution of the inverse logistic map converging to the same cycle as in panel (a). Obtained from Cvitanović et al. (2020). 21
2.4 A chaotic trajectory, $\dot{x}(t)$, shadowing an unstable periodic orbit, p, resulting in a close recurrence of the trajectory before being repelled along the unstable manifold of the orbit. 23
2.5 Abstract schematic showing the global modification of a state-space loop performed by the global method, gradually increasing the agreement with the governing equations until it reaches a periodic solution p. . . . 25
2.6 Chaotic Hènon-Heiles system solved using the Newton flow method described in Lan and Cvitanović (2004). Panel(a): initial loop guess. Panel (b): converged unstable periodic orbit. Panel (c): decrease in the residual against the fictitious variational time τ. 26
2.7 Convergence of the error norm when finding unstable equilibrium for 2D Kolmogorov flow using the adjoint solver method, from Farazmand (2016). 28
2.8 Gradient descent with fixed step size near a minimum of a quadratic well, with the different vertical and horizontal scales (semi-major and -minor axis sizes of each level ellipse) due to different value eigenvalues of the Hessian matrix at the minimum. Obtained from Nocedal and Wright (2006) 29
2.9 Space-only POD analysis of incompressible flow over a NACA0012 aerofoil at $Re = 23000$ and $\alpha = 9^\circ$, showing a snapshot of turbulent flow, the mean field subtracted for the analysis, and the first four dominant modes. Obtained from Taira et al. (2017). 33
2.10 Relative strength of the POD (left) and SPOD (right) eigenvalues for a compressible turbulent jet ($Re = 10^6$, $Ma = 0.4$). The SPOD eigenvalues are only shown for a Strouhal number of $St = 0.6$ at which the lowest rank behaviour occurs. Obtained from Towne et al. (2018). 34
2.11 Dominant POD mode (left) and SPOD mode at $St = 0.6$ (right) for the same compressible turbulent jet as in Figure 2.10. Obtained from Towne et al. (2018). 35
2.12 Block diagram representation of the relationship between the flow state, $\boldsymbol{u}$ and nonlinear forcing, $\boldsymbol{f}$ that maintains turbulent flow. Obtained from Sharma (2019). 38
2.13 Resolvent-based solution for a Taylor-Couette flow at $Re = 400$, showing the mean velocity derived from the Reynolds stresses of the model solution (a), and the first four Fourier modes obtained from the model solution (b), (c), and (d), all compared to the DNS solution shown at the dots. Obtained from Barthel et al. (2021) 39
2.14 ECSs solution for a pipe flow (left), the projection onto the five dominant resolvent response modes (centre) for each Fourier mode in the homogeneous directions, and the projection onto a single dominant resolvent response mode (right), capturing 95% and 98% of the fluctuation energy, respectively. Obtained from Sharma et al. (2016b). 40
2.15 Percentage energy capture of a channel flow ECS for each velocity component, dominant Reynolds stress, and nonlinear convection term. Obtained from Sharma et al. (2016b) 41

3.1 Schematic of an arbitrary loop in state-space that does not satisfy the governing equation as its tangent vector $\partial \boldsymbol{u}/\partial t$ is not aligned with right hand side of the momentum equations $(\boldsymbol{u} \cdot \boldsymbol{\nabla})\,\boldsymbol{u} + (1/Re)\,\boldsymbol{\Delta u} - \boldsymbol{\nabla} p$. . . 45
3.2 Evolution of a state-space loop, starting with the red inner loop that does not obey the Navier-Stokes equations eventually being modified under some optimisation law to the green loop that does obey the Navier-Stokes equations. 47
3.3 Schematic for a Galerkin projection of a 3-dimensional state-space trajectory and its dynamics (not shown) onto a 2-dimensional linear subspace. 63
3.4 Flow diagram of the optimisation procedure used to compute the residual and its gradient starting from a velocity field defined by the velocity coefficients. 66

4.1 An experimental (stereoscopic) PIV setup for RPCF from an isometric view in panel (a), and top view in panel (b), where the turntable induces a Coriolis and centrifugal force, the latter being absorbed into the pressure since it is isotropic. Obtained from Kawata and Alfredsson (2016) . 70
4.2 Schematic of the geometry for RPCF with spanwise (anticyclonic) rotation, with the spanwise direction perpendicular to the page. 71
4.3 Energy dissipation rate against energy input from the walls for $Re = 450$, $Re = 1000$, and $Re = 5000$, in panels (a-c), respectively. 75
4.4 Mean velocity profiles of RPCF at various Reynolds numbers, plotted with the laminar Couette flow profile for comparison. 76
4.5 Non-zero Reynolds stresses of RPCF at $Re = 5000$. 76
4.6 Spanwise spectra of RPCF at $Re = 25$, in panel (a), and $Re = 50$, in panel (b), plotted against the wall-normal coordinate. 77
4.7 Spanwise and temporal spectra at $Re = 450$ located at wall-normal positions of $y \approx -0.88$ in panel (a) and $y \approx 0$ in panel (b). 78
4.8 Spanwise spectra over the wall-normal height at $Re = 450$, sampled at frequencies $k_t = i/25$ for $i \in \{1, 2, 3\}$ in panels (a-c), respectively. 79
4.9 Spanwise and temporal spectra at $Re = 5000$ located at wall-normal positions of $y \approx -0.88$ in panel (a) and $y \approx 0$ in panel (b). Cut-outs of the spectra are shown corresponding to the similar spectral range as displayed in Figure 4.7. 80
4.10 Spanwise spectra over the wall-normal height at $Re = 5000$, sampled at the same temporal frequencies as in Figure 4.8. 81
4.11 Snapshots of the velocity fields at $Re = 25$, $Re = 50$, $Re = 450$, and $Re = 5000$, in panels (a-d), respectively. 81
4.12 Streamwise vorticity snapshots of the flow at $Re = 450$, with a temporal separation of 5 time units. 82
4.13 Streamwise vorticity snapshots of the flow at $Re = 5000$, with a temporal separation of 5 time units. 82
4.14 First 18 SPOD eigenvalues for RPCF at $Re = 450$ plotted against the temporal frequency, with panels (a-b) corresponding to spanwise wavenumbers of $k_z = 0$ and $k_z = 2\beta$, respectively. 85
4.15 Select set of temporally steady ($k_t = 0$) SPOD modes for RPCF at $Re = 450$. Panels (a,b) and (c,d) show the SPOD modes at spanwise wavenumbers of $k_z = 2\beta$ and $k_z = 4\beta$, respectively. Panels (a,c) and (b,d) show the first and second dominant modes, respectively. 85

4.16 First 6 SPOD eigenvalues for RPCF at $Re = 5000$ plotted against the temporal frequency, with panels (a-b) corresponding to spanwise wavenumbers of $k_z = 0$ and $k_z = 2\beta$, respectively. 86
4.17 Select set of SPOD modes for RPCF at $Re = 5000$. Panels (a,b) and (c,d) show the SPOD modes at spanwise wavenumbers of $k_z = 2\beta$ and $k_z = 4\beta$, respectively. Panels (a,c) and (b,d) show the first and second dominant modes, respectively. 86
4.18 Projection error of DNS data from $Re = 50$ and $Re = 450$ in panels (a), and (b), respectively, plotted against the number of modes used for the projection at every spanwise wavenumber and temporal frequency. The complete set of 64 and 128 resolvent modes for each case, respectively, are generated using a laminar base profile. 93
4.19 First four resolvent modes, panels (a-d), respectively, for $Re = 50$ for a spanwise wavenumber of $k_z = 2/L$ where $L_z = 8$. 94
4.20 First two resolvent modes, panels (a-b), respectively, as well as the 12th and 15th resolvent modes, panels (c-d), respectively, for $Re = 450$ at a spanwise wavenumber of $k_z = 2/L$ where $L_z = 8$. 94
4.21 Projection error of the dominant steady SPOD mode shown in Figure 4.15 (at $Re = 450$) onto the resolvent modes used in Figure 4.18 for the corresponding spanwise wavenumber. 95

5.1 Schematic for the projection of the state onto the subspace defined by the column vectors/space of the matrix $\mathbf{\Psi}_n$, denoted with the subscripts 1 and 2. 104
5.2 Ratio of the singular values for the Lorenz system plotted against the frequency. 105
5.3 Flow diagram of a single iteration of the optimisation loop used to compute the residual and its gradient starting from the modal coefficients $\boldsymbol{a}_n$. 107
5.4 Residual trace in panel (a) and the state space evolution in panel (b) of the shortest UPO of the Lorenz system that circulates both attractor lobes, with a period of $T \approx 1.5586$. Also plotted in panel (b) with grey dots is the initial condition used for the optimisation. 108
5.5 Sample of a few known UPOs for the Lorenz system, see Dong (2018) for details of the UPOs. 109
5.6 Optimisation of a quasi-trajectory, with the state space points shown in panels (a,c,e,g), and the probability distribution functions over the z-direction shown in panels (b,d,f,h), with the blue line corresponding to the Quasi-Trajectory (QT) and the dashed grey line corresponding to the distribution obtained from chaotic data. The initial trajectory (iteration 0) is shown in panels (a-b), iteration 100 is shown in panels (c-d), iteration 1000 is shown in panels (e-f), and iteration 10000 is shown in panels (g-h). 111
5.7 Tails of the PDF (Probability Distribution Function) shown in panel (h) of Figure 5.6, panel (a) near $z = 0$, and panel (b) near the extreme RHS of the distribution. 113
5.8 Comparisons of the power spectra obtained from the final quasi-trajectory in Figure 5.6 at 100, 1000, and 10000 iterations, and chaotic data. The spectra at each iteration (along with the corresponding chaotic spectra) is plotted offset from each other to improve readability. 115

5.9 Trace plots of the global residual normalised by the size of the system response g quasi-trajectory at the end of the optimisation x_f in panel (a), and the mean observables over the quasi-trajectory at each iteration of the optimisation in panel (b), shown with the values obtained from a long chaotic trajectory as horizontal grey lines. Annotated on the plots are the iterations corresponding to the reconstructions shown in Figure 5.6. 116
5.10 The ensemble average and standard deviations of the period averaged observables over a batch optimisation of 50 quasi-trajectories, performed over a range of periods T. The optimisations were terminated at 100, 1000, and 10000 iterations. Panels (a,c) show the observable $\overline{\mathcal{J}_1}$, and Panels (b,d) show the observable $\overline{\mathcal{J}_2}$. Panels (a-b) show the ensemble averages, and Panels (c-d) show the standard deviations. 117
5.11 The ensemble average of the standard deviation in panels (a-b), skewness in panels (c-d), and kurtosis in panels (e-f) of the observables J_1 and J_2 over the same set of batch optimisation as in Figure 5.10. 118

6.1 Diagram of the spectral plane, showing the subsets that make up the top half-plane. The bottom half-plane is Hermitian symmetric to the top half-plane. 125
6.2 Snapshots of the flows before and after the optimisation at $Re = 50$ and $Ro = 0.5$, along with the solution obtained from DNS. Panel (a): the initial flow used for the optimisation, obtained by perturbing the stable solution obtained from DNS at the same Reynolds and Rotation numbers. Panel (b): the result of the optimisation with a residual of $\mathcal{R} < 10^{-12}$. Panel (c): the original solution obtained from DNS. 126
6.3 Residual trace for the optimisation of the initial flow given in Figure 6.2(a), using Gradient Descent (GD), Conjugate Gradient (CG), and L-BFGS optimisation algorithms. All solutions converge towards the solution obtained in Figure 6.2(b). 127
6.4 Final snapshots of the solutions obtained by optimising from various synthetic initial flow fields, each called EQ2, EQ3, and EQ4, for panels (a-c), respectively. The optimisations were performed at $Re = 50$ and Ro, with each residual obtaining $\mathcal{R} < 10^{-12}$. 128
6.5 Initial guesses for the unstable equilibrium solutions shown in Figure 6.4, with each panel labelled to correspond to the given solution in the first figure. 129
6.6 Spanwise power spectra of EQ2 of the solutions obtained at specific iterations of its optimisation, sampled at the channel midpoint ($y = 0$). . . . 130
6.7 Snapshots of the periodic solution ($\mathcal{R} \approx 5 \times 10^{-10}$) obtained for $Re = 450$ with a period of $T \approx 25.41$, for times of $t = 0$, $T/4$, $T/2$, and $3T/4$ in panels (a-d), respectively. 131
6.8 Spanwise and temporal power spectrum of the periodic solution in Figure 6.7 at $y \approx -0.86$ in panel (a) and $y \approx 0$ in panel (b). Only a slice of the spectrum is shown, showing only the lower spanwise and positive temporal modes. 132
6.9 Traces of the global residual in panel (a), and the solution period in panel (b), of the periodic solution in Figure 6.7 over the duration of the optimisation. 133

6.10 Energy dissipation and production of the solution shown in Figure 6.7 shown over the course of the optimisation, showing iterations 0, 100, 200, 500, 1000, 5800 in panels (a-f), respectively. 134
6.11 Energy dissipation and production of the all the solutions shown in preceding section, with the stars ($\star$) representing the equilibrium solutions at $Re = 50$, the solid line displaying the periodic solution of Figure 6.7, and the dashed line representing $\mathcal{E} = \mathcal{I}$. 136
6.12 Panel (a): global residual traces for the optimisation of a perturbed EQ2 solution, performed using $M = 8$, 16, 32, and 64 resolvent modes, all starting from the same initial flow, using the L-BFGS algorithm. Panel (b): Accuracy of the resulting solutions found by the optimiser relative to the "base" case obtained for 64 resolvent modes, plotted against the number of modes used for the projection, each solution being converged such that $\mathcal{R} < 10^{-12}$. 138
6.13 Singular values of the resolvent operator with a laminar base flow for a select number of spanwise frequencies at $Re = 50$ and $Ro = 0.5$. 139
6.14 Snapshots of the solutions obtained from the projected optimisation of the perturbed EQ2 solution, for $M = 3, 4, 5, 64$ in panels (a-d), respectively. 140

7.1 Hybrid solver approach, using variational optimisation (adjoint decent) as an initialiser with a large radius of convergence that moves a solution to within the much smaller radius of convergence for the faster converging Newton-GMRES-Hookstep (NGh) solver. Obtained from Farazmand (2016) 151

Declaration of Authorship

I declare that this thesis and the work presented in it is my own and has been generated by me as the result of my own original research.

I confirm that:

1. This work was done wholly or mainly while in candidature for a research degree at this University;
2. Where any part of this thesis has previously been submitted for a degree or any other qualification at this University or any other institution, this has been clearly stated;
3. Where I have consulted the published work of others, this is always clearly attributed;
4. Where I have quoted from the work of others, the source is always given. With the exception of such quotations, this thesis is entirely my own work;
5. I have acknowledged all main sources of help;
6. Where the thesis is based on work done by myself jointly with others, I have made clear exactly what was done by others and what I have contributed myself;
7. Parts of this work have been published as: T. Burton, S. Symon, A. S. Sharma, and D. Lasagna. Resolvent-based optimization for approximating the statistics of a chaotic Lorenz system. *Physical Review E*, 2025

Signed:.. Date:..................

Research Outputs

Journal Articles:

T. Burton, S. Symon, A. Sharma, and D. Lasagna. Resolvent-based optimization for approximating the statistics of a chaotic Lorenz system. Phys. Rev. E, 2025

T. Burton, S. Symon, and D. Lasagna. Robust Resolvent-Based Optimisation for Finding Invariant Solutions of Channel Flows. *Planned submission: Summer 2025*

Conference Presentations:

UK Fluid 2023, Glasgow, UK, 17-19th October: Modelling Rotating Channel Flow using Resolvent Analysis

11th European Nonlinear Dynamics Conference, Delft, Netherlands, 22-26th July: Robust Gradient-Based Solver for Invariant Solutions to the Navier-Stokes Equations using Resolvent Analysis

1st European Fluid Dynamics Conference, Aachen, Germany, 16-20th September: Robust Gradient-Based Solver for Invariant Solutions to the Navier-Stokes Equations using Resolvent Analysis

APS Division of Fluid Dynamics 2024, Salt Lake City, USA, 24-26th November: Robust Gradient-Based Solver for Invariant Solutions to the Navier-Stokes Equations using Resolvent Analysis

Acknowledgements

I am deeply grateful to my supervisors, Dr. Davide Lasagna and Dr. Sean Symon, for their unwavering support, patience, and deep understanding throughout my research journey. Their astute and compassionate guidance have provided me with the confidence to tackle challenges and the freedom to explore new ideas. Their thoughtful feedback and willingness to accommodate my unique approach have not only shaped this thesis but also fostered my development as a researcher.

My heartfelt thanks go to my parents for their constant support and encouragement throughout my academic journey. Their belief in my abilities and reassurance during challenging times have been invaluable. Without their guidance and sacrifices, this thesis would not have been possible.

I would like to express my gratitude to James Saletes for his friendship and support throughout my time at university. His encouragement to join the triathlon society not only introduced me to a new passion but also provided a much-needed balance to my academic pursuits. The perspective he brought greatly contributed to my maintaining balance during challenging times.

I also extend my sincere gratitude to my academic peers and colleagues within the aerodynamics group, whose collaboration, discussions, and camaraderie have enriched my research experience.

Chapter 1

Introduction

For over 100 years, fluid dynamics research has been dominated by the pursuit of understanding turbulence and the chaotic motion of deterministic systems in general. The importance of turbulence in nature cannot be overstated. It is prominent in engineering applications where quick and accurate estimations of useful observables are required. These observables, such as drag for aerodynamic objects, skin friction coefficients for internal flows such as transport pipes for the energy industry, and mixing properties for combustion engines, are primarily determined by the turbulent properties of the given flow. Turbulence is the dominant feature of astrophysical flows where scales are exceedingly large, ranging from the weather patterns of planets' atmospheres to the formation and stability of stars and galaxies. Physically speaking, turbulence is generally a result of fluid instability being magnified over time or along certain flow directions, leading to nonlinear interactions that cannot be neglected in the flow analysis. Instabilities are generally amplified in the presence of shear flows, primarily flows near walls or in jets (free shear flows).

For turbulent fluids, the ultimate theoretical goal is a model applicable to the general prediction of the effects of turbulent fluctuations on the mean state of the flow. The majority of advancements in this realm have had a foundation in the concept of eddy viscosity: the idea that the main effect of turbulence is to enhance the mean dissipation of the fluid. Expressed through the Boussinesq hypothesis, introduced in Boussinesq (1877), this relates the Reynolds stresses of the fluid to the mean shear through the eddy viscosity variable ν_T which is generally inhomogeneous and needs to be determined throughout the flow field. Providing a value, or transport equation for the eddy viscosity then constituted a closure to the mean governing equations. The prominent examples of this include the simple mixing layer model proposed by Ludwig Prandtl (Prandtl, 1925), the Spalart-Allmaras model (Spalart and Allmaras, 1992) which provides a single transport equation for ν_T, and the two-equation k-ϵ model of Jones and Launder (1972). All of these have been successfully employed in practice, with each model performing best for particular flows for which they were developed/tuned. The fundamental problem with the eddy viscosity model, however, is its motivation as an analogy with the kinetic theory of gases. The simple mechanical assumptions that can be made about particles are not remotely valid for turbulent eddies, which interact in a complex nonlinear fashion, resisting the attempts to reduce the fluctuating flow into a few turbulent properties such as kinetic energy, dissipation, eddy viscosity, etc. Thus, there is good reason to look elsewhere for a more physically consistent, and mathematically rigorous, model for turbulent flow.

Fluid turbulence is a specific example of the more general phenomenon of deterministic chaos. Chaotic dynamics, although not formalised at the time, was first appreciated by Henri Poincaré in his work on the three-body problem. The study of chaos developed gradually over the next 100 years, with the advent of large scale computation and the seminal work of Edward Lorenz (Lorenz, 1963) who demonstrated deterministic chaos in a simple, low-dimensional system. Characterising turbulence is intricately linked to advances in the understanding of chaos theory and nonlinear dynamics in general. A detailed picture of the dynamical processes and structures that give rise to chaotic dynamics provide a necessary a foundation to build a comprehensive theory of turbulence.

Chaos for low-dimensional dissipative dynamical systems is generally understood to occur on a complex (usually fractal) structure called the strange attractor. This attractor, if it exists, is generally sufficient to completely define the long-time properties of the systems. The fractal structure of the attractor is key to the complex motion of the state within a finite space without ever having to repeat itself. The Navier-Stokes equations define the evolution of an infinite-dimensional state, existing as an element of some well-defined function space. In Ruelle and Takens (1971) the view of turbulence in terms of this state-space picture is established, with an underlying strange attractor that governs the turbulence of the fluid. It was conjectured that the complexity of this structure was completely defined by a parameter of the flow, which is understood to be (in most cases) the Reynolds number. For low Reynolds numbers the state-space is rather simple, with only an attracting fixed point, represented physically by a stable laminar solution. As the Reynolds number increases, this fixed point bifurcates into unstable equilibrium, travelling wave, relative periodic, and periodic (or quasi-periodic as proposed in Landau and Lifshitz (1987)) solutions, with the trend being an increase in topological complexity. This is a supercritical route to turbulence, whereby each solution becomes linearly unstable prompting the flow to move to a new point in state-space. There is also a subcritical route to chaos, whereby the flow transitions away from a linearly stable non-turbulent solution due to a finite amplitude perturbation. The state is pushed outside of the basin of attraction for that particular solution and into the region of space attracted to a new and more complex solution, or a turbulent attractor. For flows governed by this type of subcritical transition, the likelihood of such an event occurring still increases with the Reynolds number, due to a generally shrinking basin attraction for the particular non-turbulent solution being studied which means less energetic inputs are required to transition the fluid to a different region of the state-space. The main point is that at some sufficiently large Reynolds number the attractor of the fluid can be understood to be complex enough to contain chaotic/turbulent solutions within itself, according to the analysis of Ruelle and Takens (1971). There has been exploratory research into the existence and nature of these attractors that contain turbulence, such as in Keefe et al. (1992); Takens (1981), although no rigorous proof of the existence of a general turbulent attractor for various flow configurations currently exists. This idea remains useful however in its ability in drawing parallels between the study of low-dimensional chaotic systems and high-dimensional chaotic systems. It provides insight into the dynamics of turbulence and new routes for a unified theory of turbulence, built upon the invariant measures of an abstract dynamical state-space rather than the statistical averaging approach represented by eddy viscosity and the Boussinesq hypothesis. The goal being models derived from representative dynamics of the system and its structure in state-space rather than nonphysical and empirically tuned macroscopic representations of turbulent flows. This is the stage upon which this project is presented, using the dynamical systems perspective of turbulence to motivate the application of low-dimensional chaos theories in determining the character of chaotic and turbulent flows.

1.1 Invariant Skeletons of Chaotic Motion

Models of turbulence are difficult to formulate, as fluid dynamics contains many complicated nonlinear interactions at many different scales, resisting the standard reductive attempts of physicists to formulate a universal theory. Here, instead the theory for low-dimensional chaotic systems can lend a hand in providing a route to finding new models for turbulence. It has been shown for low-dimensional systems by Predrag Cvitanović (Auerbach et al., 1987) that a strange attractor can be analysed in terms of the set of Unstable Periodic Orbits (UPOs). These UPOs are densely embedded within the strange attractor and provide a “skeleton” for the dynamics. The fact that these orbits are dense within the attractor means that any chaotic trajectory gets arbitrarily close to an orbit, at which point it shadows it for a finite amount of time. Due to the instability of the orbit, the chaotic trajectory is eventually repelled along its unstable manifold leading to the trajectory then shadowing a new orbit for a finite amount of time. The result is a continuous and never-ending set of shadowing events that define the evolution of the chaotic trajectory. Figure 1.1 shows how a set of invariant solutions, specifically fixed points and periodic orbits, can be used to partition the state-space and consequently approximate the smooth dynamics

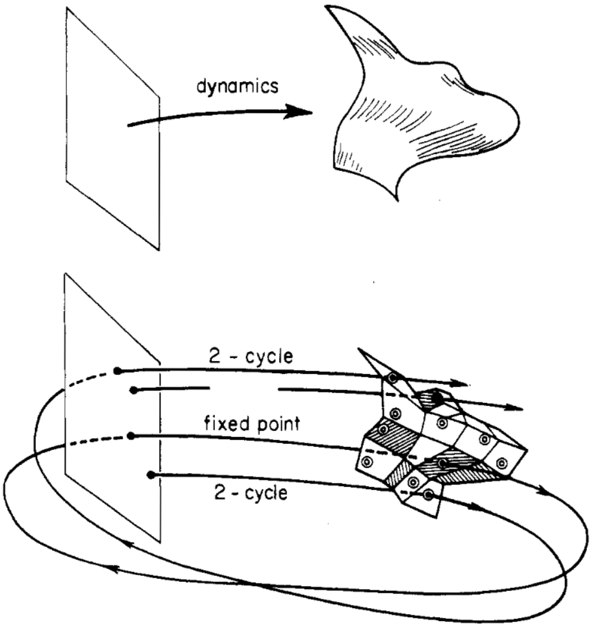

FIGURE 1.1: Approximation of a smooth state-space with the linearised dynamics around a set of invariant (periodic) solutions, obtained from Artuso et al. (1990).

with the linearised behaviour in the neighbourhood of the invariant solution. Thus, if enough of these UPOs can be found then the statistical behaviour of the chaotic trajectory can be defined. This naturally leads to the method of cycle expansions, developed in Cvitanović (1988, 1995), where ergodic properties of the chaotic dynamics are expressed in terms of a weighted sum over the set of UPOs for the given system. This method was shown to possess exponential convergence in Artuso et al. (1990) with the length of the orbit used.

The picture of chaotic dynamics as built up in terms of a set of invariant solutions can be directly extended to fluid dynamics cases. In fact, Eberhard Hopf did so in Hopf (1942, 1948), conjecturing turbulence to be a random walk between unstable invariant solutions that are embedded within a relatively low-dimensional structure (attractor) in the infinite-dimensional state-space. These invariant flow solutions can include from equilibria (dynamical fixed points), to travelling wave solutions, periodic flows, and even quasi-periodic flows. These ideas were given little attention for much time after their original publication, however, more recently numerical methods have been increasingly employed to explore the possibility of these invariant structures existing for the Navier-Stokes equations as well as the role they play in turbulence. Specifically, the work of Stephen Kline and collaborators (Kline et al., 1967; Kline and Robinson, 1990) extensively studied the structure of wall-bounded flows, with different coherent structures being identified as playing important roles in the dynamics. Much work has been done to find examples of similar structures such as in Waleffe (1998, 2001); Wedin and Kerswell (2004); Robinson (1991); Faisst and Eckhardt (2003); Kawahara and Kida (2001); Fazendeiro et al. (2010) in various flows. These

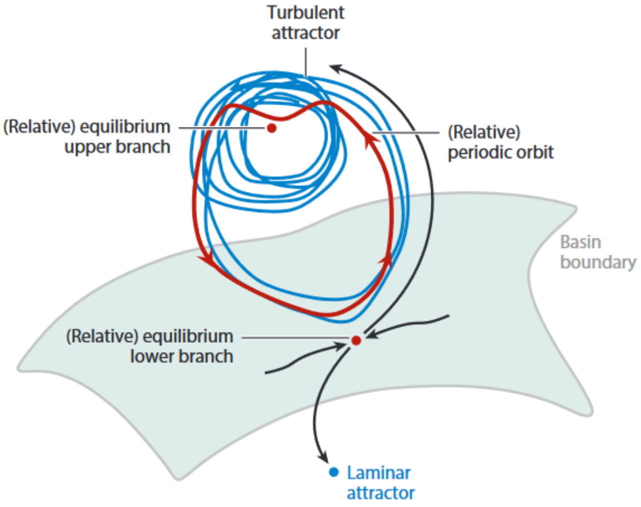

FIGURE 1.2: State-space cartoon denoting evolution of wall-bounded turbulent flow along with ECSs that characterise the local topology, obtained from Graham and Floryan (2021)

unstable structures are typically labelled Exact Coherent Structures (ECSs) due to their qualitative resemblance to observed coherent structures in experimental and DNS studies. This resemblance hints at turbulent flows shadowing closely to ECSs over the duration of their evolution, with evidence for this provided in Suri et al. (2020); Krygier et al. (2021); Crowley et al. (2022). Figure 1.2 depicts a rough picture of how various ECSs are embedded in the state-space of the turbulent flow. In general, certain ECS solutions characterise different parts of the state-space topology, partitioning it along the unstable manifolds of each solution. For instance the so called "lower branch" solutions usually represent the boundary of the basin of attraction of the laminar attractor. The lower branch solutions are saddle points of the dynamics, with its stable manifold defining the edge between the attracting sets of the laminar and turbulent dynamics. The lower branch solutions are distinct from both the laminar and fully turbulent solutions (Wang et al., 2007; Viswanath, 2008; Nagata, 1997). The "upper branch" solutions typically represent structures observed in fully developed turbulent flows, possibly including rarer extreme events/intermittence (Park and Graham, 2015; Kushwaha et al., 2017; Whalley et al., 2019). A more comprehensive review of the significance of invariant solutions for turbulent flows can be found in Kawahara et al. (2012). An example of a turbulent solution shadowing an ECS (relative periodic orbit) in Taylor-Couette flow is given in Figure 1.3.

Linking back to the idea of cycle expansions in low-dimensional chaotic systems, it has been shown that this is in principle possible for turbulent flows in Chandler and Kerswell (2013); Page et al. (2024b). The culmination of this is a relatively new framework upon which models for turbulent flow can be based. Instead of having to somehow directly reduce the complex self-interactions of turbulence to a simple

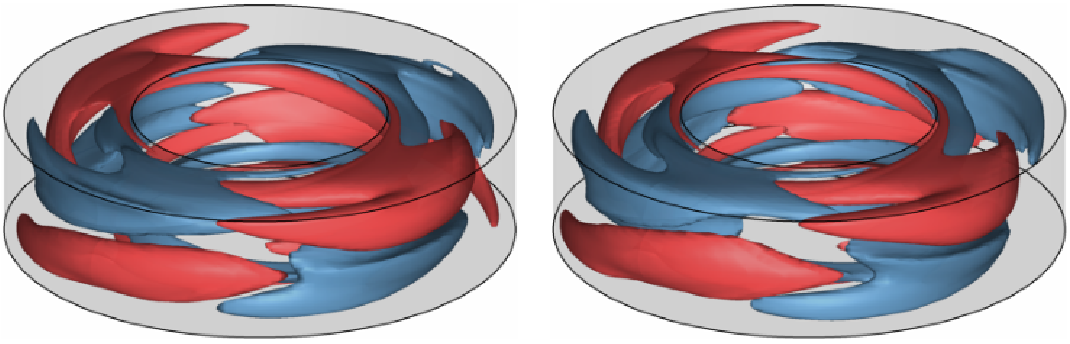

FIGURE 1.3: Turbulent snapshot (left) and relative periodic orbit (right) for Taylor-Couette flow at an instant where they are close to each other, followed by a finite time shadowing. The velocity fields of each flow are visualised using two isosurfaces of the azimuthal velocity, one being a positive value (red) and the other being a negative value (blue). Obtained from Krygier et al. (2021).

relation with the mean flow via the proxy variable of eddy viscosity that does not have a strong physical foundation, ECSs can be used to determine the statistical properties directly. Determining a sufficiently large set, or particularly dynamically significant set of ECSs could provide a complete deterministic picture of the dynamics.

1.1.1 Approximating Chaos With Large Orbits

The work of Chandler and Kerswell (2013) and Page et al. (2024b) are useful demonstrations of the principle of using cycles as the basis for modelling turbulent flow, but the practical applications of the methodology remains difficult. The details of the difficulties associated with turbulent flows are further discussed in Chapter 2, where the methods used to determine invariant solutions to dynamical systems are described. Fundamentally, the state-space of fluid turbulence is very high, increasing rapidly with Reynolds number, making the methods used for finding ECSs more expensive and less robust to initial guesses. In addition ECSs typically bifurcate, becoming more unstable, which can lead to an additional degradation in performance of certain methods due to potentially shrinking basins of attraction. The evolution of the basin attraction of solutions with the Reynolds number is, however, very complex and highly dependent on the method being used to find the solution. It is desirable, therefore, to find a more accessible alternative, perhaps sacrificing some of the favourable convergence properties and rigorous backing of cycle expansions for a slightly more heuristic approach that can yield useful predictions for a smaller cost.

An alternative heuristic approach is proposed in Lasagna (2020), whereby a single large period periodic solution can be used instead of a complete hierarchy of invariant solutions contributing through a weighted sum. Such an observation was motivated for the Lorenz system, where it was observed by Saiki and Yamada (2009) that a small number of solutions provides a good approximation to the mean statistics of the

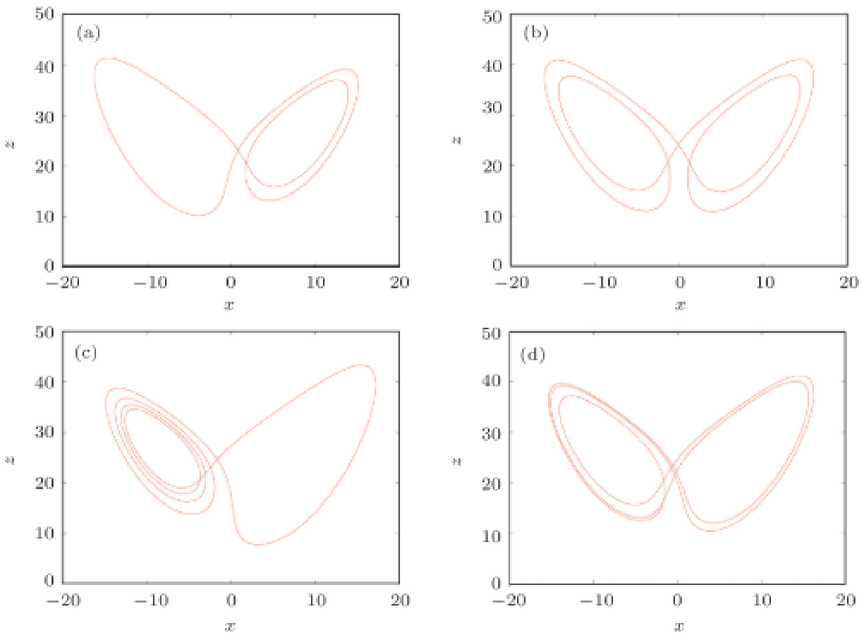

FIGURE 1.4: A sample of four UPOs for the Lorenz system of varying length, showing the repeated patterns in the longer UPOs observed in the shorter UPOs. Obtained from Dong (2018)

chaotic solutions. Longer periodic solutions of the Lorenz system are very similar to the shorter ones, potentially obtained by reflecting and gluing a shorter UPO to itself such as through the procedure performed in Dong (2018), of which a small sample of UPOs is seen in Figure 1.4.

Ultimately, the usefulness of long UPOs is expected from the ergodic properties of the strange attractor in which they are embedded. Ergodicity guarantees that in the limit of a long enough time horizon a solution on the strange attractor will explore the entire subset of the state-space that defines the attractor. The result can be observed in Figure 1.5, where a particularly long UPO of the Lorenz system is shown to be distributed over the z-component of the state in a very similar way as a standard chaotic solution obtained from a time-stepping method. It can be seen that the solution spans a large fraction of the attractor, and is qualitatively indistinguishable from a chaotic trajectory.

Although this has been motivated here only using the Lorenz system, there is reason to believe that this principle will hold for more complex high-dimensional chaotic system. The theory of cycle expansions was originally developed for hyperbolic dynamical systems, and although the Navier-Stokes is not a strictly hyperbolic system, the high-dimensionality of the attractor implies a high level of structural stability, minimising the hyperbolic violation of the system (Albers and Sprott, 2006), the so-called "chaotic hypothesis" as described in Gallavotti and Cohen (1995). In fact, the Lorenz system is an example of chaotic system that is not strictly hyperbolic due to

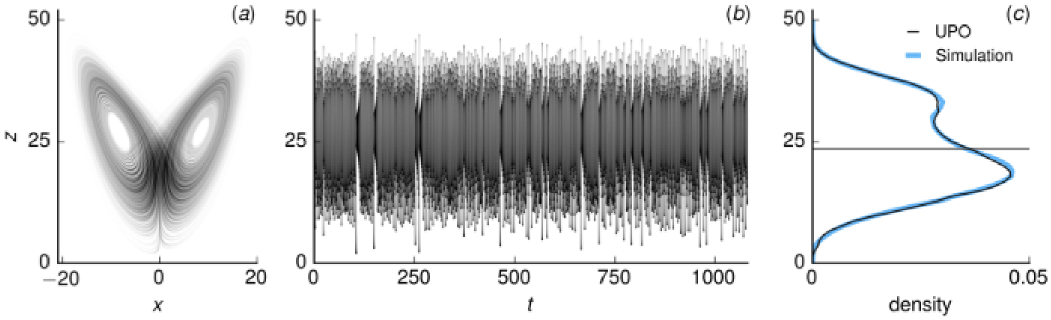

FIGURE 1.5: Panel (a): A long UPO for the Lorenz system projected onto the x-z plane. Panel (b): time series of the z-component of the state. Panel (c): probability distribution of the z-component of the state compared to the distribution obtained from a time-stepping simulation of the equations. Obtained from Lasagna (2018).

the presence of fixed points with complex stability exponents, as well as associated large changes in UPO characteristics for small perturbations of control parameters. The quasi-hyperbolic nature of the Lorenz system (Viana, 2000) does not, in practice, mean that the cycle expansion theory developed for hyperbolic systems does not apply. Instead such mild violations of hyperbolicity would generally have effects on the convergence rates of ergodic properties. Thus, it is not necessary that fluid turbulence be an example of strict hyperbolic dynamics for the same theory to apply. Physically, fluid turbulence is ultimately governed by a similar set of dissipative dynamics with quadratic non-linearities. The benefit of this approach would be a relief from the technical burden of determining the required cycle expansion coefficients to form the correct weights sum for the statistics as observed in Chandler and Kerswell (2013); Lucas and Kerswell (2015); Van Veen et al. (2019). In addition, owing to the temporal periodicity of UPOs, adjoint methods for time periodic systems (Hwang and Choi, 2008; Giannetti et al., 2010; Sierra et al., 2021) may be used despite the instability, to obtain sensitivities of the statistical properties of the dynamics as shown in Lasagna (2018). This gradient information can be leveraged to design flow control strategies such as in Meliga et al. (2016) and Giannetti et al. (2019). The primary problem with this approach is that periodic solutions for chaotic systems become progressively harder to compute the longer they get. It would be beneficial if there was a less computationally expensive method to estimate statistics using long orbits without having to exactly locate solutions to the governing equations.

1.2 Modal Projections of ECSs

There remains the problem, however, of actually computing these long periodic solutions. For simple systems such as the Lorenz system, knowing the basic features of the shorter orbits can inform on how to search for the longer orbits. For more

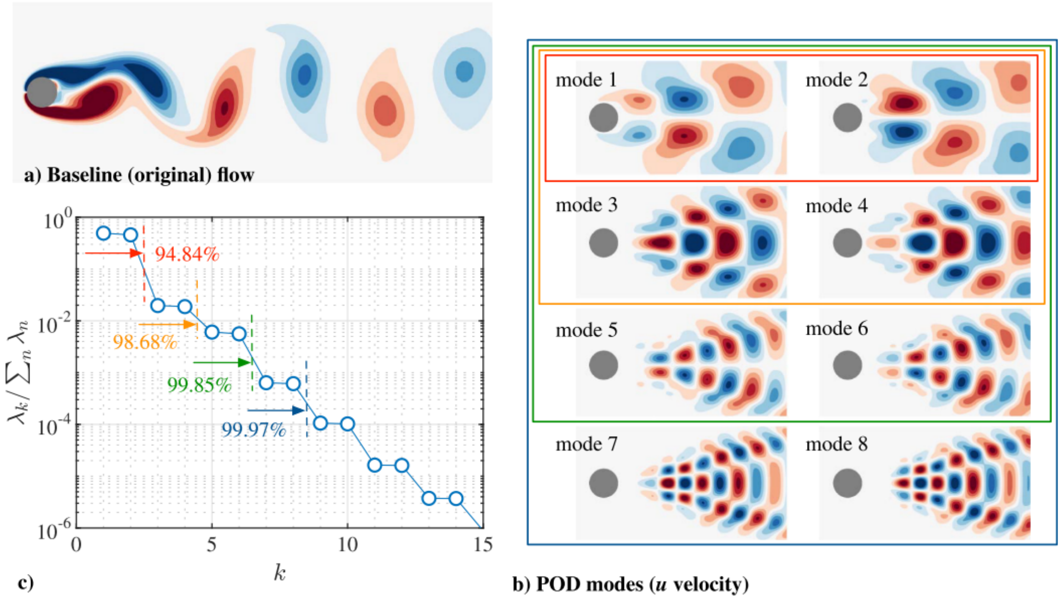

FIGURE 1.6: Summary of a POD analysis on a cylinder. Panel (a): snapshot of the analysed flow field. Panel (b): sample of the first eight modes obtained from the analysis. Panel (c): relative proportion of the kinetic energy (ratio of eigenvalues) of each mode. Obtained from Taira et al. (2020).

complex systems this approach are less fruitful as the dimensions of the attractor would generally be larger and possess more varied dynamics. This problem is compounded by the numerical difficulties that naturally arise when the dimension of the problem is increased, coupled with the high sensitivities of chaotic systems, which leads to extreme difficulty in finding exact solutions to the governing equations as the length of desired solution increases.

A possible remedy to this problem is provided through the use of modal analysis techniques. These techniques, applied to flow problems, provide a set of underlying structures that in some way optimally represent some aspect of the dynamics. From a mathematical point of view, these modes represent basis vectors in the state-space which can be used instead of the standard basis obtained from evaluation at certain points in the flow domain. The right choice of these bases can therefore greatly reduce the dimension of the problem by providing the smallest set of vectors that form a subspace containing the turbulent attractor governing the flow. However, this is a highly non-trivial problem. Some methods require large sets of spatiotemporally resolved data sets to educe any coherence in the flow through analysis of the velocity cross-correlations such as done in Spectral Proper Orthogonal Decomposition (SPOD). Other methods obtain their basis using the governing equations directly, typically via some form of stability analysis with respect to a base flow prescribed a-priori. A canonical example of such low-dimensionality that can be achieved through modal analysis is given in Figure 1.6 which depicts the dominant modes obtained through Proper Orthogonal Decomposition (POD), the space only variant of SPOD, for a cylinder experiencing von Kármán shedding along with the relative kinetic energy capture from each (pair) of modes. Modes like the ones obtained from SPOD are well suited to finding periodic solutions for fluid problems since they are inherently periodic themselves, being constructed relative a set of Fourier modes in time.

Another example of a commonly used modal analysis technique is Dynamic Mode Decomposition (DMD), first introduced in Schmid (2010). DMD aims to generate a set of spatially coherent modes along with an associated eigenvalue that encodes both the frequency and growth/decay rates of each mode. Like POD, DMD relies on time-resolved experimental or simulation data to derive its modes. DMD, being built upon a purely linear algebra approach to dynamical systems, can be applied readily to many varied fields. Turbulent flows are the origin of the method and its most common application (Rowley et al., 2009; Mezić, 2013; Tu et al., 2014), and other fields where DMD have been applied include (but are not limited to) finance (Mann and Kutz, 2016), robotics (Berger et al., 2015), and neuroscience (Brunton et al., 2016). It should be noted that the method fundamentally relies on the approximating the highly nonlinear dynamics characteristic of fluid turbulence with a linear relation, and as such can provide unreliable results, as outlined in Williams et al. (2015). Before moving on, it is also worth briefly mentioning the use of machine learning/neural networks to try to determine coherent structures. This is primarily done through the use of autoencoders that attempt to compress large sets of flow data into a low-dimensional latent subspace that represents the given data set in as few dimensions as possible by minimising some sort of loss function. Examples of this method are given in Fukami et al. (2020); Agostini (2020); Eivazi et al. (2022); Solera-Rico et al. (2024); Zhang (2023); Page et al. (2024b,a). This approach is relatively new but has promise due to the recent advances in neural network architecture. Unfortunately it does not provide any additional physical insights, unlike many of the other methods available.

Turbulent flows when simulated using Direct Numerical Simulation (DNS) can have many degrees-of-freedoms well into the millions required to resolve all the small scale motions. However, the limited attempts to quantify the dimensionality of the underlying attractor of turbulent Poiseuille flow in Keefe et al. (1992) have given estimates in the hundreds, implying orders of magnitudes of computational energy could be conserved through the correct choice of basis. The modes provided by SPOD by design come associated with a set of weights that contains the relative dynamical importance of each mode. Other techniques such as resolvent analysis, which is discussed in more depth in Section 2.2.3, do not come with a set of dynamical weights which makes their direct application to modelling flows less obvious. In Barthel et al. (2021) these dynamical weights are determined through an optimisation approach, which converts the purely kinematic representation provided by resolvent modes to a more useful dynamically weighted basis set.

1.3 Variational Optimisation for Fluid Dynamics

This brief section outlines the role of variational methods in fluid dynamics and provides some wider context to the details discussed in Section 2.1.2. Variational methods in physics are a large class of tools that are concerned with the study of physical systems via the stationary points of various dynamical quantities. Many physical systems can be reformulated in terms of an optimal solution to some functional that defines the global action of some quantity over the domain of the problem being considered, and many problems of optimal control and design are naturally formulated in terms of an optimisation problem over sets of possible functions. In the field of fluid dynamics research typically the objectives of variational optimisation problems are parameterised by a high dimensional object, as well as coming coupled with equality constraints, usually the Navier-Stokes equations themselves. Thus, and adjoint formulation is typically employed which makes the computation of the constrained objective gradient independent of the dimension of the problem.

Searching for minimal seeds for turbulent transition is a problem that is naturally formulated as an optimisation problem: find the flow field with a given initial kinetic energy that has the largest growth in kinetic energy. This problem is tackled for pipe flow in Pringle and Kerswell (2010); Pringle et al. (2012), boundary layer flow in Cherubini et al. (2011, 2010), and Couette flow Rabin et al. (2012); Monokrousos et al. (2011), which collectively showed the existence of certain minimal energy flows that exist on the “edge” of the laminar basin which when evolved lead to turbulent solutions. Kerswell et al. (2014) also used a similar formulation to study the nonlinear stability of particular fluid states, trying to find the least energetic input that is maximally amplified when evolved. Ayala and Protas (2011) studied a similar problem, focusing on the enstrophy of the Burgers equation (as simpler toy-model for the inviscid Euler equations), solving an adjoint optimisation problem in the process.

Classical methods of control rely on linear methods and are solved in a closed form fashion. Variational methods allow a formulation of nonlinear control schemes that can be generally solved using numerical methods. These methods properly account for the nonlinear interactions of the flow, unlike the linear methods, and thus lead to much more effective control schemes. This literature of this field is vast, as it has many applications, such as perturbation control in boundary layers (Cherubini et al., 2013; Passaggia and Ehrenstein, 2013), thermal control of buoyancy driven flows in urban environments (Nabi et al., 2019), and velocity state control using large-eddy simulations (Haçat et al., 2025).

The primary theme in all of these applications is the ability to properly incorporate the nonlinear effects that strongly effect the stability and sensitivity characteristics of flows, as opposed to the majority of classical methods which only take into account the linear effects of the dynamics. In this thesis, a closely related method is utilised which was originally developed in Farazmand (2016), coupled with an added projection step onto a set of well-chosen modes, to allow nonlinear models of fluid flows to be constructed solely out of the building blocks of spatially and temporally coherent modes.

1.4 Quasi-Trajectories and Statistical Estimates

The previous discussions in Section 1.2 have established the possibility of using modal analysis techniques to construct low-order models of the dynamics and reduce the cost of finding ECSs, especially those with large periods. There is another possible application of the low-order models constructed using the projection of the dynamics onto a small set of well-chosen modes. Any simulation of a chaotic system using a standard time-stepping method necessarily does not represent the "true" chaotic solution for the given initial condition. This is a natural result of the exponential divergence of nearby trajectories in chaotic systems along with inevitable errors resulting from the chosen numerical algorithms and floating point arithmetic. The shadowing lemma described in Hammel et al. (1988) ensures (except for special cases as discussed in Chandramoorthy and Wang (2021)) that such orbits in fact shadow a theoretical true chaotic trajectory, and are therefore useful in determining the statistics of the true chaotic solution. Figure 1.7 depicts this idea of the shadowing lemma, with the left showing a true chaotic trajectory and a numerical trajectory (obtained through a time-stepping scheme) diverging after a finite amount of time due to the accumulation of simulation errors. The right shows a different nearby chaotic trajectory that actually shadows the numerical trajectory, guaranteed to exist according to the shadowing lemma. A given ECS shadows a chaotic trajectory for a finite amount of time, primarily depending on its stability characteristics. When solving the Navier-Stokes equations numerically using a standard time-stepping scheme, the result is a trajectory that will continually shadow a set of ECSs, which is one of the reasons that these structures could be used to derive the statistics of the flow. Solving the Navier-Stokes equation this time using a numerical method specifically designed to find ECSs, the goal effectively is to solve for (or minimise) the shadowing distance of the flow to a desired ECS.

Building on the implications of the shadowing lemma, a low-order model of the flow is constructed using a small set of modes which are then optimised, using an variational optimisation method as described in Section 1.3, to optimally satisfy the governing equation. The minima in such an optimisation would represent the best possible approximation to an ECS that the modes can achieve in their reduced space, a sort of least-squares approximation. If the model is aggressive enough, i.e. if a very small set of modes are used relative to the number of points in the flow required to

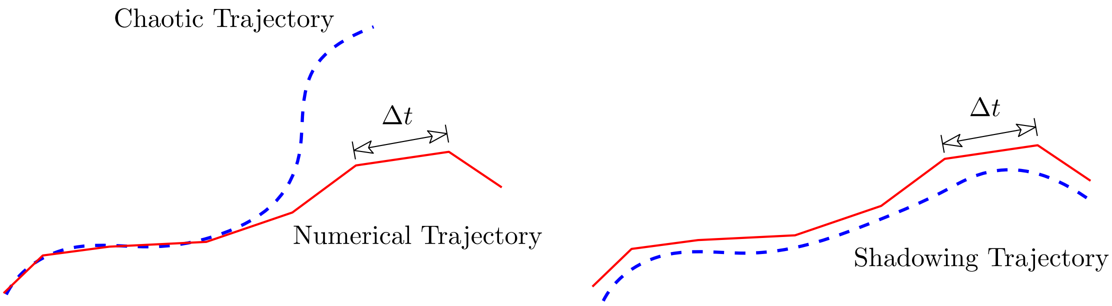

FIGURE 1.7: Left: true chaotic trajectory and a trajectory obtained through a numerical (time-stepping) algorithm, showing they initially shadow each other before diverging due to accumulation of numerical and computation errors. Right: the numerical trajectory being shadowed for all time by a nearby chaotic trajectory.

fully resolve it, then no solution actually exists and the optimiser will not be able to reach a global minimum. In spite of this, due to the density of possible periodic solutions embedded within a strange attractor, the optimisation is expected to very quickly seek out the attractor as it provides the quickest way to satisfy the governing equations. The result is a model for the chaotic dynamics based on a small set of modes that exist on the attractor (as much as is possible in the modal subspace) without exactly satisfying the governing equations. Conceptually this is very similar to a direct numerical solution of the system which shadows a true solution, and under some more accurate numerical scheme would not truly satisfy the dynamics. Referencing Figure 1.7, the numerical trajectory does not satisfy the governing equations as it diverges from the true chaotic trajectory, but it still has accurate statistics due to the guaranteed shadowing by a different nearby chaotic trajectory. This new type of trajectory, constructed from the low-order modal based model which doesn't satisfy the governing equations are called *quasi-trajectories* in this work. A quasi-trajectory with a sufficiently large period would presumably possess the same predictive power for the ergodic properties of the system as a long UPO/ECS would, without requiring as large an overhead as required to find such long recurring flows in an exact manner. Depending on the number of modes used and the resulting accuracy of the captured strange attractor in the lower dimensional state-space, using a quasi-trajectory could be more computationally efficient than a direct simulation of the governing equations. This would be partly as a result of the of the dimensionality reduction afforded by the low-order model, as well as the global temporal resolution that can reduce the required length of the orbit to optimally capture the desired statistics. It is one of primary aims of this thesis to show that these structures provide useful statistical approximations to the chaotic dynamics in a similar way as time-stepping methods, with the added benefit of control over the fidelity of the resulting model, ideally at the lower bound required to completely represent the studied strange attractor. This concept of quasi-trajectories would provide a much lower overhead to finding long orbits that could be used to estimate chaotic statistics as discussed in Section 1.1.1.

1.5 Thesis Aims and Objectives

With the preceding context, the main aim of the thesis can now be stated. In this thesis the resolvent analysis formalism as described in McKeon and Sharma (2010), a modal analysis technique related to SPOD, is used to generate low-order nonlinear models for the dynamics of wall-bounded fluid flow and chaotic dynamical systems. These nonlinear models will be constructed using a variational optimisation methodology that aims to satisfy the Navier-Stokes equations as best as possible within the subspace defined by the resolvent modes. The methodology developed here is applied to a variation of planar Couette flow set on a rotating reference frame, defined and discussed in detail in chapter 4. This approach inspired from the work in Barthel et al. (2021), with the novel framework presented here providing a more general methodology to constructing the dynamical weights for each mode. The specific novelty of the methodologies and their applications are given next in the discussion of the primary objectives of this thesis.

1. Assess Resolvent Model Efficacy

The first objective is to investigate how well resolvent modes generated for the rotating planar Couette flow do at capturing the dominant energetic structures of the flow. The goal is to motivate their use for constructing the low-order models that will be done in the succeeding chapter. This is done by comparing not only directly with DNS data obtained from a custom solver, but comparing the resolvent modes to the dominant modes obtained from SPOD analysis for the same sets of DNS data.

2. Finding Exact Invariant Solutions

The next objective is to actually construct the nonlinear models for the rotating planar Couette flow using the resolvent-subspace variational optimisation methodology that is developed in this thesis, with the goal of finding exact invariant solutions to the Navier-Stokes equations, primarily equilibrium and periodic flows. It is shown that using by a standard Galerkin projection of the velocity field the noted difficulties in the literature with the boundary conditions and pressure terms in the governing equations are resolved. This is natural consequence of the fact that resolvent modes are divergence-free and obey any no-slip boundary conditions when they are computed, leading to an optimisation that is restricted to the linear subspace defined by these kinematic constraints on the dynamics, as discussed in detail in Chapter 3. The methodology developed in the thesis is shown to be able to generate exact solutions for various initial conditions that do not closely resemble the final solution, demonstrating that the Galerkin projection of the methodology does not impact the observed robustness of the variational optimisation to the initial conditions, i.e. a large radius of convergence.

3. Demonstrate Convergence Speed-Up Via Model Truncation

Truncating the number of modes utilised in the Galerkin projection of the dynamics reduces the dimensionality of the space on which the dynamics are constrained. It is shown in this thesis that not only can you in achieve a speed-up in computation time from the dimensionality reduction, but in addition the truncation acts to improve the conditioning of the optimisation problem leading to improved convergence rates. The slow convergence rate of the variational optimisation methodology for solving the Navier-Stokes equations is a notorious problem in the literature, and this truncation-based speed-up makes the method more powerful in its use as a hybrid solver (coupled with an accurate Newton iteration), or as a type of multigrid method that gradually builds up solution complexity as the optimal solution is approached by successively adding back modes to the dynamics.

4. Quasi-Trajectory Statistics

The final objective is to demonstrate the heuristic framework for estimating chaotic statistics as described in Section 1.4. This is demonstrated on the Lorenz system of Lorenz (1963) as a computationally accessible proof of concept on a well understood chaotic system with an ergodic attractor. Due to the low-dimensionality of the problem, only a modest low-order model is possible, achieved through an exact reduction via an algebraic manipulation of the nonlinearities of the system when deriving the resolvent modes. A remaining significant goal is the demonstration of this framework on a turbulent flow, or a generally high-dimensional system, where the reduction in dimensionality of the low-order models is more pronounced. Additionally such a reduction would not be exact, as will be done for the Lorenz system, which is a special instance of the general case where the low-order models neglect some dynamical information.

1.6 Chapter Structure

The thesis is structured with a total of seven chapters. Chapter 2 analyses the details of the surrounding literature. The discussion focuses primarily on two aspects of the literature. The first is about the available numerical methods for finding UPOs of chaotic systems, outlining their respective strengths and weaknesses especially in the context of high-dimensional systems and turbulence applications. This is where the optimisation methodology that will be utilised is introduced as an alternative to the other available solvers for the chaotic systems, one that is particularly robust to the initial guess. The second part of the chapter focuses on modal analysis techniques, with most attention being paid to SPOD and resolvent analysis as the primary methods utilised in this work. The effectiveness of the modes generated from resolvent analysis are justified through their various applications in the literature, making clear their particular ability to efficiently represent ECSs for certain wall-bounded flows.

Chapter 3 provides the mathematical details of the resolvent-based optimisation methodology that will be utilised later in the thesis to generate the majority of the results. To this end, the solver methodology based on a variational optimisation framework for wall-bounded flows is explained. A novel technique utilising the aforementioned resolvent modes in a Galerkin projection is then introduced to properly satisfy the boundary conditions and incompressibility conditions which form a set coupled nonlinear evolution equations.

Chapter 4 constitutes the first set of results presented in the thesis, and tackles the first objective listed in Section 1.5. First, the rotating planar Couette flow is introduced as the primary flow of study, then describing how resolvent modes are generated for this flow. The chapter then moves to a general characterisation of the flow, analysing the velocity statistics, behaviour of the system as it transitions to chaos, velocity spectra, and characterising the dominant coherent structures using SPOD. Finally the resolvent modes of the flow are analysed at select Reynolds numbers, inspecting their ability to represent the given flow in a low-dimensional manner.

Chapter 5 departs from the discussion of RPCF to apply the variational optimisation methodology to a simple low-dimensional case study on the chaotic Lorenz system (Lorenz, 1963). The chapter begins by specialising the mathematics outlined in Chapter 3 to ordinary differential equation systems. Additionally, a specialisation of resolvent analysis is also formulated for the Lorenz system, demonstrating a novel projection of the dynamics from the standard 3-dimensional space down to a 2-dimensional space, where all the presented optimisations are performed, without any loss of information in the nonlinear dynamics. The optimisation methodology is then briefly demonstrated by finding a handful of known UPOs for the system, validating the implementation. The chapter then concludes by tackling the final objective listed in Section 1.5. It is demonstrated that large period quasi-trajectories that do not satisfy the governing equations accurately reproduce the chaotic statistics. This is primarily expressed through the statistics of certain observables of the system, observing how they vary with the number of iterations performed in the optimisation and period of quasi-trajectory.

Chapter 6 then focuses back on RPCF, tackling the second objective listed in Section 1.5, generating exact solutions to the Navier-Stokes equations for wall-bounded flows using the resolvent-subspace optimisation methodology that is detailed in Chapter 3. The methodology is demonstrated on the rotating Couette flow analysed in the previous chapter. A set of equilibrium and periodic solutions are presented, showing that the basis provided by resolvent analysis is sufficient in properly describing the flow, even when some of the modes are removed. In the same chapter, objective three in Section 1.5 is focused on, truncating the number of modes used to represent one of the equilibrium flows found earlier in the chapter and observing the effect this change has on the convergence rate and accuracy of the resulting solution. This ultimately demonstrates the power of the resolvent-based optimisation to accelerate the convergence of the optimisation at only a small cost to the accuracy of the resulting solution.

The thesis is then concluded with Chapter 7 which reiterates the main aims of the thesis and the degree to which the results presented have satisfied them. The prospects of the further work that can be performed utilising the described frameworks are outlined to finish.

Chapter 2

Numerical Methods for Finding ECSs and Modal Analysis

The importance of ECSs as a basis to derive new models for turbulence based on the deterministic dynamics is promising, however, there is the obvious problem of how these solutions should be found. Since the time of Henri Poincaré who established the importance of recurrent solutions for chaotic systems on his work with the three-body problem, summarised in Poincaré (2017), work has been done to formulate methods to determine invariant solutions to chaotic dynamical systems. Concretely, an invariant solution refers to a solution of the governing equations that is somehow invariant to the action of the dynamics, with most dynamical systems work focusing on fixed points and periodic orbits. This work is summarised in Section 2.1, providing the necessary background to understand the various issues that still remain in the literature. After summarising the numerical methods used to determine invariant solutions to chaotic systems, the review moves onto a discussion of modal analysis techniques in Section 2.2. In particular resolvent analysis is introduced as the primary method used here for constructing efficient low-order models for the fluid flow. The chapter then concludes in Section 2.3 where the main points of the literature review are summarised along with the main gaps that this thesis intends to fill.

2.1 Numerical Method for Finding Invariant Solutions

To be able to find exact periodic solutions to dynamical system special numerical methods have to be devised to somehow restrict the initial conditions of the system such that the trajectory closes in upon itself in a finite amount of time. This required a global picture of the dynamics, having to modify earlier parts of the orbit according to the state at a later time.

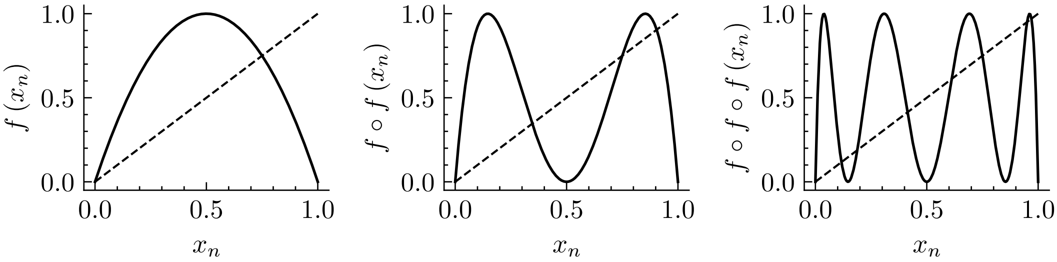

FIGURE 2.1: First, second, and third iterates of the logistic map, defined by the function $x_{n+1} = f(x_n) = rx_n(1 - x_n)$, with a parameter value of $r = 4$ which is known to chaotic. Fixed points are defined by the intersection of the resulting curve with the straight line. The number of intersections grows exponentially with the period of the possible orbits.

Poincaré sections allow the conversion of a continuous dynamical system into a lower-dimensional iterative map. For iterative maps, fixed points

$$x_{n+k} = f^k(x_n) = \underbrace{f \circ f \circ \ldots f \circ}_{k \text{ times}} (x_n), \tag{2.1}$$

where n is the index of the current state and k is the number of iterations of the map that have been applied, are equivalent to periodic trajectories in continuous dynamical systems, with a period determined by the number of iterations before the state is mapped back onto itself. Figure 2.1 displays a number of iteratives of the logistic map, an iterative map popularised through the work of Lorenz (1964) and May (1976), defined as $x_{n+1} = rx_n(1 - x_n)$. The parameter r determines the complexity of the system, with values of $r \gtrsim 3.57$ leading to chaotic dynamics, achieved through a set of period doubling bifurcations as first noted in Feigenbaum (1979). The intersection of the curve f^k and the line $x_{n+k} = x_n$ (the diagonal dashed line in Figure 2.1) defines a particular fixed point of the map f^k, corresponding to a periodic orbit of the base map f with a period of k. It can be seen that the number of fixed points grows exponentially, with 2^k fixed points for orbits of period k. This is a notable trend for many chaotic systems, where the number of (unstable) periodic solutions that exists with a period at or below a certain value grows exponentially with the period. This concept is known as topological entropy, first introduced in Adler et al. (1965), and when applied to chaotic systems by Smale (1967); Sinai (1972) was shown to be generally positive. This is shown for the Lorenz system in Figure 2.2, where the number of detected UPOs for the chaotic system increases exponentially with the length of the orbits. Note that the defined of the orbits in Figure 2.2 are defined by the number of loops they take around each lobe of the attractor rather than the exact period of each orbit.

A simple method to determine unstable fixed points of the logistic map is the inverse map (a specific example of the more general fixed-point iteration), which inverts the update function for the map. Fixed points in the original map that were unstable are

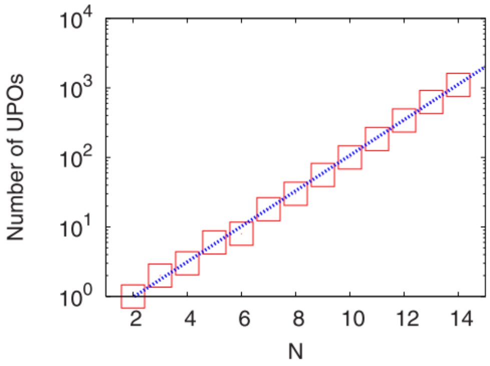

FIGURE 2.2: Number of detected UPOs of specific cycle length (defined relative to a given Poincaré section) for the Lorenz system, obtained from Saiki and Yamada (2009)

now stable under the inverse map Cvitanović et al. (2020). This is demonstrated in Figure 2.3 which shows both the inverse evolution (reversed time) of the logistic map with $r = 4$ showing an unstable cycle on the left, and the forward evolution of the inverse dynamics towards the same cycle which is stable under the new dynamics. This method is difficult to generalise and slow to converge so is not used in practice for any higher-dimensional problems, however it does demonstrate one of the key aspects of methods for determining unstable solutions. Typically the dynamics are modified such as in Lucas and Yasuda (2022) adding a time-delay term which stabilises certain solutions or a whole new set of dynamics are derived. Under the new dynamics the solution that was unstable now becomes an attracting fixed point. These new dynamics can then be evolved to converge towards these fixed points that represents an unstable invariant solution.

When discussing methods used in practice to determine invariant solutions to dynamical systems, it is possible to loosely classify the methods used in research into two broad classes: local, and global. Local methods modify an instantaneous state,

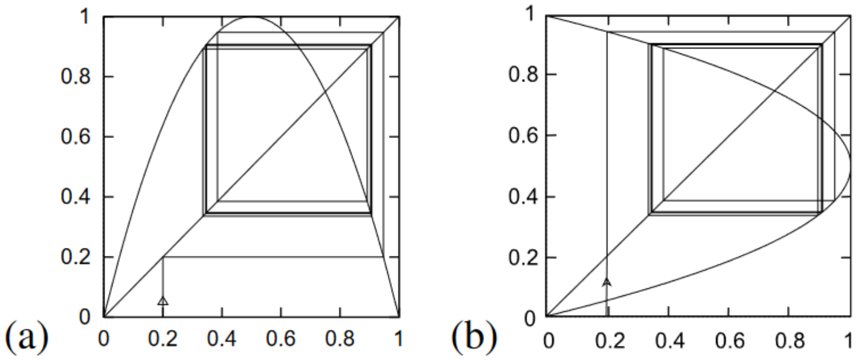

FIGURE 2.3: Panel (a): inverse time evolution of the logistic map with $r = 4$ approaching a period-2 cycle. Panel (b): forward evolution of the inverse logistic map converging to the same cycle as in panel (a). Obtained from Cvitanović et al. (2020).

generally an initial condition, of the trajectory. The change to the state is then propagated by evolving the trajectory according to the given dynamics with the ultimate aim closing the resulting trajectory. These methods are typically called shooting methods. Global methods instead take a complete trajectory that is not prescribed by the dynamics, but instead already satisfies the desired invariance (is already periodic) and is modified over its whole length simultaneously until it satisfies the governing equations. Put another way, the difference between local and global methods is that the first tries to close a trajectory onto itself under the constraint of the dynamics of the governing equations of the prescribed system, and global methods try to find trajectories that obey the governing equations under the constraint that they are periodic. Broadly speaking, local methods are simpler to implement, with practitioners typically able to use standard time-stepping simulators for the propagation step of the solver which is then coupled with a root-finder of minimiser to modify the initial condition. This simplicity comes at the cost of poor robustness to initial guesses, i.e. a small radius of convergence, as a result of the chaotic sensitivities. Global methods largely solve the issue of high sensitivity to initial conditions since they not advance the trajectory under the standard chaotic dynamics, however this comes with a trade-off on the memory and time complexity of the algorithm, due to the requirement of having to store and solve the entire trajectory at each iteration. There is also the added technical burden required to implement global methods, as they will typically require their own unique implementation to solve the derived “loop dynamics”. More of the strengths and weaknesses of these respective approaches will now be discussed in the following subsections.

2.1.1 Shooting Methods

The shooting method begins with an initial condition which is then evolved under the prescribed dynamics for a prescribed time, after which the distance of the tail of the trajectory from its base is used to modify the initial condition in such a way as to decrease the distance for the next evolution. This method is employed successfully for low-dimensional chaotic systems such as in Viswanath (2003) but has only been utilised in a more limited capacity for high-dimensional systems. Examples for fluid turbulence include Kawahara and Kida (2001) where the shooting method is employed to find periodic solutions for plane Couette flow, and Tomoaki and Sadayoshi (2001) where travelling wave solutions are found for channel flow. The difficulties associated with the method can be seen in Chandler and Kerswell (2013) and Van Veen et al. (2019) for 2D Kolmogorov flow and box turbulence, respectively.

Typically shooting methods are initialised using a close-recurrence, shown in Figure 2.4. If the evolution of a state $\boldsymbol{x}$ for a time of t is given by the flow map $f^t(\boldsymbol{x})$,

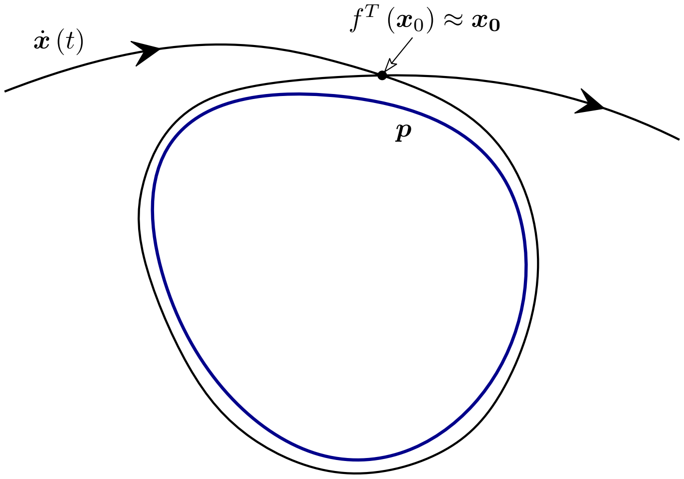

FIGURE 2.4: A chaotic trajectory, $\dot{x}(t)$, shadowing an unstable periodic orbit, p, resulting in a close recurrence of the trajectory before being repelled along the unstable manifold of the orbit.

then a close recurrence can be expressed as

$$G(\boldsymbol{x}_0, T) = f^T(\boldsymbol{x}_0) - \boldsymbol{x}_0 < \epsilon \tag{2.2}$$

for a period T and recurrence bound ϵ decided a priori. The trajectory comes sufficiently close to itself at some later time as a result of temporarily shadowing a particular UPO. A shooting method will then modify $\boldsymbol{x}_0$ and T in an attempt to find a zero of the function G. The iteration of the seed $\boldsymbol{x}_0$ and period T is typically done with a Newton-Raphson approach

$$\boldsymbol{J} \cdot \begin{pmatrix} \delta \boldsymbol{x}_0 \\ \delta T \end{pmatrix} = -G(\boldsymbol{x}_0, T), \tag{2.3}$$

where $\boldsymbol{J}$ is the Jacobian matrix of the objective function G, and $\delta \boldsymbol{x}_0$ and δT represent the resulting changes to the seed and period, respectively. It should be noted that in practice there is an extra constraint to account for the system degeneracy as a result of the system symmetry when perturbed along the trajectory prescribed by the dynamics f^t. Finding a closed-form expression for $\boldsymbol{J}$ is not possible for chaotic systems due to the governing nonlinear dynamics, and even if it were the high-dimensionality of fluid problems would make it prohibitively expensive to store in memory. Thus, to practically solve the Newton-Raphson iteration problem in Equation 2.3 a matrix-free approach has to be employed. Typically this is provided with the Generalised Minimum RESidual (GMRES) method, a subtype of general Krylov subspace solvers, first introduced in Saad and Schultz (1986). This method forms an iterative scheme that solves Equation 2.3 to within a given tolerance in as small a space as possible, without having to explicitly form $\boldsymbol{J}$. In addition, a hookstep is typically added to this method, first done in Viswanath (2007), which adds a trust-region to the Newton-Raphson step leading to improved robustness to the initial guesses further away from a solution. This forms the well-known Newton-GMRES-Hookstep method, the current gold standard method to solve for invariant solutions in high-dimensional systems.

The data used to initialise the search, the close recurrences, is obtained from external sources: experiment, and DNS simulations typically. This adds an extra overhead for the practitioner when utilising this method. This is usually necessary since the shooting method is a very difficult method to converge, even with the added hookstep, as a consequence of its sensitivity to initial conditions characteristic of chaotic systems. This high sensitivity can result in a very small radius of convergence, especially for high-dimensional systems. Extreme events are common in turbulent flows (Batchelor et al., 1949; Sreenivasan and Antonia, 1997) which poses a further complication, since they are not often visited by data sets obtained in practice. As such, it is difficult to obtain an initial condition for the method that is close to a periodic solution that represents the extreme event in question (Krygier et al., 2021). Recently in Redfern et al. (2024) a modified recurrent flow analysis method with triadic interaction weighting is used to preferentially extract more extreme orbits with larger dissipation rates.

Taking all of this together, the shooting method, and local methods in general, suffer greatly from the sensitive dependence on initial conditions of chaotic systems. This makes them difficult to use in practice, especially for high-dimensional systems. The method as a result leads to a non-systematic approach to obtaining solutions since it has to rely on practical data sets obtained from external sources, biasing the method towards solutions that are more commonly observed in practice. Although this could be useful in practice since the more common solutions are more likely to describe the ergodic dynamics better, it also precludes the possibility of studying more atypical and intermittent processes that are known to play an important role of fluid turbulence. The more unstable the periodic orbit the less likely it is to be shadowed for an extended length of time by the chaotic trajectory and the more difficult it is to extract a useful initial condition that will converge towards it. A generalisation, called the multi-point shooting method, provides a slightly more robust alternative, utilised in Christiansen et al. (1997); Sánchez et al. (2004); Budanur et al. (2017). Instead of attempting to close the trajectory over the total length of the period, the trajectory is sliced into multiple segments and a set of coupled shooting problems are solved simultaneously which reduces the effect of exponential divergence of nearby trajectories and enlarges the radius of convergence. Taking this concept to the limit of a shooting method for each infinitesimal point along an orbit leads the idea utilised in global (or variational) methods that will now be discussed.

2.1.2 Global Methods

In an effort to provide alternatives to shooting methods that can converge for a larger set of initial guesses, various global methods have been developed. These methods partially solve the issue of high sensitivities of the chaotic system to its initial condition by treating the problem of finding invariant solutions as a problem to be solved over the whole domain and time window simultaneously. The most prevalent approach, proposed in Lan and Cvitanović (2004), formulates the problem of finding periodic orbits as a continuous deformation of a state-space loop that decreases the violation of the governing equations. Figure 2.5 is a schematic for such a process, whereby a state-space loop is gradually deformed to agree with the governing equations of the dynamical system. The loop in Figure 2.5 is being deformed continuously, red denoting a large residual and green denoting a zero residual, such that at the end of the process the governing equations are satisfied. The general procedure of these global methods is to construct a new set of dynamics in a fictitious time τ as follows

$$\frac{\partial \boldsymbol{x}}{\partial \tau} = \boldsymbol{M}\left(\boldsymbol{x}\right). \tag{2.4}$$

Given a residual for a flow solution defined as $\boldsymbol{r} = \dot{\boldsymbol{x}} - \boldsymbol{F}\left(\boldsymbol{x}\right)$, the operator $\boldsymbol{M}$ is specifically designed such that $\|\boldsymbol{r}\| \to 0$ as $\tau \to \infty$. In other words, every attracting fixed point of the newly constructed dynamics corresponds to an invariant solution of the original dynamics. The evolution of the norm of the residual can be expressed in

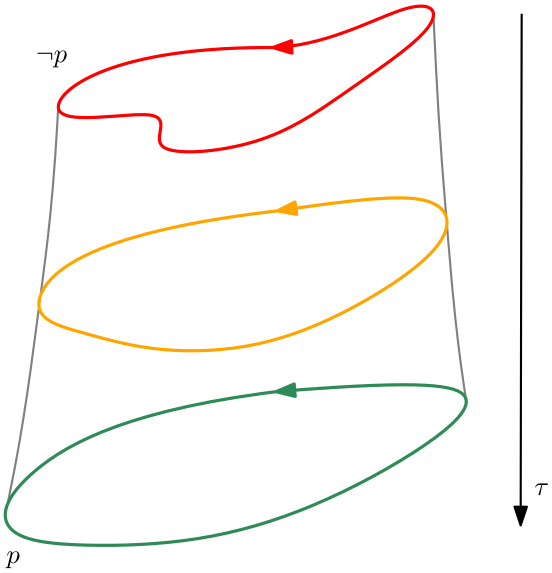

FIGURE 2.5: Abstract schematic showing the global modification of a state-space loop performed by the global method, gradually increasing the agreement with the governing equations until it reaches a periodic solution p.

terms of the current state and prescribed evolution due to $\boldsymbol{M}$

$$\frac{\partial}{\partial \tau}\|\boldsymbol{r}\|^2 = 2\left\langle \mathcal{D}\left(\boldsymbol{x},\, \boldsymbol{M}\left(\boldsymbol{x}\right)\right), \boldsymbol{r}\right\rangle, \tag{2.5}$$

where $\mathcal{D}\left(\boldsymbol{x},\, \boldsymbol{M}\left(\boldsymbol{x}\right)\right)$ is the Gateaux derivative, a sort of functional directional derivative evaluated with the state-space loop $\boldsymbol{x}$ in the direction $\boldsymbol{M}\left(\boldsymbol{x}\right)$. Clearly, a decrease in the residual norm is achieved by enforcing that

$$\mathcal{D}\left(\boldsymbol{x},\, \boldsymbol{M}\left(\boldsymbol{x}\right)\right) = -\boldsymbol{r}. \tag{2.6}$$

This condition fully determines the action of the operator for any given loop $\boldsymbol{x}$, however it is implicit, requiring the solution of a linear system at each step to advance τ. Once $\boldsymbol{M}$ has been obtained by solving Equation 2.6 then the loop $\boldsymbol{x}$ can be advanced forward in τ using some form of integration scheme, such as simple first order Euler method

$$\boldsymbol{x}_{i+1} = \boldsymbol{x}_i + \Delta\tau \boldsymbol{M}\left(\boldsymbol{x}\right). \tag{2.7}$$

Important to note that Equation 2.6 is an analogue to the standard linear system formed when solving a system using the Newton-Raphson technique, and by setting $\Delta\tau = 1$ in Equation 2.7 the standard Newton-Raphson step is recovered. Thus any $\Delta\tau < 1$ can be viewed as a damped Newton iteration. These details are further discussed in Section 3.2. The linear system in Equation 2.6 can, in contrast to the linear system that needs be solved in the shooting method, can in fact be derived in a closed-form expression and solved directly. However, as noted in Fazendeiro et al. (2010) for the same reasons as as for the shooting method, the memory requirements of forming and solving this linear system for high-dimensional problems such as those tackled in fluid dynamics research is prohibitively large. Thus, as before this linear system is solved using the Newton-GMRES-Hookstep method mentioned in the previous section. As such, the cost of each iteration of the Newton solver step in the

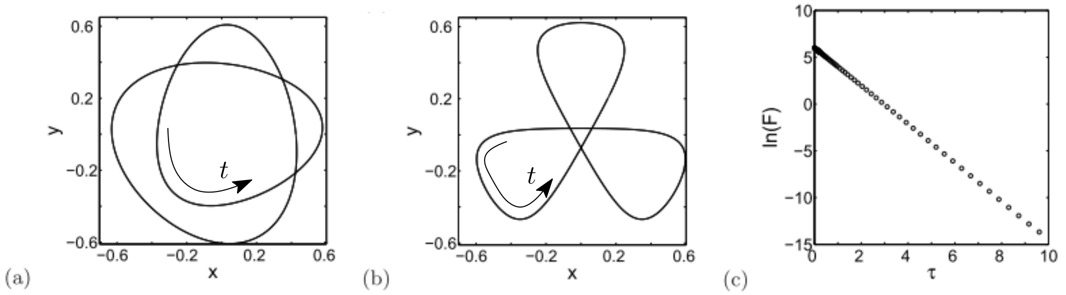

FIGURE 2.6: Chaotic Hènon-Heiles system solved using the Newton flow method described in Lan and Cvitanović (2004). Panel(a): initial loop guess. Panel (b): converged unstable periodic orbit. Panel (c): decrease in the residual against the fictitious variational time τ.

algorithm in terms of memory and CPU time scales linearly with the degrees-of-freedom of the dynamical system, including the spatial and temporal variation of the loop. This does, however, come at the cost of having an inexact method for solving the linear system at each iteration, which means that the cost of each advancement in τ also depends on the dimension of the Krylov subspace used to approximately solve the linear system resulting from the Newton iteration. There are still, however, issues remaining, particularly that the radius of convergence for the Newton-GMRES methods is still rather modest as noted in Ashtari and Schneider (2023), which is a pertinent problem for fluid dynamics where close recurrences or continuation methods are still utilised to provide initial guesses that can be reasonably expected to converge as done in van Veen et al. (2006); Cvitanović and Gibson (2010). The closeness of recurrences is less likely the longer the period of the solution being sought, making the Newton flow method less practical as the size of the orbit grows. This issue stems largely from the Newton-Raphson method itself, and the known issues it has with convergence when initial conditions and/or the objective function are not well behaved Skowronek and Gora (2007). A practical example of the Newton flow method described in Lan and Cvitanović (2004) is shown in Figure 2.6, which shows an initial loop in panel (a) being iterated to an unstable periodic solution of the Hènon-Heiles system in panel (b), with panel (c) notably displaying the exponential rate of convergence of the loop to the periodic solution with the fictitious variational time τ, which demonstrates the very favourable convergence behaviour of the method when close to a solution.

An alternative to using the Newton-Raphson method, first proposed in Farazmand (2016), is to instead use a set of adjoint operators to construct a new set of "variational dynamics" that decreases the total violation of the governing equations along the direction of steepest descent. In Farazmand (2016) this was formulated via a the corresponding set of adjoint dynamics of Equation 2.5. Specifically, denoting the adjoint of an operator with as $(\cdot)^\dagger$, Equation 2.5 is rearranged

$$\frac{\partial}{\partial \tau}\|\boldsymbol{r}\|^2 = 2\left\langle \boldsymbol{M}\left(\boldsymbol{x}\right), \mathcal{D}^\dagger\left(\boldsymbol{x}, \boldsymbol{r}\right)\right\rangle . \tag{2.8}$$

To guarantee a decrease in the residual norm now, we can set the variational dynamics as follows

$$\boldsymbol{M}\left(\boldsymbol{x}\right) = -\mathcal{D}^\dagger\left(\boldsymbol{x}, \boldsymbol{r}\right). \tag{2.9}$$

This different definition of the new dynamics $\boldsymbol{M}$ is mathematically equivalent to the minimisation of the norm of the residual, as is explicitly shown in Section 3.2. The (multiple) global minima of such a problem is represented by a zero residual $\boldsymbol{r} = 0$. When discretised in τ, similar to in Equation 2.7 using the Euler method, a gradient descent formulation is obtained. Using this method, or some other optimisation algorithm ensures a decrease in the residual norm at each iteration, irrespective of the

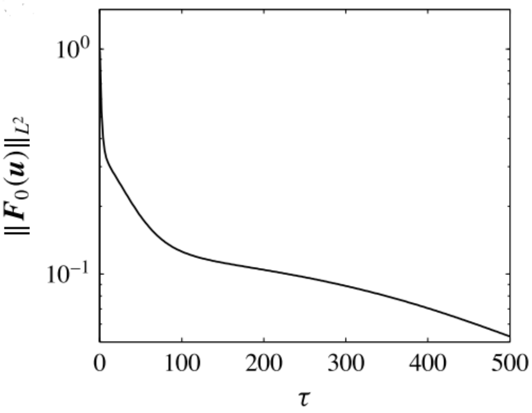

FIGURE 2.7: Convergence of the error norm when finding unstable equilibrium for 2D Kolmogorov flow using the adjoint solver method, from Farazmand (2016).

current state of the loop. This is reflected in the much larger radius of convergence of the adjoint formulation compared to the Newton flow method of Lan and Cvitanović (2004). The improved robustness to the initial guess, however, does come at a sharp cost to the impressive convergence rate of the Newton flow algorithm. As noted in Figure 2.6 the Newton flow method can achieve exponential convergence rates in τ once sufficiently close to a solution, whereas the adjoint dynamics does not guarantee such favourable performance. The method was applied to finding equilibrium and travelling wave solutions to 2D Kolmogorov flow in Farazmand (2016), and with notable solutions found that represent the intermittent character of the flow, represented by short periods of high kinetic energy and dissipation growth rates. The reduced convergence rate of the derived adjoint dynamics is displayed in Figure 2.7 with the convergence of an equilibrium solution of the 2D Kolmogorov flow. Additionally, in Parker and Schneider (2022) the methodology were utilised for several different formulations of the governing equations of 2D Kolmogorov flow to compare their relative performances. The method was also developed further to find periodic solutions of the Kuramoto-Sivashinsky equations in Azimi et al. (2022), focusing primarily on the performance of the method compared to shooting methods and Newton-based global methods. In Ashtari and Schneider (2023) the methodology was extended to be able to find equilibria for wall-bounded flows, using the Influence Matrix (IM) method (Kleiser and Schumann, 1980; Canuto et al., 1988) to allow the addition of no-slip boundary conditions to the problem, which applied to the plane Couette flow. While Ashtari and Schneider (2023) primarily focuses on the development and performance of the variational optimisation methodology with the added boundary constraints due to the wall, there is also presented a method used to improve the convergence of the method once it is close to a solution. This novel approach is based on DMD, and effectively attempts to linearly extrapolate the solution along the direction the optimiser is moving in one large step, displaying impressive improvements in convergence rate. The IM method allows the velocity and pressure terms to be solved simultaneously, avoiding the boundary errors that are a result of the lack of an explicit boundary condition for the pressure when solving the Pressure Poisson Equation (PPE). Convergence of the variational optimisation is initially rapid but slows down considerably as the desired minimum is approached. In the original paper Farazmand (2016) proposed the optimisation as a supplementary tool that could be used in conjunction with the Newton-based approaches. This entails converging a loop that is not particularly close to a given solution until the more rapidly converging methods can take over, which was successfully employed to universally converge a set of solutions for 2D Kolmogorov flow. To this end, if the variational optimisation methodology can be used as a tool to accelerate the systematic search for new ECSs in turbulent flow regimes, then it would be desirable if the method can be accelerated further in its initial convergence towards a solution. This could come at the cost of some accuracy of the resulting solution since the result can then be used as input to a Newton-GMRES-Hookstep solver which converges quickly to an accurate result.

In Farazmand (2016); Azimi et al. (2022) and Ashtari and Schneider (2023), the main works utilising the variational optimisation methodology, the continuous dynamics are discretised using a simple first order Euler scheme,. This is motivated primarily by its simplicity, as the accuracy of the intermediate dynamics is not important, only the accuracy of the final solution is sought, which is not affected by the order of accuracy for the method used. This allows larger steps to be taken. However, as already noted when viewed from the optimisation point of view, the first order Euler scheme is equivalent to the gradient descent algorithm with a fixed step size (shown in Section 3.2), which is known to have very poor convergence properties when approaching a minimum (Nocedal and Wright, 2006). If an objective function has a poorly conditioned Hessian matrix, i.e. if the largest and smallest eigenvalues of the Hessian have very different scales, then fixed step gradient descent tends to bounce back and forth to either side of the minimum, requiring small step sizes to ensure a

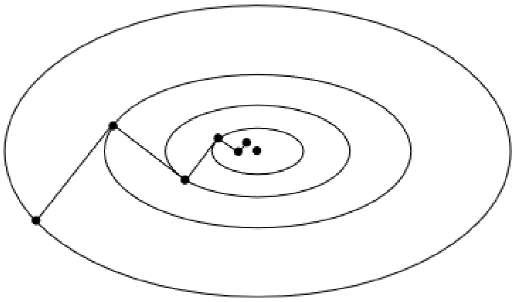

FIGURE 2.8: Gradient descent with fixed step size near a minimum of a quadratic well, with the different vertical and horizontal scales (semi-major and -minor axis sizes of each level ellipse) due to different value eigenvalues of the Hessian matrix at the minimum. Obtained from Nocedal and Wright (2006)

decrease at every iteration. This situation is depicted in Figure 2.8, with the different scales of Hessian eigenvalues creating an elliptical well near the minimum. As gradient descent attempts to move towards the minimum it bounces along each side of the well slowing the overall convergence rate. Poor convergence due to the Hessian also reduces convergence rates of algorithms that don't suffer from the "zig zagging" problem of gradient descent. Fluid dynamics problems are commonly poorly conditioned primarily due to the spectrum of the Laplace operator governing the diffusion, which has unbounded eigenvalues. This naturally leads to the observed poor convergence when discretised, with convergence rates further deteriorating as the discretisation is further refined. As shown in this work, a better choice is the quasi-Newton optimisation algorithms, which do not require any extra information about the objective function and have far better convergence rates near the minimum as a result of approximately accounting for the curvature around the minimum.

What is clear from the above discussions of the available numerical methods for finding invariant solutions to dynamical systems is that they all have downsides when applied to chaotic systems, especially when the system is high-dimensional. Shooting methods are conceptually simple but require very accurate initial guesses to successfully converge which adds a large overhead. The global Newton methods, especially those of Lan and Cvitanović (2004) are somewhat more robust to the initial guess than shooting methods but are inherently more costly since the whole evolution of the trajectory has to be stored every iteration. Convergence is rather good, but in practice a good initial guess is still required. Variational optimisation from Farazmand (2016); Azimi et al. (2022) possesses the largest radius of convergence of the methods discussed here by far, converging to something reasonable from much more arbitrary initial conditions. However, this comes at the significant cost of convergence rate, which can be prohibitively slow for high-dimensional systems. The variational optimisation method also requires some special treatment when no-slip boundary conditions are present.

Many of the problems listed here become more severe as the dimensionality of the problem increases, however, it is known that many of the attractors that govern the flows are in fact relatively low-dimensional objects compared to the state-space they exist within. Thus, a systematic method to extract the most dynamically significant dimensions of the flow is highly desirable, as it would alleviate one of the main issues associated with finding ECSs. The next section introduces the methods used in fluid dynamics research that are designed to answer the question of 'what basis is best?' when trying to model turbulent flows.

2.2 Modal Analysis Techniques

The presence of coherent structures has been noted for essentially as long as turbulence research has been conducted. Their importance in certain physical mechanisms have been noted in a number of prominent cases. Famous example being hairpin vortices in turbulent boundary layers (Kline et al., 1967; Head and Bandyopadhyay, 1981), von Kármán shedding in turbulent wakes (von Kármán, 1911), and Tollmien-Schlichting waves in boundary layer transitions (Tollmien, 1928; Schlichting, 1933) which were first observed in Schubauer and Skramstad (1947). As discussed, observations of coherent structures in real flows can be understood in terms of shadowing of unstable invariant solutions to the Navier-Stokes equations for a finite amount of time. Motivated by the desire to educe these structures from flows, modal analysis techniques have been developed. The main goal of these methods have been to dissect data sets or the governing equations to find particular solutions that have more statistical or dynamical importance compared to the rest of the flow. The resulting structures are then applicable to modelling, prediction, and data compressions. What follows is an overview of the main techniques currently employed in the literature, then moving onto a more in-depth discussion of the two methods that are of most importance to the current work: SPOD, and resolvent analysis.

2.2.1 Data-Based vs. Operator-Based Methods

Modal analysis techniques can be split into two broad groups: data-based methods, and operator-based methods. Data-based methods were the first developed due to the desire to try to isolate the structures observed in experimental studies. As the name suggests, data-based methods process large sets of spatially and temporally resolved flow fields. Operator-based methods instead try to obtain similar results directly from the Navier-Stokes, possibly using some form of limited data input, such as a base flow. Overviews of each of the methods mentioned in this subsection, including application examples, can be found in Taira et al. (2017, 2020); Rowley and Dawson (2017).

The seminal work of John L. Lumley (Lumley, 1967, 1970) introduced SPOD, which remains one of the most widely used methods available. SPOD is a data-based method which produces structures from a set of temporally resolved flow data in terms of optimal energy capture, leading the modes that provide the most efficient basis for the dynamics of the flow. A note should be made that due to limitations in computational resources SPOD has typically been implemented in a space only fashion, introduced in Sirovich (1987); Aubry et al. (1988). The original method as proposed by Lumley takes into account the full spatiotemporal correlations of the data. In this work we utilise the nomenclature of Towne et al. (2018) whereby space-only SPOD is called

POD, and the full space-time version is called SPOD. Despite the prevalence of POD in the literature, here the main focus is on SPOD as it provides a more rigorous decomposition of the dynamics as will be discussed in Section 2.2.2.

Operator-based methods do not require a data-heavy input, instead requiring only the important dynamical operators of the governing equations, typically linearised about some base flow that has some physical significance. A classical example is linear stability analysis, which provides the growth/decay characteristics of a base flow. The analysis is typically performed relative to the laminar or equilibrium solutions of the flow and using Floquet analysis the same principles can be extended to treat periodic solutions. The result is a set of modes and their associated stability exponents, which can be used to understand the long-term behaviour of the linearised dynamics. Another example is resolvent analysis, which is the primary method used in this work. Resolvent analysis reformulates the governing equations into an input-output form for the nonlinear interactions and any external forcing, with the linearised operator being the mediator between the two. When decomposed it provides a ranking of the most linearly receptive and amplified modes of the governing equations, useful for stability analysis, control, and modelling of fluids. The more in-depth discussion of the method and its application is postponed until Section 2.2.3.

2.2.2 SPOD

As mentioned previously, SPOD extends the space-only POD method to properly account for spatiotemporal coherence. Formally, SPOD can be expressed in terms of the following optimisation problem

$$\max_{\boldsymbol{\phi}(\boldsymbol{x},t)} \quad \frac{\mathscr{E}\left(\left|\left\langle \boldsymbol{q}\left(\boldsymbol{x},\, t\right),\, \boldsymbol{\phi}\left(\boldsymbol{x},\, t\right)\right\rangle_{x,t}\right|^{2}\right)}{\left\langle \boldsymbol{\phi}\left(\boldsymbol{x},\, t\right),\, \boldsymbol{\phi}\left(\boldsymbol{x},\, t\right)\right\rangle_{x,t}}, \tag{2.10}$$

where $\boldsymbol{q}\left(\boldsymbol{x},\, t\right)$ is the flow state of a realisation which is time-dependent, $\boldsymbol{\phi}\left(\boldsymbol{x},\, t\right)$ is the proposed spatio-temporal mode, the operator $\mathscr{E}\left(\cdot\right)$ is the expectation over all realisations of the flow available in the data, and the inner-product is defined over the spatial and temporal domain of the flow

$$\left\langle \boldsymbol{u},\, \boldsymbol{v}\right\rangle_{x,t} = \int_{-\infty}^{\infty}\int_{\Omega} \boldsymbol{v}^{*}\left(\boldsymbol{x},\, t\right)\boldsymbol{u}\left(\boldsymbol{x},\, t\right)\mathrm{d}\boldsymbol{x}\,\mathrm{d}t\,. \tag{2.11}$$

In words, Equation 2.10 aims to find a single mode $\boldsymbol{\phi}$ that maximises the correlation between all the available realisation of the a finite set of temporally varying flow data. The purpose of the denominator in the quotient of Equation 2.10 is to impose the additional constraint that the norm (kinetic energy) of the mode $\boldsymbol{\phi}$ is fixed at unity.

This problem can be reformulated as an eigenvalue problem as follows

$$\int_{-\infty}^{\infty}\int_{\Omega} \boldsymbol{C}\left(\boldsymbol{x},\, \boldsymbol{x}',\, \tau\right) \boldsymbol{\phi}\left(\boldsymbol{x},\, t\right) \mathrm{d}\boldsymbol{x}'\, \mathrm{d}t = \lambda \boldsymbol{\phi}\left(\boldsymbol{x},\, t\right), \tag{2.12}$$

with the tensor $\boldsymbol{C}\left(\boldsymbol{x},\, \boldsymbol{x}',\, \tau\right)$ representing the cross-correlation of the flow at two different points $\boldsymbol{x}$, and $\boldsymbol{x}'$ at a temporal offset τ. The eigenvalue λ is the maximum output of Equation 2.10 and tells us how much of the total flow energy the mode $\boldsymbol{\phi}$ captures of the original flow data. This problem is then Fourier transformed in time to get

$$\int_{\Omega} \boldsymbol{S}\left(\boldsymbol{x},\, \boldsymbol{x}',\, f\right) \boldsymbol{\psi}\left(\boldsymbol{x}',\, f\right) \mathrm{d}\boldsymbol{x}' = \lambda\left(f\right) \boldsymbol{\psi}\left(\boldsymbol{x},\, f\right), \tag{2.13}$$

where $\boldsymbol{S}\left(\boldsymbol{x},\, \boldsymbol{x}',\, f\right)$ is called the cross-spectral density tensor, which is simply the Fourier transform of the cross-correlation tensor in time. The cross-spectral density tensor encodes the repeated cross-correlations of different points in the flow with a frequency of f. The mode $\boldsymbol{\psi} e^{i2\pi f \tau}$ is a solution of the original eigenvalue problem in Equation 2.12. The result is a set of modes spatial modes $\boldsymbol{\psi}$, along with the relative importance λ at each frequency f. The original (Fourier transformed) flow field can then be expressed as a sum of the resulting modes

$$\hat{\boldsymbol{q}}\left(\boldsymbol{x},\, f\right) = \sum_{j}^{\infty} a_j\left(f\right) \boldsymbol{\psi}\left(\boldsymbol{x},\, f\right) \tag{2.14}$$

with $\hat{\boldsymbol{q}}$ is the Fourier transform of $\boldsymbol{q}$ in time. As shown in Towne et al. (2018) the modes produced from space-only POD can be expressed as the combination of the modes produced by SPOD over all frequencies. The method used to compute the SPOD modes and associated energies can also be found in Towne et al. (2018), with a summary given here in Section 4.2.4.1. A notable example where POD is able to produce well defined structures is for the wake behind bodies that exhibit a strong

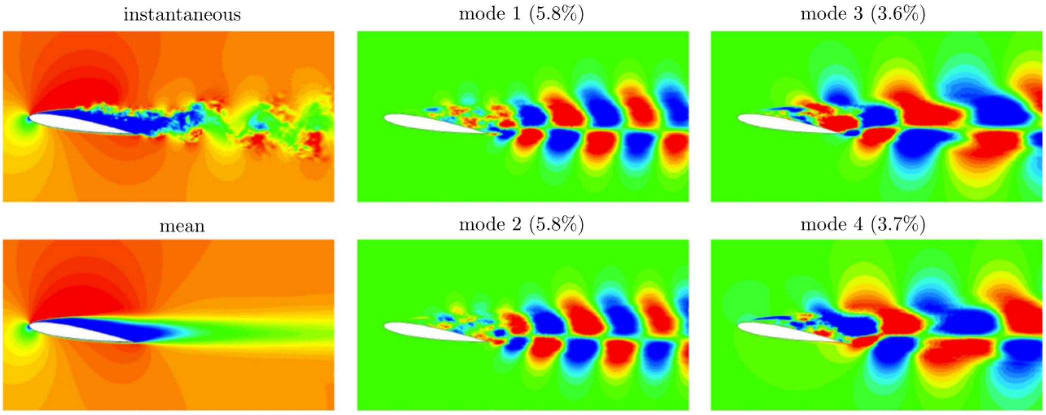

FIGURE 2.9: Space-only POD analysis of incompressible flow over a NACA0012 aerofoil at $Re = 23000$ and $\alpha = 9°$, showing a snapshot of turbulent flow, the mean field subtracted for the analysis, and the first four dominant modes. Obtained from Taira et al. (2017).

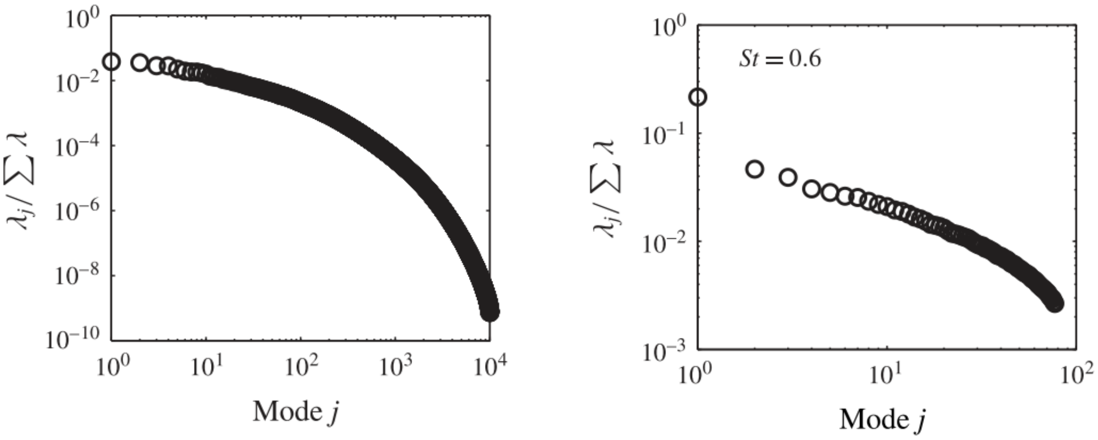

FIGURE 2.10: Relative strength of the POD (left) and SPOD (right) eigenvalues for a compressible turbulent jet ($Re = 10^6$, $Ma = 0.4$). The SPOD eigenvalues are only shown for a Strouhal number of $St = 0.6$ at which the lowest rank behaviour occurs. Obtained from Towne et al. (2018).

von Kàrmàn shedding, as shown in Figure 2.9, where roughly 19% of the fluctuation energy is captured by the first four modes (Taira et al., 2017). The success is a result of the vortex shedding being largely monochromatic, dominated by the shedding frequency of the vortices.

If a particular flow contains more than one frequency that is important in the fluctuations, the POD will produce far more muddled modes, containing information from all the frequencies that are important making it more difficult to parse the important features of the flow. To illustrate this, Towne et al. (2018) performed both a POD and SPOD analysis on a compressible turbulent jet flow. The resulting relative strength of the eigenvalues are shown in Figure 2.10, with the left being the eigenvalues for POD and the right being the eigenvalues for SPOD at a particular frequency (corresponding a Strouhal number of $St = 0.6$) that displays a large separation. The result is pronounced, with POD unable to produce the same separation between the largest eigenvalues and the remaining spectrum as SPOD, since the latter is considering individual frequencies in its decomposition. Figure 2.11 further emphasises this point, with the dominant POD (left) displaying very little local coherence and thus providing very little insight into the dynamics of the flow, whereas the dominant SPOD modes at $St = 0.6$ (right) displaying well defined wavepacket structures with only local support which can be linked to specific instabilities in the flow. As a general note, if a flow has particular structures that clearly arise at regular intervals, such as von Kàrmàn shedding, then it can be predicted ahead of time what frequency the dominant SPOD modes will be present allowing the analysis to be performed with this in mind to minimise the total cost. In other words, the analysis can be performed at a slightly lower cost if some patterns of the flow are known a priori. For these fundamental reasons, in this work SPOD is

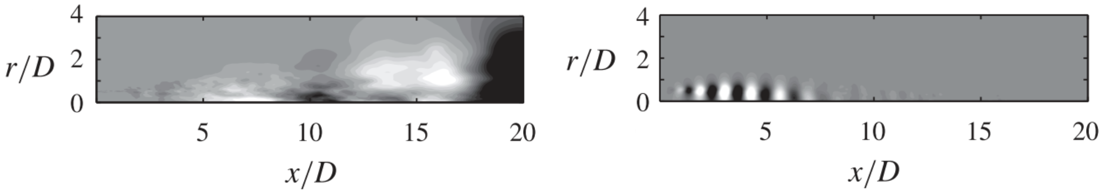

FIGURE 2.11: Dominant POD mode (left) and SPOD mode at $St = 0.6$ (right) for the same compressible turbulent jet as in Figure 2.10. Obtained from Towne et al. (2018).

used to modally analyse the data sets obtained from DNS, as we can be confident that the resulting modes are not a complex mix of multiple spectral components.

SPOD has been applied to many common flows, such as pipe flows (Hellström and Smits, 2014), boundary layers (Tutkun and George, 2017), wakes (Araya et al., 2017; Tutkun et al., 2008), and aerofoil flows (Abreu et al., 2017). Either experimental or simulation (DNS or LES typically) have been shown to be effective as inputs in Sinha et al. (2014); Semeraro et al. (2016); Towne et al. (2015); Schmidt et al. (2018). The main downsides of SPOD relate to its reliance on data. For example, a typical two-dimensional turbulent flow past an aerofoil can have of the order of 10000 spatial points. To determine the first M modes, using the methodology described in Towne et al. (2018) which avoids explicitly forming the cross-correlation tensors, the flow field needs to be split into M blocks of data each of which being large enough to capture the temporal coherence of the data. As M grows larger the required set of temporal data required to determine the trailing modes can become prohibitive, requiring the order of GB or TB of memory. This is not a significant problem when there are clearly dominant modes, but in cases where flows have a more broadband spectral structure the cost of SPOD can become prohibitively expensive. This problem generally becomes worse as the Reynolds number increases due to the additional small structures that require larger spatial and temporal resolution to properly capture. The method described in Towne et al. (2018) for computing SPOD modes, is similar to the snapshot method commonly used to compute POD modes (Sirovich, 1987), reducing the cost of computing the modes and eigenvalues at the expense of the spectral resolution analogous to Welch's method. There is also a burden on the researcher to obtain high quality sets of data from experiment or simulation which can be rather difficult and time consuming on its own. To restate the main goals of this thesis, we aim to be able to construct exact solutions as well as statistical approximations to turbulent flows using some form of coherent structure as the basis. SPOD, although providing a physically significant basis requires large sets of data to obtain. Ideally, a set of modes that provide an efficient basis can be obtained without requiring a complete simulation of the flow that is being studied. Resolvent analysis, discussed next, is better suited to this task. Resolvent analysis is an operator-based method that only requires a base flow to output a set of spatially and temporally coherent modes, and as discussed in Towne et al. (2018) these resolvent modes have are closely linked to SPOD modes under certain circumstances.

2.2.3 Resolvent Analysis

Resolvent analysis is an operator-based modal analysis technique that focuses on the pseudo-spectra of the linearised Navier-Stokes equations, providing insight to the linear growth mechanisms of the system subject to harmonic forcing Trefethen et al. (1993); Schmid and Henningson (2001); Jovanović and Bamieh (2005). Consider the linear dynamical system with an added forcing term at a particular frequency

$$\frac{\mathrm{d}\boldsymbol{q}}{\mathrm{d}t} = \boldsymbol{A}\boldsymbol{q} + \hat{\boldsymbol{f}}e^{i\omega t}, \tag{2.15}$$

where $\hat{\boldsymbol{f}}$ is the magnitude of the forcing, and ω is the frequency of the forcing. The response to such a forcing (the particular integral of the differential equation) will have same frequency, $\boldsymbol{q} = \hat{\boldsymbol{q}}e^{i\omega t}$. Substituting this in and factoring out the common exponential from each term we get the following system

$$\hat{\boldsymbol{q}} = \left(i\omega\boldsymbol{I} - \boldsymbol{A}\right)^{-1}\hat{\boldsymbol{f}} = \boldsymbol{H}_{\omega}\hat{\boldsymbol{f}}, \tag{2.16}$$

which shows that the magnitude of the response is determined by the magnitude of the forcing and any additional amplification obtained from the operator $\boldsymbol{H}_{\omega} = \left(i\omega\boldsymbol{I} - \boldsymbol{A}\right)^{-1}$, which is defined to be the resolvent operator. Assuming the linear dynamical operator of the system has a well-defined eigendecomposition, i.e. $\boldsymbol{A} = \boldsymbol{V}\boldsymbol{\Lambda}\boldsymbol{V}^{-1}$ exists, then we can obtain the following bounds

$$\left\|i\omega\boldsymbol{I} - \boldsymbol{\Lambda}\right\|^{-1} \leq \left\|\boldsymbol{H}_{\omega}\right\| \leq \underbrace{\left\|\boldsymbol{V}\right\|\left\|\boldsymbol{V}^{-1}\right\|}_{\kappa(\boldsymbol{V})}\left\|i\omega\boldsymbol{I} - \boldsymbol{\Lambda}\right\|^{-1}. \tag{2.17}$$

This bound on the resolvent shows that the resolvent can amplify the forcing of the system not only through linear instability of a particular mode (system resonance), but also through the condition number of the eigenvector matrix $\kappa\left(\boldsymbol{V}\right)$, called pseudo-resonance. If $\boldsymbol{A}$ is normal ($\boldsymbol{A}^{*}\boldsymbol{A} = \boldsymbol{A}\boldsymbol{A}^{*}$) then it follows that the eigenvectors form an orthonormal basis, thus giving $\boldsymbol{V}$ a unitary condition number. If, however, $\boldsymbol{A}$ is non-normal, then $\kappa\left(\boldsymbol{V}\right) > 1$ leading to pseudo-resonance of the solution. This linear amplification due to pseudo-resonance is observed in practice as an initial transient in the system response. This non-normal amplification of can be rather large, especially as the non-normality of $\boldsymbol{A}$ increases, leading to very large growth simply due to linear mechanisms.

When applied to nonlinear systems, following the formalism of McKeon and Sharma (2010), the interpretation is slightly different. First consider the nonlinear dynamical system

$$\frac{\mathrm{d}\boldsymbol{q}}{\mathrm{d}t} = \boldsymbol{N}(\boldsymbol{q}). \tag{2.18}$$

Taking a certain base state $\boldsymbol{q}_b$ and linearising about it, without removing any of the higher-order terms from the nonlinearity, leads to the general result

$$\frac{\mathrm{d}\boldsymbol{q}'}{\mathrm{d}t} = \boldsymbol{N}_b + \boldsymbol{L}\boldsymbol{q}' + \boldsymbol{f}', \tag{2.19}$$

where $\boldsymbol{q}'$ is the state fluctuation about $\boldsymbol{q}_b$, $\boldsymbol{N}_b = \boldsymbol{N}(\boldsymbol{q}_b)$, and $\boldsymbol{f}' = \boldsymbol{f}(\boldsymbol{q}')$. Fourier transforming in time we have the following

$$\hat{\boldsymbol{q}}' = (i\omega\boldsymbol{I} - \boldsymbol{L})^{-1}\hat{\boldsymbol{f}}' = \boldsymbol{H}_\omega\hat{\boldsymbol{f}}' \tag{2.20}$$

which is precisely the same expression obtained for the linear system, except now instead of having an external monochromatic forcing, the forcing obtained from the nonlinear interactions of the flow. This forcing term $\hat{\boldsymbol{f}}'$ will in general have a very broadband content, and so Equation 2.20 shows that the state of a nonlinear system is a result of the nonlinear interactions of the system over all the total spectrum, moderated by the resolvent operator $\boldsymbol{H}_\omega$. This reciprocatory relationship over the whole spectrum is summarised in Figure 2.12. Under this framework, the resolvent provides framework to interpret turbulence as the complicated nonlinear triadic interactions at multiple frequencies amplified by the resolvent. The broadband content of the state means that the resolvent has to be analysed at all frequencies ω to provide insight into these interactions. However, simply by inspection it is clear that non-normality would play a key role in amplifying certain frequencies of the system. In the case of fluid dynamics, shear stresses have the effect of increasing the non-normality of the linearised Navier-Stokes equations $\boldsymbol{L}$, discussed in detail in Symon et al. (2018). The resulting large non-normal amplifications can trigger subcritical transitions to turbulence.

The resolvent modes are obtained via a Singular Value Decomposition (SVD) of the operator as $\boldsymbol{H}_\omega = \boldsymbol{\Psi}_\omega\boldsymbol{\Sigma}_\omega\boldsymbol{\Phi}_\omega$. The left singular matrix $\boldsymbol{\Psi}_\omega$ contains the response modes, and the right singular matrix $\boldsymbol{\Phi}_\omega$ contains the forcing modes. These modes are ordered in a decreasing fashion, such that the maximal response of the system at the frequency ω and the associated forcing that produces it can be obtained from the first response and forcing modes in $\boldsymbol{\Psi}$ and $\boldsymbol{\Phi}$ respectively. The magnitude of this response is given by the associated singular value in $\boldsymbol{\Sigma}_\omega$. This decomposition then provides the basis and relative strength describing the receptive directions of the linear dynamics as well as the forcing that will produce them. If there is a large separation of scale between the singular values, i.e. if the first few singular values are much larger than the successive

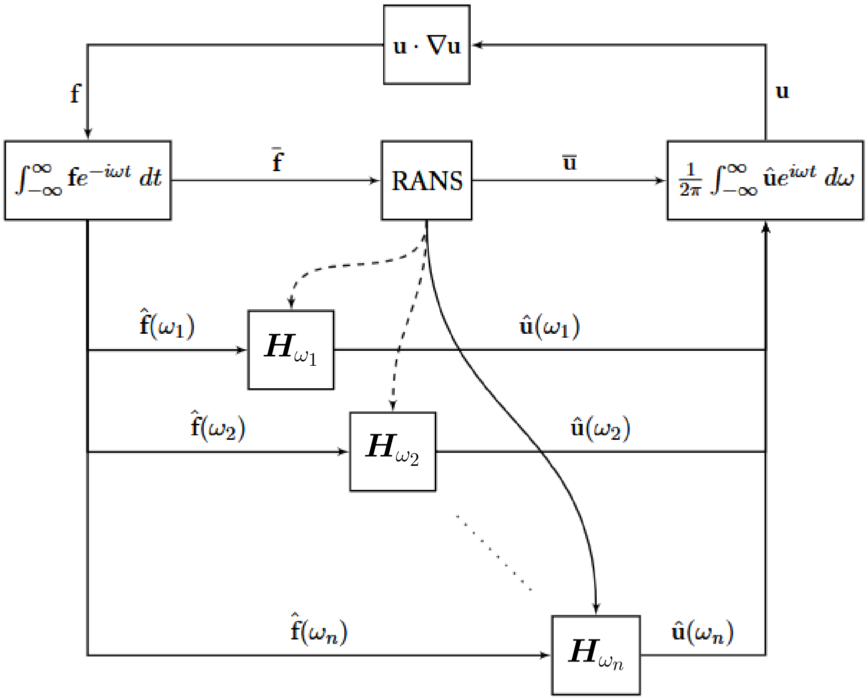

FIGURE 2.12: Block diagram representation of the relationship between the flow state, u and nonlinear forcing, f that maintains turbulent flow. Obtained from Sharma (2019).

singular values, then the resolvent is said to be low rank and can be accurately approximated with only the modes associated with the largest singular values.

In McKeon et al. (2013), where this framework for modelling fluids using resolvent analysis was introduced, a model is constructed for pipe flow, using the low-rank nature of the resolvent, which is used to analyse the critical layer framework for the dominant structures in the turbulent flow. There are many examples of the resolvent being used for many different types of flow, possessing a very broad literature. Some examples include modelling cavity flow (Gómez et al., 2016) and wall turbulence (Gayme and Minnick, 2019), reconstructing flow data (Beneddine et al., 2017), controlling cylinder wakes (Jin et al., 2022) and Couette flow (Gayme, 2010), and to determine optimal forcings of jets (Garnaud et al., 2013).

Within the framework of McKeon and Sharma (2010), coherent structures can be interpreted as solutions in the frequency domain constituted of multiple resolvent modes and their relative motions. McKeon et al. (2013) introduced the idea of “closing the loop” for resolvent analysis, where not only the linear responses of the flow were modelled, but the full nonlinear problem is included as part of the analysis. The idea of using resolvent analysis for the purpose of solving the complete nonlinear problem was pursued in Barthel et al. (2021), where the resolvent modes were used as a basis to reconstruct Taylor vortices in a Taylor-Couette flow. By retaining a relatively small number of resolvent modes (22 and 10 modes below and beyond a spectral cut-off for

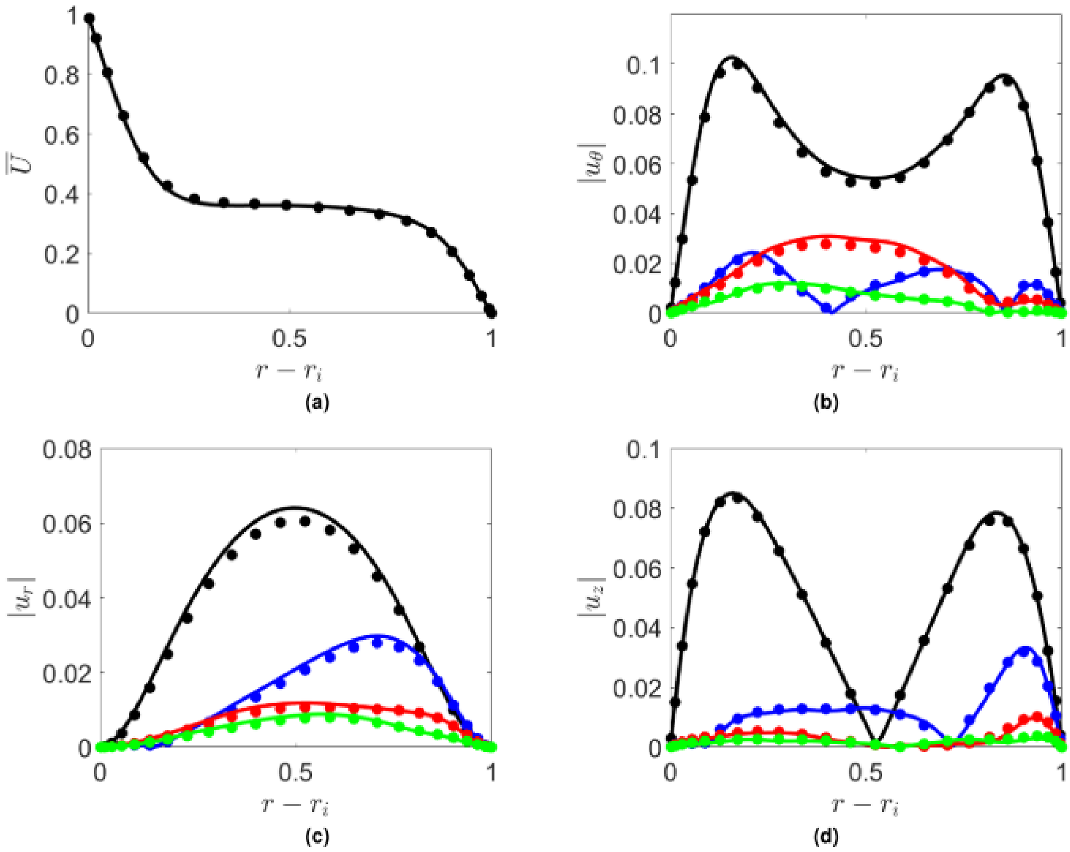

FIGURE 2.13: Resolvent-based solution for a Taylor-Couette flow at $Re = 400$, showing the mean velocity derived from the Reynolds stresses of the model solution (a), and the first four Fourier modes obtained from the model solution (b), (c), and (d), all compared to the DNS solution shown at the dots. Obtained from Barthel et al. (2021)

the axial wavenumber) the dominant Fourier modes could be reconstructed by solving an optimisation problem as shown in Figure 2.13. This idea is central to this work, as we perform the same fundamental steps to allow the construction of exact solutions to the Navier-Stokes equations in terms of resolvent modes, in addition to using the modes as a low-order basis to approximate the statistics of chaotic/turbulent systems.

With the idea of using resolvent modes as a basis to produce solutions to the Navier-Stokes equations, closing the loop, Sharma et al. (2016b) provided evidence that the response modes of resolvent analysis provide a particularly efficient basis to express ECSs for pipe and channel flows. Figure 2.14 displays an illustrative, albeit optimistic, result from Sharma et al. (2016b) displaying a particular ECSs (left) studied in Sharma et al. (2016b), along with its projection onto five (centre) and a single (right) resolvent modes for each Fourier mode in the homogeneous flow directions, capturing 98% and 95% of the fluctuation energy, respectively. This represents a very large dimensionality reduction while retaining the qualitative, and most of the quantitative features of the solution. The link between resolvent analysis, DMD/Koopman

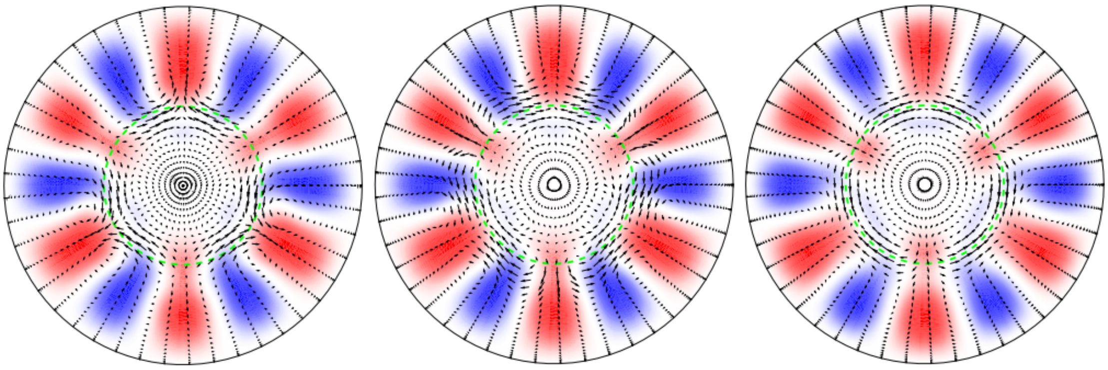

FIGURE 2.14: ECSs solution for a pipe flow (left), the projection onto the five dominant resolvent response modes (centre) for each Fourier mode in the homogeneous directions, and the projection onto a single dominant resolvent response mode (right), capturing 95% and 98% of the fluctuation energy, respectively. Obtained from Sharma et al. (2016b).

analysis, and ECSs is discussed in Sharma et al. (2016a), providing an analytical reason for resolvent modes providing an efficient basis for ECSs.

Figure 2.15 displays the percentage of energy capture for the projection of a channel flow solution in Sharma et al. (2016b) onto a truncated set of resolvent modes for all the velocity components (u, v, and v), as well as the dominant Reynolds stress ($\overline{uv}$) and the total nonlinear convection ($\boldsymbol{u} \cdot \boldsymbol{\nabla} \boldsymbol{u}$). The projection clearly captures the streamwise velocity very accurately using only a small number of modes, while the other velocity components, requiring a larger set of modes to be faithfully recovered. This projection is still able to capture 92% of the fluctuation energy with five resolvent modes, implying that the majority of the energy is stored in the streamwise components anyway. It is argued in Sharma et al. (2016b) that the fact that the nonlinear interactions are not completely captured by the truncation is a feature of resolvent analysis filtering out the nonlinear terms that are not important to the Navier-Stokes equations.

With all of this in mind, there is good reason to believe that using resolvent modes provide a very efficient basis for expressing ECSs without having to rely on the large sets of data that limits applications of SPOD. These basis functions are especially suited to model time-periodic exact solutions, as a hierarchy of modes is obtained at each temporal frequency (and spatial wavenumber for problems with statistically homogeneous spatial directions), so that temporal periodicity is built in explicitly in the modal expansion. As a final point, a method proposed by Ahmed and Sharma (2020) utilises resolvent modes as a basis to search for new equilibrium and periodic solutions to Couette flow using a "project-then-search" methodology. In this method known solutions or close recurrences are projected onto the resolvent subspace which is used as the new initial condition for the search of new solutions, providing examples of solutions that had not yet been observed in the literature. The current

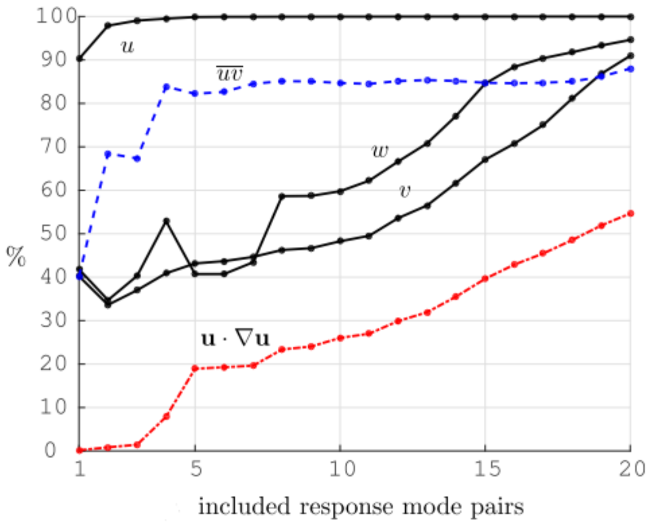

FIGURE 2.15: Percentage energy capture of a channel flow ECS for each velocity component, dominant Reynolds stress, and nonlinear convection term. Obtained from Sharma et al. (2016b)

literature indicates that resolvent modes can be particularly useful in modelling ECSs for certain wall-bounded flows without requiring the large data overhead of SPOD.

2.3 Summary of the Gaps in the Literature

The gaps in the literature are two-fold. The first, from the Section 2.1 relates the practicality of the available methods to find invariant solutions of high-dimensional chaotic systems. Currently the methods available suffer from issues related to robustness to initial guesses and/or convergence rates, problems that are built into the dynamics of the chaotic systems, especially as the dimensions increase. The second gap relates to resolvent analysis. As discussed, Barthel et al. (2021) aimed to construct a model for Taylor-Couette flow based solely on resolvent modes. This “closes the loop” of resolvent analysis, providing dynamical information related to the modes for particular flow, rather than the kinematic information from the singular values which do not necessarily represent the flow in question. Currently there has not been any other attempt to extend this for more general flows.

Combining the variational optimisation of Farazmand (2016); Azimi et al. (2022) with a projection onto a resolvent basis provides a method to compute dynamical weights for the resolvent modes, constructing a model for the flow based solely on resolvent modes. This would be a more complete version of what is done in Barthel et al. (2021). The work in this thesis describes a general framework upon which this can be achieved for any wall-bounded (internal or external) flow. It is shown that this can not only provide the desired dynamical information associated with each resolvent mode, but additionally improve the performance of the variational optimisation.

Chapter 3

Variational Optimiser

This chapter is devoted to the derivation of the governing equations for the gradient-based variational optimisation of wall-bounded incompressible fluid flows. This method facilitates the construction of the resolvent-based models, finding the best possible combination of modes that satisfy the Navier-Stokes equations. The mathematics is presented for a non-specific flow domain with a mix of no-slip and periodic boundary conditions, to emphasise the general applicability of the method, and how the issues that arise are directly related to the presence of the walls in the domain. The chapter then moves to the Galerkin projection of the optimisation onto a subspace defined by a set of incompressible modes that obey the boundary conditions. This projection constitutes a general solution for the issues that are encountered with applying the variational optimiser to wall-bounded incompressible flows.

3.1 Optimisation Problem for the Navier-Stokes Equations

In this section the general process of setting up the optimisation problem for which minima represent solutions to the Navier-Stokes equations is described. The procedure is described for a simple flow domain that contains a mix of periodic and no-slip boundary conditions for any number of spatial dimensions, with an application to channel flow in Chapter 6.

Assume $\boldsymbol{u}$ is a three-dimensional vector field defined on a simply connected and compact domain $\Omega \subseteq \mathbb{R}^n$ where $n \in \mathbb{N}$ is the number of dimensions of the underlying space (typically $n = 2$ or 3). Also denote the boundary of the domain Ω with $\partial\Omega$. Thus, the interior of the domain can be expressed as $\tilde{\Omega} = \Omega \setminus \partial\Omega$. Interest is only given to solutions of finite time, thus define the interval $[0, T]$, where $T \in \mathbb{R}_{>0}$, to be the length of the time interval over which solutions to the Navier-Stokes equations are considered. Time periodic solutions to the Navier-Stokes equations will be sought. A combination of the spatial domain and time horizon of the solutions is defined as $\Omega_t = \Omega \times [0, T]$. The pressure field, p, is a scalar field defined over the same domain as $\boldsymbol{u}$. Typically the domain Ω is defined by some Cartesian or curvilinear coordinate system, with orthogonal directions, with some of those directions being statistically homogeneous and the other being inhomogeneous. Periodic boundary conditions are imposed on the homogeneous directions, and some form of no-slip boundary condition is assumed for the inhomogeneous directions. This motivates a partitioning of the domain boundary according to the different boundary conditions. This partition is summarised as $\partial\Omega = \partial\Omega_{\mathrm{ns}} \cup \partial\Omega_{\mathrm{pi}} \cup \partial\Omega_{\mathrm{po}}$, where $\partial\Omega_{\mathrm{ns}}$ is the portion of $\partial\Omega$ for which a no-slip boundary condition is imposed, and $\partial\Omega_{\mathrm{pi}}$ and $\partial\Omega_{\mathrm{po}}$ are the inflow and outflow periodic boundaries. The corresponding no-slip and periodic boundary conditions are thus denoted as $\boldsymbol{u}|_{\partial\Omega_{\mathrm{ns}}} = \boldsymbol{C}$ and $\boldsymbol{u}|_{\partial\Omega_{\mathrm{pi}}} = \boldsymbol{u}|_{\partial\Omega_{\mathrm{po}}}$, respectively. The function $\boldsymbol{C}$ is a mapping $\boldsymbol{C} \colon \partial\Omega_{\mathrm{ns}} \to \mathbb{R}$ that prescribes the value of the velocity at the no-slip boundary, which here is assumed to be constant in time.

The Navier-Stokes equations can be expressed as

$$\frac{\partial \boldsymbol{u}}{\partial t} = -\left(\boldsymbol{u} \cdot \boldsymbol{\nabla}\right)\boldsymbol{u} + \frac{1}{Re}\Delta \boldsymbol{u} - \boldsymbol{\nabla} p, \tag{3.1a}$$

$$\boldsymbol{\nabla} \cdot \boldsymbol{u} = 0. \tag{3.1b}$$

We define an inner product on the total spatiotemporal domain Ω_t is defined as such

$$\langle \boldsymbol{u}, \boldsymbol{v} \rangle_{\Omega_t} := \int_0^T \int_\Omega \boldsymbol{u} \cdot \boldsymbol{v} \, \mathrm{d}V \, \mathrm{d}t, \tag{3.2}$$

which induces the norm

$$\|\boldsymbol{u}\|_{\Omega_t}^2 := \langle \boldsymbol{u}, \boldsymbol{u} \rangle_{\Omega_t}, \tag{3.3}$$

for which any velocity field with finite kinetic energy $\boldsymbol{u}$ is a member of some Hilbert space, denoted here by χ. Although the inner product of Equation 3.2 is only strictly defined for two vector fields, it can be extended to scalar fields by simply replacing the dot product inside the integral with a scalar product. This is not the only norm used in this thesis. Typically any norm denoted without the subscript Ω_t refers to the standard Euclidean norm for the vector spaces of $\mathbb{R}^n$ or $\mathbb{C}^n$. The exception to this is in chapter 5, where a specific norm is defined for dynamical systems that are not spatially extended.

The variational optimisation methodology seeks a solution to Equation 3.1a, given the incompressibility constraint Equation 3.1b, by modifying the velocity field $\boldsymbol{u}$ to minimise an objective functional that is zero only if the governing equations are satisfied. To properly express this optimisation problem, it is necessary to define both the space over which the given optimisation variables be varied as well as the

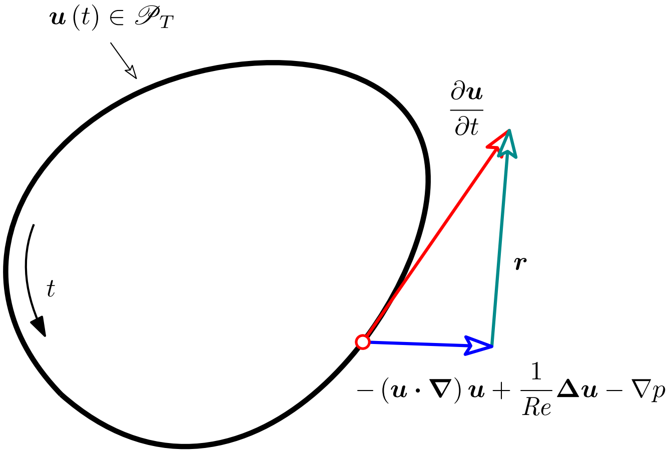

FIGURE 3.1: Schematic of an arbitrary loop in state-space that does not satisfy the governing equation as its tangent vector $\partial \boldsymbol{u}/\partial t$ is not aligned with right hand side of the momentum equations $(\boldsymbol{u} \cdot \boldsymbol{\nabla})\,\boldsymbol{u} + (1/Re)\,\boldsymbol{\Delta u} - \boldsymbol{\nabla} p$.

objective that should be minimised. First, the optimisation space is defined as follows

$$\mathscr{P}_T := \left\{\boldsymbol{u} \in \chi \,:\, \boldsymbol{\nabla} \cdot \boldsymbol{u} = 0,\ \boldsymbol{u}|_{t=0} = \boldsymbol{u}|_{t=T},\ \boldsymbol{u}|_{\partial\Omega_{\text{ns}}} = \boldsymbol{C},\ \boldsymbol{u}|_{\partial\Omega_{\text{pi}}} = \boldsymbol{u}|_{\partial\Omega_{\text{po}}}\right\}. \tag{3.4}$$

In words, the space $\mathscr{P}_T \subset \chi$ is the space of all incompressible flows of period T with finite kinetic energy, which are periodic in time and obey the no-slip and periodic boundary conditions on $\partial\Omega_{\text{ns}}$, $\partial\Omega_{\text{pi}}$, and $\partial\Omega_{\text{po}}$, respectively. There is a subset of $\mathscr{P}$ that also satisfies Equation 3.1a in the domain Ω. To find elements of this subspace a mapping can be introduced, $\mathcal{R} : \mathscr{P} \to \mathbb{R}_{\geq 0}$, for which $\boldsymbol{u} \in \mathscr{P} \mapsto \mathcal{R}[\boldsymbol{u}] = 0$ if and only if $\boldsymbol{u} \in \mathscr{P}$ and $\boldsymbol{u}$ also satisfies Equation 3.1a for all $\boldsymbol{x} \in \Omega$. This is equivalent to saying that the global minima of $\mathcal{R}$ correspond to periodic solutions to the Navier-Stokes equations in Ω. A more physical interpretation of $\mathcal{R}$ is that of a measure for the violation of the momentum equation provided by a trial flow field $\boldsymbol{u} \in \mathscr{P}$, which should be minimised to solve the governing equations. The expression for such a mapping is obtained by first defining the violation of Equation 3.1a at each space-time location in the field, called the local residual as such

$$\boldsymbol{r} := \frac{\partial \boldsymbol{u}}{\partial t} + (\boldsymbol{u} \cdot \boldsymbol{\nabla})\,\boldsymbol{u} - \frac{1}{Re}\Delta\boldsymbol{u} + \boldsymbol{\nabla} p. \tag{3.5}$$

The geometric representation of the local residual is shown in Figure 3.1. A given periodic velocity field $\boldsymbol{u}$ that doesn't satisfy Equation 3.1a can be represented by a loop in some strictly infinite-dimensional state-space. At each point along the loop, there is some forcing imposed by the right-hand side of the Navier-Stokes equations that prescribes how a solution should evolve, and the local residual is the vector between this and actual evolution of the loop in time.

Taking the norm of the local residual leads to a mapping for each element of $\mathscr{P}_T$ to a non-negative number as follows

$$\mathcal{R}\left[\boldsymbol{u}\right] := \frac{1}{2}\|\boldsymbol{r}\|^2_{\Omega_t}, \tag{3.6}$$

which here is called the global residual. It should be noted that if $\boldsymbol{u} \in \mathscr{P}_T$, for a given period T, then generally $\boldsymbol{r} \notin \mathscr{P}_T$ due to the momentum equation not being satisfied at the boundary. This fact has important implications for finding solutions to the optimisation problem, which is discussed in depth in Section 3.3.1. The global residual as defined in Equation 3.6 possesses the desired properties of the mapping discussed earlier, as $\mathcal{R}\left[\boldsymbol{u}\right] = 0$ if and only if $\boldsymbol{r} = 0$ for all points in the spatiotemporal domain Ω_t which is in turn true if and only if $\boldsymbol{u} \in \mathscr{P}_T$ is a solution to the Navier-Stokes equations, otherwise $\mathcal{R}$ is positive. Given that $\boldsymbol{u}$ is assumed to be smooth, $\mathcal{R}$ must also be a smooth non-negative scalar field defined over $\mathscr{P}_T$ that possesses absolute minima at the best possible solution of Equation 3.1a for any given constraints on $\boldsymbol{u}$.

Geometrically, minimising $\mathcal{R}$ is equivalent to continuously deforming a loop in the infinite-dimensional state-space of the flow field, constrained to the linear subspaces that represent the boundary conditions and incompressibility conditions. This process terminates when the rate of change of the state vector and nonlinear operator ($\mathcal{N}$) are as closely aligned as possible, as shown in Figure 3.2. An alternative perspective is to view the scalar field $\mathcal{R}$ as a potential field, where the modification of the flow field $\boldsymbol{u}$ to try to reduce $\mathcal{R}$ can be seen as an evolution of a new dynamical system for $\mathscr{P}$ itself. In this view, the minimisers (global and local) of $\mathcal{R}$ are fixed-point attractors. This perspective is further discussed in Section 3.2 where the equivalence of adjoint solver of Farazmand (2016); Azimi et al. (2022); Ashtari and Schneider (2023) and residual optimisation is shown.

Finally, the solution of Equation 3.1 can be expressed in terms of the following optimisation problem

$$\min_{\boldsymbol{u}\in\mathscr{P}_T,\, T} \quad \mathcal{R}\left[\boldsymbol{u}\right]. \tag{3.7}$$

This simple expression contains all the constraints on $\boldsymbol{u}$ (boundary conditions, periodicity, and incompressibility) within the constrained optimisation space $\mathscr{P}_T$. The mathematical consequences of these constraints on $\boldsymbol{u}$ become important for the derivation of the gradient of $\mathcal{R}$. The optimisation problem Equation 3.7 is a nonlinear non-convex optimisation problem, and therefore possesses many possible solutions. Since global minima are equivalent to periodic solutions to the Navier-Stokes equations, it is not known exactly how many global minima should exist. However, optimisation theory guarantees there will at least be multiple local minima. It has been suggested in Zheng et al. (2024) that local minima can represent “ghosts” of solutions that exist at different parameter values. These ghosts still influence the dynamics

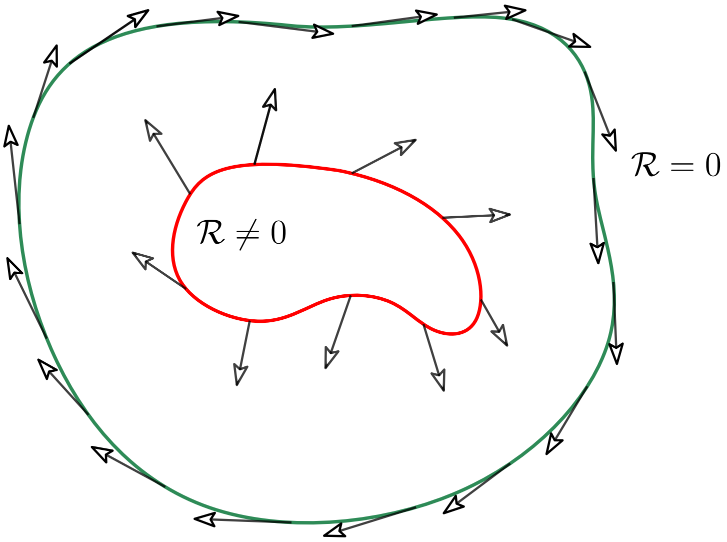

FIGURE 3.2: Evolution of a state-space loop, starting with the red inner loop that does not obey the Navier-Stokes equations eventually being modified under some optimisation law to the green loop that does obey the Navier-Stokes equations.

despite not being strictly present. Regardless of the interpretation, it is guaranteed that Equation 3.7 will converge to some minima.

3.2 Equivalence of Adjoint Dynamics and Gradient-Based Optimisation

In the literature there are two main variational approaches that have been utilised to find invariant solutions to the Navier-Stokes equations: first the direct approach pioneered in Lan and Cvitanović (2004), and the adjoint solver developed in Farazmand (2016); Azimi et al. (2022). In this subsection it will be shown that the adjoint solver is mathematically equivalent to the variational optimisation approach developed here in the special case of the gradient descent algorithm being used to solve Equation 3.7. The methods described here are not on their own new, but to the best of the authors knowledge the explicit mathematical link between the adjoint dynamics of Farazmand (2016) and the variational optimisation methodology of Azimi et al. (2022); Ashtari and Schneider (2023) has never been shown.

Using the residual definitions from Equation 3.5 and Equation 3.6, the goal of the adjoint method is to construct a new set of dynamics for $\boldsymbol{u} \in \mathscr{P}_T$ in some “fictitious” variational time τ as follows

$$\frac{\partial \boldsymbol{u}}{\partial \tau} = \mathcal{G}\left(\boldsymbol{u}\right), \tag{3.8}$$

such that

$$\frac{\partial \mathcal{R}}{\partial \tau} \leq 0. \tag{3.9}$$

Using the definition of the global residual, an expression for the evolution of $\mathcal{R}$ with respect to τ is given as

$$\frac{\partial \mathcal{R}}{\partial \tau} = \frac{1}{2}\frac{\partial}{\partial \tau}\|\boldsymbol{r}\|^2_{\Omega_t} = \left\langle \frac{\partial \boldsymbol{r}}{\partial \tau}, \boldsymbol{r} \right\rangle_{\Omega_t}.$$

Using the definition of the derivative for ordinary functions gives

$$\frac{\partial \boldsymbol{r}}{\partial \tau} = \lim_{\Delta\tau \to 0} \frac{\boldsymbol{r}(\boldsymbol{u} + \Delta \boldsymbol{u}) - \boldsymbol{r}(\boldsymbol{u})}{\Delta \tau} = \lim_{\Delta\tau \to 0} \frac{\boldsymbol{r}(\boldsymbol{u} + \Delta\tau \mathcal{G}(\boldsymbol{u})) - \boldsymbol{r}(\boldsymbol{u})}{\Delta \tau}, \tag{3.10}$$

where $\Delta \boldsymbol{u}$ is the change of the velocity due to a temporal perturbation $\tau + \Delta\tau$ prescribed by the operator $\mathcal{G}$. The last expression in Equation 3.10 is equal to the Gateaux derivative of $\boldsymbol{r}$ at $\boldsymbol{u}$ with respect to the direction $\mathcal{G}$, denoted here as

$$\frac{\partial \boldsymbol{r}}{\partial \tau} = \mathcal{L}_{\boldsymbol{r}}(\boldsymbol{u}, \mathcal{G}), \tag{3.11}$$

which when substituted back into Equation 3.2 gives the general expression for the evolution of the global residual under the variational dynamics

$$\frac{\partial \mathcal{R}}{\partial \tau} = \langle \mathcal{L}_{\boldsymbol{r}}(\boldsymbol{u}, \mathcal{G}), \boldsymbol{r} \rangle_{\Omega_t}. \tag{3.12}$$

The method of Lan and Cvitanović (2004) sets the variational dynamics $\mathcal{G}$ such that $\mathcal{L}_{\boldsymbol{r}}(\boldsymbol{u}, \mathcal{G}) = -\boldsymbol{r}$, which implies

$$\frac{\partial \mathcal{R}}{\partial \tau} = -\|\boldsymbol{r}\|^2_{\Omega_t} = -2\mathcal{R}. \tag{3.13}$$

This leads to an exponential convergence of $\mathcal{R}$ to zero. The Gateaux derivative is defined by

$$\mathcal{L}_r(\boldsymbol{u}, \mathcal{G}) = \lim_{\epsilon \to 0} \frac{\boldsymbol{r}(\boldsymbol{u} + \epsilon \mathcal{G}) - \boldsymbol{r}(\boldsymbol{u})}{\epsilon}. \tag{3.14}$$

Taking a Taylor expansion of the local residual gives

$$\boldsymbol{r}(\boldsymbol{u} + \epsilon \mathcal{G}) = \boldsymbol{r}(\boldsymbol{u}) + \epsilon \boldsymbol{J}_{\boldsymbol{r}}(\boldsymbol{u})\,\mathcal{G} + \mathcal{O}\left(\epsilon^2\right), \tag{3.15}$$

where $\boldsymbol{J}_{\boldsymbol{r}}$ denotes the linearisation of the residual expression in Equation 3.5, equivalent to the Jacobian matrix in a finite-dimensional context. Ignoring all the higher order ϵ terms in Equation 3.15, and substituting it into Equation 3.14 implies the system that needs to be solved at each step of the method of Lan and Cvitanović (2004) is

$$\mathcal{L}_{\boldsymbol{r}}(\boldsymbol{u}, \mathcal{G}) = \boldsymbol{J}_{\boldsymbol{r}}(\boldsymbol{u})\,\mathcal{G} = -\boldsymbol{r}, \tag{3.16}$$

which is precisely the linear system solved at each iteration of the Newton-Raphson method, solving for the residual $\boldsymbol{r}$ over the whole trajectory $\boldsymbol{u}$.

The continuous dynamics in τ in principle ensures that the Newton flow method converged globally, however, as noted in Farazmand (2016) when discretised using a first order Euler scheme for τ, a damped Newton-Raphson method is recovered as such

$$\boldsymbol{u}_{k+1} = \boldsymbol{u}_k + \Delta\tau \boldsymbol{J}_{\boldsymbol{r}}^{-1} \boldsymbol{r} \tag{3.17}$$

thus losing the guaranteed global convergence but retaining the rapid convergence rates typical for Newton-Raphson iterations when close to the solution.

The alternative approach taken in Farazmand (2016) and Azimi et al. (2022) is to take the adjoint of the Gateaux derivative in Equation 3.12 (denoted with the superscript †) as follows

$$\frac{\partial \mathcal{R}}{\partial \tau} = \left\langle \mathcal{G}, \mathcal{L}_{\boldsymbol{r}}^{\dagger} \left(\boldsymbol{u}, \boldsymbol{r}\right) \right\rangle_{\Omega_t}. \tag{3.18}$$

where $(\cdot)^{\dagger}$ denotes the adjoint of a given operator. The variational evolution operator $\mathcal{G}$ is then set to $\mathcal{G} = -\mathcal{L}_{\boldsymbol{r}}^{\dagger}\left(\boldsymbol{u}, \boldsymbol{r}\right)$, which ensures a monotonic decrease in $\mathcal{R}$. This provides a simpler closed-form expression for $\mathcal{G}$, as opposed to the Newton evolution case above where a linear system has to be solved at each iteration to find $\mathcal{G}$. However, the gain in computational simplicity comes at the cost of the exponential convergence.

Some small evolution of $\boldsymbol{u}$ under the dynamics of $\mathcal{G}$ produces a small change in the global residual, denoted as $\delta\mathcal{R}$. Using Equation 3.18 the following expression for this variation in the global residual can be expressed as

$$\delta\mathcal{R} = \left\langle \mathcal{L}_{\boldsymbol{r}}^{\dagger}\left(\boldsymbol{u}, \boldsymbol{r}\right), \Delta\tau\mathcal{G} \right\rangle_{\Omega_t}. \tag{3.19}$$

Variational calculus provides the following identity

$$\delta\mathcal{R} = \left\langle \frac{\delta\mathcal{R}}{\delta\boldsymbol{u}}, \Delta\boldsymbol{u} \right\rangle_{\Omega_t} = \left\langle \frac{\delta\mathcal{R}}{\delta\boldsymbol{u}}, \Delta\tau\mathcal{G} \right\rangle_{\Omega_t}, \tag{3.20}$$

which relates the infinitesimal change in the field $\boldsymbol{u}$ to the resulting change in the residual $\delta\mathcal{R}$ via the functional gradient $\delta\mathcal{R}/\delta\boldsymbol{u}$. This is effectively an infinite dimensional chain rule, where the inner-product sums all first-order contributions of the perturbation in $\boldsymbol{u}$ to the variation in the residual. When compared to Equation 3.19, this leads to the following relationship between the adjoint Gateaux derivative of the local residual and the gradient of the global residual

$$\frac{\delta\mathcal{R}}{\delta\boldsymbol{u}} = \mathcal{L}_{\boldsymbol{r}}^{\dagger}\left(\boldsymbol{u}, \boldsymbol{r}\right). \tag{3.21}$$

This means that the adjoint solver methodology has the variational dynamics given by $\mathcal{G} = \delta\mathcal{R}/\delta\boldsymbol{u}$, or in other words, the adjoint solver is equivalent to a gradient-based optimisation where the velocity field is modified in the steepest descent direction of the global residual. When discretised in τ with the Euler method the adjoint solver corresponds to a gradient descent algorithm

$$\boldsymbol{\Delta u} = \Delta\tau\mathcal{G} = -\Delta\tau\mathcal{L}_{\boldsymbol{r}}^{\dagger}\left(\boldsymbol{u}, \boldsymbol{r}\right) = -\Delta\tau\frac{d\mathcal{R}}{d\boldsymbol{u}}. \tag{3.22}$$

Given the poor convergence properties of the gradient descent algorithm, for fixed $\Delta\tau$, it is obvious why the adjoint solvers are slow to converge to invariant solutions once the minimum is approached. In practice, therefore, a gradient descent algorithm for minimising $\mathcal{R}$ is not a very good choice. Instead of using gradient descent, the majority of this work utilises quasi-Newton optimisation algorithms which provide more useful search directions. The quasi-Newton method for the optimisation replaces $\delta\mathcal{R}/\delta\boldsymbol{u}$ with a different descent direction that although is not the greatest descent direction, allows for larger steps that more quickly approach the desired minimum. Effectively, the adjoint dynamics are replaced with a slightly more optimal choice of search direction which takes into account some local curvature information to better minimise the residual. When solving a nonlinear optimisation problem, the quasi-Newton algorithms above provide the search direction information, but not how large the step size should be. A naïve approach is to fix the step size to some sufficiently small value as to ensure the residual will decrease each iteration. This however is generally not optimal, as larger step sizes might be possible at different points during the optimisation, and required trial and error approaches to find the right step size to ensure the problem converges. To solve this problem, a line search method is coupled with the rest of the quasi-Newton algorithm. An exact line search method would, given a search direction prescribed by the optimisation algorithm, find the step size that produces that largest possible decrease in the residual. This sub-problem of the total optimisation problem is naturally difficult to solve exactly, and so there are many algorithms that aim to approximate the exact solution at a much lower cost. These inexact line search methods are generally constructed to find the largest step size possible while ensuring the Wolfe conditions are satisfied Wolfe (1969, 1971). The Wolfe conditions effectively provide an upper and lower bound on the step length that ensures the residual, and its gradient reduce a sufficient amount. Details of quasi-Newton optimisation algorithms and general line search methods are given in Nocedal and Wright (2006)

3.3 Residual Gradient Derivation

With the equivalence of the adjoint and optimisation approaches to finding invariant solutions to the Navier-Stokes equations established, this subsection focuses on the derivation of the explicit expression for $\delta\mathcal{R}/\delta\boldsymbol{u}$. This derivation is equivalent to the derivations found in Farazmand (2016); Azimi et al. (2022); Ashtari and Schneider

(2023), with a few key differences. The first, primarily superficial, difference is that this problem is explicitly framed as a gradient-based optimisation problem, whereas the previously mentioned works frame the problem through the adjoint dynamics discussed in Section 3.2. The second more substantial difference is the generality of the following derivation. In the literature the derivation of the required dynamics for the adjoint problem have been for the specific flows studied in each case. However, here a more general formulation is adopted, proving the identities for any incompressible flow field in a connected compact domain with a mix of both periodic and no-slip boundary conditions. As stated, this derivation is only for incompressible flow fields, with the linear divergence constraint on the velocity field. Compressible flows replace this constraint with a separate dynamical equation for the evolution of the fluid density, along with energy equations and some equation of thermodynamic state (such as the ideal gas law). Mathematically speaking, the formulation is simpler when the fluid is compressible, as will be seen later, since the incompressibility constraint and required no-slip boundary conditions require special treatment to properly compute the residual gradient. Since this is not in the scope of the current study it is not discussed any further.

To start, it is first best to define a new objective that includes the incompressible constraint on the velocity field in the form of a Lagrange multiplier. First, define the new search space that only includes the periodicity and boundary conditions

$$\mathscr{P}_T^{\mathrm{BC}} := \left\{ \boldsymbol{u} \in \chi \,:\, \boldsymbol{u}|_{t=0} = \boldsymbol{u}|_{t=T}\,,\ \boldsymbol{u}|_{\partial\Omega_{\mathrm{ns}}} = C,\ \boldsymbol{u}|_{\partial\Omega_{\mathrm{pi}}} = \boldsymbol{u}|_{\partial\Omega_{\mathrm{po}}} \right\}. \tag{3.23}$$

The constant value C is the velocity of the wall at the no-slip boundary. For Couette flow, the primary focus of application in this thesis, this velocity is set to ±1 at the top and bottom walls respectively. Then, define a modified optimisation problem as follows

$$\min_{\boldsymbol{u}\in\mathscr{P}_T^{\mathrm{BC}},\, T} \quad \mathscr{L}\left[\boldsymbol{u},\, q\right] = \mathcal{R} + \langle q,\, \nabla\cdot\boldsymbol{u}\rangle_{\Omega_t}\,. \tag{3.24}$$

The Lagrange multiplier q is a scalar field, of the same type as the pressure p, and could be referred to as an "adjoint pressure" due to its role in enforcing the incompressibility of the velocity field under evolution in the variational dynamics. To solve this modified optimisation problem, Equation 3.24, it is necessary for both $\delta\mathcal{R}/\delta\boldsymbol{u} = 0$ and $\delta\mathcal{R}/\delta q = 0$. It is relatively simple to show that $\delta\mathcal{R}/\delta q = \nabla\cdot\boldsymbol{u}$, and so the second condition is a restatement of the incompressibility constraint $\nabla\cdot\boldsymbol{u} = 0$. The first derivative is equal to

$$\frac{\delta\mathscr{L}}{\delta\boldsymbol{u}} = \frac{\delta\mathcal{R}}{\delta\boldsymbol{u}} + \frac{\delta}{\delta\boldsymbol{u}}\langle q,\, \nabla\cdot\boldsymbol{u}\rangle_{\Omega_t}\,. \tag{3.25}$$

The standard approach in variational calculus to derive the equation for the functional derivative is to perturb the velocity by some small amount and observe the resulting linearised response in the functional $\mathcal{R}$. Let $\boldsymbol{\delta u}$ denote the form of the perturbation, satisfying the constraints $\nabla \cdot \boldsymbol{\delta u} = 0$, $\boldsymbol{\delta u}|_{\partial\Omega_{\mathrm{ns}}} = 0$, $\boldsymbol{\delta u}|_{\partial\Omega_{\mathrm{pi}}} = \boldsymbol{\delta u}|_{\partial\Omega_{\mathrm{po}}}$, and $\boldsymbol{\delta u}$ is periodic in time, or in other words let $\boldsymbol{\delta u} \in \mathscr{P}_T$ with $C = 0$. The perturbation is then denoted as $\boldsymbol{u} \to \boldsymbol{u} + \epsilon\boldsymbol{\delta u}$, where $\epsilon > 0$ is a real number sufficiently small so that $\epsilon^2 \approx 0$ allowing the higher-order terms to be neglected in the following derivation. We also perturb the pressure $p \to p + \epsilon\delta p$. The pressure variation, δp, does not have similar constraints imposed on it as $\boldsymbol{\delta u}$. It is seen later in the derivation that by imposing the proper constraint on $\boldsymbol{r}$ the pressure variation is removed from the resulting expressions. Calculus of variations then provides the following identity

$$\frac{\mathrm{d}}{\mathrm{d}\epsilon}\mathscr{L}\left[\boldsymbol{u} + \epsilon\boldsymbol{\delta u}\right]\bigg|_{\epsilon=0} = \left\langle \frac{\delta\mathscr{L}}{\boldsymbol{\delta u}}, \boldsymbol{\delta u} \right\rangle. \tag{3.26}$$

for which it is guaranteed that $\delta\mathscr{L}/\boldsymbol{\delta u} \in \mathscr{P}_T$ by the Riesz representation theorem (Bachman and Narici, 2000). To compute the explicit expression for $\delta\mathcal{R}/\boldsymbol{\delta u}$ it is necessary to propagate the perturbation in the velocity field through all the variables that depend on it. Starting with the local residual we have

$$\boldsymbol{r}\left(\boldsymbol{u} + \epsilon\boldsymbol{\delta u}\right) = \boldsymbol{r} + \boldsymbol{\delta r} = \frac{\partial \boldsymbol{u}}{\partial t} - \mathcal{N}\left(\boldsymbol{u}\right) + \boldsymbol{\nabla} p + \left(\epsilon\frac{\partial}{\partial t}\boldsymbol{\delta u} - \delta\mathcal{N} + \epsilon\boldsymbol{\nabla}\delta p\right), \tag{3.27}$$

where $\mathcal{N} = -\left(\boldsymbol{u} \cdot \boldsymbol{\nabla}\right)\boldsymbol{u} + \frac{1}{Re}\Delta\boldsymbol{u}$. An expression for the perturbation of the Navier-Stokes operator $\delta\mathcal{N}$ can be derived as follows

$$\begin{aligned}\mathcal{N}\left(\boldsymbol{u} + \epsilon\boldsymbol{\delta u}\right) &= \mathcal{N} + \delta\mathcal{N} \\ &= -\left(\boldsymbol{u} \cdot \nabla\right)\boldsymbol{u} + \frac{1}{Re}\Delta\boldsymbol{u} \\ &\quad + \epsilon\left(-\left(\boldsymbol{u} \cdot \nabla\right)\boldsymbol{\delta u} - \left(\boldsymbol{\delta u} \cdot \nabla\right)\boldsymbol{u} + \frac{1}{Re}\Delta\boldsymbol{\delta u}\right) + \epsilon^2\left(\boldsymbol{\delta u} \cdot \nabla\right)\boldsymbol{\delta u}.\end{aligned}$$

Substituting this into Equation 3.27 and rearranging for the the perturbation $\boldsymbol{\delta r}$ gives

$$\boldsymbol{\delta r} = \epsilon\left(\frac{\partial}{\partial t}\boldsymbol{\delta u} - \left(\boldsymbol{u} \cdot \nabla\right)\boldsymbol{\delta u} - \left(\boldsymbol{\delta u} \cdot \nabla\right)\boldsymbol{u} + \frac{1}{Re}\Delta\boldsymbol{\delta u} + \boldsymbol{\nabla}\delta p\right) - \epsilon^2\left(\boldsymbol{\delta u} \cdot \nabla\right)\boldsymbol{\delta u}. \tag{3.28}$$

Now, propagating the perturbation to the Lagrangian $\mathscr{L}$ we get

$$\begin{aligned}\mathscr{L}\left[\boldsymbol{u} + \epsilon\boldsymbol{\delta u}\right] &= \frac{1}{2}\|\boldsymbol{r} + \boldsymbol{\delta r}\|^2_{\Omega_t} + \left\langle q, \boldsymbol{\nabla} \cdot \boldsymbol{u} + \epsilon\boldsymbol{\delta u}\right\rangle_{\Omega_t} \\ &= \frac{1}{2}\|\boldsymbol{r}\|^2_{\Omega_t} + \left\langle \boldsymbol{r}, \boldsymbol{\delta r}\right\rangle_{\Omega_t} + \frac{1}{2}\left\langle \boldsymbol{\delta r}, \boldsymbol{\delta r}\right\rangle_{\Omega_t} + \left\langle q, \boldsymbol{\nabla} \cdot \boldsymbol{u}\right\rangle_{\Omega_t} + \epsilon\left\langle q, \boldsymbol{\nabla} \cdot \boldsymbol{\delta u}\right\rangle_{\Omega_t},\end{aligned}$$

and then substituting in Equation 3.28 to get

$$\begin{aligned}
&\mathscr{L}\left[\boldsymbol{u}+\epsilon\delta\boldsymbol{u}\right] = \frac{1}{2}\|\boldsymbol{r}\|^2_{\Omega_t} + \langle q,\, \boldsymbol{\nabla}\cdot\boldsymbol{u}\rangle_{\Omega_t} + \\
&\epsilon\left(\left\langle \boldsymbol{r},\, \frac{\partial}{\partial t}\delta\boldsymbol{u} - \left(\boldsymbol{u}\cdot\nabla\right)\delta\boldsymbol{u} - \left(\delta\boldsymbol{u}\cdot\nabla\right)\boldsymbol{u} + \frac{1}{Re}\Delta\delta\boldsymbol{u} + \boldsymbol{\nabla}\delta p\right\rangle_{\Omega_t} + \langle q,\, \boldsymbol{\nabla}\cdot\delta\boldsymbol{u}\rangle_{\Omega_t}\right) \\
&+\mathcal{O}\left(\epsilon^2\right).
\end{aligned} \tag{3.29}$$

where all the higher order terms in ϵ have been grouped into the term $\mathcal{O}\left(\epsilon^2\right)$. Substituting Equation 3.29 into the left-hand side of Equation 3.26 gives

$$\begin{aligned}
\left\langle \frac{\delta\mathscr{L}}{\delta\boldsymbol{u}},\, \delta\boldsymbol{u}\right\rangle = \left\langle \boldsymbol{r},\, \frac{\partial}{\partial t}\delta\boldsymbol{u} + \left(\boldsymbol{u}\cdot\nabla\right)\delta\boldsymbol{u} + \left(\delta\boldsymbol{u}\cdot\nabla\right)\boldsymbol{u} - \frac{1}{Re}\Delta\delta\boldsymbol{u} + \boldsymbol{\nabla}\delta p\right\rangle_{\Omega_t} \\
+ \langle q,\, \boldsymbol{\nabla}\cdot\delta\boldsymbol{u}\rangle_{\Omega_t}.
\end{aligned} \tag{3.30}$$

The objective is now to convert the right-hand side of Equation 3.30 to resemble its left-hand side. This is done by computing the adjoints of the derivative operators using integration by-parts. To achieve this without resorting to defining the exact geometry to be able to compute the integration by-parts, a few vector calculus identities will be useful. Specifically the product rule for divergence

$$\nabla\cdot(u\boldsymbol{v}) = u\nabla\cdot\boldsymbol{v} + \boldsymbol{v}\cdot\nabla u, \tag{3.31}$$

and the divergence theorem over the spatial domain

$$\int_{\Omega}\nabla\cdot(u\boldsymbol{v})\,\mathrm{d}V = \int_{\partial\Omega} u\boldsymbol{v}\cdot\hat{\boldsymbol{n}}\,\mathrm{d}S\,, \tag{3.32}$$

where $\hat{\boldsymbol{n}}$ is the outward pointing unit normal vector at the boundary of the flow domain $\partial\Omega$. Taking each term inside the inner products of Equation 3.30 we start with the time derivative

$$\left\langle \boldsymbol{r},\, \frac{\partial}{\partial t}\delta\boldsymbol{u}\right\rangle_{\Omega_t} = \int_{\Omega}\int_0^T \boldsymbol{r}\cdot\frac{\partial}{\partial t}\delta\boldsymbol{u}\,\mathrm{d}t\,\mathrm{d}V = \int_{\Omega}\left(\Big[\boldsymbol{r}\cdot\delta\boldsymbol{u}\Big]_0^T - \int_0^T\frac{\partial\boldsymbol{r}}{\partial t}\cdot\delta\boldsymbol{u}\,\mathrm{d}t\right)\mathrm{d}V\,, \tag{3.33}$$

where integration by parts on the time integral has been used for the second equality. Noting that both $\boldsymbol{u}$ and $\boldsymbol{r}$ are periodic in time, the boundary terms vanishes, leaving

$$\left\langle \boldsymbol{r},\, \frac{\partial}{\partial t}\delta\boldsymbol{u}\right\rangle_{\Omega_t} = -\int_{\Omega}\int_0^T\frac{\partial\boldsymbol{r}}{\partial t}\cdot\delta\boldsymbol{u}\,\mathrm{d}t\,\mathrm{d}V = \left\langle -\frac{\partial\boldsymbol{r}}{\partial t},\, \delta\boldsymbol{u}\right\rangle_{\Omega_t}, \tag{3.34}$$

Next, taking the first convective term we get

$$
\begin{aligned}
\langle \boldsymbol{r},\, (\delta\boldsymbol{u}\cdot\nabla)\,\boldsymbol{u}\rangle_{\Omega_t} &= \int_0^T \int_\Omega \boldsymbol{r}\cdot(\delta\boldsymbol{u}\cdot\nabla)\,\boldsymbol{u}\,\mathrm{d}V\,\mathrm{d}t\,, \\
&= \int_0^T \int_\Omega \boldsymbol{r}\cdot[(\nabla\boldsymbol{u})\,\delta\boldsymbol{u}]\,\mathrm{d}V\,\mathrm{d}t\,, \\
&= \int_0^T \int_\Omega \left[(\nabla\boldsymbol{u})^\top \boldsymbol{r}\right]\delta\boldsymbol{u}\,\mathrm{d}V\,\mathrm{d}t = \left\langle (\boldsymbol{\nabla}\boldsymbol{u})^\top \boldsymbol{r},\, \delta\boldsymbol{u}\right\rangle_{\Omega_t}\,,
\end{aligned}
\tag{3.35}
$$

The second convective term has to be handled by exchanging the derivatives using the vector calculus identities Equation 3.31 and Equation 3.32 as follows

$$
\begin{aligned}
\langle \boldsymbol{r},\, (\boldsymbol{u}\cdot\nabla)\,\delta\boldsymbol{u}\rangle_{\Omega_t} &= \int_0^T \int_\Omega \boldsymbol{r}\cdot((\boldsymbol{u}\cdot\nabla)\,\delta\boldsymbol{u})\,\mathrm{d}V\,\mathrm{d}t \\
&= \int_0^T \left(\int_{\partial\Omega} (\boldsymbol{r}\cdot\delta\boldsymbol{u})\,\boldsymbol{u}\cdot\hat{\boldsymbol{n}}\,\mathrm{d}S - \int_\Omega ((\boldsymbol{u}\cdot\nabla)\,\boldsymbol{r})\cdot\delta\boldsymbol{u}\,\mathrm{d}V\right)\mathrm{d}t\,.
\end{aligned}
\tag{3.36}
$$

Due to the no-slip boundary condition for $\boldsymbol{u}$ and periodic boundary conditions for both $\boldsymbol{u}$ and $\boldsymbol{r}$ on $\partial\Omega$, the boundary integral term in Equation 3.36 vanishes leaving

$$
\langle \boldsymbol{r},\, (\boldsymbol{u}\cdot\nabla)\,\delta\boldsymbol{u}\rangle_{\Omega_t} = -\int_0^T \int_\Omega ((\boldsymbol{u}\cdot\nabla)\,\boldsymbol{r})\cdot\delta\boldsymbol{u}\,\mathrm{d}V\,\mathrm{d}t = \langle -(\boldsymbol{u}\cdot\nabla)\,\boldsymbol{r},\, \delta\boldsymbol{u}\rangle_{\Omega_t}\,. \tag{3.37}
$$

Using the product rule and divergence theorem twice, the diffusion term in Equation 3.30 can be rearranged to

$$
\begin{aligned}
\langle \boldsymbol{r},\, \Delta\delta\boldsymbol{u}\rangle_{\Omega_t} &= \int_0^T \int_\Omega \boldsymbol{r}\cdot(\Delta\delta\boldsymbol{u})\,\mathrm{d}V\,\mathrm{d}t\,, \\
&= \int_0^T \left(\int_{\partial\Omega} (\boldsymbol{r}\cdot\nabla\delta\boldsymbol{u} - (\Delta\boldsymbol{r})\cdot\delta\boldsymbol{u})\cdot\hat{\boldsymbol{n}}\,\mathrm{d}S + \int_\Omega (\Delta\boldsymbol{r})\cdot\delta\boldsymbol{u}\,\mathrm{d}V\right)\mathrm{d}t\,,
\end{aligned}
\tag{3.38}
$$

which is equivalent to integrating by parts twice, leaving derivative terms in both $\boldsymbol{r}$ and $\delta\boldsymbol{u}$ at the boundaries. The second boundary integral term vanishes at the boundaries due to the constraints on $\delta\boldsymbol{u}$ to satisfy the no-slip and periodicity boundary conditions. The second boundary term, however, does not vanish with the current boundary conditions imposed for the problem. In fact, it is necessary to introduce extra boundary conditions, called natural/adjoint boundary conditions, for the local residual such that this boundary integral vanishes. Specifically, we require that $\boldsymbol{r}|_{\partial\Omega_{\mathrm{ns}}} = 0$ and $\boldsymbol{r}|_{\partial\Omega_{\mathrm{pi}}} = \boldsymbol{r}|_{\partial\Omega_{\mathrm{po}}}$. In other words, the local residual field must obey the same periodic boundary conditions as the velocity field (which is trivially true given a periodic $\boldsymbol{r}$), as well as homogeneous no-slip boundary conditions at the same locations as $\boldsymbol{u}$. The second of these constraints is far more difficult to enforce, as it requires that the Navier-Stokes equations be exactly solved at the no-slip boundaries. When solving the incompressible Navier-Stokes equations using some form of standard time-stepping scheme, the pressure is typically determined via some solution of the associated Poisson problem with boundary conditions derived from evaluating the Navier-Stokes equations at the no-slip boundaries, which enforces this boundary condition. With the new boundary conditions on $\boldsymbol{r}$ both of the boundary integral terms in Equation 3.38 vanish giving

$$\langle \boldsymbol{r}, \Delta\delta\boldsymbol{u}\rangle_{\Omega_t} = \int_0^T \int_\Omega (\Delta\boldsymbol{r}) \cdot \delta\boldsymbol{u} \, \mathrm{d}V \, \mathrm{d}t = \langle \Delta\boldsymbol{r}, \delta\boldsymbol{u}\rangle_{\Omega_t}. \tag{3.39}$$

The pressure term in Equation 3.30 is again handled via integration by-parts, utilising the natural boundary conditions for $\boldsymbol{r}$ such that the resulting boundary integral vanishes, giving

$$\langle \boldsymbol{r}, \nabla\delta p\rangle_{\Omega_t} = \int_0^T \boldsymbol{r} \cdot \nabla\delta p \, \mathrm{d}V \, \mathrm{d}t = -\int_\Omega \delta p \, (\boldsymbol{\nabla} \cdot \boldsymbol{r}) \, \mathrm{d}V \, \mathrm{d}t = \langle -\boldsymbol{\nabla} \cdot \boldsymbol{r}, \delta p\rangle_{\Omega_t}. \tag{3.40}$$

Utilising the commutativity of the inner product, the fact that the adjoint of the gradient is the negative divergence leads directly to adjoint of the divergence being the negative gradient. Using this, the adjoint of the final term in Equation 3.30 for the Lagrange multiplier can be determined

$$\langle q, \boldsymbol{\nabla} \cdot \delta\boldsymbol{u}\rangle_{\Omega_t} = \langle -\boldsymbol{\nabla} q, \delta\boldsymbol{u}\rangle_{\Omega_t}. \tag{3.41}$$

Taking all of the adjoint operators derived above and applying them to Equation 3.30 gives

$$\begin{aligned} \left\langle \frac{\delta\mathscr{L}}{\delta\boldsymbol{u}}, \delta\boldsymbol{u} \right\rangle = \left\langle -\frac{\partial\boldsymbol{r}}{\partial t} - (\boldsymbol{u} \cdot \boldsymbol{\nabla})\,\boldsymbol{r} + (\boldsymbol{\nabla}\boldsymbol{u})^\top \boldsymbol{r} - \frac{1}{Re}\Delta\boldsymbol{r} - \boldsymbol{\nabla} q, \delta\boldsymbol{u} \right\rangle_{\Omega_t} \\ - \langle \boldsymbol{\nabla} \cdot \boldsymbol{r}, \delta p\rangle_{\Omega_t}. \end{aligned} \tag{3.42}$$

In its current form, Equation 3.42 does not provide the desired closed-form expression for $\delta\mathscr{L}/\delta\boldsymbol{u}$. This is due to the presence of the pressure perturbation term. The only way to remove this term from the expression is to set $\boldsymbol{\nabla} \cdot \boldsymbol{r} = 0$. This is equivalent to enforcing Equation 3.1a to obey the pressure Poisson equation throughout the domain. This incompressibility constraint for $\boldsymbol{r}$ along with the natural boundary condition $\boldsymbol{r}|_{\partial\Omega_{\mathrm{ns}}} = 0$ ensures that any evolution of the velocity field in variational space is completely divergence free and obeys the no-slip boundary conditions. Applying this added body constraint on the local residual gives the final expression for the functional derivative

$$\frac{\delta\mathscr{L}}{\delta\boldsymbol{u}} = -\frac{\partial\boldsymbol{r}}{\partial t} - (\boldsymbol{u} \cdot \nabla)\,\boldsymbol{r} + (\nabla\boldsymbol{u})^\top \boldsymbol{r} - \frac{1}{Re}\Delta\boldsymbol{r} - \nabla q. \tag{3.43}$$

This expression includes the added incompressibility constraint and boundary conditions on $\boldsymbol{r}$. Taken together, these constraints imply that $\boldsymbol{r} \in \mathscr{P}_T$ with $C = 0$ is required for the gradient in Equation 3.43 to be a valid expression. It is also clear from Equation 3.43 that the Lagrange multiplier term q acts as a pressure term, ensuring that the evolution of $\boldsymbol{u}$ under the variational dynamics is incompressible. Using the incompressibility constraint of $\boldsymbol{r}$, an adjoint pressure Poisson problem could be derived and solved in a similar way as done for the primitive variables when solving the Navier-Stokes equations using a traditional time-stepping scheme, in line with what was done in Ashtari and Schneider (2023) where the same problem was encountered. In the rest of this text the expression in Equation 3.43 will be denoted as $\delta\mathcal{R}/\delta\boldsymbol{u}$ as opposed to a gradient of the Lagrangian. This is done to make it clear that we are optimising the global residual. The expression given, along with the boundary and incompressibility constraints, ensure that the optimisation of $\mathcal{R}$ stays within the space $\mathscr{P}_T$.

3.3.1 Residual Constraint Implications

Now that the derivations of all the relevant quantities to perform a basic optimisation of $\mathcal{R}$ have been derived, it is worth discussing the implications of the extra constraints imposed on $\boldsymbol{r}$ and their effect on the solution method that will be used. The homogeneous no-slip boundary condition $\boldsymbol{r}|_{\partial\Omega_{\text{ns}}} = 0$ and the incompressibility constraint $\boldsymbol{\nabla} \cdot \boldsymbol{r} = 0$ mirror the constraints imposed on the velocity field, and together ensure that the evolution of the solution in variational space towards some periodic flow is incompressible and obeys the no-slip boundary conditions.

Natural boundary conditions is a term used in finite element analysis and more generally calculus of variations. These boundary conditions are automatically satisfied by any dynamical solution to the governing equations. In this case this is trivial since any solution to the Navier-Stokes equations (and thus minimises $\mathcal{R}$) would necessarily have $\boldsymbol{r} = 0$ everywhere, including any no-slip boundaries. However, this condition is important in this case because without it a valid closed-form expression for residual gradient cannot be obtained. If $\boldsymbol{r}|_{\partial\Omega_{\text{ns}}} \neq 0$ then Equation 3.43 is not a descent direction for the functional $\mathcal{R}$.

The question of how to best impose these conditions remains. One might first attempt this by constructing a velocity field $\boldsymbol{u} \in \mathscr{P}_T$ for a given period T, and solve the pressure Poisson equation at each instant. This would be done by taking the divergence of Equation 3.1a and using the incompressibility of the velocity field at all instants in time to get

$$\Delta p = \boldsymbol{\nabla} \cdot \mathcal{N}(\boldsymbol{u}), \tag{3.44}$$

along with a set of Neumann boundary conditions, obtained by evaluating Equation 3.1a at the no-slip boundaries

$$\nabla p \cdot \hat{\mathbf{n}} = \mathcal{N}\left(\boldsymbol{u}\right) \cdot \hat{\mathbf{n}}, \quad \text{on } \partial\Omega_{\mathrm{ns}}. \tag{3.45}$$

Typically, the right-hand side of Equation 3.44 consists of the divergence convection terms of the Navier-Stokes equations, and the right-hand side of Equation 3.45 is the diffusion term evaluated normal to the no-slip boundary. By solving this Poisson problem an expression for the pressure is determined (up to an additive constant), which can then be used in Equation 3.5 to compute the local residual. This would produce a local residual field that is divergence free throughout Ω_t, however, the required constraint on $\boldsymbol{r}$ at the no-slip boundary is not automatically satisfied. In fact, the boundary condition of Equation 3.45 is just equivalent to enforcing $\boldsymbol{r} \cdot \hat{\mathbf{n}}|_{\partial\Omega_{\mathrm{ns}}} = 0$. As a consequence, the tangential components of the local residual at the no-slip boundaries are in general non-zero. This is only a problem due to the fact that the whole temporal evolution of the velocity field is prescribed before the pressure is solved for. If instead, the evolution of the velocity field was determined by solving the Navier-Stokes equations via some time-stepping scheme, solving for the pressure at each time step using Equation 3.44 and Equation 3.45, then the tangential components of the local residual at the no-slip boundaries would in fact be zero. This is discussed in detail in Gresho and Sani (1987); Gresho (1991) and Chen and Jiang (1996), where the equivalence between the Neumann and Dirichlet style boundary conditions for solving Equation 3.44 is shown. In other words, even if you start with a velocity field such that $\boldsymbol{u} \in \mathscr{P}_T$ and solve the pressure Poisson equation with either Neumann of Dirichlet boundary conditions derived by evaluating the Navier-Stokes equations at the no-slip boundaries, it is not true that $\boldsymbol{r} \in \mathscr{P}_T$. Specifically, the local residual at the no-slip boundaries will be non-zero, invalidating the expression Equation 3.43 making a gradient-based optimisation impossible.

The conclusion that some variation of a decoupled solver that computes pressure and velocity separately is not viable. The pressure in Equation 3.1a acts to ensure the velocity evolves in a very certain way, and simply prescribing a velocity field satisfying $\boldsymbol{u} \in \mathscr{P}_T$ is not sufficient to satisfy this constraint. As mentioned a few time previously, Ashtari and Schneider (2023) encountered the same problem when formulating the three-dimensional variational problem for channel flow. They overcame this problem using the Influence Matrix (IM) method to compute an update to the velocity field that ensures both $\nabla \cdot \boldsymbol{r} = 0$ and $\boldsymbol{r}|_{\partial\Omega_{\mathrm{ns}}} = 0$ are satisfied at the next iteration. In general, if the solution is to be solved in form of primitive variables, then a coupled solver for both velocity and pressure is required to ensure compatible spatiotemporal fields. In the next section a unified description of the problem will be presented, describing two approaches to solve the problem with the application and analysis of these methods detailed.

3.3.2 Period Gradient

To complete the gradient-based optimisation of Equation 3.7 an expression for the gradient with respect to the solution period, $\partial\mathcal{R}/\partial T$ is required. This is obtained in Azimi et al. (2022) using the adjoint dynamics framing, whereas here the optimisation framing is used for the derivation. This gradient is simpler to obtain, as basic methods of differentiation can be used directly since the period T is just a scalar value rather than an object existing in some infinite-dimensional function space.

To this end, the global residual, Equation 3.6, is expressed as follows

$$\mathcal{R} = \frac{\omega^2}{2}\left\|\frac{\partial \boldsymbol{u}}{\partial t^*}\right\|_{\Omega_t}^2 - \omega\left\langle\frac{\partial \boldsymbol{u}}{\partial t^*}, \mathcal{N}\left(\boldsymbol{u}\right) - \boldsymbol{\nabla} p\right\rangle_{\Omega_t} + \frac{1}{2}\left\|\mathcal{N}\left(\boldsymbol{u}\right) - \boldsymbol{\nabla} p\right\|_{\Omega_t}^2, \tag{3.46}$$

where $\omega = 2\pi/T$ is the fundamental frequency of the flow or the smallest frequency oscillation that can be permitted in the finite window permitted by the period T. This variable has been extracted from the time derivative by defining $t^* = \omega t$, which is a scaled time direction such that $t^* \in [0, 2\pi)$. Using the chain rule we obtain $\partial/\partial t = \omega\, \partial/\partial t^*$. It should be noted that Equation 3.46 is a quadratic function with respect to ω, with the shape of the given velocity field $\boldsymbol{u}\left(\boldsymbol{x}, t^*\right)$ determining the coefficients. Taking the derivative of Equation 3.46 with respect to ω gives

$$\frac{\partial\mathcal{R}}{\partial\omega} = \omega\left\|\frac{\partial \boldsymbol{u}}{\partial t^*}\right\|_{\Omega_t}^2 - \left\langle\frac{\partial \boldsymbol{u}}{\partial t^*}, \mathcal{N}\left(\boldsymbol{u}\right) - \boldsymbol{\nabla} p\right\rangle_{\Omega_t}. \tag{3.47}$$

The pressure gradient in Equation 3.46 can be eliminated. This is due to the flow field being incompressible at all times, so $\boldsymbol{\nabla}\cdot\left(\partial\boldsymbol{u}/\partial t^*\right) = 0$, which when combined with the adjoint of the gradient being the negative divergence gives

$$\left\langle\frac{\partial \boldsymbol{u}}{\partial t^*}, \boldsymbol{\nabla} p\right\rangle_{\Omega_t} = \left\langle -\boldsymbol{\nabla}\cdot\frac{\partial \boldsymbol{u}}{\partial t^*}, p\right\rangle_{\Omega_t} = 0. \tag{3.48}$$

It is possible to set $\partial\mathcal{R}/\partial\omega = 0$ in Equation 3.47 to determine the optimal frequency ω^* (and thus period) for a given flow $\boldsymbol{u}$, which could be used as the determined period at each iteration. This optimal frequency is given as

$$\omega^* = \frac{\left\langle\frac{\partial \boldsymbol{u}}{\partial t^*}, \mathcal{N}\left(u\right)\right\rangle_{\Omega_t}}{\left\|\frac{\partial \boldsymbol{u}}{\partial t^*}\right\|_{\Omega_t}^2} \tag{3.49}$$

This expression has not been shown in the literature, although it is very easy to obtain so has likely been considered before in earlier examples of this type of work. This is likely due to a practical implementation of the optimisation problem using this optimal frequency at each iteration instead of including the frequency gradient as part of the total gradient leads to very unstable iterations that typically diverge very quickly, unless the flow $\boldsymbol{u}$ is already very close to particular minimum. This is primarily a result of the abstract vectors $\partial \boldsymbol{u}/\partial t^*$ and $\mathcal{N}(\boldsymbol{u})$ being highly misaligned unless a velocity field is already very close to a solution, which produces a frequency ω that gets arbitrarily close to zero and thus a period T that will get arbitrarily large. In practice, then, the gradient Equation 3.47 is used directly in the optimisation. Rearranging Equation 3.47, grouping the like terms in the inner-product and substituting the definition of the local residual Equation 3.5, the following expression can be obtained

$$\frac{\partial \mathcal{R}}{\partial \omega} = \frac{1}{\omega}\left\langle \frac{\partial \boldsymbol{u}}{\partial t}, \boldsymbol{r} \right\rangle_{\Omega_t}. \tag{3.50}$$

The gradient with respect to the period can be obtained using the definition of the fundamental frequency, $\omega = 2\pi/T$, and the chain rule to get

$$\omega \frac{\partial \mathcal{R}}{\partial \omega} = T \frac{\partial \mathcal{R}}{\partial T}. \tag{3.51}$$

3.4 DAE Formulation of Gradient-Based Variational Optimisation

Combining the previous results on the residual gradient derivation with the definition of the local residual given in Equation 3.5 and the incompressibility and boundary conditions on the velocity field $\boldsymbol{u}$ yields the following Differential Algebraic Equations (DAEs) for the evolution in the variational time τ defined in Section 3.2

$$\frac{\partial \boldsymbol{u}}{\partial \tau} = -\frac{\partial \boldsymbol{r}}{\partial t} - (\boldsymbol{u}\cdot\nabla)\,\boldsymbol{r} + (\nabla \boldsymbol{u})^{\top}\boldsymbol{r} - \frac{1}{Re}\Delta \boldsymbol{r} - \nabla q, \tag{3.52a}$$

$$0 = \frac{\partial \boldsymbol{u}}{\partial t} + (\boldsymbol{u}\cdot\nabla)\,\boldsymbol{u} - \frac{1}{Re}\Delta \boldsymbol{u} + \nabla p - \boldsymbol{r}, \tag{3.52b}$$

$$0 = \nabla\cdot\boldsymbol{u}, \tag{3.52c}$$

$$0 = \nabla\cdot\boldsymbol{r}, \tag{3.52d}$$

$$0 = \boldsymbol{u}|_{\partial\Omega_{\mathrm{ns}}} - \boldsymbol{C} = \boldsymbol{u}|_{\partial\Omega_{\mathrm{pi}}} - \boldsymbol{u}|_{\partial\Omega_{\mathrm{po}}}, \tag{3.52e}$$

$$0 = \boldsymbol{r}|_{\partial\Omega_{\mathrm{ns}}} = \boldsymbol{r}|_{\partial\Omega_{\mathrm{pi}}} - \boldsymbol{r}|_{\partial\Omega_{\mathrm{po}}}. \tag{3.52f}$$

Equation 3.52 is a summary of the variational dynamics induced by gradient-based optimisation of Equation 3.7. The period gradient has been excluded since it does not require any special treatment once a set of compatible $\boldsymbol{u}$ and $\boldsymbol{r}$ fields have been computed. The dynamics can be evolved forward in the direction of greatest descent,

$\partial \boldsymbol{u}/\partial \tau$, to monotonically decrease $\mathcal{R}$. In the literature, a first order forward Euler scheme has typically been used to evolve the spatiotemporal field $\boldsymbol{u}$ forward in τ, as discussed in Section 3.2. Viewed like this, it becomes clear the difficulty in solving the variational problem in the presence of no-slip boundaries. It is necessary to solve for two scalar pressure fields, p and q, such that incompressibility constraints $\nabla \cdot \boldsymbol{u} = \nabla \cdot \boldsymbol{r} = 0$ are satisfied, while at the same time ensuring that the no-slip boundary conditions $\boldsymbol{u}|_{\partial\Omega_{\mathrm{ns}}} = \boldsymbol{r}|_{\partial\Omega_{\mathrm{ns}}} = 0$ are enforced. Complications arise from the standard method used to solve the pressure Poisson equation due to the non-physical Neumann boundary conditions. So far, the only method in the literature that addresses these problems is given in Ashtari and Schneider (2023). Using the IM method to update $\boldsymbol{u}$ and $\boldsymbol{r}$ to obey the incompressibility constraint and no-slip boundary conditions without having to explicitly compute the pressure fields.

In principle Equation 3.52 could be solved directly using standard methods for DAEs. A simple example would be to discretise the gradient $\partial \boldsymbol{u}/\partial \tau$ using a backwards Euler scheme. Applied to Equation 3.52, for a given step in the variational time denoted with $\Delta\tau$ and the current state of the flow variables denoted with $\boldsymbol{q}^i$, we get an implicit algebraic equation for an update to the flow variables

$$0 = \boldsymbol{u}^{i-1} - \boldsymbol{u}^i - \Delta\tau \left(\frac{\partial \boldsymbol{r}^i}{\partial t} - \left(\boldsymbol{u}^i \cdot \nabla\right) \boldsymbol{r}^i + \left(\nabla \boldsymbol{u}^i\right)^\top \boldsymbol{r}^i - \frac{1}{Re}\Delta \boldsymbol{r}^i - \nabla q^i \right), \tag{3.53a}$$

$$0 = \frac{\partial \boldsymbol{u}^i}{\partial t} + \left(\boldsymbol{u}^i \cdot \nabla\right) \boldsymbol{u}^i - \frac{1}{Re}\Delta \boldsymbol{u}^i + \nabla p^i - \boldsymbol{r}^i, \tag{3.53b}$$

$$0 = \nabla \cdot \boldsymbol{u}^i, \tag{3.53c}$$

$$0 = \nabla \cdot \boldsymbol{r}^i, \tag{3.53d}$$

$$0 = \boldsymbol{u}^i\Big|_{\partial\Omega_{\mathrm{ns}}} - \boldsymbol{C} = \boldsymbol{u}^i\Big|_{\partial\Omega_{\mathrm{pi}}} - \boldsymbol{u}^i\Big|_{\partial\Omega_{\mathrm{po}}}, \tag{3.53e}$$

$$0 = \boldsymbol{r}^i\Big|_{\partial\Omega_{\mathrm{ns}}} = \boldsymbol{r}^i\Big|_{\partial\Omega_{\mathrm{pi}}} - \boldsymbol{r}^i\Big|_{\partial\Omega_{\mathrm{po}}}. \tag{3.53f}$$

If it is assumed that the flow variables of the previous iteration $(i-1)$ are known, then solving Equation 3.53 leads to the desired update the velocity, as well as the rest of the flow variables, that minimises the global residual by stepping in the direction of steepest descent that obeys all the constraints of Equation 3.53c to Equation 3.53f. In practice, if one was planning to implement such a method, it would be a bad idea to use a standard Newton-Raphson method to compute the roots of Equation 3.53. This is result of requiring the Jacobian matrix which, besides the difficulty in deriving and implementing, is very memory inefficient. For a typical spatial and temporal discretisation of a turbulent flow there could be millions of degrees of freedom for each scalar flow field, with eight individual scalar fields, leading to a massive Jacobian matrix. If this matrix is not sparse it would be extremely hard to solve and would require some method to invert it at each iteration, since it would change as the optimisation evolves. For these reasons the only viable method would be to use the Newton-GMRES method, a matrix-free alternative to the standard Newton-Raphson method, making the solution tractable.

However viable as this approach may be in principle, it is not particularly efficient. It enforces the use of some time-stepping scheme, the example given above still being equivalent to gradient descent of the global residual. Higher-order time-stepping schemes may allow for more accuracy and larger step sizes, but it still has to solve Equation 3.52 to within machine precision each time. In this case the goal is the solution as $\tau \to \infty$, not on the intermediate states of the variational dynamics. Therefore it makes most sense to use an optimisation algorithm that does not have to move in the exact direction as $\delta\mathcal{R}/\delta\boldsymbol{u}$. Given this, it is best to derive a methodology that can compute $\delta\mathcal{R}/\delta\boldsymbol{u}$ without having to resort to implicit coupled solver based on a specific numerical scheme. The method given in Ashtari and Schneider (2023) solves some of the problems given, but still relies on the time-stepping approach for evolving the loop in state-space and cannot take advantage of the improved efficiency that could be gained from using a quasi-Newton optimisation algorithm. The solution we propose to this problem in the next section allows for easy application of various optimisation algorithms for improved convergence rates.

3.5 Galerkin Projection

The set of equations governing the gradient-based optimisation of the global residual for wall-bounded flows are difficult to solve, due to the coupled constraints of incompressibility and no-slip boundary conditions. In this section a Galerkin projection is proposed as a novel way to solve this problem. If the fields $\boldsymbol{u}$ and $\boldsymbol{r}$ are expressed as a linear sum of a set of basis functions that are divergence-free, as well as obeying the required boundary conditions then it can be shown that the complex DAE presented in Equation 3.52 is reduced to a simpler set of equations that can be solved explicitly. Using a Galerkin projection to enforce boundary conditions and the incompressibility constraints is not a new concept, the novelty here being the application of the method to the variational methodology.

First assume that the flow domain can be split into mutually orthogonal homogeneous and inhomogeneous directions, denoting the set of coordinates for each of those directions as $\boldsymbol{x}$ and $\boldsymbol{y}$, respectively. To provide a concrete example, consider the fully developed turbulent flow through a pipe. The streamwise and azimuthal directions are statistically homogeneous, so the coordinate vector $\boldsymbol{x}$ will have two components for each of these directions. The wall-normal direction is statistically inhomogeneous, and so the coordinate vector $\boldsymbol{y}$ will have a single component corresponding to the wall-normal direction. Denote the number of dimensions for the homogeneous spatial directions with N, which implies the $\boldsymbol{x} \in \mathbb{R}^N$. The statistically homogeneous spatial directions are modelled with a finite domain with periodic boundary conditions permitting the use of Fourier series to represent the flow in these directions. The inhomogeneous directions have a no-slip boundary condition. The standard choice of basis function for the periodic spatial directions are Fourier modes, which automatically satisfy the periodicity boundary conditions. As the current work is concerned with periodic solutions to the Navier-Stokes equations, the temporal direction is Fourier transformed as well. First, an expansion of the velocity field is defined

$$\boldsymbol{u} = \boldsymbol{u}_b + \sum_{i=1}^{M} \sum_{\boldsymbol{k} \in \mathbb{Z}^{N+1}} a_{\boldsymbol{k}i} \boldsymbol{\psi}_{\boldsymbol{k}i} e^{i\boldsymbol{k}\cdot\boldsymbol{\xi}}, \tag{3.54}$$

with Fourier modes in the homogeneous directions and time, and an inhomogeneous set of modes $\boldsymbol{\psi}_{\boldsymbol{k}i}\left(\boldsymbol{y}\right)$, and i being the corresponding mode number summed over M. The coefficients $a_{\boldsymbol{k}i} \in \mathbb{C}$ are the weighting of each resolvent mode at each frequency. The number of inhomogeneous modes, M, can either be defined as an integer value or as infinity in the limit of continuity. Note that the inhomogeneous modes are defined for every frequency $\boldsymbol{k}$. $\boldsymbol{u}_b$ is a base flow, and the vector $\boldsymbol{\xi}$ is composed of N homogeneous coordinates $\boldsymbol{x}$ plus time t normalised with the domain size and period in each direction such that they range from 0 to 2π. The frequencies $\boldsymbol{k}$ are summed over the homogeneous spatial wavenumbers plus the temporal frequency. The mode $\boldsymbol{\psi}_{\boldsymbol{k}i}$ are defined to be divergence-free and obey the no-slip boundary conditions, i.e.

$$\nabla_{\boldsymbol{k}} \cdot \boldsymbol{\psi}_{\boldsymbol{k}i} = 0 \qquad\qquad \boldsymbol{\psi}_{\boldsymbol{k}i}|_{\partial\Omega_{\text{ns}}} = 0, \tag{3.55}$$

in addition to being orthonormal

$$\left(\boldsymbol{\psi}_{\boldsymbol{k}i}, \boldsymbol{\psi}_{\boldsymbol{k}j}\right) = \delta_{ij}. \tag{3.56}$$

with the inner product $(\cdot, \cdot)$ defined as an integral over the inhomogeneous spatial directions. If M as a finite number, the sum in Equation 3.54 represents a Reduced Order Model (ROM) of the flow restricted to the linear subspace defined by the finite basis set $\left\{\boldsymbol{\psi}_{\boldsymbol{k}i}\colon\ \boldsymbol{k} \in \mathbb{Z}^{N+1}\right\}_{i=1}^{M}$. In the limit of infinitely many modes ($M \to \infty$), a full basis set is produced for the required function space and any field in $\mathscr{P}_T$ can be expressed in terms of them. When discretised, the number of modes required to produce a full basis is only equal to the number of points used in the discretisation of the physical space. The inclusion of the frequency vector $\boldsymbol{k}$ in the mode is to allow for a different set of modes for each frequency considered for a given solution. In principle this is not a requirement but it is used here to better allow the integration of resolvent analysis in the later chapters. The main role of the base flow is to ensure that the inhomogeneous component of the no-slip boundary condition for the velocity is properly enforced, and so it is required that $\boldsymbol{u}_b|_{\partial\Omega_{\text{ns}}} = \boldsymbol{C}$. Thus, any set of coefficients $a_{\boldsymbol{k}i}$, for a given base flow, defines a unique velocity field that is both incompressible

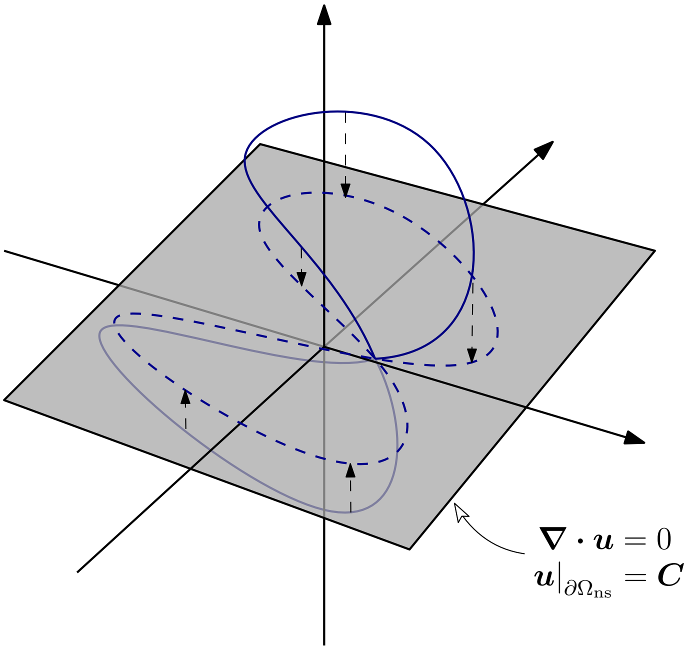

FIGURE 3.3: Schematic for a Galerkin projection of a 3-dimensional state-space trajectory and its dynamics (not shown) onto a 2-dimensional linear subspace.

and obeys all the required boundary conditions.

In the language of linear algebra, the basis $\boldsymbol{\psi}_{ki}$ forms a linear subspace within the full state-space of all possible periodic flows. This subspace is defined as the space of all incompressible flows $\boldsymbol{u}$ that are periodic in time and obey the periodic and no-slip boundary conditions. In addition, the projection operation is a least-squares (orthogonal) projection onto this linear subspace. Figure 3.3 shows a schematic for a Galerkin projection of a simple 3-dimensional state-space with a trajectory embedded within it. The fact that this is a least-squares projection ensures that the gradient $\partial\mathcal{R}/\partial\boldsymbol{u}$ is still guaranteed to be a descent direction for the global residual, and the gradient-based optimisation dynamics are preserved.

The optimisation problem of Equation 3.7 can now be expressed in terms of the new coefficients a_{ki} as follows

$$\min_{a_{ki},\, T} \quad \mathcal{R}\left(a_{ki}\right), \quad \forall i \in \{1..M\}, \forall \boldsymbol{k} \in \mathbb{Z}^{N+1} \tag{3.57}$$

which has automatically restricted the optimisation problem to the space of all incompressible flows that obey the required periodic and no-slip boundary conditions, $\mathscr{P}_T$.

A similar coefficient expansion for the local residual is defined as

$$\boldsymbol{r} = \sum_{i=1}^{M} \sum_{\boldsymbol{k} \in \mathbb{Z}^{N+1}} s_{ki} \boldsymbol{\psi}_{ki} e^{i\boldsymbol{k}\cdot\boldsymbol{\xi}}. \tag{3.58}$$

with s_{ki} being the corresponding weighting similar to a_{ki} for contribution of each resolvent mode to the local residual. Note that there is no base flow for the local residual included in Equation 3.58 as is done for Equation 3.54, since the no-slip boundary condition for the local residual has no inhomogeneous component. The value of the velocity coefficients a_{ki} and residual coefficients s_{ki} can be computed by exploiting the orthogonality of the basis functions

$$a_{ki} = \frac{1}{|\Omega| T} \left\langle \boldsymbol{u} - \boldsymbol{u}_b, e^{-i\boldsymbol{k}\cdot\boldsymbol{\xi}} \boldsymbol{\psi}_{ki} \right\rangle_{\Omega_t} = \frac{1}{|\Omega| T} \int_0^T \int_\Omega \left(\boldsymbol{u} - \boldsymbol{u}_b\right) e^{-i\boldsymbol{k}\cdot\boldsymbol{\xi}} \cdot \boldsymbol{\psi}_{ki} \, \mathrm{d}V \, \mathrm{d}t, \tag{3.59}$$

$$s_{ki} = \frac{1}{|\Omega| T} \left\langle \boldsymbol{r}, e^{-i\boldsymbol{k}\cdot\boldsymbol{\xi}} \boldsymbol{\psi}_{ki} \right\rangle_{\Omega_t} = \frac{1}{|\Omega| T} \int_0^T \int_\Omega \boldsymbol{r} e^{-i\boldsymbol{k}\cdot\boldsymbol{\xi}} \cdot \boldsymbol{\psi}_{ki} \, \mathrm{d}V \, \mathrm{d}t, \tag{3.60}$$

where $|\Omega|$ is the volume of the spatial domain. The identities of Equation 3.59 and Equation 3.60 can be used directly on Equation 3.52 to project the gradient-based optimisation dynamics onto the subspace defined by the set of basis functions. This leads to a set of evolution equations in terms of the modal coefficients a_{ki}. Note that if the expansions of Equation 3.54 and Equation 3.58 are substituted into Equations 3.52(c-f) then the constraints are automatically satisfied as desired. To prove that such a projection results in a set of optimisation dynamics restricted to the basis functions, the functional derivative of the global residual using the chain rule can be expanded into

$$\frac{\delta \mathcal{R}}{\delta \boldsymbol{u}} = \frac{\partial \mathcal{R}}{\partial a_{ki}} \frac{\delta a_{ki}}{\delta \boldsymbol{u}}^*, \tag{3.61}$$

where $(\cdot)^*$ denotes the complex conjugate. The functional derivative of a_{ki} with respect to the velocity field $\boldsymbol{u}$ can be derived from Equation 3.59 using the same perturbation method used in Section 3.3 to derive the gradient of the global residual

$$\frac{\delta a_{ki}}{\delta \boldsymbol{u}} = e^{-i\boldsymbol{k}\cdot\boldsymbol{\xi}} \boldsymbol{\psi}_{ki}. \tag{3.62}$$

Substituting Equation 3.62 into Equation 3.61 and applying the projection operation of Equation 3.59 gives

$$\frac{1}{|\Omega| T} \left\langle \frac{\delta \mathcal{R}}{\delta \boldsymbol{u}}, e^{-i\boldsymbol{k}\cdot\boldsymbol{\xi}} \boldsymbol{\psi}_{ki} \right\rangle_{\Omega_t} = \frac{1}{|\Omega| T} \left\langle \frac{\partial \mathcal{R}}{\partial a_{nj}}, e^{-i(\boldsymbol{k}-\boldsymbol{n})\cdot\boldsymbol{\xi}} \boldsymbol{\psi}_{nj}^{\dagger} \cdot \boldsymbol{\psi}_{ki} \right\rangle_{\Omega_t}, \tag{3.63}$$

which, when the mutual orthonormality of the basis functions is utilised simply gives

$$\frac{\partial \mathcal{R}}{\partial a_{ki}} = \frac{1}{|\Omega| T} \left\langle \frac{\delta \mathcal{R}}{\delta \boldsymbol{u}}, e^{-i\boldsymbol{k}\cdot\boldsymbol{\xi}} \boldsymbol{\psi}_{ki} \right\rangle_{\Omega_t} \tag{3.64}$$

Therefore, substituting the expansions into Equation 3.52a and Equation 3.52b and applying the projection gives

$$\frac{\partial \mathcal{R}}{\partial a_{ki}} = -ik_t\omega s_{ki} + \left\langle -\left(\boldsymbol{u}\cdot\boldsymbol{\nabla}\right)\boldsymbol{r} + \left(\boldsymbol{\nabla}\boldsymbol{u}\right)^{\top}\boldsymbol{r} - \frac{1}{Re}\Delta\boldsymbol{r},\, e^{-i\boldsymbol{k}\cdot\boldsymbol{\xi}}\boldsymbol{\psi}_{ki}\right\rangle_{\Omega_t}, \tag{3.65a}$$

$$s_{ki} = ik_t\omega a_{ki} - \left\langle \left(\boldsymbol{u}\cdot\boldsymbol{\nabla}\right)\boldsymbol{u} - \frac{1}{Re}\boldsymbol{\Delta}\boldsymbol{u},\, e^{-i\boldsymbol{k}\cdot\boldsymbol{\xi}}\boldsymbol{\psi}_{ki}\right\rangle_{\Omega_t}. \tag{3.65b}$$

where k_t is the integer frequency for time specifically (a single component of the vector $\boldsymbol{k}$), and $\omega = 2\pi/T$ is the fundamental frequency of the flow. ω represents the frequency of the slowest possible wave that can fit in the finite window defined by the period T.

Note that the pressure terms in both expressions have vanished, which is the primary result of using a divergence-free basis, i.e.

$$\left\langle \boldsymbol{\nabla}\cdot q,\, e^{-i\boldsymbol{k}\cdot\boldsymbol{\xi}}\boldsymbol{\psi}_{ki}\right\rangle_{\Omega_t} = \left\langle q,\, e^{-i\boldsymbol{k}\cdot\boldsymbol{\xi}}\nabla_{\boldsymbol{k}}\cdot\boldsymbol{\psi}_{ki}\right\rangle_{\Omega_t} = 0, \tag{3.66}$$

and similarly for $\boldsymbol{\nabla}p$. As mentioned briefly earlier in this section, the set of modes $\boldsymbol{\psi}_{ki}$ are not required to be a complete basis for the velocity field $\boldsymbol{u}$ and $\boldsymbol{r}$ for every frequency $\boldsymbol{k}$. The sums in Equation 3.54 and Equation 3.58 can be truncated for a finite M, leading to a finite-dimensional linear subspace onto which the fields, and dynamics, are projected. A reference to Figure 3.3 reinforces this concept. With a suitable choice of the basis $\boldsymbol{\psi}_{ki}$ it is possible that the dimensionality of the problem could be greatly reduced, reducing the difficulties of the variational optimisation has with convergence rates as the minimum is approached.

The final result is that Equation 3.65 is a far easier set of equations compared to Equation 3.52 to use for the evolution of $\boldsymbol{u}$ to decrease $\mathcal{R}$. Instead of having to enforce a set of linear and nonlinear constraints throughout the domain and its boundary through some coupled implicit scheme to be able to find the residual gradient, it is possible to, given a_{ki}, compute s_{ki}. These coefficients can then finally be used to compute $\partial\mathcal{R}/\partial a_{ki}$.

It is now possible to state the complete procedure used to find periodic solutions to the Navier-Stokes equations. Figure 3.4 is a flow diagram for the order of computation in a single loop of the optimisation. Beginning with the velocity coefficients a_{ki} the local residual coefficients s_{ki} can be computed using Equation 3.65b. This is practically done by expanding the coefficients a_{ki} back into the full velocity field $\boldsymbol{u}$, which is then used to compute the terms inside the inner product of Equation 3.65b, after which the result is projected back onto the modal subspace. Then, using both the velocity and local residual coefficients, the global residual and its gradient with respect to the velocity coefficients can be computed using Equation 3.65a, using the same expansion-projection method used to compute s_{ki}. The global residual could be

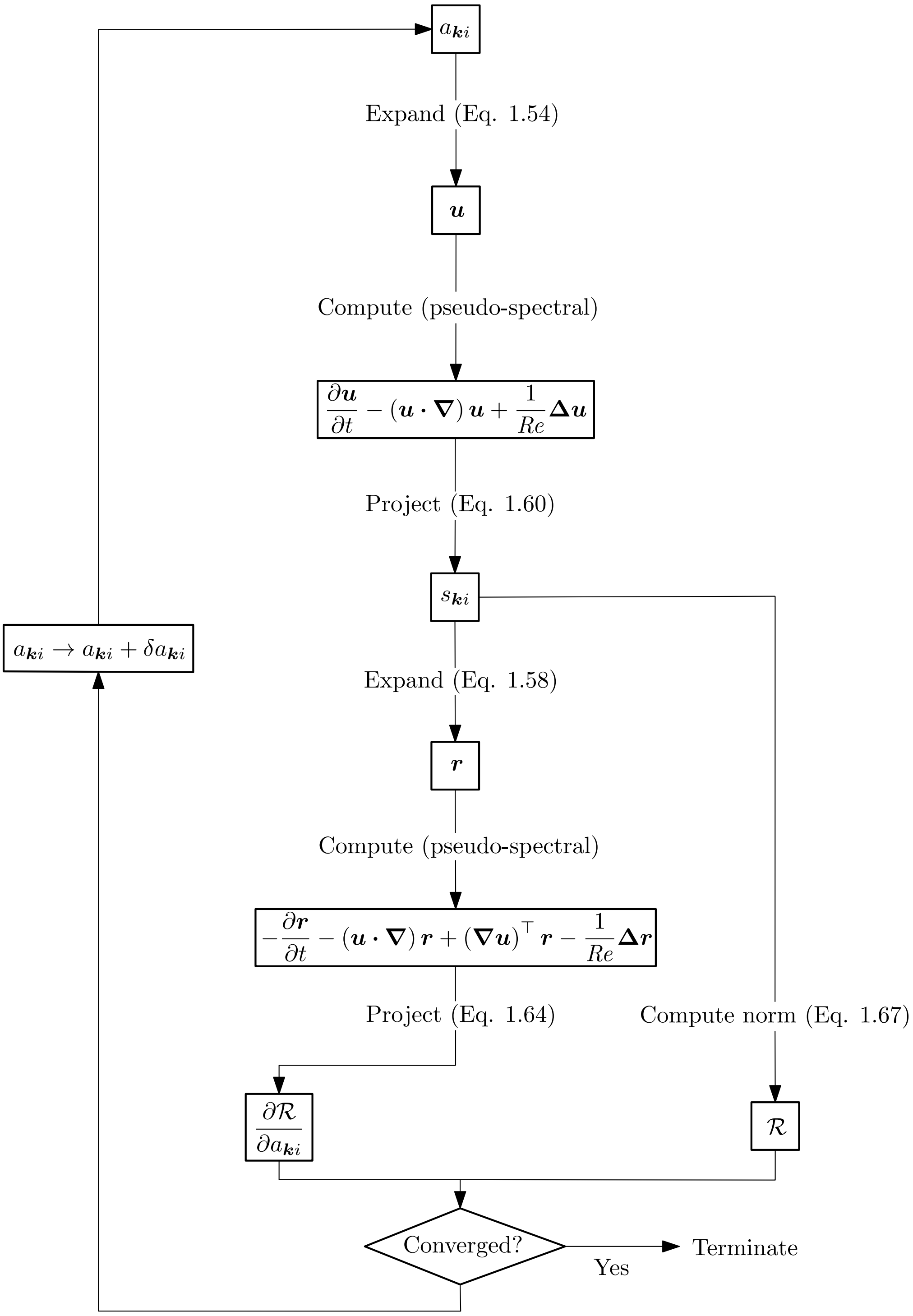

FIGURE 3.4: Flow diagram of the optimisation procedure used to compute the residual and its gradient starting from a velocity field defined by the velocity coefficients.

computed by first expanding out the local residual coefficients into the local residual using Equation 3.58, but a simpler expression can be obtained by expanding

Equation 3.6 using Equation 3.58 to get

$$\mathcal{R} = \frac{1}{2}\sum_{i=1}^{M}\sum_{\boldsymbol{k}\in\mathbb{Z}^{N+1}} |s_{\boldsymbol{k}i}|^2, \tag{3.67}$$

which is an instance of Parseval's theorem. The method used to terminate the optimisation is determined by the user, typically being some small global residual threshold. If this condition has not been met then an update to the velocity coefficients $a_{\boldsymbol{k}i}$ is computed using some optimisation algorithm and the loop returns to the beginning.

3.6 Summary

The methodology used in this thesis to generate periodic solutions to the Navier-Stokes equations has been described in this chapter. It is possible to extend the methodology to treat relative periodic orbits by applying the appropriate symmetry transformations, and including the required spatial shifts as part of the optimisation problem. This has not been considered here since it is not of fundamental importance the method or results that are being presented. The basis is the variational optimisation which was derived here for a general wall-bounded flow with some periodic directions. The resulting set of equations governing the update to the velocity field $\boldsymbol{u}$ are shown to be difficult to solve due to the interplay between the incompressibility constant and no-slip boundary conditions. This issue relates to the lack of proper boundary conditions for the pressure, which leads to some induced slip at the boundary. A novel solution to this problem is proposed using a Galerkin projection onto a set of divergence-free modes that satisfy the no-slip boundary conditions, and it is shown that this approach decouples the velocity and pressure problems from each other leading to a simpler set of equations for the update to $\boldsymbol{u}$. The methodology presented represents an alternative approach to that in Ashtari and Schneider (2023) on how to properly handle the incompressibility and no-slip constraints together. The techniques used in this chapter are not on their own revolutionary, with the novelty coming from the unique combination. An additional layer of novelty comes from the ability to construct low-order models via a truncation of the number of modes used in the Galerkin projection. This restricts the velocity to a finite-dimensional subspace which can contain the most important dynamical information, depending on the choice of the modes. As will be seen in chapter 6, this approach to low-order modelling of the flow can achieve a significant improvement in convergence rates.

The implementation of this methodology is in the Julia programming language, with the code available freely on GitHub under the organisation The-ReSolver, specifically the residual calculations being performed in the Fields.jl.

Chapter 4

Rotating Couette Flow and Resolvent Analysis

Rotating Plane Couette Flow (RPCF) is chosen as the main flow of study in this thesis. RPCF is a type of channel flow, possessing only a single statistically inhomogeneous direction due to the walls at the top and bottom of the domain. Couette flow is an extensively studied and well understood flow, in terms of the characterisation of the turbulent structures that occur within it, as well as the types of instabilities that lead to said turbulence. Before the projected optimisation methodology described in Chapter 3 is applied to RPCF to find equilibrium and periodic solution, this chapter characterises the flow at a few different regimes in Section 4.2, ranging from stable steady, to quasi-periodic and turbulent. The low-dimensionality of the flow is quantified utilising SPOD modes. The section then moves to resolvent analysis of the flow, outlines the procedure used to generate the resolvent modes in Section 4.3.1 used here and in Chapter 6, following the framework used in McKeon and Sharma (2010). Then the ability for the resolvent modes to capture the low-dimensionality of RPCF is assessed in Section 4.3.2.

4.1 Rotating Plane Couette Flow

The flow can be derived as a small gap limit of the general Taylor-Couette flow with two counter-rotating cylinders with equal (and opposite) rotation rates. The result is that curvature of the system has a negligible effect on the flow, and the system resembles a Couette flow between two parallel walls moving in opposite directions, with the addition of a Coriolis acceleration term. This type of flow can serve as a very simple model for atmospheric flow (Dubrulle et al., 2005; Vanneste and Yavneh, 2007), and has an analogy with general convective flows as discussed in Section 4.1.2. RPCF is noted to be more difficult to study experimentally, however it has certain theoretical

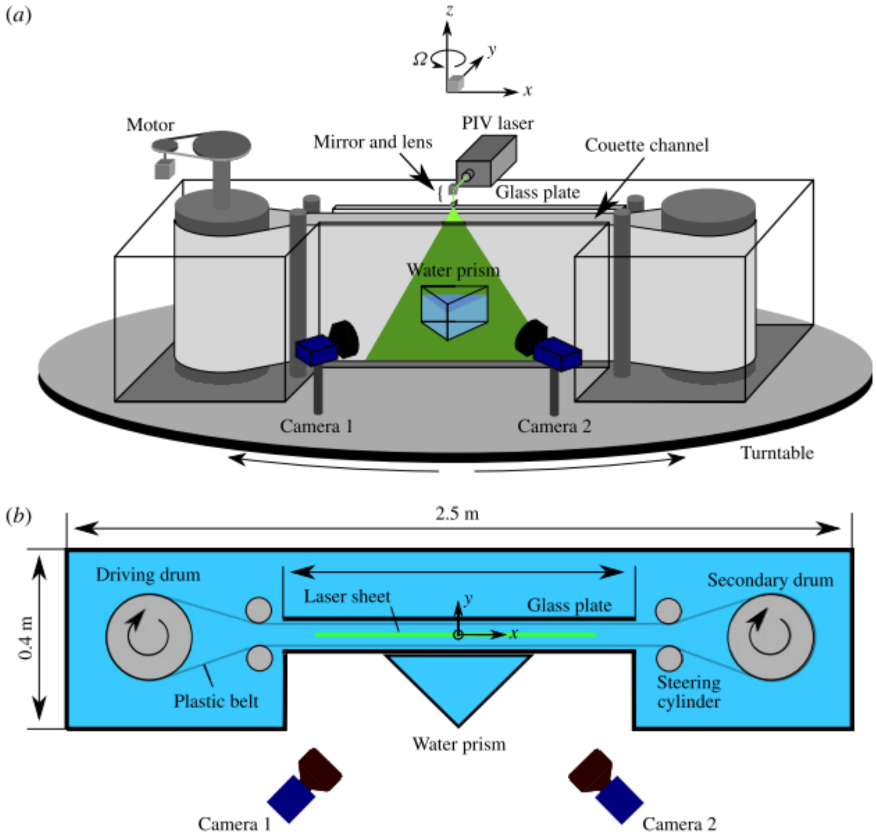

FIGURE 4.1: An experimental (stereoscopic) PIV setup for RPCF from an isometric view in panel (a), and top view in panel (b), where the turntable induces a Coriolis and centrifugal force, the latter being absorbed into the pressure since it is isotropic. Obtained from Kawata and Alfredsson (2016)

and numerical benefits due to it permitting Cartesian geometry (Daly et al., 2014). This term promotes instabilities in the flow and enhances transfer of momentum between the streamwise and wall-normal directions. The plane Couette flow is linearly stable for all Reynolds numbers, however the rotation of RPCF makes it unstable at a finite (and relatively small) Reynolds number. This leads to a series of bifurcations eventually resulting in full spatiotemporal turbulence. This rotation number can be recreated in experiment by adding a total system rotation as shown in the experimental setup in Figure 4.1, used by Kawata and Alfredsson (2016) to investigate the effect of rolling structures on the momentum transport of the flow. The Coriolis acceleration can also be interpreted as a by-product of a rotating (non-inertial) reference frame.

The first to systematically study the flow was Johnston et al. (1972), with the linear stability of the system for various rotation rates established in Lezius and Johnston (1976). Further study on the stability characteristics is available in Hiwatashi et al. (2007) and the resulting structures observed at each bifurcation is discussed in Nagata (2013); Nagata et al. (2021). An in depth experimental study of the parameter space for

RPCF can be found in Tsukahara et al. (2010), with a corresponding DNS study replicating many of the same features in Tsukahara (2011).

4.1.1 Flow Geometry and Governing Equations

Consider the incompressible flow between two infinitely long and broad flat parallel plates moving at velocities of $\pm U_w$ (upper and lower plates, respectively), with an additional imposed body rotation in the spanwise direction. The schematic for such a flow is shown in Figure 4.2, with Ω_z denoting the spanwise system rotation, not to be confused with Ω in Chapter 3 that denoted the flows general spatial domain. There are two cases for the general behaviour of the fluid based on the direction of the system rotation: "cyclonic" and "anticyclonic". The first is for a rotation vector pointing in the same direction as the mean vorticity field; into the page in Figure 4.2. The second is for a rotation vector pointing in the opposite direction as the mean vorticity field; out of the page in Figure 4.2. The Coriolis effect in the anticyclonic case is known to promote instabilities (Tsukahara et al., 2010), and is the only case considered in the current work.

The origin of the coordinate system is defined to be at the midpoint of the plates, and the x-, y-, and z-axes are taken to be the streamwise, wall-normal, and spanwise directions, respectively. In addition, the unit vectors for the respective axes are defined as $\hat{\boldsymbol{\imath}}$, $\hat{\boldsymbol{\jmath}}$, and $\hat{\boldsymbol{k}}$. Therefore, the rotating vector for the system can be expressed as $\Omega_z\hat{\boldsymbol{k}}$. Normalising all dimensions using the wall velocity U_w, the half-wall height h, and fluid density ρ the governing equations can be expressed as

$$\frac{\partial \boldsymbol{u}}{\partial t} + (\boldsymbol{u}\cdot\boldsymbol{\nabla})\,\boldsymbol{u} = -\boldsymbol{\nabla} p + \frac{1}{Re}\boldsymbol{\Delta}\boldsymbol{u} - Ro\left(\hat{\mathbf{k}}\times\boldsymbol{u}\right), \tag{4.1a}$$

$$\nabla\cdot\boldsymbol{u} = 0, \tag{4.1b}$$

where $Re = U_w h/\nu$ and $Ro = 2\Omega_z h/U_w$ are the Reynolds and rotation numbers, respectively, where ν is the kinematic viscosity. Reynolds number and Rotation

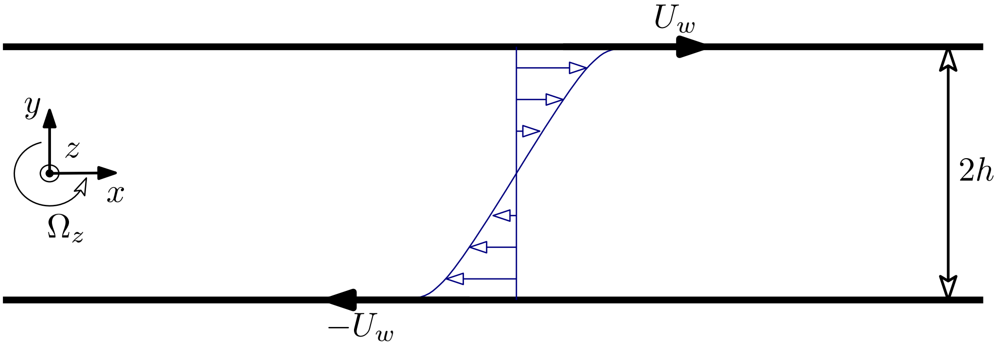

FIGURE 4.2: Schematic of the geometry for RPCF with spanwise (anticyclonic) rotation, with the spanwise direction perpendicular to the page.

number are the only non-dimensional parameters governing this flow, measuring the mutual strength of the inertial, viscous, and rotational forces present in the system. At the walls the no-slip boundary condition is imposed, which in normalised units is

$$\boldsymbol{u}\big|_{y=\pm 1} = \pm 1\hat{\boldsymbol{\imath}}. \tag{4.2}$$

The flow geometry is defined to be infinite in the streamwise and spanwise directions and is therefore statistically homogeneous, resulting in periodic boundary conditions for the prescribed domain size, expressed as

$$\boldsymbol{u}\big|_{z=0} = \boldsymbol{u}\big|_{z=L_z}, \tag{4.3}$$

$$\boldsymbol{u}\big|_{x=0} = \boldsymbol{u}\big|_{x=L_x}, \tag{4.4}$$

where L_x and L_z are the length of the channel in streamwise and spanwise directions, respectively.

4.1.2 Streamwise Independence and the Rayleigh-Bénard Analogy

In this work, there is an additional assumption that the flow is streamwise independent, i.e. $\partial/\partial x = 0$, which has the primary consequence of reducing the size of the domain, alleviating some of the computational burden in finding solutions. This results in a 2-Dimensional 3-Component (2D3C) flow, where all three Cartesian components of the vector fields are retained, but they are restricted to only vary over two spatial dimensions: the spanwise and wall-normal directions.

It is known that 2D turbulence has a distinctly different flavour to the more complete 3D turbulence observed in nature, but despite limiting the RPCF to two spatial dimensions there is extensive evidence that the key features of turbulence are retained, as long as the three components of the velocity are retained in the simulation. There has been a known link between the dynamics of rotating shear flows and convective thermal flows for decades, as described in Chandrasekhar (1961); Yih (1965), with the link between Taylor-Couette flow and Rayleigh-Bénard convection being discussed in Eckhardt et al. (2007). The specific flow configuration of streamwise independent RPCF has been shown to be directly analogous to Rayleigh-Bénard convection in Eckhardt et al. (2020). This means that the restricted flow, despite losing a whole dimension of degrees-of-freedom, still undergoes a transition to turbulence akin to the full 3-dimensional case. It has also been shown independently in Gayme (2010) and Farrell et al. (2012) that streamwise independent flows can accurately capture the mean statistics of the fully 3-dimensional flow, as well as display turbulent behaviour analogous to the 3-dimensional case. The exact route to chaos taken by the streamwise independent flow is naturally different to that taken for full 3-dimensional case, not allowing for bifurcations into stable flows that display some waviness in the streamwise direction, typically called the Wavy Vortex Flow (WVF). This has little consequence, however, on the ability of the flow to obtain turbulence once the critical Reynolds number has been surpassed. Thus 2D3C RPCF is a valid model for turbulent flow, albeit with some altered instability mechanisms.

4.1.3 Bifurcations and Transitions of RPCF

The transition to turbulence of RPCF is through a series of linear bifurcations to more spatially and temporally complex stable solutions until what could be considered a turbulent state is reached. Turbulence is heuristically defined here as a generally broadband structure to the spectrum of the flow in both time and space. The flow starts as with a stable laminar solution that is identical that of plane Couette flow. Linear stability analysis shows the boundary of stability for the laminar flow has the following relationship

$$Re = \sqrt{\frac{107}{Ro\,(1 - Ro)}}, \tag{4.5}$$

given in Lezius and Johnston (1976). This shows that the laminar flow is most unstable for $Ro = 0.5$, which is the rotation number of choice for this work. At $Re \approx 20.7$ a bifurcation occurs, the laminar solution becomes unstable, and a new stable equilibrium solution is found. This equilibrium solution has the characteristic streamwise rolls that are present throughout the total set of regimes accessible by varying Re, as shall be seen later in this chapter. As the Reynolds number is further increased above the laminar bifurcation the streamwise rolls grow in strength until the flow undergoes a type of Hopf bifurcation yielding a stable periodic orbit. It should be noted that. From experience, as the Reynolds number is increased beyond this point the spatial structures of the flow do not vary much, however the overall complexity of the flow increases. More precisely the spectral content of the flow becomes more broadband as the Reynolds number increases, until a threshold has been reached in which the flow is deemed sufficiently complex to be turbulent.

4.2 Characteristics of 2D3C RPCF

This section presents the analysis of DNS simulations of RPCF at various Reynolds numbers. The goal is to characterise the behaviour of the flow in different regimes as it transitions from stable laminar flow to fully turbulent flow. This is achieved by analysing the velocity statistics and spectra of the flow as well as a SPOD analysis to elucidate the dominant coherent structures of the flow. As mentioned, all of the analysis here is performed at $Ro = 0.5$, since it maximally destabilises the laminar flow.

4.2.1 Computational Grid

To facilitate the analysis of RPCF, a custom DNS solver was utilised, originally developed for Lasagna et al. (2016). To account for the incompressibility the solver uses a vorticity-streamfunction formulation of the governing equations. The resulting formulation requires the solution to a couple of Helmholtz problems for the velocity, streamfunction, and vorticity. The bulk of the computational time is naturally spent solving these problems.

Periodic boundary conditions are imposed in the spanwise direction by expanding the flow variables into a Fourier series, and the wall-normal direction is discretised uniformly with collocation points, with derivatives in the wall-normal direction being computed using a central differencing scheme. An implicit-explicit splitting scheme is used for each time step. The result of the discretisation is a set of Helmholtz problems for the three flow variables. These Helmholtz problems are where the majority of the computational time is spent. The overall time taken to generate the sets of data are listed in Table 4.1. The code used is available on GitHub.

There are various Reynolds numbers considered in the following sections. The spatial discretisation used for each of these Reynolds number, as well as the time step used and the total time span of the simulation, are summarised in Table 4.1. The reason for the longer time spans in the lower Reynolds number cases is to ensure that any transients have decayed such that the desired stable solution can be completely accurately identified. All the cases are simulated with a spanwise length of $L_z = 8$. Some limited cases were examined to investigate the effect of varying this parameter on the resulting solution, where it was found that the exact size of the resulting structures did vary their overall character is invariant to variations in L_z. This can be justified by linking this flow back to the Taylor-Couette flow from which it can be derived. The spanwise direction corresponds there to the axial direction along the length of the co-rotating cylinders. Lengthening or shortening this distance in the computational domain would not produce any changes to the overall character of the dynamics, just the size of the resulting vortices that form, as they have to fit in some integer division within the finite domain size.

Re	N_y	N_z	dt	T	Wall-time (hh:mm:ss)
25	64	32	0.01	500	00:01:08
50	64	32	0.01	2000	00:01:43
450	128	64	0.01	5000	00:08:56
1000	256	128	0.005	6000	00:59:09
5000	1024	512	0.0002	1500	76:16:16

TABLE 4.1: Summary of the computational grids used for the DNS simulations at the Reynolds numbers featured in this chapter.

4.2.2 Velocity Statistics

In Figure 4.3 the turbulent dissipation and the energy input rates from the wall shear stress, computed using the following relationships

$$\mathcal{E} = \int_{\Omega} \|\nabla \times \boldsymbol{u}\|_2 \, \mathrm{d}V \qquad\qquad \mathcal{I} = \int_{\partial\Omega} \frac{\partial \boldsymbol{u}}{\partial y} \cdot \hat{\boldsymbol{\imath}} \, \mathrm{d}S$$

are plotted against each other for flows at $Re = 450$, $Re = 1000$, and $Re = 5000$, in panels (a-c), respectively. Note that the norm used primarily in this chapter, $\|(\cdot)\|_2$, refers to the standard Euclidean norm. This demonstrates the periodic, quasi-periodic, and turbulent regimes of the flow. The flow at $Re = 450$ forms a closed loop that is assumed here to be exactly periodic. As the Reynolds number is increased to $Re = 1000$ the loop spreads out as the state-space attractor becomes more complex, bifurcating into a torus. The result is a flow that still seems rather periodic, but with variations that can only be accounted for by the presence of lower frequency modes becoming active. Finally Figure 4.3(c) demonstrates the turbulent case well at $Re = 5000$.

Figure 4.4 shows the mean velocity profiles obtained for each Reynolds numbers mentioned above, with the laminar profile included, representing any solution of a sufficiently low Reynolds number. There is a clear trend with the profiles as the Reynolds number increases. As the Reynolds number increases, the mean momentum transfer of the flow increases, transporting velocity from the walls to the core of the channel. This is reflected in a steeper velocity gradient in the centre of the channel, equal to twice the laminar profile gradient. This double gradient region becomes larger as the Reynolds number increases, and as the flow reaches the wall the velocity changes ever more rapidly to match the wall velocity. This leads to higher shear stresses at the walls as the Reynolds number increases as expected.

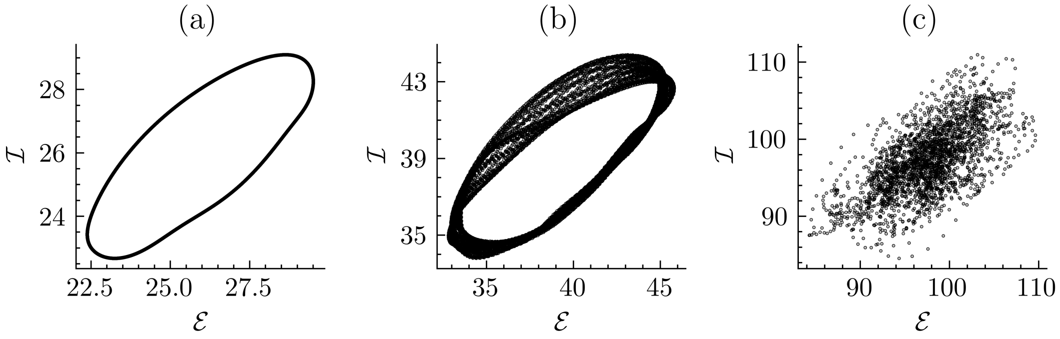

FIGURE 4.3: Energy dissipation rate against energy input from the walls for $Re = 450$, $Re = 1000$, and $Re = 5000$, in panels (a-c), respectively.

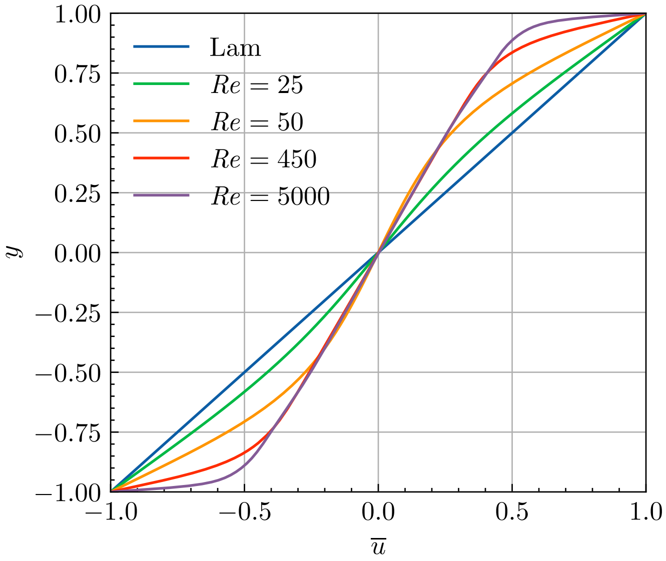

FIGURE 4.4: Mean velocity profiles of RPCF at various Reynolds numbers, plotted with the laminar Couette flow profile for comparison.

Applying the RANS equations to Couette flow gives the following relation between the mean shear and Reynolds stress

$$-\overline{u'v'} + \frac{1}{Re}\frac{\partial \overline{\boldsymbol{u}}}{\partial y} = u^*, \tag{4.6}$$

where u^* is the (non-dimensional) friction velocity, obtained by taking the boundary value of the mean shear stress. Since in the core of the flow the mean velocity gradient is linear, Equation 4.6 implies that the Reynolds stress $\overline{u'v'}$ is constant over the same region. This is a well-known fact of Couette flow and is unaffected by the presence of the Coriolis term in the governing equations. Figure 4.5 displays the non-zero

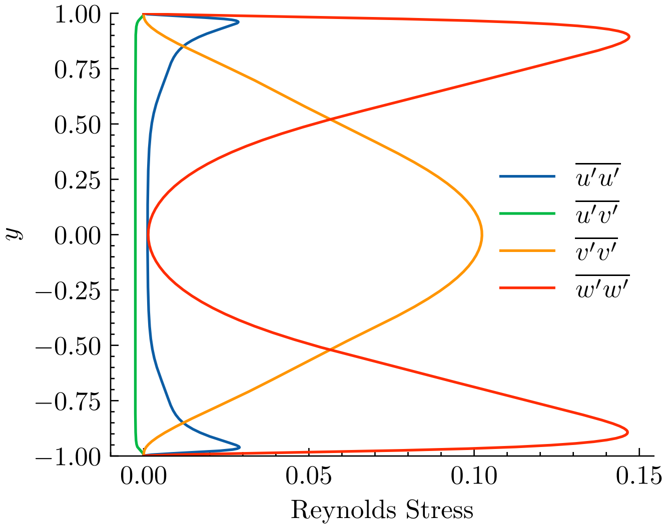

FIGURE 4.5: Non-zero Reynolds stresses of RPCF at $Re = 5000$.

Reynolds stresses for $Re = 5000$. The invariability of $\overline{u'v'}$ is confirmed by this plot, with the other cross-component Reynolds stresses being exactly zero. The other stresses represent the relative mean energy content of each velocity component over the height of the channel. The wall-normal velocity contains the majority of its energy in the core since the flow has to be parallel to the wall. The streamwise and spanwise velocities are most energetic near the walls, where relatively small but energetic vortical structures reside. As will be seen in Section 4.2.4 the primary structure of the flow is the streamwise roll in the centre of the channel, that act to transfer momentum from the walls to the centre of the flow. These rolls are the primary source of the unsteady energies of the wall-normal and spanwise velocities.

4.2.3 Spectral Analysis

The following spectral analysis have been performed over the homogeneous spanwise direction and time. Due to the spanwise direction being modelled with periodic boundary conditions, the raw velocity fields can simply be analysed using a discrete spectra through the application of an FFT. Welch's method is used for the temporal spectra, with Hann windowing to reduce the effects of spectral leakage, given by the function

$$w(s) = \frac{1}{2}(1 - \cos(2\pi s)), \tag{4.7}$$

for $s \in [0, 1]$.

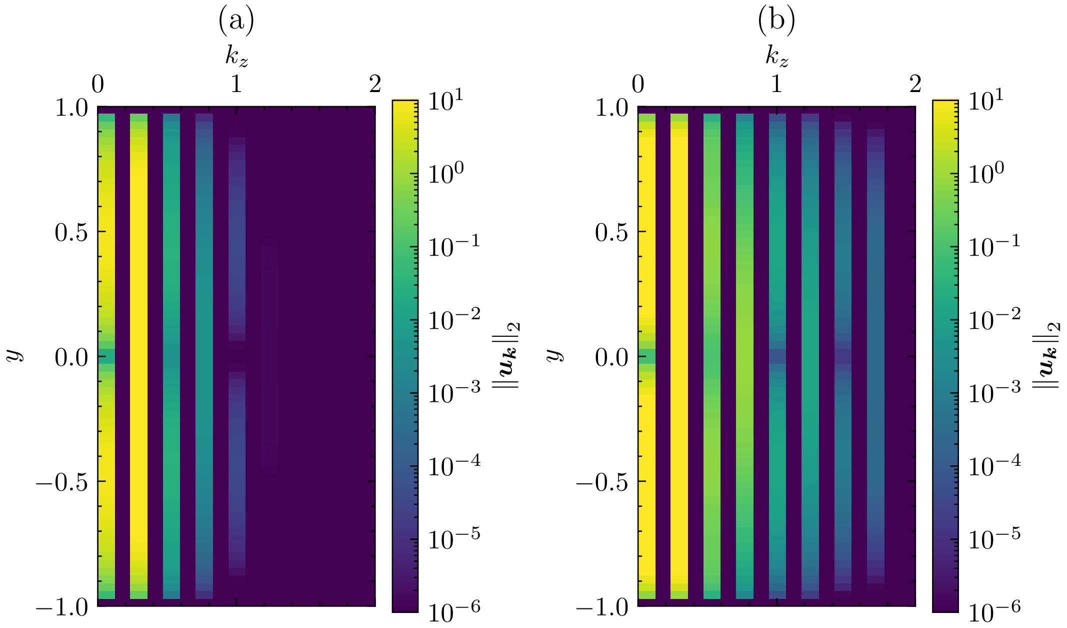

FIGURE 4.6: Spanwise spectra of RPCF at $Re = 25$, in panel (a), and $Re = 50$, in panel (b), plotted against the wall-normal coordinate.

Figure 4.6(a-b) displays the spectra at $Re = 25$ and $Re = 50$, respectively. The spanwise wavenumber is denoted as k_z which is evaluated at multiples of the fundamental wavenumber $\beta = 2\pi/L_z$ which defines the largest wave permissible in the finite domain size. The flows at these Reynolds numbers are stable equilibrium, and thus no temporal spectra are presented, instead only showing the spanwise spectra against the wall-normal height. The two spectra are very similar in form, notably with $Re = 50$ being larger in magnitude than $Re = 25$. This extra energy primarily comes from the spanwise constant mode, $k_z = 0$, and is a consequence of the growing strength of the primary streamwise vortex that dominates the flow. The effect of these vortices on the spanwise constant mode can be seen for $Re = 25$ as well, with the spectral peak being slightly more towards the centre of the channel. This implies that the vortices grow as the Reynolds number increases, shifting some of the energy towards the walls. Otherwise, the spectra for both flows drop off very quickly, showing the dominant modes have a wavenumber of $k_z = 2\beta$, i.e. the third columns of Figure 4.6(a) and (b). This is a common trend that will persist throughout all the regimes featured here.

Moving onto the case of $Re = 450$ where the flow has since bifurcated to a stable periodic solution. As mentioned, Welch's method with Hann windowing is used to obtain the temporal spectra. Since the flow here is periodic, however, it is not necessary to average the spectra over multiple sections of the data. Instead, a single slice of the flow, at a given wall-normal location, is extracted. Due to the finite sampling rate, the resulting data is not exactly periodic, which would lead to spectral leakage if a FFT was used directly. Instead, the slice of the flow is windowed in time which minimises the spectral leakage and leads to much more well-defined set of spectral peaks. Figure 4.7 illustrates the resulting spectra obtained with this method, at wall-normal locations of $y \approx -0.88$ and $y \approx 0$ in panels (a-b), respectively. Only a

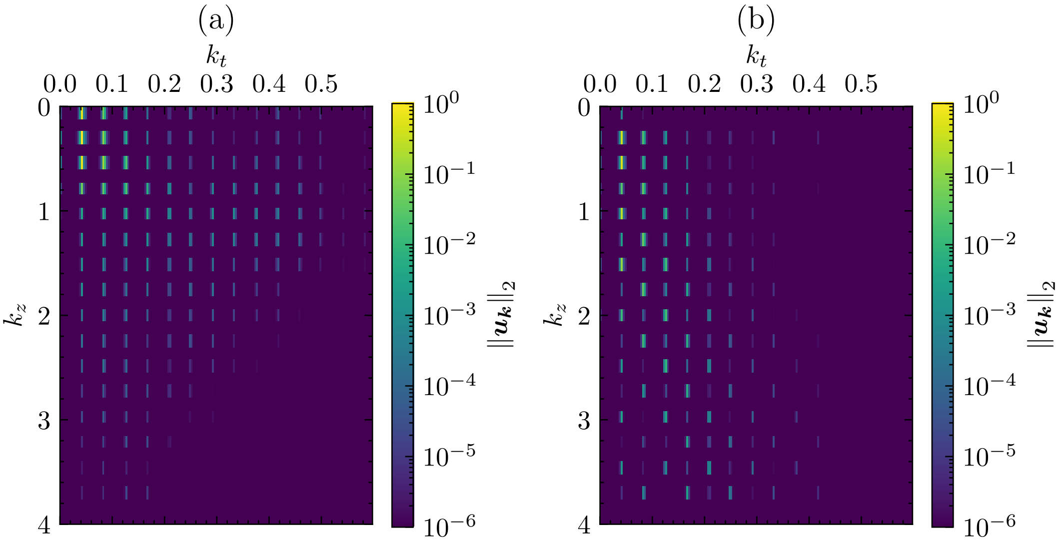

FIGURE 4.7: Spanwise and temporal spectra at $Re = 450$ located at wall-normal positions of $y \approx -0.88$ in panel (a) and $y \approx 0$ in panel (b).

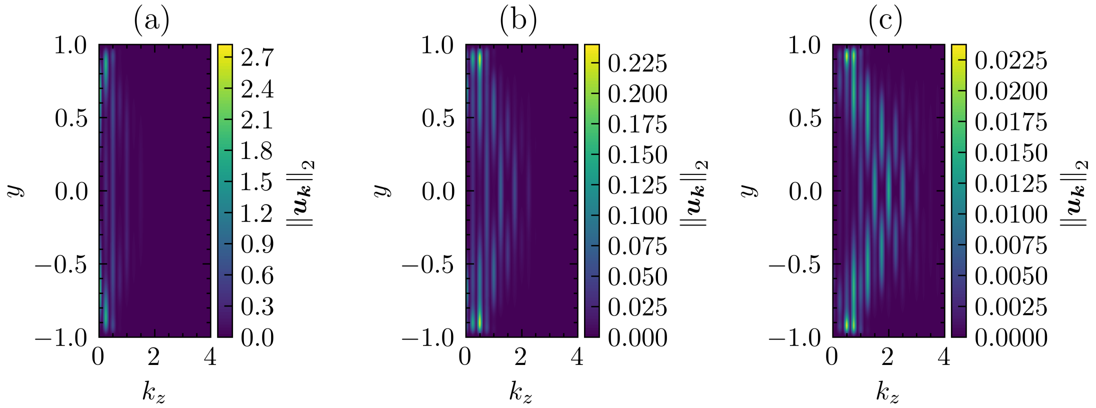

FIGURE 4.8: Spanwise spectra over the wall-normal height at $Re = 450$, sampled at frequencies $k_t = i/25$ for $i \in \{1, 2, 3\}$ in panels (a-c), respectively.

small section of the total computed spectra is shown, representing the relatively small number of active spanwise and temporal modes in the flow. The base fundamental frequency for the flow corresponds to a period of $T = 25$ which is the period of the flow. The only other significant spectral content is contained in the harmonics of this fundamental frequency, with a little spectral leakage due to the sampling error. The spanwise modes still contain most of their energy in the dominant vortices with a wavelength of 4 spanwise units. The main takeaway of this set of spectra is to confirm the periodicity of the flow with a single strong frequency underlying it, as opposed to quasi-periodic flows that would have multiple fundamental frequencies with their associated harmonics.

Figure 4.8 shows the spanwise spectra of the periodic flow at $Re = 450$ over the height of the channel, selected at the fundamental frequency of the flow and the two consecutive harmonics in panels (a-c), respectively. The spectral energy of the flow at the fundamental frequency of the flow is concentrated near the walls and for the small spanwise wavenumbers, representing the large magnitudes of the streamwise rolls. The larger harmonics in Figure 4.8(b-c) show a gradual spread of the energy over more of the channel and to higher spanwise wavenumbers. The trend is that higher temporal frequencies are better correlated with higher spanwise wavenumber, as faster evolving structures are typically smaller, reflected in the spectra of Figure 4.8. The total magnitude of the spectral energies also decreases for the larger temporal harmonics as expected. These results, being somewhat typical for fluid flows, is useful to establish the growing complexity of the flow, and understand exactly where the energy containing structures are located.

Moving onto the turbulent regime, Figure 4.9 shows the spanwise-temporal spectra of the flow at $Re = 5000$, at the same wall-normal locations as in Figure 4.7. The first thing to note is the spectrum is much more broadband in both the spanwise and temporal directions, with few distinct spectral peaks, indicating that the flow is made up of a set of modes over a continuum of frequencies. The flow near the channel

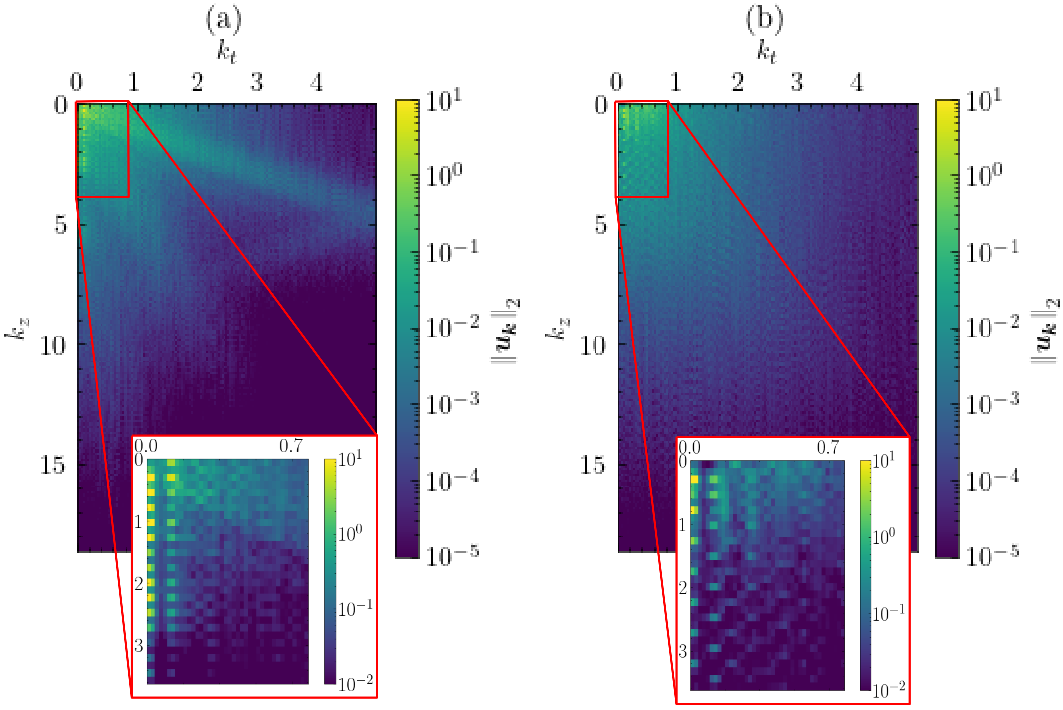

FIGURE 4.9: Spanwise and temporal spectra at $Re = 5000$ located at wall-normal positions of $y \approx -0.88$ in panel (a) and $y \approx 0$ in panel (b). Cut-outs of the spectra are shown corresponding to the similar spectral range as displayed in Figure 4.7.

centre has a slower spectral decay in the temporal direction, implying more of a mix of large and small scale eddies in the flow, as opposed to near the wall where the flow is more structured due to the restrictions imposed by the rigid boundary. In fact, the effect of the rigid boundary can be seen in Figure 4.9(a) where higher wavenumber (smaller wavelength) modes have a larger proportion of the energy compared to the lower wavenumber (larger wavelength) modes. The cutouts of the spectra, showing a similar spectral range as in Figure 4.7 are done to better inspect the strength of the structures that were dominant at $Re = 450$. It is clear that the same streamwise rolls with a wavelength of 4 spanwise units are still energetically dominant in the flow and are present at the same fundamental frequency corresponding to a period of $T = 25$.

Figure 4.10 shows the spanwise spectra of the flow at $Re = 5000$ plotted over the height of the channel, similarly to Figure 4.8. The spectra are sampled at the temporal frequencies corresponding to periods of $T = 25$, $T = 12.5$, and $T = 25/3 \approx 8.33$, which represent the dominant unsteady temporal modes and its two harmonics. The spectra show the largest energies near the walls of the domain at spanwise wavenumber corresponding to structures that vary with a wavelength of 4 spanwise units. This once again corresponds to a set of vortices that vary twice over the length of the domain in the spanwise direction. The decay is relatively fast, going below an order of magnitude after only a few harmonics. The centre of the channel shows regular peaks corresponding the same vortices, however with a smaller magnitudes. It should also be noted that magnitude of the total spectra does not monotonically

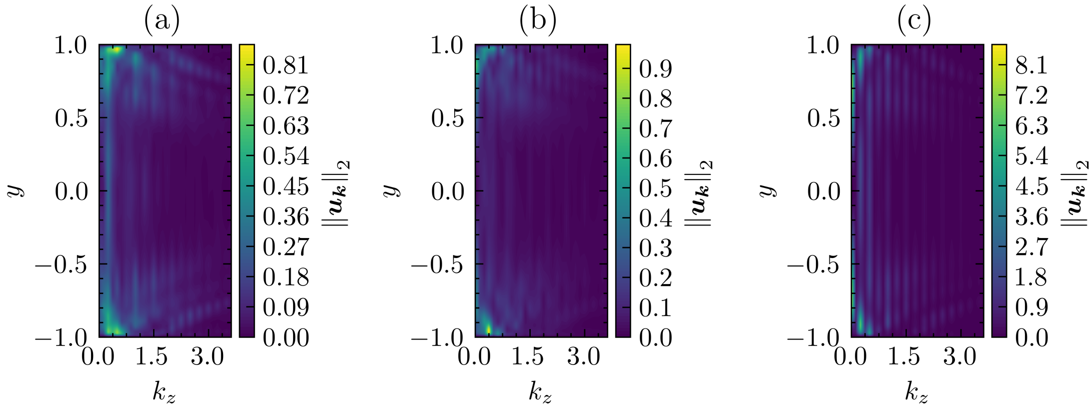

FIGURE 4.10: Spanwise spectra over the wall-normal height at *Re* $= 5000$, sampled at the same temporal frequencies as in Figure 4.8.

decrease as the temporal frequency increases, implying a complex and finer-grained structure to the flow. This will be clearly observed in the next section.

4.2.4 Dominant Turbulent Structures and SPOD

The analysis of RPCF will now conclude by demonstrating the dominant features of the flow, including over the statistically inhomogeneous wall-normal direction, utilising SPOD for the analysis. Figure 4.11 displays snapshots of the DNS flow obtained for *Re* $= 25$, *Re* $= 50$, *Re* $= 450$, and *Re* $= 5000$ in panels (a-d), respectively. The primary feature in all of the flows are the streamwise rolls, shown to be very prominent in the spectra of the flows. The rolls in the equilibrium cases, Figure 4.11(a-b), only differ in their strength, with the higher Reynolds number equilibrium clearly hosting stronger vortices that transfer the momentum more effectively. The unsteady flows in Figure 4.11(c-d) also have the same rolls, however,

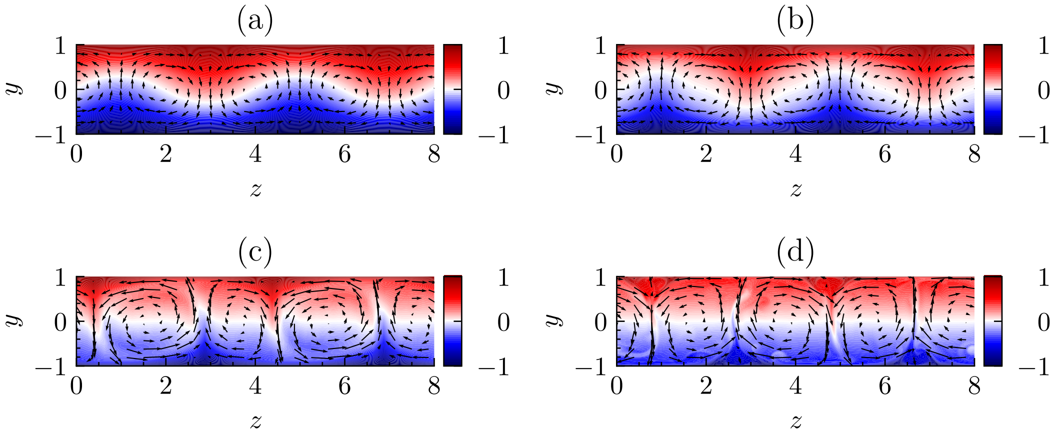

FIGURE 4.11: Snapshots of the velocity fields at *Re* $= 25$, *Re* $= 50$, *Re* $= 450$, and *Re* $= 5000$, in panels (a-d), respectively.

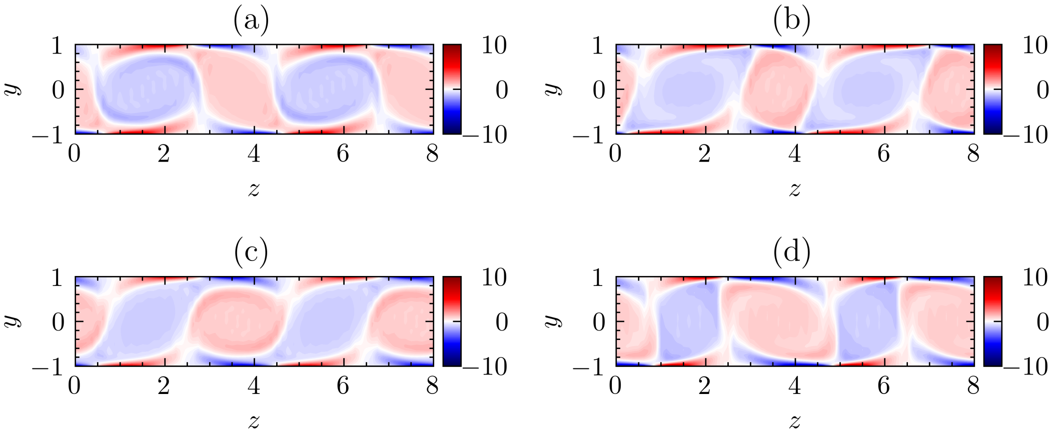

FIGURE 4.12: Streamwise vorticity snapshots of the flow at $Re = 450$, with a temporal separation of 5 time units.

they instead oscillate, growing and shrinking in size. The characteristic time for the rolls to grow and shrink is $T = 25$, identified from the spectral analysis.

The flows in Figure 4.11(c-d) at $Re = 450$ and $Re = 5000$, respectively, have many of the same features as each other, however close inspection of the turbulent flow in Figure 4.11(d) reveals the presence of small scale variations that are not present at $Re = 450$, which varies more monotonically over its domain. The effect of these smaller scale motions at $Re = 5000$ can be most clearly seen by comparing Figure 4.12 and Figure 4.13. These figures show a handful of snapshots, separated by 5 time units, of the streamwise vorticity of the flow for $Re = 450$ and $Re = 5000$, respectively. The vorticity field for $Re = 450$ is clearly more coherent, with the streamwise rolls featuring heavily. The largest proportion of the vorticity, however, comes from the near wall region, at the top of the large rolls. This is where the majority of the flow energy is added as the large shear forces generate vortices that are shed into the core of the flow. This is even more pronounced in Figure 4.13 where the magnitude of the

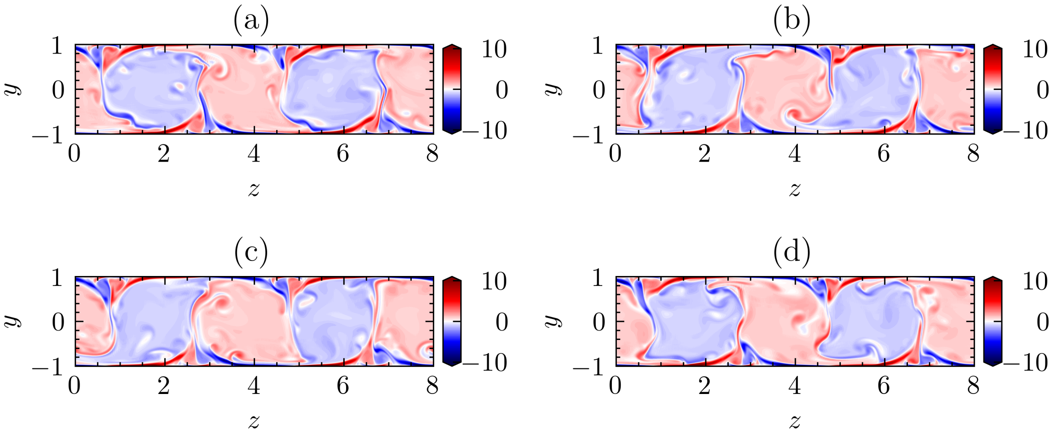

FIGURE 4.13: Streamwise vorticity snapshots of the flow at $Re = 5000$, with a temporal separation of 5 time units.

near the walls is several times larger while the core of the flow maintains a very similar total vorticity. The flow at $Re = 5000$ is clearly more chaotic, with eddies of various sizes originating from the wall shear stresses being subsequently shed into the flow without a regular pattern. However, underneath all the noisy fluctuations created by the turbulent eddies, the same pattern of oscillating rolls are clearly present at both $Re = 450$ and $Re = 5000$. The flow clearly has a large amount of coherence that is present throughout its various regimes up to turbulence.

4.2.4.1 SPOD Methodology

To quantify the degree of coherence, an SPOD analysis is performed for Reynolds numbers of $Re = 450$ and $Re = 5000$. The methodology used to generate the SPOD is described in Towne et al. (2018), utilising a spectral averaging technique similar to Welch's method for single dimensional periodograms. Before presenting the results of the SPOD analysis, a little space is dedicated to describing the methodology used to compute the modes and their rankings.

Let $\boldsymbol{q}_{k_z,i} \in \mathbb{C}^N$ denote the instantaneous state vector at time t_i for all the points in the domain Ω, where N denotes the number of discrete points making up the domain. $i \in \{1, \ldots, M\}$, where M denotes the number of available snapshots, and k_z denotes the spanwise wavenumber used. The state vector is indexed in the spanwise wavemumber domain since the flow is known to be homogeneous in this direction, and is best decomposed into a Fourier basis in this direction prior to the SPOD analysis. The result is that the SPOD analysis is restricted to constructing a set of modes in the inhomogeneous wall-normal direction for every spanwise wavenumber k_z available. The data matrix is then formed as such

$$\boldsymbol{Q}_{k_z} = \begin{pmatrix} \boldsymbol{q}_{k_z,1} & \boldsymbol{q}_{k_z,2} & \cdots & \boldsymbol{q}_{k_z,M} \end{pmatrix}, \tag{4.8}$$

where $\boldsymbol{Q}_{k_z} \in \mathbb{C}^{N \times M}$. It is a bad idea to directly Fourier transform this data matrix in time to obtain the cross-spectral density matrix, since the Fourier coefficients obtained will not converge as M tends to infinity. This is where the Welch method is utilised to give a more well-defined set of Fourier coefficients at the cost of spectral resolution. The data matrix $\boldsymbol{Q}_{k_z}$ is split into multiple (optionally overlapping) blocks, denoted as $\boldsymbol{Q}_{k_z}^{(n)} \in \mathbb{C}^{N \times N_f}$ where N_f is the number of snapshots in each block. Let N_b denote the number of blocks, and N_o denote the number of snapshots that overlap between each $\boldsymbol{Q}_{k_z}^{(n)}$. At this point, the data in each block is windowed, and the result is Fourier transformed in time to give the following block spectral matrix

$$\hat{\boldsymbol{Q}}_{k_z}^{(n)} = \begin{pmatrix} \hat{\boldsymbol{q}}_{k_z,1}^{(n)} & \hat{\boldsymbol{q}}_{k_z,2}^{(n)} & \cdots & \hat{\boldsymbol{q}}_{k_z,N_f}^{(n)} \end{pmatrix}, \tag{4.9}$$

where $\hat{\boldsymbol{q}}_{k_z,k}^{(n)}$ is the Fourier coefficient of the windowed data at the temporal frequency f_k. A new matrix is now formed $\hat{\boldsymbol{Q}}_{k_z}^{(k)}$ where each column is the Fourier coefficient $\hat{\boldsymbol{q}}_{k_z,k}^{(n)}$ for all blocks $n \in \{1, \dots, N_b\}$, and a fixed frequency f_k. The cross-spectral density matrix is then computed as $\boldsymbol{S}_{k_z}^{(k)} = \hat{\boldsymbol{Q}}_{k_z}^{(k)} \hat{\boldsymbol{Q}}_{k_z}^{(k)\dagger}$, where $(\cdot)^\dagger$ denotes the conjugate transpose of the a matrix. The problem of finding the SPOD is then reduced to finding the eigenvalues and eigenvectors of $\boldsymbol{S}_{k_z}^{(k)}$. However, since this is a $N \times N$ eigenvalue problem, and N can be very large compared to N_b it is far more efficient to compute the following eigenproblem instead

$$\hat{\boldsymbol{Q}}_{k_z}^{(k)\dagger} \hat{\boldsymbol{Q}}_{k_z}^{(k)} \boldsymbol{\Theta}_{k_z}^{(k)} = \boldsymbol{\Theta}_{k_z}^{(k)} \boldsymbol{\Lambda}_{k_z}^{(k)}. \tag{4.10}$$

It can be shown that the eigenvalues obtained from this adjoint eigenproblem are the same as the eigenvalues of $\boldsymbol{S}_{k_z}^{(k)}$, with the eigenvectors being related as follows

$$\boldsymbol{\Psi}_{k_z}^{(k)} = \hat{\boldsymbol{Q}}_{k_z}^{(k)} \boldsymbol{\Theta}_{k_z}^{(k)} \, \boldsymbol{\Lambda}_{k_z}^{(k)\,-\frac{1}{2}}. \tag{4.11}$$

Solving this problem provides the first N_b SPOD modes and their relative contribution to the original data set, and this is done for all the spanwise wavenumbers k_z available in the data. There are the additional considerations of the quadrature weights to ensure the eigenvectors are correctly scaled, as well as the effect of the window on the eigenvalues obtained, details of which can be found in Towne et al. (2018). The issue of quadrature weights comes up later in this thesis when implementing the variational optimiser, and the details of the method used is discussed in Section 6.1.

4.2.4.2 SPOD Analysis

As already noted the flow at $Re = 450$ is highly periodic, and so the SPOD analysis splits the DNS data into blocks corresponding to two periods of the flow ($\sim$ 50 time units) with no overlap in the windows. As with the previous spectral analysis, Hann windowing is included to account for any deviation from periodicity introduced from the finite sampling rate.

Figure 4.14 shows the top 18 eigenvalues obtained from the SPOD analysis of the flow $Re = 450$ plotted against the temporal frequency k_t. Figure 4.14(a) shows the spanwise constant eigenvalues ($k_z = 0$) and Figure 4.14(b) shows the eigenvalues for $k_z = 2\beta$. The first thing to note is a relatively uniform but rapid decrease in eigenvalue magnitude at each frequency, with each eigenvalue generally being separated by a couple orders of magnitude. Any eigenvalues at off spanwise mode numbers are negligibly small. The largest magnitude eigenvalue is present at the temporally steady and spanwise wavenumber of $k_z = 2\beta$.

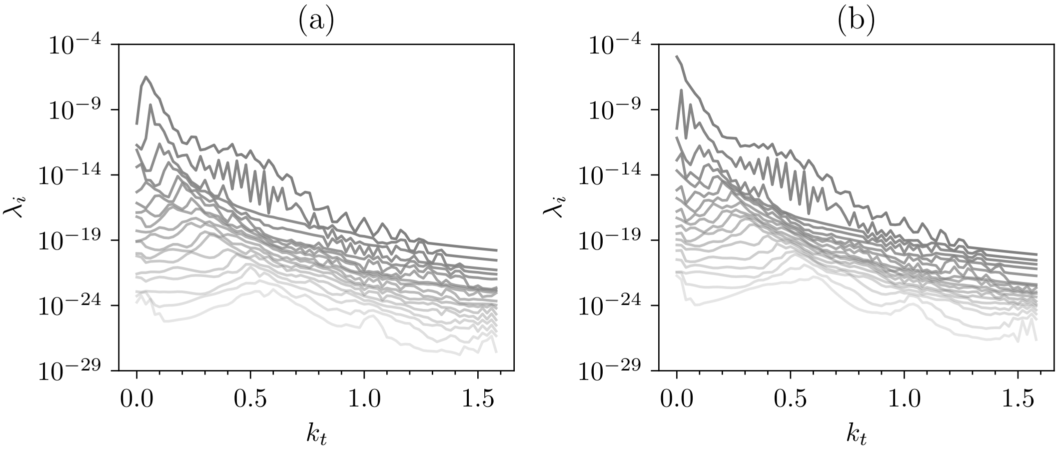

FIGURE 4.14: First 18 SPOD eigenvalues for RPCF at $Re = 450$ plotted against the temporal frequency, with panels (a-b) corresponding to spanwise wavenumbers of $k_z = 0$ and $k_z = 2\beta$, respectively.

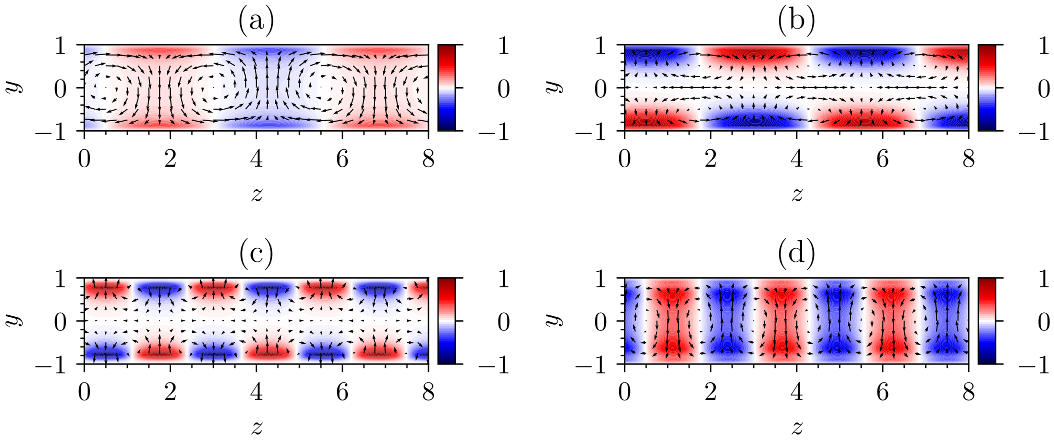

FIGURE 4.15: Select set of temporally steady ($k_t = 0$) SPOD modes for RPCF at $Re = 450$. Panels (a,b) and (c,d) show the SPOD modes at spanwise wavenumbers of $k_z = 2\beta$ and $k_z = 4\beta$, respectively. Panels (a,c) and (b,d) show the first and second dominant modes, respectively.

Figure 4.15 displays a number of the significant SPOD modes of the flow at $Re = 450$. Figure 4.15(a-b) show the modes at the spanwise wavenumber of $k_z = 2/L$, and Figure 4.15(c-d) show the modes at the spanwise wavenumber of $k_z = 4/L$. Figure 4.15(a,c) show the dominant modes at the given spanwise wavenumber, and Figure 4.15(b,d) show the second most dominant modes. The mode in Figure 4.15(a) corresponds to the most dominant eigenvalue throughout the SPOD spectrum and contains the vast majority of the streamwise roll structures. The majority of the energy in the mode is contained in the cross-stream (wall-normal and spanwise) components of the velocity, with a slightly weaker streamwise contribution focused near the walls at the points where the large vortices are colliding. The mode in Figure 4.14(b) is separated from the mode in Figure 4.14(a) by around five orders of magnitude, meaning that it has a negligible effect on the overall flow. The modes in

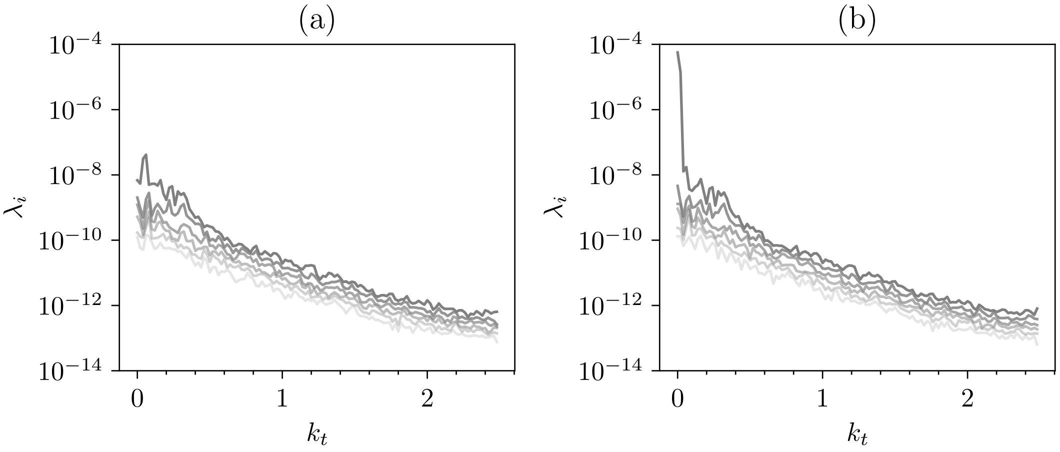

FIGURE 4.16: First 6 SPOD eigenvalues for RPCF at $Re = 5000$ plotted against the temporal frequency, with panels (a-b) corresponding to spanwise wavenumbers of $k_z = 0$ and $k_z = 2\beta$, respectively.

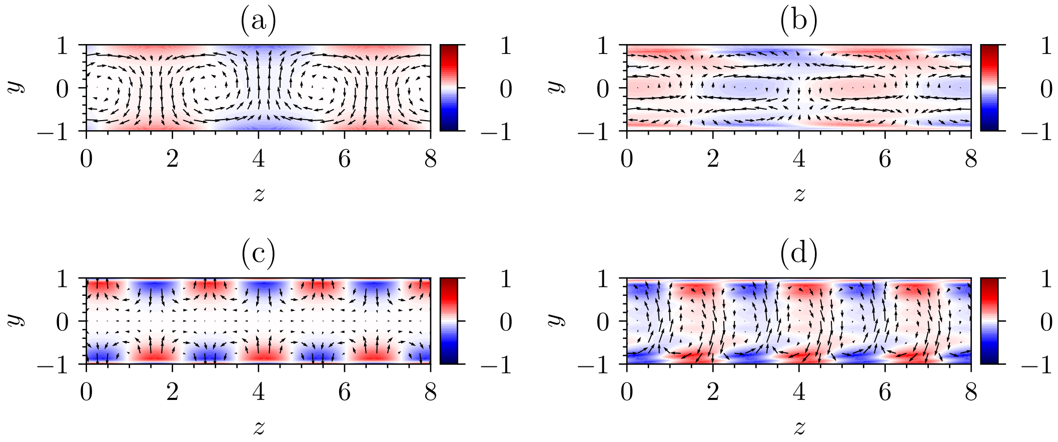

FIGURE 4.17: Select set of SPOD modes for RPCF at $Re = 5000$. Panels (a,b) and (c,d) show the SPOD modes at spanwise wavenumbers of $k_z = 2\beta$ and $k_z = 4\beta$, respectively. Panels (a,c) and (b,d) show the first and second dominant modes, respectively.

Figure 4.15(c-d) are difficult to link to exact structures in the flow seen in Figure 4.11, which makes sense since the SPOD eigenvalues of all the modes are already roughly two orders of magnitude lower than the dominant modes in Figure 4.15(a-b).

Moving onto the turbulent flow at $Re = 5000$, the eigenvalues at the same spanwise wavenumbers are shown in Figure 4.16. Only the first 6 SPOD modes are shown, which was done due to the memory restrictions. Still, at all frequencies shown there at least a separation of two orders of magnitude between the largest and smallest eigenvalues. The most obvious feature is the absolute dominance of the temporally steady eigenvalues. This large spike is present in all non-zero and even spanwise mode numbers, with a three to four orders of magnitude separation to the next eigenvalue. Figure 4.17 show the set of modes corresponding to the same frequencies as in Figure 4.15. The mode in Figure 4.17(a) corresponds to the dominant eigenvalue in Figure 4.16 and once again corresponds closely to the streamwise vortices, implying that at this higher Reynolds numbers this structure is not only still important but is in fact even more dominant over the total kinetic energy of the flow. It can be seen that the streamwise velocity component of the streamwise vortex mode in Figure 4.17(a) is weaker than in Figure 4.15, implying that a larger portion of the energy is held in the cross-stream velocity components showing that the vortex has grown in strength. The second largest mode in Figure 4.17(b) shows the same double vortex feature as in Figure 4.15, but due to even larger separation in scale between the eigenvalues clearly contributes even less to the energy of the flow. The higher spanwise wavenumber modes show a similar large separation of eigenvalues at $k_t = 0$ (not shown in Figure 4.16), although with a lower total magnitude. The dominant mode at this frequency, in Figure 4.17(c), has the majority of its energy concentrated near the walls, and a large portion of the energy of the secondary vortices observed in Figure 4.13 near the walls where the vortices periodically meet. An additional mode with a spanwise offset is required to cancel out the effect periodically, corresponding the parts of the flow where the large streamwise vortices are separating instead of colliding.

4.3 Resolvent Analysis

Moving on from the general characterisation of the 2D3C RPCF, we will now discuss resolvent analysis of the given flow. This section is divided into two parts: the first details how the modes are derived and what they represent, and the second takes resolvent modes generated for some modest Reynolds numbers and assesses how well they can reconstruct the desired flow for the same Reynolds number for which they were generated. The goal of this section is not prediction, which requires a method to produce the dynamical weights discussed in chapter 2. The reconstructions presented later in this section are useful as initial estimate for how many resolvent modes are required to accurately represent the desired flows studied in chapter 6.

4.3.1 Deriving Resolvent Modes

To derive the modes $\boldsymbol{\psi}_{ki}$ required for the Galerkin projection described in Section 3.5, we use the resolvent analysis framework as described in McKeon and Sharma (2010). The benefit of this approach is that it is a systematic method for generating a unique set of modes for every frequency $\boldsymbol{k}$ that have been shown to provide an efficient basis for expressing ECSs for wall-bounded flows (Sharma et al., 2016b). Here the derivation is performed specifically for the 2D3C RPCF configuration, a slight variation to the application of the method to channel flows in literature, for which the biggest notable difference is the addition of the Coriolis acceleration.

To start, the velocity and pressure fields are decomposed into a steady base component and the fluctuations around this base flow as follows

$$\boldsymbol{u}\left(y,z,t\right)=\boldsymbol{u}_b\left(y\right)+\boldsymbol{u}'\left(y,z,t\right), \tag{4.12}$$

$$p\left(y,z,t\right)=p_b\left(y\right)+p'\left(y,z,t\right). \tag{4.13}$$

where the base flow only varies over the wall-normal (inhomogeneous) direction. Although the pressure is explicitly decomposed here, an expression for p_b is not required for the implementation of the method, as it is completely prescribed by the fluctuations $\boldsymbol{u}'$ and the base velocity $\boldsymbol{u}_b$. Physically, the base pressure would be streamwise and spanwise independent in this flow. Typically the base flow $\boldsymbol{u}_b$ is set to be the turbulent mean $\overline{\boldsymbol{u}}$, given by

$$\overline{\boldsymbol{u}}\left(y\right)=\lim_{T\to\infty}\frac{1}{T}\int_0^T\boldsymbol{u}\left(y,z,t\right)\mathrm{d}t. \tag{4.14}$$

In this derivation, however, an arbitrary steady base flow is used instead of the mean. When resolvent analysis is used to generate the modes for the analysis later in this chapter, in Section 4.3.2, and for the optimisation in chapter 6, the laminar solution as the base flow. This is a pragmatic choice and the reasons behind it are discussed in some detail at the end of this section. In this work the primary goal is to utilise these modes to construct models based on projections onto sets of resolvent modes. Thus, although it is a departure from the literature to not use the mean profile as the base flow in this derivation, as long as the modes produced are orthonormal and resemble the flow then they can be used for the desired modelling purpose. It should be noted that due to continuity, the base flow is in the streamwise direction only, i.e. $\boldsymbol{u}_b=u_b\hat{\boldsymbol{\imath}}$. Substituting the decomposition into Equation 4.1 provides an evolution equation for the fluctuations, expressed compactly as

$$\boldsymbol{M}\frac{\partial\boldsymbol{q}'}{\partial t}=\mathcal{N}_{\text{cont}}\left(\boldsymbol{q_b}\right)+\mathcal{L}_{\boldsymbol{q}_b}\boldsymbol{q}'+\boldsymbol{M}\boldsymbol{f}\left(\boldsymbol{u}'\right). \tag{4.15}$$

where $\boldsymbol{q}=\begin{pmatrix}\boldsymbol{u} & p\end{pmatrix}^\top$ is a concatenated state vector of the velocity and pressure fields. The operator $\mathcal{N}_{\text{cont}}\left(\boldsymbol{q}\right)$ is the Navier-Stokes operator for RPCF, including the continuity equation and pressure gradient term, given by

$$\mathcal{N}_{\text{cont}}\left(\boldsymbol{q}_b\right)=\begin{pmatrix}-\left(\boldsymbol{u}_b\cdot\boldsymbol{\nabla}\right)\boldsymbol{u}_b-\boldsymbol{\nabla}p_b+\frac{1}{Re}\boldsymbol{\Delta}\boldsymbol{u}_b-Ro\left(\hat{\mathbf{k}}\times\boldsymbol{u}_b\right)\\ \boldsymbol{\nabla}\cdot\boldsymbol{u}_b\end{pmatrix}. \tag{4.16}$$

$\mathcal{L}_{\boldsymbol{q}_b}$ is the linearisation of $\mathcal{N}_{\text{cont}}$ evaluated at the base flow $\boldsymbol{q}_b$, given by

$$\mathcal{L}_{\boldsymbol{q}_b}=\begin{pmatrix}-\left(\boldsymbol{u}_b\cdot\boldsymbol{\nabla}\right)-\left(\boldsymbol{\nabla}\boldsymbol{u}_b\right)+\frac{1}{Re}\boldsymbol{\Delta}-Ro\,\hat{\mathbf{k}}\times & -\boldsymbol{\nabla}\\ \boldsymbol{\nabla}\cdot & 0\end{pmatrix}, \tag{4.17}$$

and $\boldsymbol{f}\left(\boldsymbol{u}'\right) = -\left(\boldsymbol{u}' \cdot \boldsymbol{\nabla}\right)\boldsymbol{u}'$ is the nonlinear term for the fluctuations $\boldsymbol{u}'$. The continuity equation is time-independent, so its inclusion in Equation 4.15 requires an influence matrix $\boldsymbol{M} = \begin{pmatrix}\boldsymbol{I} & \boldsymbol{0}\end{pmatrix}^\top$ to ensure that the time derivative and the nonlinear influence $\boldsymbol{f}\left(\boldsymbol{u}'\right)$ are restricted to the first three components corresponding to the momentum equation in Equation 4.1a.

Now, define the Fourier expansion of the state fluctuation vector $\boldsymbol{q}'$ in the homogeneous spatial and time directions as follows

$$\boldsymbol{q}'\left(y, z, t\right) = \sum_{\boldsymbol{k}\in\mathbb{Z}^2} \boldsymbol{q}'_{\boldsymbol{k}}\left(y\right) e^{i\boldsymbol{k}\cdot\boldsymbol{\xi}}, \tag{4.18}$$

where $\boldsymbol{k} = \begin{pmatrix}k_z & k_t\end{pmatrix}^\top$ and $\boldsymbol{\xi} = \begin{pmatrix}\beta z & \omega t\end{pmatrix}$. These are the same variables as used in Equation 3.54, with the homogeneous streamwise component not included to reflect the streamwise independence restriction for the flow. The coefficients $\beta = 2\pi/L_z$ and $\omega = 2\pi/T$ are the fundamental wavenumbers and frequencies, respectively, for the spanwise and temporal directions determined by the size of their relative domains. It should be noted that since $\boldsymbol{q}_b \neq \overline{\boldsymbol{q}}$ then it is possible that $\boldsymbol{q}'_{\boldsymbol{0}} \neq 0$. The corresponding identity for the Fourier coefficients

$$\boldsymbol{q}'_{\boldsymbol{k}} = \frac{1}{L_z T}\int_0^T \int_0^{L_z} \boldsymbol{q}' e^{i\boldsymbol{k}\cdot\boldsymbol{\xi}}\,\mathrm{d}z\,\mathrm{d}t\,. \tag{4.19}$$

Substituting Equation 4.18 into Equation 4.15 and applying Equation 4.19 to each term, the following is obtained for the Fourier coefficients of the velocity fluctuations

$$ik_t\omega\boldsymbol{M}\boldsymbol{u}'_{\boldsymbol{k}} = \mathcal{L}_{q_b k}\boldsymbol{q}'_{\boldsymbol{k}} + \boldsymbol{M}\boldsymbol{f}_{\boldsymbol{k}}, \quad \boldsymbol{k} \in \mathbb{Z}^2 \setminus \{\boldsymbol{0}\}\,. \tag{4.20}$$

The Fourier transformed nonlinearities on the RHS of Equation 4.20 are given by $\boldsymbol{f}_k = \sum_{\boldsymbol{l}}\left(\boldsymbol{u}'_{\boldsymbol{l}} \cdot \boldsymbol{\nabla}\right)\boldsymbol{u}'_{\boldsymbol{k}-\boldsymbol{l}}$ and represents the triadic interactions of the flow, the nonlinear feedback that transports energy between scales and sustains any unsteady motion in the flow. Triadic interactions refers to the interactions of velocity fluctuations at different frequencies that produce a forcing in a third frequency. These interactions are the drivers of the interactions in the flow that produce self-sustaining turbulence. Equation 4.20 can now be rearranged to give a linear relationship between the velocity fluctuations and the corresponding nonlinear interactions of the flow

$$\boldsymbol{u}'_{\boldsymbol{k}} = \mathcal{H}_{\boldsymbol{k}}\boldsymbol{f}_{\boldsymbol{k}}, \quad \boldsymbol{k} \in \mathbb{Z}^2 \setminus \{\boldsymbol{0}\}\,. \tag{4.21}$$

The operator $\mathcal{H}_{\boldsymbol{k}}$ is the resolvent and is defined as

$$\mathcal{H}_{\boldsymbol{k}} = \left(ik_t\omega\boldsymbol{M} - \mathcal{L}_{q_b k}\right)^{-1}\boldsymbol{M}, \quad \boldsymbol{k} \in \mathbb{Z}^2 \setminus \{\boldsymbol{0}\}\,. \tag{4.22}$$

The resolvent operator relates the unsteady response of the system to finite amplitude forcings to the system via the linear mechanisms of the system. In this formalism however, the nonlinear self-interaction of the fluid is viewed as the forcing, leading to a feedback system that aims to balance the nonlinear interactions with the linear response of the system that result from the nonlinearities. In depth discussions on the interpretation of the resolvent can be found in McKeon and Sharma (2010) and Symon et al. (2018). The explicit form of the resolvent for RPCF is given as

$$\mathcal{H}_{\boldsymbol{k}} = \left(\begin{array}{ccc|c} ik_t\omega - \frac{1}{Re}\boldsymbol{\Delta}_{\boldsymbol{k}} & \frac{\partial u_b}{\partial y} - Ro & 0 & \\ Ro & ik_t\omega - \frac{1}{Re}\boldsymbol{\Delta}_{\boldsymbol{k}} & 0 & \boldsymbol{\nabla} \\ 0 & 0 & ik_t\omega - \frac{1}{Re}\boldsymbol{\Delta}_{\boldsymbol{k}} & \\ \hline & -\boldsymbol{\nabla}\cdot & & 0 \end{array}\right)^{-1} \boldsymbol{M}. \tag{4.23}$$

where $\boldsymbol{\Delta}_{\boldsymbol{k}}$ is the Fourier transform of the Laplace operator. Due to the base flow $\boldsymbol{u}_b$ being purely streamwise and only varying in the wall-normal direction, all the convective terms in $\mathcal{L}_{q_b k}$ reduce to single base shear stress term $\partial u_b/\partial y$. In plane Couette flow, this term is responsible for the non-normality of the resolvent operator, leading to the amplification of finite amplitude inputs to the system which have been linked to sub-critical bifurcations of the fluids from a laminar solution (Chapman, 2002; Symon et al., 2018). In the case of RPCF, the Coriolis force introduces an additional off-diagonal component which can either amplify or reduce the resulting non-normality. Without either of these terms the resolvent would in fact be completely self-adjoint, and any forcing to the system would decay with time as a result of the diffusive effects of the Laplace operator, especially at lower Reynolds numbers.

Applying the Schmidt decomposition, equivalently the Singular Value Decomposition if the operator were discretised, gives the following decomposition

$$\mathcal{H}_{\boldsymbol{k}}\left(\cdot\right) = \sum_{i=1}^{\infty} \sigma_{ki} \boldsymbol{\psi}_{ki} \left(\boldsymbol{\phi}_{ki}, \cdot\right), \tag{4.24}$$

where the inner-product in Equation 4.24 is the same as the one used in Equation 3.56. The modes $\boldsymbol{\psi}_{ki}$ and $\boldsymbol{\phi}_{ki}$ form an orthonormal basis set under this inner product for each frequency

$$\left(\boldsymbol{\psi}_{ki}, \boldsymbol{\psi}_{kj}\right) = \int_{-1}^{1} \boldsymbol{\psi}_{ki}^{\dagger} \boldsymbol{\psi}_{kj} \mathrm{d}y = \delta_{ij}, \tag{4.25}$$

$$\left(\boldsymbol{\phi}_{ki}, \boldsymbol{\phi}_{kj}\right) = \int_{-1}^{1} \boldsymbol{\phi}_{ki}^{\dagger} \boldsymbol{\phi}_{kj} \mathrm{d}y = \delta_{ij}, \tag{4.26}$$

and σ_i denotes the singular value associated with each input-response mode pair. These modes are ranked in order of the associated singular values $\sigma_i \geq \sigma_{i+1} \geq 0$, for all $i \in \mathbb{N}$. The modes $\boldsymbol{\psi}_{ki}$ and $\boldsymbol{\phi}_{ki}$ are the left and right singular modes and form a complete basis for the range (response) and domain (input) of the resolvent for every $\boldsymbol{k} \in \mathbb{Z}^2 \setminus \{0\}$, respectively. The range of the resolvent operator is the set of incompressible fluctuations that obey the no-slip boundary conditions, and therefore the set of modes $\boldsymbol{\psi}_{ki}$ are divergence-free and obey the no-slip boundary condition. Thus the resolvent response modes, just called response modes from hereon, satisfy the desired properties in Equation 3.55 and thus can be used as the required basis for the Galerkin projection of the optimisation problem. There is the problem, however, that the resolvent is technically only defined for the non-zero frequencies $\boldsymbol{k} \neq 0$. If a solution to the Navier-Stokes equations are sought, then in lieu of an accurate profile for the mean known a priori, a basis for the mean is also required so that it can be properly modelled for the variational optimisation in Chapter 3. To circumvent this issue, it has been found that the resolvent of Equation 4.22 can be decomposed using Equation 4.24 for $\boldsymbol{k} = 0$, at least as long as a laminar base flow is provided. In general, the exact physical interpretation of the basis used for the Galerkin projection is less important as its ability to provide a valid orthonormal basis in the space of divergence free and no-slip fields. In principle this basis can be obtained from many sources, such as the eigenvectors of the Laplace operator which would produce a set of orthonormal basis functions. The choice to continue to use the resolvent modes for the mean in particular, despite their non-rigorous motivation, is a pragmatic choice.

The rate at which the singular values σ_i decay determines how accurately the decomposition Equation 4.24 can be represented with only a finite number of the modes. Formally, if

$$\sum_{i=0}^{M} \sigma_i^2 \approx \sum_{i=0}^{\infty} \sigma_i^2, \tag{4.27}$$

for a given $M \in \mathbb{N}$, then Equation 4.24 can be truncated to a finite set of modes

$$\mathcal{H}_{\boldsymbol{k}}\left(\cdot\right) \approx \sum_{i=1}^{M} \sigma_{\boldsymbol{k}i} \boldsymbol{\psi}_{\boldsymbol{k}i} \left(\boldsymbol{\phi}_{\boldsymbol{k}i}, \cdot\right). \tag{4.28}$$

This means, when using $\boldsymbol{\psi}_{ki}$ for the Galerkin projection, with the truncation in Equation 4.28, the infinite-dimensional state-space characterising the velocity field is reduced to a finite dimensional subspace (for each frequency $\boldsymbol{k}$) that aims to capture as much of the important dynamical information as possible according to the non-normal response of the system to given forcings. If the particular flow has a set of nonlinear interactions $\boldsymbol{f}_{\boldsymbol{k}}$ that align highly with the set of input forcing modes $\boldsymbol{\phi}_{\boldsymbol{k}i}$ then only the corresponding set of response modes are required to accurately reconstruct the resulting response. As mentioned, the accuracy of this truncation, and the resulting approximation of the state-space manifold on which the desired solution lies, depends on the decay rate of the singular values. The larger the decay rate, the more singular values (and associated response modes) can be discarded from the sum without sacrificing any more accuracy in the approximation of the resolvent. It should be noted that a fast decay rate in the singular values does not in itself imply a low-order model based on resolvent modes is possible. Since the nonlinear forcing component of Equation 4.21 could be preferentially directed towards sub-optimal forcing modes, which would in turn increase the contribution of the associated response modes in the output.

4.3.2 Efficacy of Resolvent Modes

In this section, the resolvent modes described previously are used as a basis to project DNS data at some modest Reynolds numbers of $Re = 50$ and $Re = 450$, which appear prominently in Chapter 6, and the dominant SPOD mode to assess how well they capture the dynamical features of the flow. The resolvent modes used here and in Chapter 6 are generated relative to a laminar base flow. The projection of a spatiotemporally varying flow field is given by Equation 3.59, which gives an array of coefficients $a_{\boldsymbol{k}i}$ for all frequencies $\boldsymbol{k}$ and resolvent modes used for the projection $i \in \{1..M\}$, where M is the number of resolvent modes utilised at each frequency. A new velocity field can then be reconstructed from the resulting coefficients using Equation 3.54, which will be denoted here as $\boldsymbol{u}_M$. The computational cost of the reconstruction is made up of the projection and expansion steps. The projection is a series of inner-product (integral) computations that grow linearly with the resolution of computational grid and with the number of modes used for the resolvent basis set. The expansion step is equivalent to a matrix-vector product over all the frequencies resolved on the computational grid, and again grows linearly with all the grid parameters and number of resolvent modes used. In practice, for the reconstructions shown in this section, the relevant computations were performed on the order of minutes. For higher Reynolds numbers, however, this cost can grow rather quickly as the required grid resolution grows in all directions as does the expected number of modes required to represent such flows accurately.

As mentioned in previous chapters, the main objective of this thesis is to construct dynamical weights for the resolvent modes generated for this particular flow. The analysis here does not construct these weights. Instead the goal here to assess how well the resolvent modes capture the dynamical when they are purely ranked according the singular values in Equation 4.28, quantitatively motivating a truncation of the resolvent modes later in chapter 6 while retaining the majority of the important information of the desired flow.

The resulting projection of DNS data at $Re = 50$ and $Re = 450$ are shown in Figure 4.18(a-b), respectively, subtracted from 1 to show the amount of missing kinetic information in the projected flow. A complete set of 64 and 128 resolvent modes are used for each Reynolds number respectively, corresponding to the number of wall-normal points used in the DNS. These basis sets are then truncated. keeping only

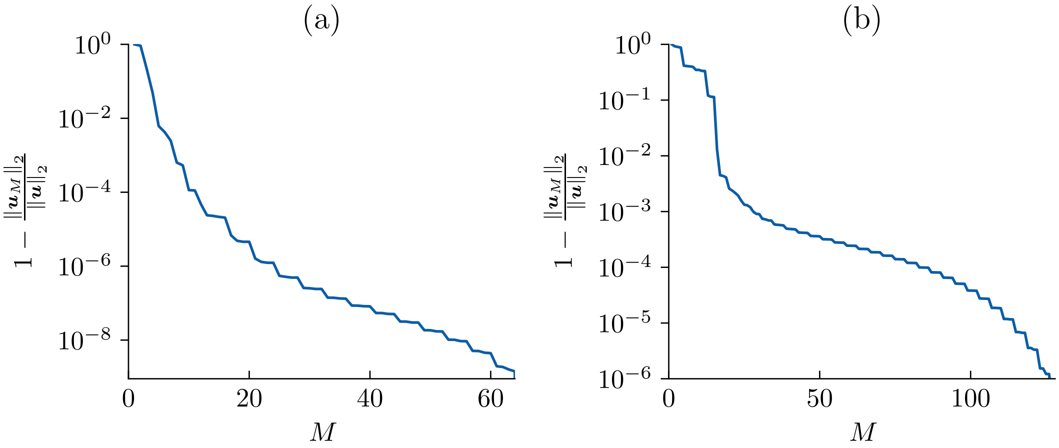

FIGURE 4.18: Projection error of DNS data from $Re = 50$ and $Re = 450$ in panels (a), and (b), respectively, plotted against the number of modes used for the projection at every spanwise wavenumber and temporal frequency. The complete set of 64 and 128 resolvent modes for each case, respectively, are generated using a laminar base profile.

the modes corresponding to the largest singular values. The reconstruction of the flow is then performed using the truncated basis set and the error in the resulting reconstruction is shown. Both plots show that over 99% of the kinetic energy is captured 5 and 16 modes, respectively. The rapid decreases in projection error when certain modes are included, versus the seemingly negligible effect of other modes shows that particular resolvent modes have a much larger dynamical importance as others, for instance the 12^{th} resolvent mode for $Re = 450$ accounts for about 40% of the total reconstruction capture on its own. An even more impressive energy capture is achieved by the 2^{nd} resolvent mode at $Re = 50$, which accounts for about 70% of the total reconstruction.

To visualise why certain resolvent modes are particularly good at capturing the dynamics of the flow, some of them are plotted in Figure 4.19 and Figure 4.20. Figure 4.19 shows simply the first 4 resolvent modes obtained ranked by their singular values. Of particular note is the second mode, in Figure 4.19(b), which bears a striking resemblance to the dominant SPOD mode shown in Figure 4.15, containing the characteristic streamwise rolls. The third and fourth modes, Figure 4.19(c-d), also show some slightly stretched or diminished streamwise rolls which explains their energy capturing abilities Figure 4.18(a). Interestingly the first mode in Figure 4.19(a) contains two counter-rotating vortices over the height of the channel, something only seen in the second dominant SPOD, which has orders of magnitude less influence on the flow, explaining why it contributes very little to the construction of the DNS data. The resolvent modes at $Re = 450$ is quite similar, with the modes associated with the largest singular values having more intricate and smaller vortices, which contribute a relatively little to the flow reconstruction, as can be seen in Figure 4.20(a-b) for the first two resolvent modes. However, at this higher Reynolds number the resolvent mode associated with the very important streamwise rolls are the 12^{th} and to a lesser extent

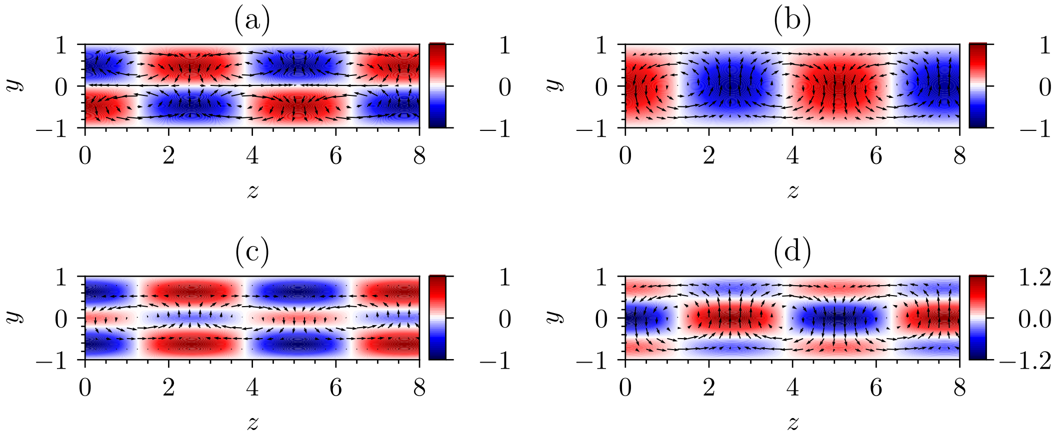

FIGURE 4.19: First four resolvent modes, panels (a-d), respectively, for $Re = 50$ for a spanwise wavenumber of $k_z = 2/L$ where $L_z = 8$.

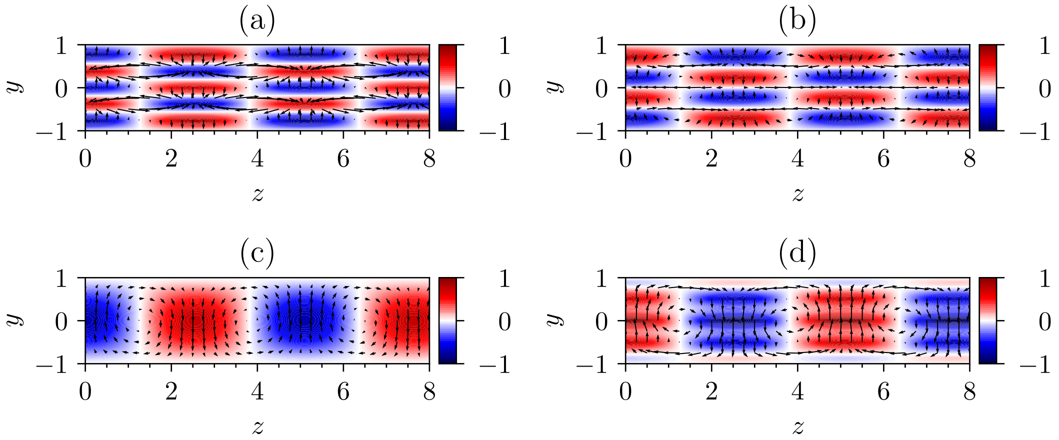

FIGURE 4.20: First two resolvent modes, panels (a-b), respectively, as well as the 12th and 15th resolvent modes, panels (c-d), respectively, for $Re = 450$ at a spanwise wavenumber of $k_z = 2/L$ where $L_z = 8$.

the 15th resolvent modes, shown in Figure 4.20(c-d). These modes correspond to the largest drops in projection error of Figure 4.18(b), which again reinforces the importance of the streamwise vortices in capturing the majority of the kinetic energy of the flow.

The final result shown here instead projects the dominant SPOD mode in Figure 4.15(a) onto a set of resolvent modes, at the corresponding frequency. Denoting the particular SPOD as $\boldsymbol{\psi}_{\text{SPOD}}$, the mode can be expressed as a linear sum of resolvent modes

$$\boldsymbol{\psi}_{\text{SPOD}} = \sum_i \gamma_i \boldsymbol{\psi}_{ki}. \tag{4.29}$$

The resulting coefficients $\gamma_i \in \mathbb{C}$ are combined into a vector denoted as $\boldsymbol{\gamma}$, with the vector only containing the first M modes denoted as $\boldsymbol{\gamma}_M$. The result is shown in Figure 4.21, which resembles closely the plot in Figure 4.18(b). This is a consequence

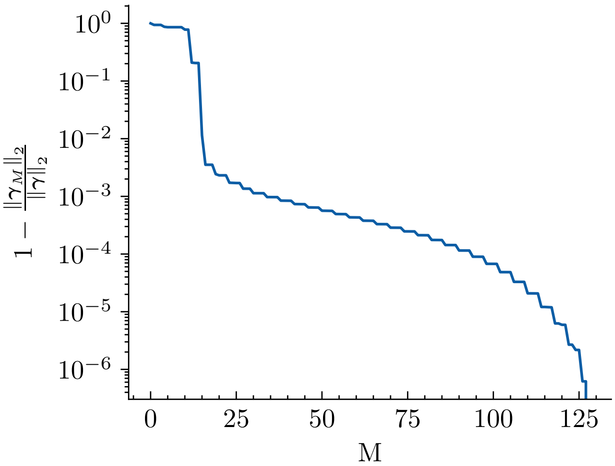

FIGURE 4.21: Projection error of the dominant steady SPOD mode shown in Figure 4.15 (at $Re = 450$) onto the resolvent modes used in Figure 4.18 for the corresponding spanwise wavenumber.

of the majority of the energy of the flow being contained at the spanwise wavenumber taken for Figure 4.21 which corresponds to the streamwise rolls. The are two very obvious decreases in error, again once the 12^{th} and 15^{th} resolvent modes are included in the projection. This is not too surprising a result due their obvious qualitative resemblance to the particular SPOD mode. Taking all of this together, it is clear that resolvent modes allow for a significant dimensionality reduction of the flow at $Re = 50$ and $Re = 450$. Due to presence of the streamwise rolls throughout the different regimes of RPCF, it is expected that resolvent analysis can provide a useful low-dimensional model for the flow based at higher Reynolds numbers.

4.4 Summary

In this chapter RPCF has been introduced and characterised using DNS simulations of the flow at various Reynolds numbers, fixed at a rotation number of $Ro = 0.5$. Analysis of the velocity spectra revealed dominant frequencies primarily corresponding to streamwise vortical structures that contain the majority of the kinetic energy of the flow. The largest of these streamwise vortices grows in strength as the Reynolds number increases and is the primary source of momentum transport of the flow between the walls. SPOD analysis of the same DNS revealed the strength of these structures have, with smaller scale and near wall structures being at least an order of magnitude less dynamically significant.

The resolvent analysis framework is described next, showing how the resolvent operator is derived and identifying the terms that contribute to the non-normality of the operator, which is responsible for some of the transient growth and instabilities in turbulent flows. Sets of resolvent modes are then generated for $Re = 50$ and $Re = 450$, Reynolds numbers that are used extensively in Chapter 6, upon which both DNS flows and the dominant SPOD mode are projected. The results showed that a relatively small number of the resolvent modes capture well over 99% of the energy of the original flows, leading to the potential for dimensionality reductions of around 80%–90% of the original system.

Chapter 5

Statistical Estimation of the Lorenz System

Before demonstrating the resolvent-based variational optimisation methodology as described in Chapter 3 the same method is developed for a simpler low-dimensional chaotic dynamical system. The basic operation of the methodology is demonstrated to be able to find exact solutions of the Lorenz equations. Then, a slight detour is taken to explore another application of the methodology as described in Section 1.5: generating quasi-trajectories to approximate the statistics of chaotic dynamics. As discussed later in this chapter, the aim is to show that these quasi-trajectories, long periodic trajectories that do not satisfy the governing equations, still encapsulate the fundamental structure of the attractor they are approximating, potentially at a lower cost if a sufficiently truncated low-order model is used. To reiterate some of the discussion in Chapter 1 and Chapter 2, the ultimate goal of building a set of invariant solutions for the Navier-Stokes equations for various flow configurations is motivated by the theory of low-dimensional chaos, which shows that these solutions provide a natural basis to express the statistical (ergodic) properties of the chaotic dynamics. As has been discussed in length, and shown in the literature, finding these solutions for high-dimensional chaotic systems is far more difficult, complicating the application of this theory in practice. The heuristic quasi-trajectories can potentially remove the burden of having to find a complete representative set of solutions to apply cycle averaging methods.

Section 5.1 takes the methodology from Chapter 3 and specialises it for finite-dimensional (ODE) dynamical systems. Section 5.2 then describes the procedure for resolvent analysis when applied to the Lorenz system of Lorenz (1963), describing the method used to achieve an exact dimensionality reduction, losing none of the dynamical information (Burton et al., 2025). The Lorenz system was chosen, despite its natural low-dimensionality, since it provides a computationally accessible test-case to demonstrate the proposed framework, and being a very well studied system it is known to possess the chaotic properties that motivate this work. The statistical properties of the proposed quasi-trajectories are then presented in Section 5.4, comparing with the statistics obtained from traditional time-stepping methods to solve chaotic systems.

5.1 Low-Dimensional Optimisation

The projected optimisation methodology described in Chapter 3 is reformulated for problems of incompressible fluid problems with Dirichlet boundary conditions. To apply the same methodology to generate trajectories for finite-dimensional dynamical systems it has to be modified. This modification is related to the inner product, the space upon which the inner product acts, and a simplification of the constraints imposed on the gradient-based optimisation. This is a result of the system not being spatially extended, and thus not requiring any boundary conditions, in addition to no incompressibility constraint and thus a pressure gradient term that requires some special treatment. This section begins with an outline of the changes to the variational optimisation, then moving on to how resolvent analysis can be performed for finite-dimensional systems.

5.1.1 Problem Definition and Residual Gradient

The modification of the variational optimisation methodology is relatively simple, taking the continuous spatial dimensions down to a finite set of state variables. The governing equation is some autonomous dynamical system given by

$$\frac{\mathrm{d}\boldsymbol{x}}{\mathrm{d}t} = \boldsymbol{g}\left(\boldsymbol{x}\right), \quad \boldsymbol{x} \in \mathcal{M} \subseteq \mathbb{R}^d, \tag{5.1}$$

where $\mathcal{M}$ is the state space (or phase space) for the system. The trajectory can be expressed as a function over time $\boldsymbol{x} \colon \; [0,\, T) \mapsto \mathbb{R}^d$, that is, the trajectory $\boldsymbol{x}$ maps a particular time $t \in [0,\, T)$ to a d-dimensional real vector. To help in the characterisation of the problem, the space of closed state space loops is defined as

$$\mathscr{P}_T^{\mathrm{ODE}} = \left\{ \boldsymbol{x}\left(t\right) \mid \boldsymbol{x}\left(0\right) = \boldsymbol{x}\left(T\right) \right\}. \tag{5.2}$$

In the space $\mathscr{P}_T^{\mathrm{ODE}}$, we define the following inner-product

$$\langle \boldsymbol{x},\, \boldsymbol{y} \rangle := \int_0^T \boldsymbol{x} \cdot \boldsymbol{y} \;\mathrm{d}t\,, \tag{5.3}$$

and induced norm $\|\boldsymbol{x}\| = \sqrt{\langle \boldsymbol{x}, \boldsymbol{x} \rangle}$. The local residual is defined as

$$\boldsymbol{r} := \frac{\mathrm{d}\boldsymbol{x}}{\mathrm{d}t} - \boldsymbol{g}\left(\boldsymbol{x}\right), \tag{5.4}$$

and the global residual is defined in the same way as in chapter 3 repeated here for convenience

$$\mathcal{R}\left[\boldsymbol{u}\right] := \frac{1}{2}\|\boldsymbol{r}\|^2, \tag{5.5}$$

where the norm induced from Equation 5.3 is used in place of the spatio-temporal integral norm for the fluid formulation. This leads to the same optimisation problem as in Equation 3.7, with the key differences being the optimisation space $\mathscr{P}$ no longer including any boundary information (since no boundaries exist) and no incompressibility constraint, as well as the global residual being defined as an integral over only the period of the solution. It should be noted that from the lack of boundary constraints on the states $\boldsymbol{x}$ it is now true that if $\boldsymbol{x} \in \mathscr{P}_T^{\mathrm{ODE}}$ then $\boldsymbol{r} \in \mathscr{P}_T^{\mathrm{ODE}}$. This is in contrast to the Navier-Stokes problem, where the no-slip boundary conditions are not necessarily satisfied if the velocity field exists in the desired optimisation space.

Finding the gradient of $\mathcal{R}\left[\boldsymbol{x}\right]$ follows a similar procedure as in the Navier-Stokes problem, albeit simpler as a result of the evolution equations being purely algebraic equations not requiring any derivations of adjoint operators or introduction of any extra constraints on $\boldsymbol{r}$. The gradient is given as

$$\frac{\delta \mathcal{R}}{\delta \boldsymbol{x}} = -\frac{\mathrm{d}\boldsymbol{r}}{\mathrm{d}t} - \boldsymbol{L}^{\top}\left(\boldsymbol{x}\right)\boldsymbol{r}, \tag{5.6}$$

where $\boldsymbol{L} = \mathrm{d}\boldsymbol{g}/\mathrm{d}\boldsymbol{x}$ is the Jacobian of $\boldsymbol{g}$ evaluated over the trajectory $\boldsymbol{x}$, and $\left(\cdot\right)^{\top}$ denotes the matrix transpose. Here the adjoint of the linearised derivative operators of the Navier-Stokes equations are replaced with the analogous matrix transpose. This is a matrix ($\boldsymbol{L} \in \mathbb{R}^{d\times d}$) populated with the partial derivatives of the components of $\boldsymbol{g}$ with respect to the components of $\boldsymbol{x}$. The gradient with respect to ω is given as

$$\frac{\partial \mathcal{R}}{\partial \omega} = \frac{1}{\omega}\left\langle \frac{\partial}{\partial,}\boldsymbol{x} \right\rangle t\boldsymbol{r}, \tag{5.7}$$

where $\omega = 2\pi/T$ is the fundamental frequency of the trajectory, defined similarly as in Chapter 3. The details of the derivation of Equation 5.6 and Equation 5.7 are omitted due to their similarity to the derivations for the Navier-Stokes problem, especially the gradient with respect to ω which is functionally identical only differing the underlying definition of the inner product.

5.1.2 Dimensionality Reduction

In the finite-dimensional case the process of the dimensionality reductions via a Galerkin projection remains the same, only with the inner-product over a set of basis functions replaced with a matrix-vector product of an appropriate, in general rectangular, orthogonal matrix. The question of how the basis is generated for dynamical systems governed by a finite number of ODEs is the topic of Section 5.2. There the special form used for resolvent analysis of ODEs is explained in detail, and how the natural structure of the problem lends itself to a dimensionality of an already very low-dimensional system. This subsection is simply a restatement of the mathematics of Section 3.5 without the added complications of boundary conditions and incompressibility.

To tackle the time periodic constraint, the system is expanded in terms of a Fourier series defined as

$$\boldsymbol{x}\left(t\right) = \sum_{n\in\mathbb{Z}} \boldsymbol{x}_n e^{in\omega t}, \tag{5.8}$$

with the Fourier coefficients defined by the integral

$$\boldsymbol{x}_n = \frac{1}{T}\int_0^T \boldsymbol{x}\left(t\right) e^{-in\omega t}\,\mathrm{d}t\,. \tag{5.9}$$

Applying this expansion to the definition of the local residual trajectory in Equation 5.4 gives

$$\boldsymbol{r}_n = in\omega\boldsymbol{x}_n - \boldsymbol{g}_n, \tag{5.10}$$

where

$$\boldsymbol{g}_n = \frac{1}{T}\int_0^T \boldsymbol{g}\left(\boldsymbol{x}\left(t\right)\right) e^{-in\omega t}\,\mathrm{d}t \tag{5.11}$$

are the Fourier coefficients of the response of the system over the trajectory $\boldsymbol{x}$. Now, defining $\boldsymbol{\Psi}_n \in \mathbb{C}^{d\times d_r}$ to be a complex valued orthogonal matrix, $\boldsymbol{\Psi}_n\boldsymbol{\Psi}_n^{\dagger} = \boldsymbol{I}$, for every $n \in \mathbb{Z}$, where $\left(\cdot\right)^{\dagger}$ denotes the conjugate transpose. It is assumed here that $d_r \leq d$, and the degree to which the dimensions are compressed. Using this rectangular matrix, the reduced-space coefficients $\boldsymbol{a}_n$ can be defined as $\boldsymbol{a}_n = \boldsymbol{\Psi}_n^{\dagger}\boldsymbol{x}_n'$. The original Fourier coefficients of the trajectory can be recovered using the orthogonality of the matrix $\boldsymbol{x}_n' = \boldsymbol{\Psi}_n\boldsymbol{a}_n$.

In this new reduced space, the global residual can be computed rather simply by defining $\boldsymbol{\rho}_n = \boldsymbol{\Psi}_n^{\dagger}\boldsymbol{r}_n$, and left-multiplying Equation 5.4 by the projection matrix to obtain

$$\boldsymbol{\rho}_n = in\omega\boldsymbol{a}_n - \boldsymbol{\Psi}_n^{\dagger}\boldsymbol{g}_n. \tag{5.12}$$

Then, using Parseval's theorem and substituting in the projection of the local residual into the expression for the global residual

$$\mathcal{R} = \sum_{n\in\mathbb{Z}} |\boldsymbol{\rho}_n|^2, \tag{5.13}$$

where $|\boldsymbol{z}| = \boldsymbol{z}^\dagger \boldsymbol{z}$ is the magnitude of a complex valued vector. Optimising over the set of coefficients $\boldsymbol{a}_n$ automatically satisfies the periodicity constraint with a dimensionality reduction from a space of d dimensions to a space of d_r dimensions. This new optimisation can be summarised as

$$\min_{\boldsymbol{a}_n,\,\omega} \quad \mathcal{R}\left(\boldsymbol{a}_n\colon\ n \in \mathbb{Z}\right). \tag{5.14}$$

To perform the gradient-based optimisation a projected form of the gradient in Equation 5.6 is required. The frequency gradient Equation 5.7 is relatively simple, since the optimisation is still performed over ω, and so can remain unchanged apart from noting then when it is computed it is typically done in terms of the respective Fourier components to save computational effort. This is less relevant here as the dimensionality of the system is so low. The projection of $\delta\mathcal{R}/\delta\boldsymbol{x}$ is achieved similarly to the infinite-dimensional case in Chapter 3, using first an expansion in terms of the Fourier modes, and then a projection directly onto the basis. For the finite-dimensional case this process gives

$$\frac{\partial\mathcal{R}}{\partial\boldsymbol{a}_n} = \boldsymbol{\Psi}_n^\dagger \frac{\partial\mathcal{R}}{\partial\boldsymbol{x}_n} = \boldsymbol{\Psi}_n^\dagger \left[-in\omega\boldsymbol{r}_n - \left(\boldsymbol{L}^\top(\boldsymbol{x})\,\boldsymbol{r}\right)_n\right]. \tag{5.15}$$

With this final expression, it is now possible to perform a gradient-based optimisation of the periodic trajectory $\boldsymbol{x}$ restricted to the linear subspace defined by the column space of $\boldsymbol{\Psi}_n$. The projection matrix is still derived using resolvent analysis, the details of which are given in Section 5.2.

5.2 Resolvent Analysis of the Lorenz System

To perform the gradient-based optimisation of the Lorenz system, we require the resolvent response basis, defined by the matrix $\boldsymbol{\Psi}_n$. This can be obtained through a very similar procedure as in Section 4.3, with a key difference being the linearity of one of the equations governing the Lorenz system, which leads to an elegant dimensionality reduction that can be achieved at no cost to the accuracy of the resulting dynamics. The Lorenz system is defined with the following dynamical system

$$\frac{\mathrm{d}x}{\mathrm{d}t} = \sigma\left(y - x\right), \tag{5.16a}$$

$$\frac{\mathrm{d}y}{\mathrm{d}t} = x\left(\rho - z\right) - y, \tag{5.16b}$$

$$\frac{\mathrm{d}z}{\mathrm{d}t} = xy - \beta z. \tag{5.16c}$$

The standard parameter values of $\sigma = 10$, $\rho = 28$, and $\beta = \frac{8}{3}$ are used, for which it is known the system exhibits chaotic motion confined to a strange attractor. The governing equations are symmetric under the transformation $[x,\, y,\, z] \rightarrow [-x,\, -y,\, z]$, which implies that the mean has the form $\overline{\boldsymbol{x}} = \begin{pmatrix} 0 & 0 & \overline{z} \end{pmatrix}^{\top}$ where $\overline{z}$ denotes the mean in the z-direction. The mean here is defined as

$$\overline{\boldsymbol{x}} = \lim_{t\to\infty} \frac{1}{t} \int_0^t \boldsymbol{x}\left(t'\right) \mathrm{d}t'\,. \tag{5.17}$$

Defining a mean-fluctuation decomposition of the state trajectory $\boldsymbol{x}(t) = \overline{\boldsymbol{x}} + \boldsymbol{x}'(t)$ and substituting it into Equation 5.16 gives an evolution equation for the fluctuations

$$\frac{\mathrm{d}x'}{\mathrm{d}t} = \sigma\left(y' - x'\right), \tag{5.18a}$$

$$\frac{\mathrm{d}y'}{\mathrm{d}t} = \left(\rho - \overline{z}\right) x' - y' - x'z', \tag{5.18b}$$

$$\frac{\mathrm{d}z'}{\mathrm{d}t} = -\beta\left(\overline{z} + z'\right) + x'y', \tag{5.18c}$$

which can be expressed compactly as

$$\frac{\mathrm{d}\boldsymbol{x}'}{\mathrm{d}t} = \boldsymbol{c} + \boldsymbol{L}\left(\overline{\boldsymbol{x}}\right)\boldsymbol{x}' + \boldsymbol{M}\boldsymbol{f}\left(\boldsymbol{x}'\right), \tag{5.19}$$

where $\boldsymbol{c} = \begin{pmatrix} 0 & 0 & -\beta\overline{z} \end{pmatrix}^{\top}$ being the constant mean response of the system, the linearised Lorenz matrix evaluated at $\overline{\boldsymbol{x}}$ is given as

$$\boldsymbol{L}\left(\overline{\boldsymbol{x}}\right) = \begin{pmatrix} -\sigma & \sigma & 0 \\ \rho - \overline{z} & -1 & 0 \\ 0 & 0 & -\beta \end{pmatrix}. \tag{5.20}$$

The nonlinear influence matrix is given as

$$\boldsymbol{M} = \begin{pmatrix} 0 & 0 \\ -1 & 0 \\ 0 & 1 \end{pmatrix}. \tag{5.21}$$

and accounts for the nonlinearity only being present in the evolution equations for the y and z components of the state. This matrix plays a similar role to the influence matrix in Equation 4.15. As a result of the influence matrix, the nonlinear forcing $\boldsymbol{f}\left(\boldsymbol{x}'\right) = \begin{pmatrix} x'z' & x'y' \end{pmatrix}^\top$ is a two-element vector.

Expanding Equation 5.19 in terms of the Fourier series defined in Equation 5.8 gives

$$\begin{aligned} in\omega \boldsymbol{x}_n' &= \boldsymbol{L}\left(\overline{\boldsymbol{x}}\right)\boldsymbol{x}_n' + \boldsymbol{f}_n, \quad n \in \mathbb{Z} \setminus \{0\}, && (5.22a)\\ 0 &= \boldsymbol{c} + \boldsymbol{f}_0, && (5.22b) \end{aligned}$$

which is the governing equation for the Fourier modes of the fluctuations in Equation 5.22a as well as the mean constraint equation in Equation 5.22b. Similar to the fluids case, Equation 5.22a can be rearranged into a linear system relating the nonlinear forcing modes to the state response modes via a finite-dimensional resolvent operator as follows

$$\boldsymbol{x}_n' = \boldsymbol{H}_n \boldsymbol{f}_n, \quad n \in \mathbb{Z} \setminus \{0\}, \tag{5.23}$$

where the resolvent operator is defined as

$$\boldsymbol{H}_n = \left(in\omega \boldsymbol{I} - \boldsymbol{L}\right)^{-1} \boldsymbol{M}, \quad n \in \mathbb{Z} \setminus \{0\}. \tag{5.24}$$

Due to the influence matrix, the resolvent matrix for the Lorenz system is rectangular by construction, specifically $\boldsymbol{H} \in \mathbb{C}^{3\times 2}$. This is the key to the dimensionality reduction of the system. Due to the relatively simple form of the linearised Lorenz matrix $\boldsymbol{L}$, an expression for the elements of the resolvent matrix can be derived resulting in

$$\boldsymbol{H}_n = \begin{pmatrix} \alpha_n & 0 \\ \beta_n & 0 \\ 0 & \gamma_n \end{pmatrix}, \tag{5.25}$$

where

$$\begin{aligned} \alpha_n &= -\sigma / D_n, && (5.26)\\ \beta_n &= -\left(in\omega + \sigma\right)/D_n, && (5.27)\\ \gamma_n &= 1/\left(in\omega + \beta\right), && (5.28)\\ D_n &= \left(in\omega + 1\right)\left(in\omega + \sigma\right) + \sigma\left(\overline{z} - \rho\right). && (5.29) \end{aligned}$$

The convenient structure also allows for an explicit expression of the singular value decomposition

$$\boldsymbol{H}_n = \boldsymbol{\Psi}_n \boldsymbol{\Sigma}_n \boldsymbol{\Phi}_n^{\dagger} \tag{5.30}$$

$$= \begin{pmatrix} \zeta_n & 0 \\ \eta_n & 0 \\ 0 & \kappa_n \end{pmatrix} \begin{pmatrix} \sigma_{1,n} & 0 \\ 0 & \sigma_{2,n} \end{pmatrix} \begin{pmatrix} 1 & 0 \\ 0 & 1 \end{pmatrix}, \tag{5.31}$$

where the coefficients of the left singular matrix $\boldsymbol{\Psi}_n$ are given as $\zeta_n = \alpha_n/\sigma_{1,n}$, $\eta_n = \beta_n/\sigma_{1,n}$, and $\kappa_n = \gamma_n/\sigma_{2,n}$. The rank-2 nature of the resolvent means there are exactly 2 singular values that govern the transfer of nonlinear forcing to the solution of the system. The response modes, defined by the columns of $\boldsymbol{\Psi}_n$, have the property that the first mode contains all the information from the xy-plane, while the second mode contains only the information in the z-direction. As such, retaining only one of the pair of modes restricts the dynamics to only the xy-plane or z-axis. Figure 5.1 shows a schematic for this projection, where the three-dimensional coefficient $\boldsymbol{x}_n$ is projected onto a two-dimensional subspace defined by the column space of $\boldsymbol{\Psi}_n$, resulting in the new two-dimensional vector $\boldsymbol{a}_n$. This is in fact the exact projection performed for the Lorenz system, as shown in Section 5.2.

Due to the right singular vector, $\boldsymbol{\Phi}_n$, being equal to the identity matrix as shown in Equation 5.31 the following expression for $\boldsymbol{\Sigma}_n$ can be derived

$$\boldsymbol{\Psi}^{\dagger}\boldsymbol{\Psi}_n = \boldsymbol{\Sigma}_{\boldsymbol{n}}^{\boldsymbol{-1}} \boldsymbol{H}_n^{\dagger} \boldsymbol{H}_n \boldsymbol{\Sigma}_n^{-1} = \boldsymbol{I}, \tag{5.32}$$

$$\Rightarrow \boldsymbol{\Sigma}_n^2 = \boldsymbol{H}_n^{\dagger} \boldsymbol{H}_n, \tag{5.33}$$

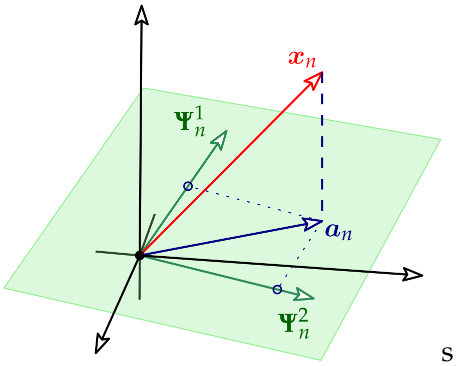

FIGURE 5.1: Schematic for the projection of the state onto the subspace defined by the column vectors/space of the matrix $\boldsymbol{\Psi}_n$, denoted with the subscripts 1 and 2.

which gives for the individual singular values

$$\sigma_{1,n} = \sqrt{\frac{(n\omega)^2 + 2\sigma^2}{|D_n|^2}}, \tag{5.34}$$

$$\sigma_{2,n} = \sqrt{\frac{1}{(n\omega)^2 + \beta^2}}. \tag{5.35}$$

Figure 5.2 shows the ratio of the singular values as given in Equation 5.34 and Equation 5.35 as the frequency $n\omega$ is varied. There is no large separation of scale observed between these singular values and so the system cannot be accurately represented with modal coefficients $\boldsymbol{a}_n \in \mathbb{C}^{d_r}$. Physically this is obvious if the response modes in Equation 5.31 are inspected. As mentioned, if one of the response modes is neglected, then the dynamics are constrained to only the xy-plane or the z-axis for the first and second mode, respectively, which cannot accurately reconstruct the structure of the strange attractor embedded in the full state space since it has a fractal dimension of larger than two.

Therefore, the dimensionality reduction used in this work is from $\mathbb{C}^3$ to $\mathbb{C}^2$, retaining both of the response modes in Equation 5.31. This is an exact projection. That is to say, there has been no rejection of any non-zero singular values. This can be considered a special case of the more general (usually higher-dimensional) setting, where there are more non-zero singular values as well as a distinctive separation of scales allowing the rejection of a finite number of relatively small singular values.

As a final note, it is not necessary to perform the analysis as shown above. A more traditional approach can be taken, akin to that featured in Section 4.3.1. This results in a set of three response modes instead of the two fundamental modes obtained here. The three singular values associated with each of these modes do not yield any approximate reductions, since they are all of very similar scale. This is not examined

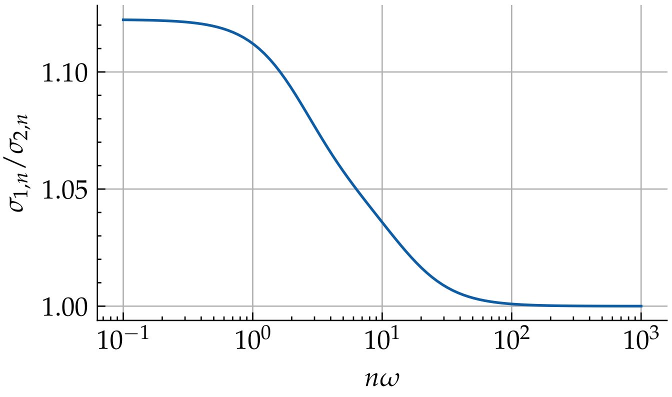

FIGURE 5.2: Ratio of the singular values for the Lorenz system plotted against the frequency.

any further in this work, as the aim to provide a conceptual link between this low-dimensional validating case and the more general high-dimensional fluid case.

5.2.1 Numerical Details

The optimisation process for each iteration is visualised with the flow diagram given in Figure 5.3. The optimisation is initialised with a mean state $\overline{x}$ and fundamental frequency ω which are used to generate the resolvent modes $\boldsymbol{\Psi}_n$ for $n \in \mathbb{Z}$. Next, the initial trajectory is generated. This flow diagram is very similar to the one shown in Figure 3.4 with the key difference being that there is no requirement to project the local residual $\boldsymbol{r}_n$ onto the resolvent subspace since there are no incompressibility and no-slip boundary constraints that need to fulfilled. In the literature, when seeking exact solutions it is common to use close recurrences of chaotic trajectories obtained from direct chaotic simulations to initialise a given trajectory, as done in Auerbach et al. (1987) and Azimi et al. (2022), which is particularly important for high-dimensional systems as the radius of convergence in such cases is small compared to the space in which the state can inhabit. For the analysis that follows, we found the results to be very robust to the initial guess for the quasi-trajectory and so the coefficients $\boldsymbol{a}_n$ were initialised randomly with a Gaussian distribution. Once $\overline{x}$, $\boldsymbol{\Psi}_n$, and an initial $\boldsymbol{a}_n$ are known, the optimisation loop can begin.

Over the duration of the optimisations performed in this chapter to obtain any UPOs and quasi-trajectories, the fundamental frequency ω and the mean state $\overline{x}$ are fixed. This is a notable difference compared to the optimisation performed to obtain exact solutions in Chapter 6. When seeking exact solutions to the governing equations, it is required to modify ω and $\overline{x}$ since they are not known a-priori. It is known that UPOs of low-dimensional dynamical systems become exponentially more common as the allowed periods is increased (Cvitanović et al., 2020). Since long periodic trajectories are sought, it is expected that for a sufficiently large period (a sufficiently small fundamental frequency) a UPO exists with a period differing by an arbitrarily small amount. This means that if the period is chosen to be large then the optimisation is not limited by the quasi-trajectory not having a sufficient amount of time to explore the strange attractor. For the optimisation a mean state $\overline{x}$ obtained by averaging a chaotic simulation, using Equation 5.17, is used. It may be the case that by restricting $\overline{x}$ and ω there does not exist any global minima for $\mathcal{R}$, meaning that no UPO exists for the given period and mean state. However, as mentioned, the difference between the period for a quasi-trajectory and an actual UPO can be made arbitrarily small by increasing the period, for which the same is true for the mean state. So if the period is large enough, the ability of the resulting quasi-trajectory to reconstruct the underlying strange attractor is not significantly affected. In addition, fixing ω and $\overline{x}$ have the

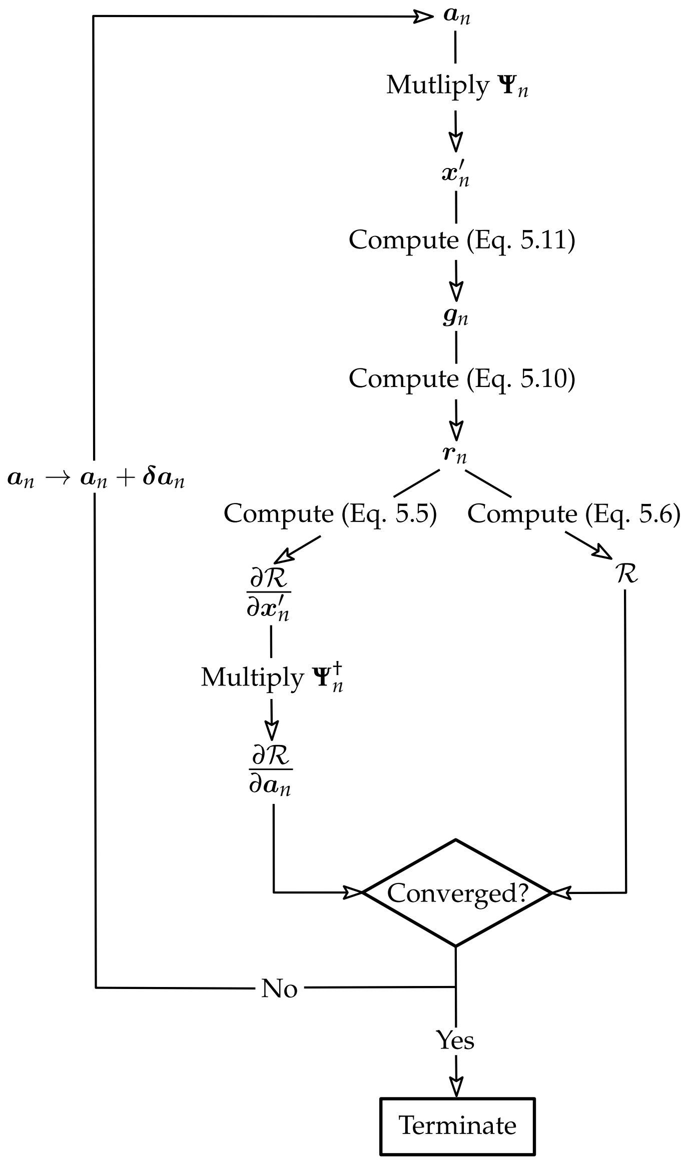

FIGURE 5.3: Flow diagram of a single iteration of the optimisation loop used to compute the residual and its gradient starting from the modal coefficients a_n.

added analytical benefit of fixing the resolvent modes over the duration of the optimisation, as the resolvent matrix H_n does not depend on anything else.

When computing the residual and its gradient, a "pseudo-spectral" method is used to reduce the time complexity of computing the nonlinear (typically quadratic) terms. This takes the form of expanding the coefficients a_n and inverse Fourier transforming the result to obtain the time domain representation of the quasi-trajectory. The nonlinear terms $f(x)$ can then be efficiently computed over the length of the quasi-trajectory, after which the result is Fourier transformed to obtain f_n. Taking note of Figure 5.3, f_n is then used directly to compute r_n. This means that over the course of the optimisation the trajectory is transformed from reduced to full space and then from spectral to time domain to be able to compute all the terms in the space where it is computationally most efficient. The result is the gradient $\partial\mathcal{R}/\partial\boldsymbol{x}_n$, which is then projected into the reduced space using Equation 5.15, providing the required gradient with respect to the coefficients $\boldsymbol{a}_n$.

The L-BFGS optimisation algorithm is utilised similarly to Chapter 6. The algorithm is implemented as part of the SciPy package, with implementation details available from Liu and Nocedal (1989); Morales and Nocedal (2011), with the line search algorithms detailed in Nocedal and Wright (2006); Fletcher (2000). For further details on the L-BFGS algorithm see Section 6.1.

The choice of convergence criteria is important in this context. Usually, a small global residual is used as it indicates that an exact solution to Equation 5.1 has been found. In this work the focus is on quasi-trajectories for which the global residual is not expected to converge to a small value. Hence, it makes more sense here to track some relevant time-averaged observable of the system and terminate the iterations once this observable has converged to some value. This is explored more in Section 5.4.1 using statistical measures of the Lorenz system.

5.3 Optimising for UPOs

The goal of this brief section to demonstrate the variational optimiser outlined above successfully constructing exact solutions for the chaotic Lorenz system. This serves as a quick validation of the method as described in the previous section, as well as acting as a precursor to the results shown in Chapter 6.

Before beginning, however, a few specific things should be noted related to the numerical details outlined above. Both the mean state and the period are fixed over the duration of the optimisation. This would in general naturally make it impossible

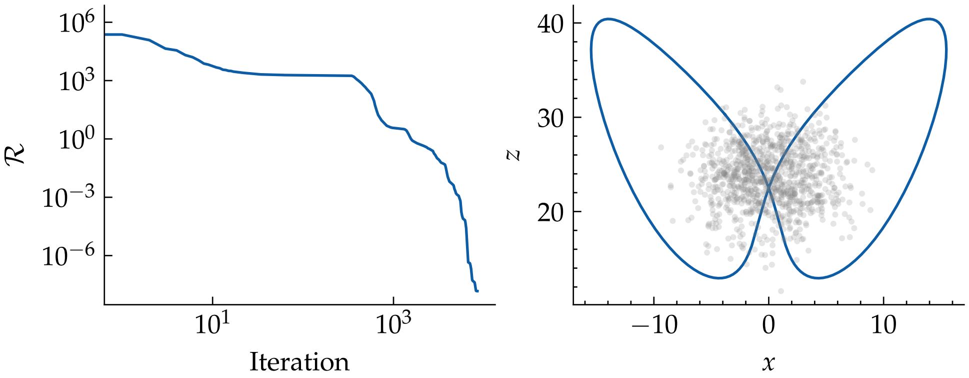

FIGURE 5.4: Residual trace in panel (a) and the state space evolution in panel (b) of the shortest UPO of the Lorenz system that circulates both attractor lobes, with a period of $T \approx 1.5586$. Also plotted in panel (b) with grey dots is the initial condition used for the optimisation.

to make the global residual zero for the solution that is being sought. The periods for the UPOs shown below are obtained from Dong (2018). This is not reflective of the general case where the period is not known and has to be optimised for as well as the shape of the trajectory. However this is not dwelled on here since the optimisation over the period has been performed in the literature many times and there is no question that its inclusion is well-defined. What is more important here is the projection aspect of the optimisation, and its effect on the convergence rates. The mean state is also fixed during the optimisation. The mean state is obtained by propagating the initial states of each UPO provided in Dong (2018) and integrating the resulting periodic orbit. This is integration is done using the "DOP853" algorithm (Hairer et al., 1993), the highest order integration scheme provided by SciPy's *solve_ivp* function. Again, it should be emphasised that the goal here is not to outright demonstrate completely new solutions being obtained using the variational optimisation. This task has already been completed for more complex situations, instead it is a quick validation of the correctness of the implementation.

Figure 5.4(a) shows the global residual over the course of the optimisation for the shortest period UPO features in Dong (2018), with a period of $T \approx 1.5586$. Figure 5.4(b) displays the projection of the initial condition used for the optimisation (gray dots) and the final solution (solid blue line). The optimisation was initialised with a set of Gaussian distributed random Fourier coefficients, as were all the optimisations performed in this section for all the UPOs shown. It was found that the

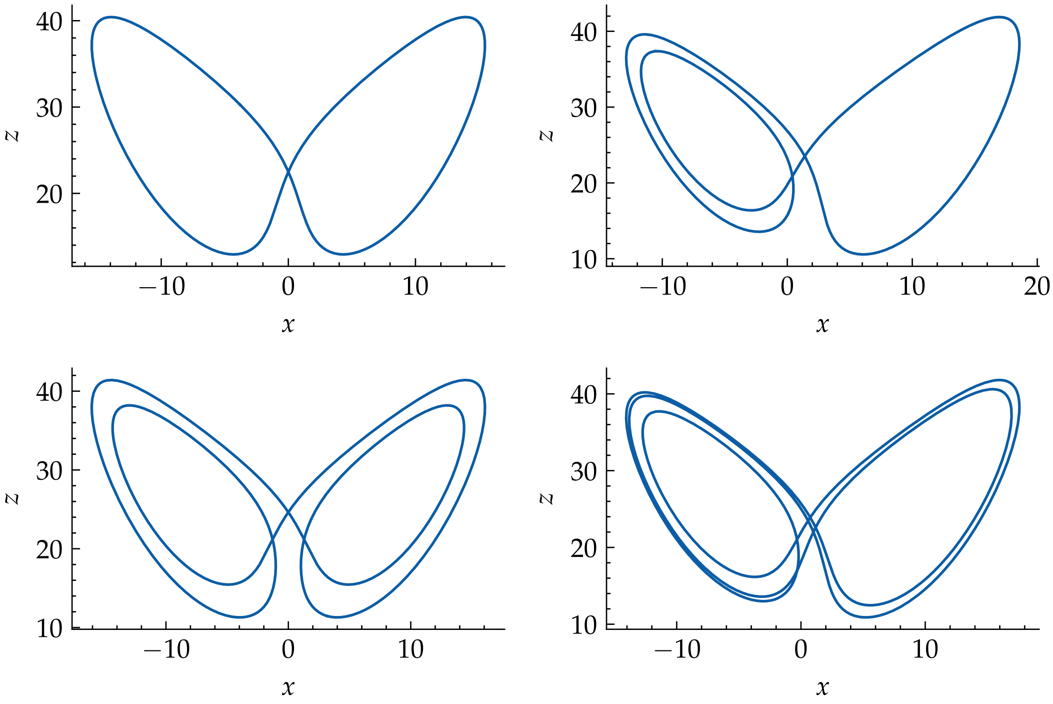

FIGURE 5.5: Sample of a few known UPOs for the Lorenz system, see Dong (2018) for details of the UPOs.

optimiser could reliably converge to the targeted UPO even with the completely random initial states. The optimiser initially decreases the residual by several orders of magnitude, after which it takes a few hundred iterations before another large decrease in the residual is observed. The initial decrease it associated with the solution quickly attracting towards the strange attractor. The rest of the time is spent organising the trajectory on the attractor before it can find the exact trajectory that globally minimises the residual. As the period grows larger, and there are more nearby UPOs with similar periods, it is expected that a more accurate initial condition would be required. Otherwise the optimiser would generally become stuck in a local minimum.

Figure 5.5 is a sample of four of other UPOs obtained from the initial conditions and periods provided in Dong (2018). Direct comparison shows that each of the UPOs is found very accurately, again using randomly distributed initial orbits. All of the solutions shown start with a global residual of the order of $\mathcal{R} \sim 10^5$, and after roughly $10,000$ iterations this is decreased to below 10^{-6}.

5.4 Quasi-Trajectories

Quasi-trajectories are obtained through the same optimisation procedure as performed in Chapter 6 to obtain exact solutions to the Navier-Stokes equations, with the key difference that the optimisation is terminated well before the residual has reached a minimum. The optimisation is instead terminated using a heuristic approach, relying on the convergence of certain observables of the system, which is shown to approach a steady value far sooner than the residual. The result is a trajectory that does not satisfy the governing equation, having a non-zero residual, while still capturing the essential features of the strange attractor governing the chaotic dynamics. What follows is first a discussion of the numerical details of the implementation of this framework, which then leads to the main results of this chapter.

5.4.1 Statistics of Quasi-Trajectories

In this section, the quasi-trajectories generated using the low-order resolvent-based model discussed in Section 5.2 for the Lorenz system are assessed in their ability to approximate the statistics of chaotic solutions. To facilitate this, the following observables are defined

$$\mathcal{J}_1(\boldsymbol{x}) = \sqrt{x^2 + y^2 + z^2}, \qquad \mathcal{J}_2(\boldsymbol{x}) = xz. \tag{5.36}$$

These observables will be averaged over the duration of a trajectory with period T, denoted by $\overline{\mathcal{J}_i}^T$.

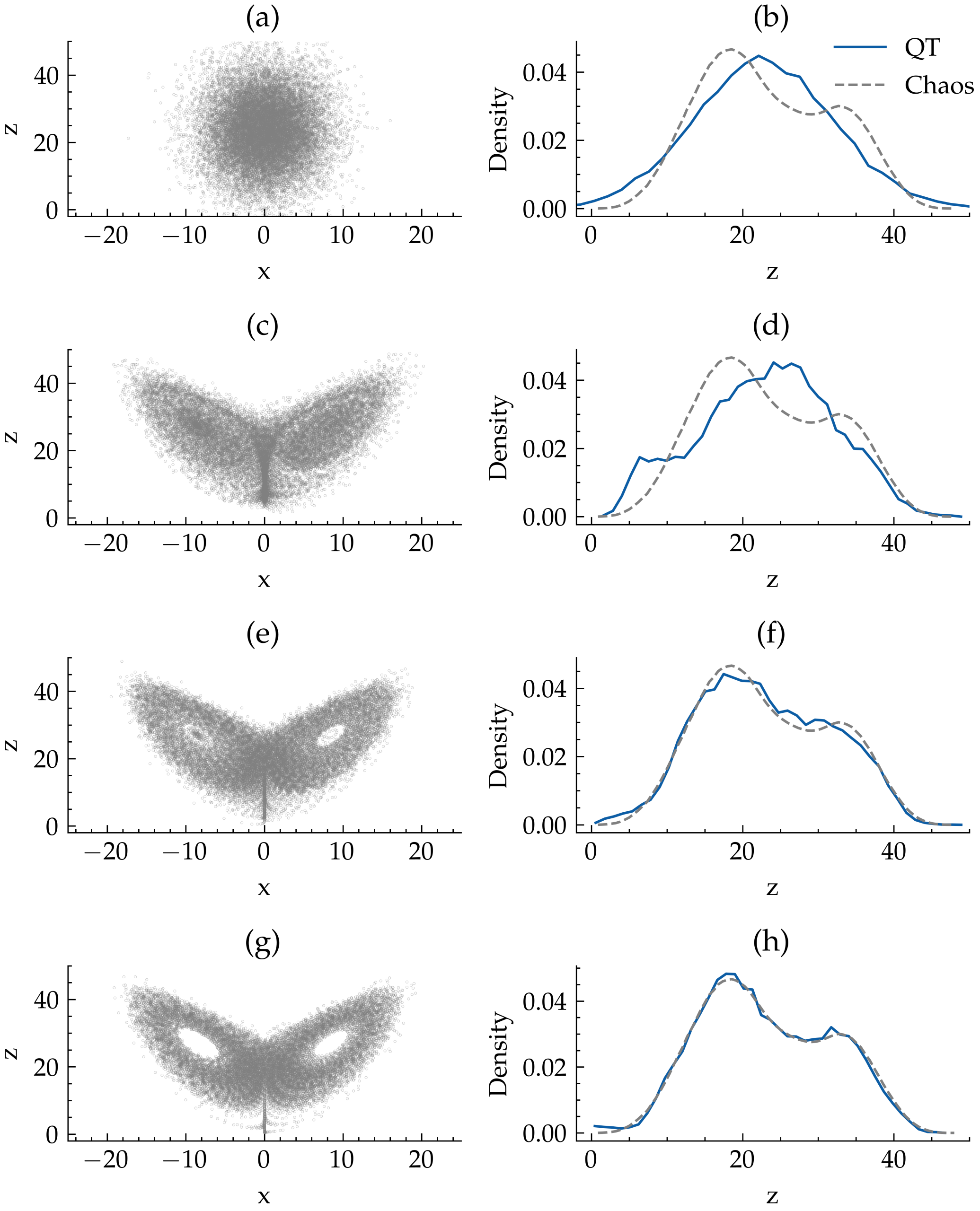

FIGURE 5.6: Optimisation of a quasi-trajectory, with the state space points shown in panels (a,c,e,g), and the probability distribution functions over the z-direction shown in panels (b,d,f,h), with the blue line corresponding to the Quasi-Trajectory (QT) and the dashed grey line corresponding to the distribution obtained from chaotic data. The initial trajectory (iteration 0) is shown in panels (a-b), iteration 100 is shown in panels (c-d), iteration 1000 is shown in panels (e-f), and iteration 10000 is shown in panels (g-h).

The data presented in this section is obtained from two sources. The first, denoted as “chaos” in the figure legends, is from chaotic simulations via black-box solvers supplied by the *solve_ivp* function from *SciPy* with an explicit Runge-Kutta 45 method with adaptive time stepping, described in Dormand and Prince (1980), with the output trajectory being uniformly sampled in time. The second source is from quasi-trajectories, labelled with “QT” in the figures. These are initialised randomly, generating the points in the time domain around the given mean $\overline{\boldsymbol{x}}$ with a standard deviation of 10. The coefficients $\boldsymbol{a}_n$ are then determined from the time domain representation of the initial quasi-trajectory so that the optimisation can begin. The mean state used for the optimisation is set to $\overline{\boldsymbol{x}} = \begin{pmatrix} 0 & 0 & 23.64 \end{pmatrix}^\top$, obtained from independent chaotic simulations of the system using Equation 5.17.

Figure 5.6 displays the optimisation of a quasi-trajectory with a period of $T = 1000$ starting from a random distribution around the mean and how it evolves over 100, 1000, and 10000 iterations. A period of $T = 1000$ is rather large for a quasi-trajectory of the Lorenz system, and so the optimisation is not expected to be largely affected by the choice of period and mean. For reference, the shortest UPO of the Lorenz equations has a period of roughly 1.55 time units. On the left side the xz-projection of the quasi-trajectory sampled for 10000 points is shown, reconstructed in the time domain from the coefficients $\boldsymbol{a}_n$. On the right side the corresponding probability distribution function (PDF) over the z-direction, with the solid line representing the PDF obtained from the quasi-trajectory and the dashed line being obtained from a chaotic solution. We first note that there is a qualitative resemblance between the quasi-trajectory and what is expected from a chaotic simulation of the Lorenz system. The noted resemblance is achieved after only roughly 1000 iterations. This is a result of the optimisation seeking out the strange attractor very early, guiding the quasi-trajectory into a shape that lies on the attractor as well as possible for the given iteration. This is reinforced with the PDFs at each iteration, with the PDF shown in Figure 5.6(f,h) agreeing well with the PDF obtained from a chaotic solution. Both the quasi-trajectory and chaotic solutions display a bimodal distribution. The PDF of the quasi-trajectory at each iteration is computed using 40 bins over the range of z values obtained by the quasi-trajectory. The coarseness of the bins used is due to the fact that as the number of bins is increased the PDF would display peaks that do not subside as the number of bins is increased. The presence of these peaks in the PDFs of periodic orbits was observed and discussed in Zoldi (1998) and is a result of the turning points in the orbits.

There is a notable feature of the quasi-trajectory that is not present in chaotic trajectories. For the Lorenz system, there exists an unstable fixed point at the origin ($\boldsymbol{x} = \begin{pmatrix} 0 & 0 & 0 \end{pmatrix}$), which repels any trajectory along its unstable manifold. However, as a consequence of the way in which the variational methodology is constructed, the residual is small around all fixed points regardless of their stability. This means that a

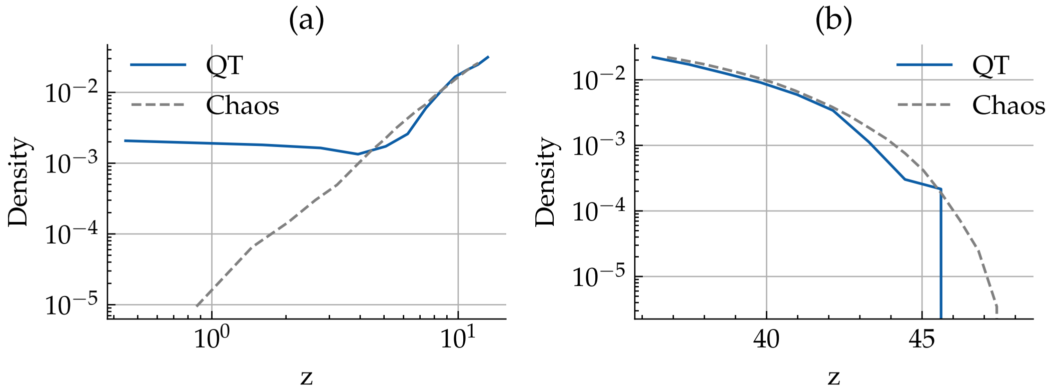

FIGURE 5.7: Tails of the PDF (Probability Distribution Function) shown in panel (h) of Figure 5.6, panel (a) near $z = 0$, and panel (b) near the extreme RHS of the distribution.

quasi-trajectory is not heavily penalised for drifting away from the strange attractor towards the unstable fixed point at the origin. Another way of thinking about this is the fact that the fixed point at the origin has two stable manifolds, one of which tends to attract trajectories on the lower part of the lobes as the loops around one side of the attractor become larger before switching sides. The unstable manifold for then propels the trajectory back up into the attractor, which is a pattern that can be partially replicated by a periodic quasi-trajectory with a long enough period. The other unstable fixed points, at the centre of each lobe around which the state rotates, have stable manifold that are directed directly outside of the attractor. It is speculated here that this means the quasi-trajectory is not biased to tracking along this manifold in the same way as near the origin, instead rotating around the other fixed points as expected. This can be observed in Figure 5.6(g,h), where there is a small increase in the density of the quasi-trajectory near the origin compared to the chaotic PDF that approaches zero as z goes to zero. In Figure 5.7(a), a slice of the PDF of Figure 5.6(h) is taken, plotted on a log-log scale, to show this trend more clearly. The chaotic PDF continues down as z decreases in the fashion of a power law, while the quasi-trajectory PDF plateaus at a particular distance from $z = 0$ after which it does not decrease any further. The effect on the statistics, however, is minimal. The quantitative effect of an unstable fixed point attracting quasi-trajectories under the variational optimisation is dependent on the stability characteristics of the particular fixed point. In general, the closer a particular fixed point (or any time-dependent solution) is to being neutrally stable, the more slowly the optimiser converges towards it. Any manifold associated with a fixed point that attracts or repels trajectories is recast as attracting under the derived variational dynamics. As a result, solutions near bifurcation points are difficult for the optimiser to identify and to account for accurately within the overall picture of the dynamics. This difficulty with marginally stable solutions is well known, as higher-order information is often required to properly characterise their structure near bifurcation. It is not yet clear what effect this limitation will have in turbulent flows, which are highly complex and contain (infinitely) many unstable solutions embedded within attractors — some of which may be arbitrarily close to bifurcating at a given Reynolds number. This question likely has a very complex and flow-dependent answer and represents a substantial direction for future work.

Figure 5.7(b) shows the far right side of the PDF from Figure 5.6(h), showing the probability of the quasi-trajectory to undergo a particularly large loop around a lobe of the strange attractor. It shows that the quasi-trajectory is able to capture some of the more unlikely/extreme events of the chaotic motion. There is an upper limit to the PDF that is smaller than that predicted from the chaotic PDF, however a larger quasi-trajectory would lead to extreme events at larger values of z being captured. A similar PDF to that in Figure 5.6 can be constructed by constructing a series of smaller quasi-trajectories, making sure to initialise them with sufficiently different (random) initial states. The expected number of quasi-trajectories required to construct a similar PDF would be such that their total period adds to the total period of the longer quasi-trajectory. However, the main bulk of the PDF may be correct, certain features, such as the more extreme events in Figure 5.7, are expected to be captured less accurately. It is possible that individual constructed quasi-trajectories could explore these rarer sections of the attractor, however, the shorter the period of the quasi-trajectory the less likely this will be. Despite certain short period UPOs being observed to explore rarer events associated with intermittency in Kolmogorov flow (Redfern et al., 2024), we would not necessarily expect this of quasi-trajectories. This is a result of them being constructed as "typical" long orbits, effectively averaging the properties of many different unstable solutions to create their overall behaviour. With this in mind, in turbulent flows that exhibit rare events such as intermittency, quasi-trajectories would need to be sufficiently long to average over unstable solutions representing both the standard dynamics and the rare extreme events.

In Figure 5.8, the power spectra of the final quasi-trajectory achieved in Figure 5.6 at 100, 1000, and 10000 iterations is compared with that obtained from the chaotic data. All spectra are obtained using Welch's method, with Hann windowing to reduce spectral leakage. Welch's method was used to compute the average power spectra of the quasi-trajectory, despite them being exactly periodic, because the coefficients $\mathbf{a}_n$ obtained from the optimisation will be different between different optimisations showing randomness with variances independent of the period T, similarly to the Fourier coefficients of long chaotic (non-periodic) solutions Andrews and Waltz (1988). A similar trend is seen as in the Figure 5.6, in that the power spectra after 100 does not particularly resemble the chaotic spectra, missing the important peak at $n\omega \approx 1.3$ and its harmonics. After 1000 iterations the quasi-trajectory spectra displays a spread out version of this peak with a couple of its harmonics, and finally 10000 iterations shows the best agreement with the spectral peaks more clearly defined and multiple of its harmonics resolved in agreement with the chaotic data. The high frequency component of the spectra also gradually reduces over the duration of the optimisation,

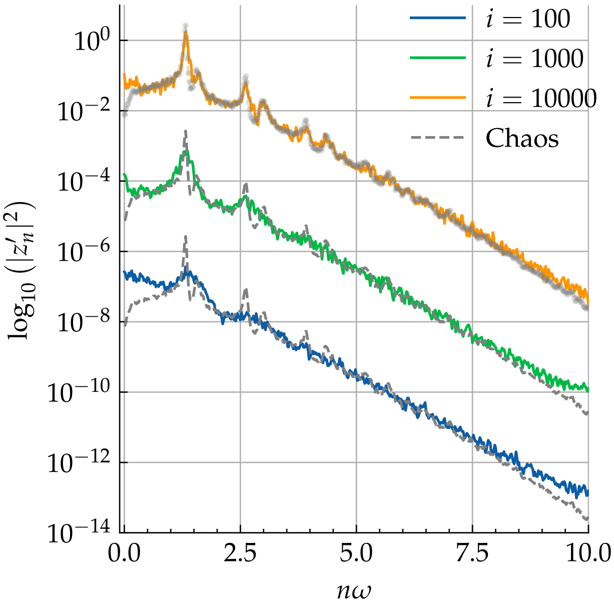

FIGURE 5.8: Comparisons of the power spectra obtained from the final quasi-trajectory in Figure 5.6 at 100, 1000, and 10000 iterations, and chaotic data. The spectra at each iteration (along with the corresponding chaotic spectra) is plotted offset from each other to improve readability.

gradually approaching the spectral decay observed from the chaotic spectra. Notably, there is an increase in the spectral energy in the low frequencies that persists in the quasi-trajectory. This is likely an artefact of the previously mentioned fixed point at the origin dragging part of the quasi-trajectory towards it. Near this point the quasi-trajectory moves rather slowly, approaching a marginally unstable manifold, which adds an extra low frequency component to the spectra. The spectra shown in Figure 5.8 makes it clear that the bulk of the early optimisation work is to determine the large scale features of the dynamics, represented with the spikes in spectral energy (and their respective harmonics). The majority of the work of the later part of the optimisation is spent tuning the finer features of the trajectory to fit as closely with the turbulent solution, especially at the very low and high frequencies. This fine tuning further decreases the residual but has little effect on the statistics of the solution.

Figure 5.9(a) the trace of the global residual, normalised by $\left\|g\left(x_f\right)\right\|^2$ for the final quasi-trajectory obtained over the duration of the optimisation of the same quasi-trajectory as in Figure 5.6. It can be seen that the global residual has not yet converged to either a zero $\mathcal{R} = 0$ or a non-zero minimum after 10000 iterations. Nevertheless, the close qualitative resemblance observed in Figure 5.6 is achieved after only a moderate number of iterations. Figure 5.9(b) shows the period-averaged observables defined in Equation 5.36 computed on the quasi-trajectory at each iteration, plotted with horizontal lines corresponding to the values of the mean observables for a long chaotic trajectory obtained from numerical integration of the equations of motion. The values of the period averaged observables over the

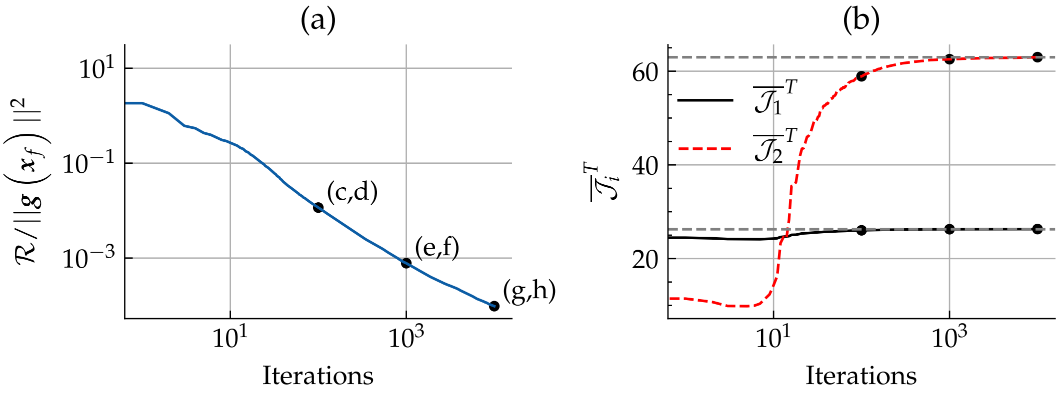

FIGURE 5.9: Trace plots of the global residual normalised by the size of the system response g quasi-trajectory at the end of the optimisation x_f in panel (a), and the mean observables over the quasi-trajectory at each iteration of the optimisation in panel (b), shown with the values obtained from a long chaotic trajectory as horizontal grey lines. Annotated on the plots are the iterations corresponding to the reconstructions shown in Figure 5.6.

quasi-trajectory approach the chaotic values, displaying a convergence of the statistics well before the residual itself has converged, with most of the improvement being done between 10 and 100 iterations. Thus, it is reasonable to say that this quasi-trajectory has converged to the point of providing useful approximations to the statistics of the chaotic dynamics at around 1000 iterations.

The local residual r in Equation 3.5 can be viewed as a small perturbation imposed on the governing equations, and therefore a quasi-trajectory can be viewed as an exact solution to this slightly perturbed system. The ratio of the global residual to the norm of the system's right hand side, $\mathcal{R}/\|g(x)\|^2$, can then be viewed as a measure of the closeness of this forced system to original system. As such, these results show that nearby systems to the Lorenz system, or equivalently a Lorenz system with a particularly chosen light forcing, have very similar statistics to each other.

Figure 5.10 shows the results of a number of batch optimisations at increasing periods T performed for 100, 1000, and 10000 iterations, with each batch consisting of 50 quasi-trajectories. Shown on the top are the ensemble averages of the period averaged observables within the batch, denoted by $\left\langle \overline{\mathcal{J}_i}^T \right\rangle$, and in the bottom is the associated standard deviation of the period averaged observables within each batch, denoted with $\sigma\left(\overline{\mathcal{J}_i}^T\right)$. The corresponding values for the period averaged observables obtained from a long chaotic trajectory are shown with the dashed grey lines. The trend for 1000 and 10000 is for the period averaged observables to approach the long chaotic values. The values of the period averaged observables for 100 iterations exhibit poorer convergence towards the chaotic values, although the relative error is still rather small, being on the order of 1% and 6% for $\left\langle \overline{\mathcal{J}_1}^T \right\rangle$ and $\left\langle \overline{\mathcal{J}_2}^T \right\rangle$, respectively. The period averaged observables for the 10000 iterations case are close to the long chaotic value even for the shortest periods shown. Figure 5.10(c-d) illustrate the change in the

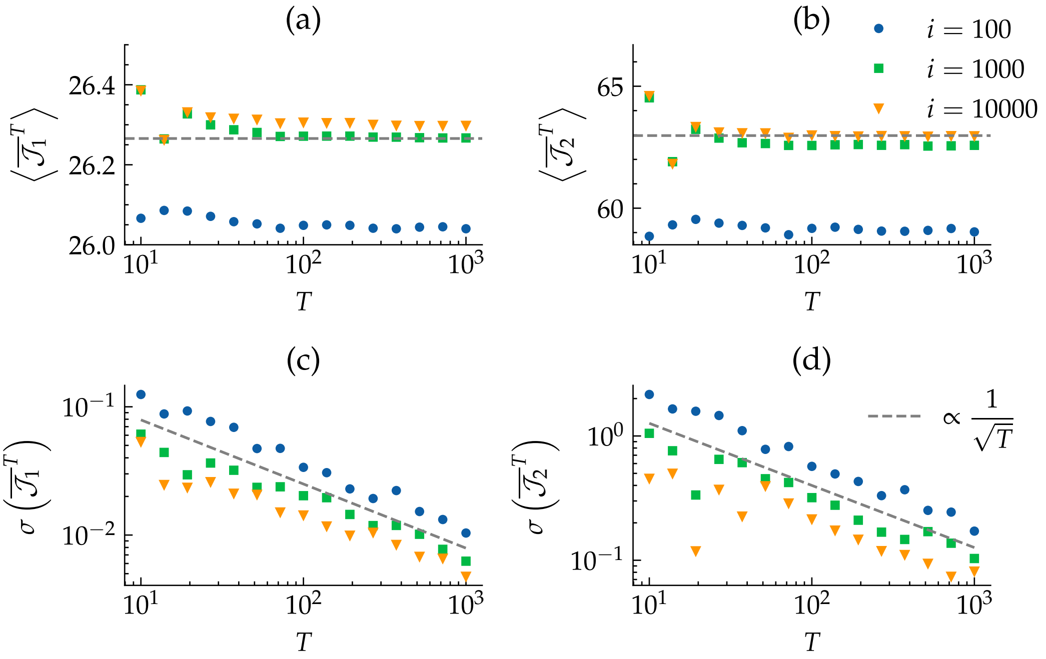

FIGURE 5.10: The ensemble average and standard deviations of the period averaged observables over a batch optimisation of 50 quasi-trajectories, performed over a range of periods T. The optimisations were terminated at 100, 1000, and 10000 iterations. Panels (a,c) show the observable $\overline{\mathcal{J}_1}$, and Panels (b,d) show the observable $\overline{\mathcal{J}_2}$. Panels (a-b) show the ensemble averages, and Panels (c-d) show the standard deviations.

standard deviation of the period averaged observables with the quasi-trajectory period exhibiting a steady decline as the period increases. The rate of this decrease is roughly proportional to the inverse square root of the period shown in Figure 5.10 with the grey dashed line, a consequence of the central limit theorem. The larger period therefore produces quasi-trajectories that become more similar from a statistical point of view.

The result that the longer quasi-trajectories (for $T \gtrsim 20$) better reflect the statistics of the chaotic trajectories stem from their ability to explore the larger fractions of the strange attractor governing the chaotic dynamics. Therefore, a trade-off exists between the accuracy of the statistical predictions obtained and the speed at which the result can be achieved by varying the period of a quasi-trajectory. It should be noted that $\left\langle \overline{\mathcal{J}_1}^T \right\rangle$ approaches the chaotic value more closely for the optimisations that terminate at 1000 iterations, whereas $\left\langle \overline{\mathcal{J}_2}^T \right\rangle$ is closer to the chaotic value for the optimisations that terminate at 10000 iterations. This result suggests that certain observables may be most accurately captured during a quasi-trajectory optimisation.

Figure 5.11 is similar to Figure 5.10, but instead shows the standard deviation, skewness, and kurtosis of the observables taken over the period T of a given quasi-trajectory, denoted with $\mathrm{std}_T(\cdot)$, $\mathrm{skew}_T(\cdot)$, and $\mathrm{kurt}_T(\cdot)$, in panels (a-b), (c-d), and (e-f), respectively. These statistical moments are then averaged over the ensemble

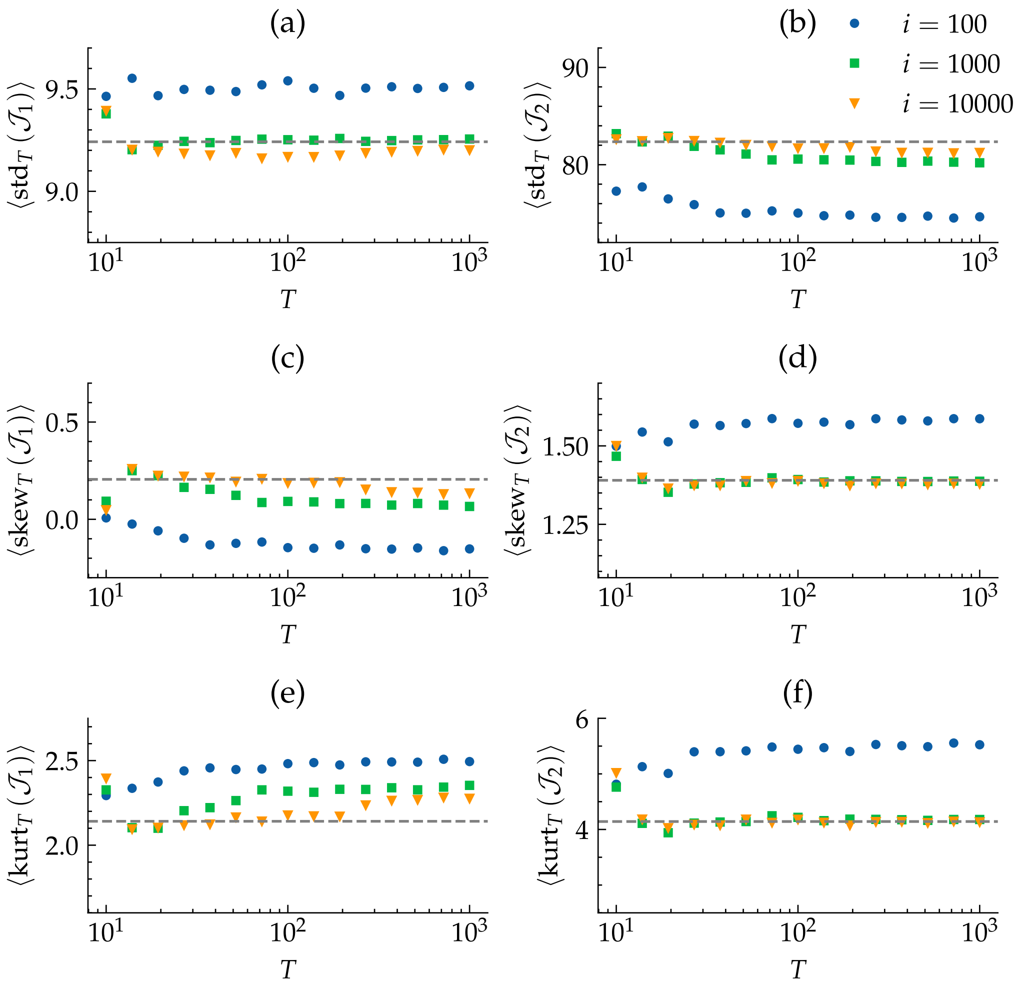

FIGURE 5.11: The ensemble average of the standard deviation in panels (a-b), skewness in panels (c-d), and kurtosis in panels (e-f) of the observables J_1 and J_2 over the same set of batch optimisation as in Figure 5.10.

of 50 optimisations. The ensemble standard deviation follows the same descent trend as in Figure 5.10, so is omitted for the sake of compactness. The expected trend is that for the same period quasi-trajectory, the higher-order statistical moments will be less accurate. Figure 5.11 agrees with this, albeit with the estimation of the higher-order modes only degrading for the first observable, J_1. In fact, the quasi-trajectory statistics of J_2 appears to be accurately reconstructed for periods $T \gtrsim 20$ for all the statistical moments shown, implying the total distribution is faithfully reconstructed including the more extreme parts which would be emphasised by the kurtosis. The deviation of the moments of J_1 are difficult to directly attribute to a particular source, although it appears that more iterations leads to slightly better agreement with the value obtained from chaotic simulation. Additionally, the moments of J_2 appear to converge to a final value at a modest period, whereas the skewness and kurtosis of J_1 have seemingly not converged to the same degree. The optimisation then prioritises capturing certain aspects of the dynamics first, in this case balancing the nonlinear interactions over the total magnitude which takes larger periods and more iterations to accurately capture. In other words, the cross-correlations, represented by the observable J_2, are very accurately captured by quasi-trajectories with a modest period and without having converged the global residual.

5.4.2 Time Cost of Computing Quasi-Trajectories

In this small test case for the Lorenz system, the computation of the quasi-trajectories is much heavier than using a simple ODE solver. There are two primary reasons for this. The first is that the variational optimization inherently scales worse than a time-stepping approach to solving the governing equations since the whole temporal evolution of the trajectory is considered simultaneously. The second and more pertinent reason for this work is the low dimensionality of the system not admitting a large dimensionality reduction. For the algorithm implemented here, depicted in Figure 5.3, each iteration of the optimisation is dominated by the computation of the FFTs in full-space and the projection or expansion steps between full- and reduced-space. The time complexities of each of these operations are given by $\mathcal{O}\left(N \log\left(N\right)\right)$ and $\mathcal{O}\left(d_r N\right)$ respectively, where N is the degrees of freedom of the system (original dimension of the system multiplied by the temporal modes used), and d_r are the number of retained modes for the projection. For the variational optimiser to arrive at a sufficiently accurate estimate of the statistics more rapidly than a time-stepping method, it is required that the optimiser requires fewer degrees-of-freedom to accurately approximate the statistics, which can be best achieved through a large dimensionality reduction, i.e. $d_r \ll d$.

To illustrate for the Lorenz system, obtaining 1000 optimization iterations of a quasi-trajectory with a period of $T = 20$ using 200 temporal modes ($N = 600$) with the dimensionality reduction $d_r = 2$ takes $\mathcal{O}\left(1\right)$ seconds. Obtaining a chaotic ODE solution of the same period using *solve_ivp* takes $\mathcal{O}\left(0.1\right)$ seconds. In short, for low-dimensional systems, where the degrees of freedom are already small and the dimensionality reduction is not large, computing quasi-trajectories is more expensive than an ODE computation.

The potential power of the method becomes more apparent when applied to high-dimensional systems, specifically fluid turbulence, where the possible dimensionality reduction can be very large. This property, combined with the possibly smaller required degrees of the freedom in the full-space, and potentially relaxed time-step constraints, could reduce the time taken to find a statistically meaningful solution. The method described here performs the majority of the computations in the full state-space, only projecting back to the reduced space for the update to the optimisation state. It is possible to perform a complete optimisation loop within the reduced-space by converting the pseudo-spectral approach to computing the nonlinear terms to convolutions in the reduced-space, resulting in projected nonlinear terms which are computed in terms of the coefficients $\boldsymbol{a}_n$. Although convolutions are known to scale worse with the size of the computation, the dimensionality reduction could actually make the convolutions in reduced-space faster than FFTs in full-space. To finish this discussion, the global-in-time description of the flow that is implicit in the current framework would also permit temporal parallelism to be exploited, which may lead to a further speed-up that is not possible in direct time-stepping methods used by most flow solvers. It is expected that if a dimensionality reduction of the same order or larger than the increased cost of computing over the entire future of the flow, then the optimiser can outperform standard integration for obtaining statistics. A less strict bound on the required dimensionality reduction required to achieve performance parity might be possible if the statistics can also be more quickly obtained when the whole length of the trajectory in state-space is resolved at once.

5.5 Summary

The main goal of this chapter was to provide a proof of concept that the statistics of chaotic dynamical systems can be approximated using intermediate trajectories obtained from the resolvent-based variational optimisation described in Chapter 3. It does so by exploiting the (assumed) ergodicity of the dynamics on the strange attractor, which allows a sufficiently long periodic trajectory to shadow true chaotic trajectories in a similar way as typical time-stepping numerical solvers. The demonstration was performed on the Lorenz system of Lorenz (1963), as it is a relatively simple low-dimensional chaotic system that is well studied, and importantly permits a dimensionality reduction through resolvent analysis. This dimensionality reduction is exact in this case, that is, there are no non-zero singular values rejected in the expansion of the resolvent operator. This is a special case of the more general case which exists for high-dimensional systems. This exact reduction also removes the concern that such a low-dimensional system would not possess a sufficiently accurate low-order model if non-zero singular values were to be rejected.

The ability for the quasi-trajectories to reconstruct the complete statistics (distribution) of the chaotic system while having a large and obviously non-converged global residual is demonstrated. It was observed that only a modest number of iterations, on the order of 1000 iterations was required to converge statistical moments of certain observables of the system. In addition, a relatively small period of $T \approx 20$ was sufficient to obtain useful approximations to the statistics of the system. It was also noted that certain features of the state-space, such as unstable fixed points, can have a negative effect on the accuracy of the quasi-trajectory statistics near them. For high-dimensional systems with more complex state-space topologies, the presence of many fixed points or rare occurrences can have negative effects on the efficacy of the quasi-trajectory. However, it was observed that by ensuring the optimisation was not allowed to run for too many iterations, the unstable fixed point had less time to introduce errors into the statistics. The effect of the unstable fixed points have on the quasi-trajectory estimation in fluid turbulence is a topic of future work.

Chapter 6

Search and Analysis of Invariant Solutions of RPCF

This chapter demonstrates the application of the methodology described in Chapter 3 to finding invariant solutions to the RPCF. The main goal of the chapter is to demonstrate that even when the resolvent modes are truncated the variational optimisation is able to find exact solutions to the Navier-Stokes equations. In addition, the ability of the truncation to improve convergence rates of the optimisation without significantly sacrificing the accuracy of the resulting solution is discussed.

This chapter, unfortunately, does not attempt to construct quasi-trajectories for turbulent flows. This is primarily a result of the time constraints as a consequence of the implementation method described at the end of Chapter 3. The details of this implementation limitation and the proposed solution is discussed in more detail at the end of this chapter and in Section 7.1.

The chapter starts in Section 6.1 with an outline of the numerical details required for the implementation of the resolvent-based optimisation methodology. Then the methodology is applied to finding equilibrium and periodic solutions to the RPCF in Section 6.2 without any significant modal truncation demonstrating the base properties of the optimisation. Section 6.3 then discusses the effects that truncating the number of modes has on these previously discussed optimisation properties.

6.1 Numerical Details of Optimisation on RPCF

Fourier modes are used for the discretisation in the spanwise and time directions. The wall-normal direction is discretised using a uniform grid of points, unless otherwise specified. A uniform grid is not the most optimal choice in terms of the ability to resolve the flow near the wall without being unnecessarily detailed in the bulk of the flow. This choice was primarily a pragmatic one, allowing for simplicity of analysis and ease of comparison between DNS and optimisation which were obtained from different sources. Any differentiation in the Fourier directions is performed using standard spectral differentiation procedures, while finite differencing is used for the wall-normal direction. A pseudo-spectral method is used to compute the nonlinear terms to avoid the computation of expensive convolutions. The modal coefficients are expanded back into physical space using Equation 3.54, where the nonlinear terms can be computed point by point, after which the result is then transformed back into the modal coefficients.

To avoid aliasing errors in computing the nonlinear terms of the Navier-Stokes equations, a 3/2 padding rule is used. This de-aliasing approach pads the fields with an extra 50% of Fourier modes in each direction. Once transformed back into physical space, the now padded arrays are more finely discretised, which allows for proper resolution of the higher frequency Fourier modes that result from the quadratic terms in the computation. Once the nonlinear term has been computed in physical space, the result is transformed back into spectral space at which point the extra Fourier modes used in the padding are neglected. This stops any of the higher frequency modes that are computed in the nonlinearity from reflecting back and contaminating the values of the lower frequency modes.

Utilising the Hermitian symmetry of the Fourier expansion, due to the flow variables being real valued, the inner product over the domain and period as defined in Equation 3.2 can be computed in terms of the modal coefficients of Equation 3.54 as follows

$$\langle \boldsymbol{u}', \boldsymbol{v}' \rangle_{\Omega_t} = TL_z \left[a_{0i} \cdot b_{0i} + 2 \sum_{i=1}^{M} \sum_{k \in A^+} a_{ki} \cdot b_{ki} \right] . \tag{6.1}$$

where T and L_z are the period and spanwise length of the domain, respectively. The fluctuation fields are used to ensure the boundary conditions are correctly accounted for by the expansion into the modal space $\boldsymbol{\psi}_{ki}$. The set $A^+ = (\mathbb{Z} \times \mathbb{N}) \cup (\mathbb{N} \times \{0\})$ is half the frequency plane over which the Fourier series is defined, making use of the Hermitian symmetry to reduce the size of the computation required. Figure 6.1 shows the frequency plane for the spanwise and time frequencies, k_z and k_t, respectively, with the Hermitian symmetry displayed.

To compute the modal coefficients a_{ki} and s_{ki} using Equation 3.59 and Equation 3.60 it is necessary to compute the integral over the wall-normal direction. To do this, the method of undetermined coefficients for quadratures (Dahlquist and Björck, 2008) is used, where the integral takes the form

$$\int_{-1}^{1} f\left(y\right) \mathrm{d}y = \sum_{j} w_j f\left(y_j\right) , \tag{6.2}$$

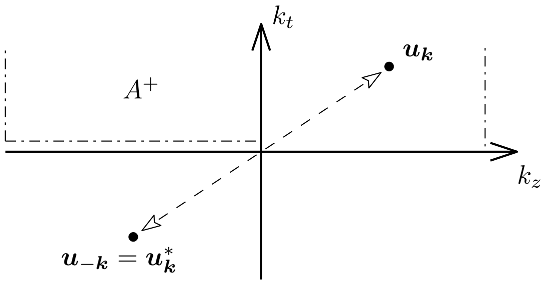

FIGURE 6.1: Diagram of the spectral plane, showing the subsets that make up the top half-plane. The bottom half-plane is Hermitian symmetric to the top half-plane.

where y_j is the wall-normal location of a point in the quadrature grid of the discretised domain, and w_j is the quadrature weight for that point determined through polynomial fitting of a given order. In this work, third order polynomials are used construct w_j.

We are free to choose the optimisation algorithm used for solving Equation 3.52 since any gradient-based method will work. Unless it is said otherwise, L-BFGS is the algorithm used here. L-BFGS is a quasi-Newton method, incorporating approximate Hessian information into each iteration, greatly improving the convergence properties of the optimisation near minima when compared to gradient descent. This is a particularly important aspect in this case, as the optimisation problem is highly non-convex, with many possible solutions potentially very close together. The problem is also generally quite poorly conditioned, mostly due to the influence of the Laplacian which has large effects on the high frequency components of the flow that decay away the most rapidly. The ability of L-BFGS to approximate the local curvature of the solution reduces the effect of this poor conditioning, where gradient descent is highly susceptible to it. This is demonstrated briefly in Section 6.2, where the convergence of each algorithm is briefly compared. Further in depth discussions on each algorithm can be found in Nocedal and Wright (2006). Any algorithm used here is also coupled with the Hager-Zhang line search algorithm as described in Hager and Zhang (2005). This further helps to improve convergence rates, albeit at the possibility of reducing the robustness of the total optimisation. In practice, however, this is not observed to be an issue.

When constructing the resolvent modes $\boldsymbol{\psi}_{ki}$, the laminar base profile is used, i.e. $\boldsymbol{u}_b = y\hat{\boldsymbol{\imath}}$, as this is simple, and provides a reliably calculable set of modes $\boldsymbol{\psi}_{ki}$ that are defined for all $\boldsymbol{k} \in \mathbb{Z}^2$. For the computation of the SVD the divide and conquer algorithm is used.

All of the above numerics are implemented in the Julia programming language, with all the code available on GitHub under the organisation The-ReSolver. Key packages used are FDGrids.jl (developed by Davide Lasagna) for the finite differencing, and the third party packages Optim.jl (Mogensen and Riseth, 2018) for solving the optimisation problem, and FFTW.jl (Frigo and Johnson, 2005), which is a set of bindings for the FFTW3 C library. Any validation is obtained relative to the solutions featured in Chapter 4, using the same DNS solver available on GitHub.

6.2 Exact Nonlinear Solutions

This section is dedicated to validating the ability for the resolvent-based optimisation to find exact solutions to the Navier-Stokes equations. This is demonstrated for both equilibrium and periodic solutions in Section 6.2.1 and Section 6.2.2, respectively. The majority of the solutions found are equilibria, with Section 6.2.2 demonstrating how the optimiser performs when applied to a periodic solution. The difficulties encountered with finding this periodic solution are discussed and are attributed partially to the computational difficulties that arise in the higher-dimensional case, and are otherwise speculated to be from other numerical and dynamical difficulties.

6.2.1 Equilibria

For all the equilibrium solutions presented in this section, the spanwise domain size is fixed to $L_z = 8$, to allow for sufficient space for the streamwise rolls identified in Chapter 4 to develop, at a Reynolds number of $Re = 50$ and Rotation number $Ro = 0.5$. Let N_y and N_z denote the number of points used in the wall-normal and spanwise directions, respectively. To begin, the optimiser is validated by its ability to reconstruct a known solution to the flow. This was obtained using the custom DNS solver, with a grid discretisation of $N_y = 64$ on a uniform grid, and $N_z = 32$

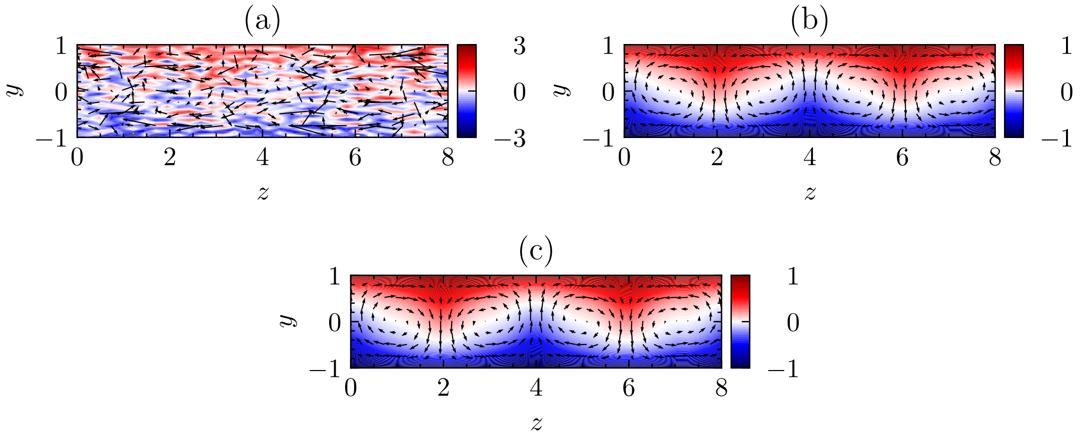

FIGURE 6.2: Snapshots of the flows before and after the optimisation at $Re = 50$ and $Ro = 0.5$, along with the solution obtained from DNS. Panel (a): the initial flow used for the optimisation, obtained by perturbing the stable solution obtained from DNS at the same Reynolds and Rotation numbers. Panel (b): the result of the optimisation with a residual of $\mathcal{R} < 10^{-12}$. Panel (c): the original solution obtained from DNS.

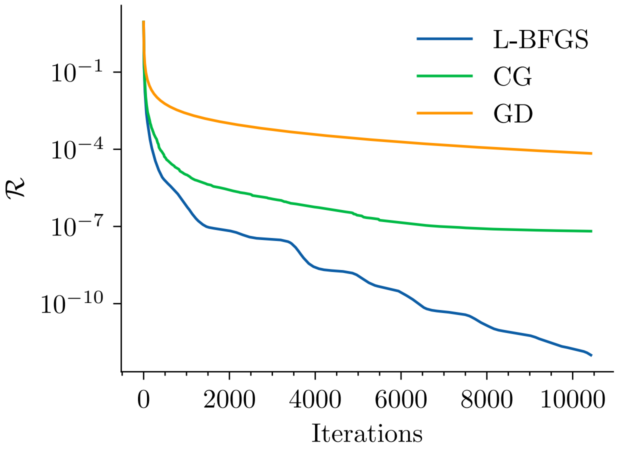

FIGURE 6.3: Residual trace for the optimisation of the initial flow given in Figure 6.2(a), using Gradient Descent (GD), Conjugate Gradient (CG), and L-BFGS optimisation algorithms. All solutions converge towards the solution obtained in Figure 6.2(b).

corresponding to 17 spanwise Fourier modes. No modes are discarded from the resolvent expansion in this case to ensure a full basis set for the wall-normal direction. This results in a full $M = 64$ being used in this case, where M denotes the number of resolvent modes. This gives the optimisation problem about 1000 degrees of freedom. The steady solution obtained from DNS is then projected onto this basis to obtain the corresponding coefficients a_{ki}. These coefficients are then perturbed with white noise, adding a random number roughly of the same magnitude as the largest coefficient at each frequency $\boldsymbol{k}$ and mode number i. This results in the highly disordered field shown Figure 6.2(a). Using L-BFGS, this initial perturbed flow is optimised to try to recover the original solution. The result of this optimisation is shown in Figure 6.2(b), with the solution originally obtained from DNS in Figure 6.2(c). It should be noted that the period was initialised to an arbitrary non-zero value as it has no effect of the computation.

The final solution obtained from the optimiser in Figure 6.2(b), labelled here as EQ1, is qualitatively indistinguishable from the original stable solution obtained from DNS, validating the optimiser's ability to accurately find steady solutions for this flow, when a full set of basis modes are provided for the modal expansion. For the sake of comparison, the same initial flow shown in Figure 6.2(a) was also optimised using the gradient descent and conjugate gradient algorithms. The traces for each algorithm applied to the initial condition in Figure 6.2(a) is shown in Figure 6.3. Clearly L-BFGS performs the best, achieving the residual of $\mathcal{R} = 10^{-12}$ after roughly 10000 iterations. Gradient descent displays an initial large decrease in residual which quickly decreases as the convergence rate slows. This slow convergence rate is ultimately due to the large separation in the eigenvalues of the Hessian matrix of the residual near the minimum, which leads to a poorly conditioned problem. Conjugate gradient also outperforms gradient descent, achieving a smaller residual for the same number of iterations, however, after the initial large decrease in the residual at the beginning of the optimisation, the convergence rate slows, approaching that achieved by gradient descent. In addition, the cost of each iteration of conjugate gradient is larger than L-BFGS. In sum, L-BFGS is able to achieve much lower residuals, several orders of magnitude over only a few thousand iterations, while each iteration can also be computed rather quickly.

One other note on what governs the convergence properties of the optimiser. As discussed in Section 5.4.1 the magnitude of the stability, or equivalently how far away a solution is from neutral stability, dictates how fast the optimiser can converge towards it. The closer the solution is to neutrally stable the slower the optimiser converges. This process continues to the limit of neutral stability where the optimiser effectively stalls some distance from the solution. With this in mind, it is clear that EQ1 is highly stable at the Reynolds number observed. The rest of the equilibria featured in this section are also far from neutrally stable, making all of their convergence rates relatively rapid.

To investigate the robustness of the optimiser to initial guesses, it was initialised with a varied set of initial conditions exciting certain spanwise wavenumbers with the intent of finding multiple new equilibrium solutions that are unstable in this Reynolds regime. Variational optimisation is guaranteed to converge to a minimum, unlike shooting methods, which are highly sensitive to initial conditions and can fail when the initial guess lies even moderately far from a root. These minima are very likely represent a solution due to the non-convex nature of the problem. The following results demonstrate that incorporating the Galerkin projection into the optimisation process has little to no impact on its robustness to initial conditions. While only a relatively small subset of possible initial configurations is presented here, it is

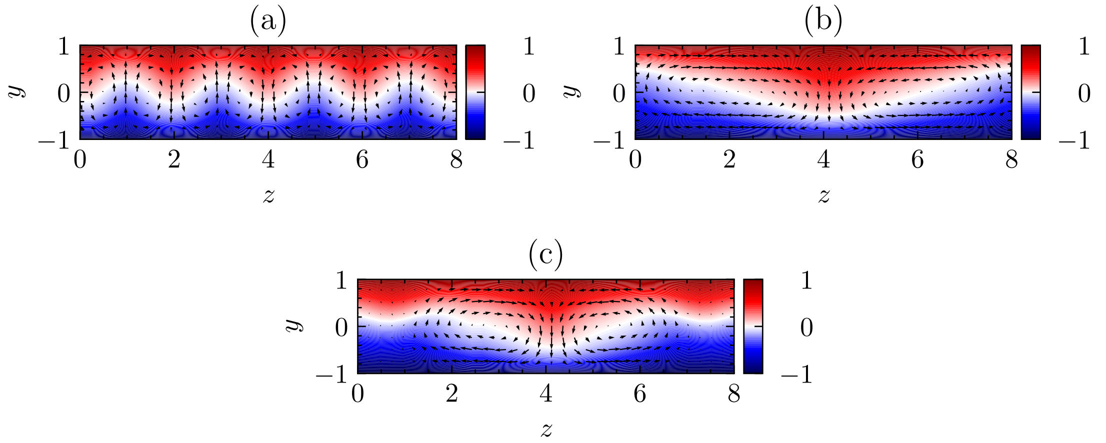

FIGURE 6.4: Final snapshots of the solutions obtained by optimising from various synthetic initial flow fields, each called EQ2, EQ3, and EQ4, for panels (a-c), respectively. The optimisations were performed at $Re = 50$ and Ro, with each residual obtaining $\mathcal{R} < 10^{-12}$.

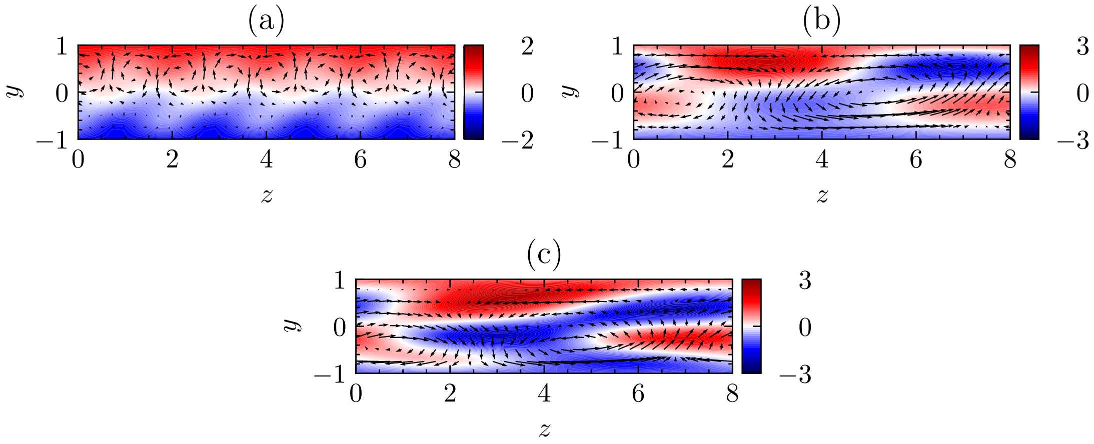

FIGURE 6.5: Initial guesses for the unstable equilibrium solutions shown in Figure 6.4, with each panel labelled to correspond to the given solution in the first figure.

noteworthy that a minimum was found for every combination of initial modes tested. In most cases, this minimum corresponded to a global solution, with the residual satisfying $\mathcal{R} \approx 0$. Each initial condition was optimised using the L-BFGS algorithm, and convergence was deemed to have been achieved once $\mathcal{R} < 10^{-12}$, and a full set of 64 resolvent modes were used for the projection. The result of these optimisations is shown in Figure 6.4, and the initial guesses for the flows shown in Figure 6.5. Figure 6.4(a) was initialised with the first 5 modal coefficients a_{ki} excited with random values at the spanwise frequency of $k_z = 4$, corresponding to streamwise rolls with half the wavelength of EQ1, with the rest of the coefficients left as zeros. This converges to the unstable equilibrium, called here EQ2, with a very similar streamwise roll pattern observed in EQ1, but with half the spanwise wavelength. EQ2, as well as the rest of the equilibria shown here are referred to unstable due to the fact that they are not observed in standard DNS. If instead the first 5 modal coefficients are excited randomly for the spanwise frequency $k_z = 1$, the solution in Figure 6.4(b) is found, called here EQ3. This solution again has the streamwise roll expected from these relatively simple solutions, but now with twice the spanwise wavelength. The highly symmetric structures of EQ2 and EQ3 closely mirror the solution of EQ1 and are ultimately expressing the same dynamics. To obtain a slightly more atypical solution, a solution that displays something other than regularly spaced rolls, the flow was initialised by exciting the first 8 resolvent modes at the steady ($k_z = 0$) and first unsteady ($k_z = 1$) spanwise frequencies with random values. The result of optimising such an initial condition is shown in Figure 6.4(c), called here EQ4. EQ4 shows a streamwise roll pattern with a width larger than in EQ1, roughly 3 spanwise units in length. This roll does not repeat over the remaining length of the domain since there is not sufficient room. Instead, the flow remains mostly stagnant in the remaining space, only expressing some very weak rolls that transports a small amount of the momentum from the top wall downwards. The equilibria EQ2, EQ3, EQ4, are all unstable. This instability was established rather crudely by taking the output from the optimiser and feeding it into the DNS solver as an initial condition. After a finite amount of time all of the solutions were observed to break down into transients that eventually decayed back to the stable solution EQ1.

It was found that if optimisations were initialised with fields that contain large excitations in exclusively high spanwise frequencies, then the optimiser would not converge to some equilibrium with dominant rolls at a similarly high spanwise frequency, instead converging towards laminar or lower spanwise frequency solutions. This is not too surprising, due to the fact that higher frequency oscillations in spatial directions decay rapidly, requiring stronger nonlinear interactions to sustain them. Since all these solutions exist at the same Reynolds numbers, the energy required to sustain some of the higher frequency structures is not present in the total energy budget of the flow, making them more unstable when compared to lower frequency oscillations. This reasoning implies that either equilibrium solutions containing smaller rolls are extremely unstable and thus have a small basin of attraction for the optimiser, or equilibrium solutions containing smaller rolls do not exist at all for the given Reynolds number. The link between the basin of attraction and the stability characteristics of a particular equilibrium are going to be quite complex, and are not investigated in depth here.

The bifurcation structure that lead to EQ2, EQ3, and EQ4 arising were not investigated in any depth in this work. Primarily this is a result of time constraints on the project. Some small exploration was performed with EQ2, continuing it backwards with Reynolds number. It was found to arise after EQ1, likely as a result of a secondary instability at the higher spanwise frequency. It is speculated that all the equilibrium displayed here arise in the same way at various Reynolds numbers.

The spanwise power spectrum of EQ2 is shown in Figure 6.6 at iteration 20, 1000, and 8000 of the optimisation. The initial field used for the optimisation was excited at

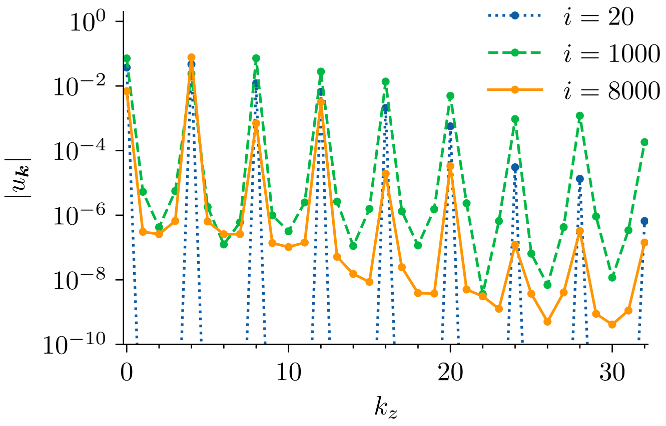

FIGURE 6.6: Spanwise power spectra of EQ2 of the solutions obtained at specific iterations of its optimisation, sampled at the channel midpoint ($y = 0$).

exactly one spanwise frequency, $k_z = 4$, and over the duration of the optimisation the spectral information is spread out over the domain. The optimiser initially increases the spectral power at the harmonics (and mean) frequencies to the dominant base at $k_z = 4$ as can be seen at iteration $i = 20$. This is then followed by a rather long process of refining, spreading out the signal to be slightly more broadband in nature, gradually reducing the residual as the final solution is sought. The takeaway from this is that the optimiser is rather quick to correctly identify the larger scale (lower frequency) structures, which leads to the large initial decrease in the residual observed in Figure 6.3, after which the optimiser goes through a much slower process of finely tuning the balance of the interactions between all the frequencies, gradually damping out higher frequency oscillations.

6.2.2 Periodic Orbits

This subsection presents a brief set of results demonstrating the optimiser solving for a periodic solution. The optimiser is tasked with generating a periodic solution at $Re = 450$, a regime where RPCF displays a stable periodic motion as shown in Chapter 4. The flow is discretised with $N_y = 128$, $N_z = 101$ corresponding to 51 spanwise modes, and $N_t = 51$, and set of $M = 128$ resolvent modes for each Fourier mode are used for the optimisation. This corresponds to a much larger problem with roughly $300,000$ degrees of freedom. To slightly reduce computational cost, the spanwise domain has been halved such that $L_z = 4$. This assumes that the dominant streamwise structures repeat twice over the domain and there are no important larger scale structures that are neglected with this change. To initialise the optimisation, the stable periodic solution obtained via DNS at $Re = 400$ is injected with noise by randomly perturbing the coefficients a_{ki} as done in the case for finding equilibrium

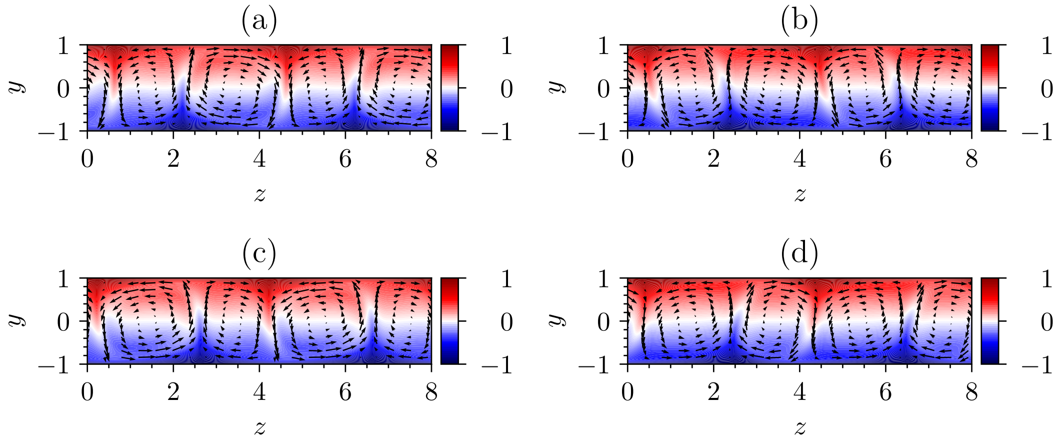

FIGURE 6.7: Snapshots of the periodic solution ($\mathcal{R} \approx 5 \times 10^{-10}$) obtained for $Re = 450$ with a period of $T \approx 25.41$, for times of $t = 0$, $T/4$, $T/2$, and $3T/4$ in panels (a-d), respectively.

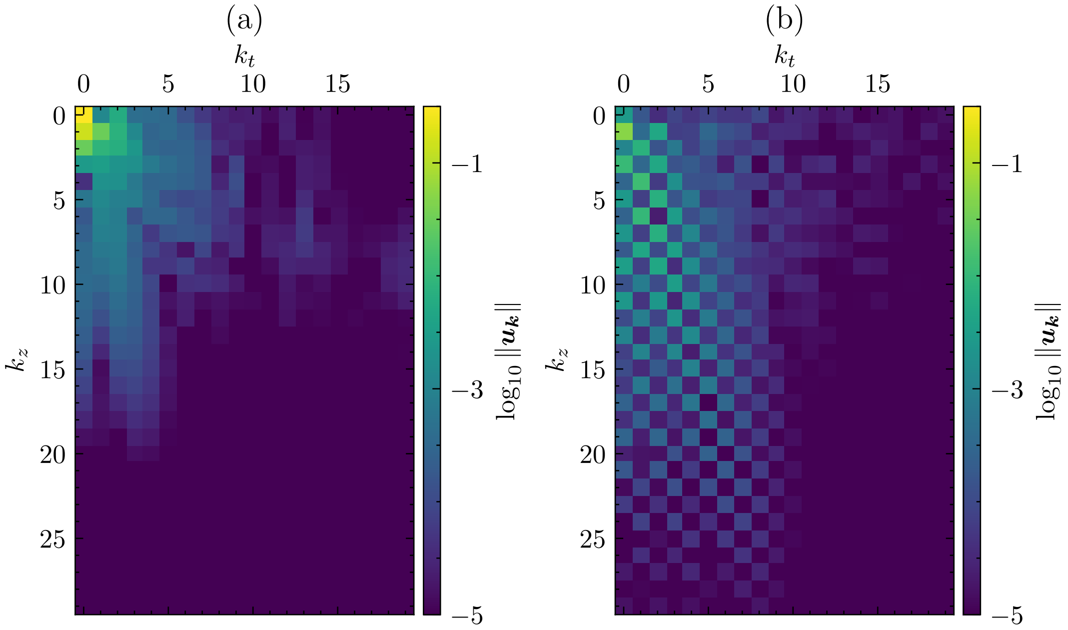

FIGURE 6.8: Spanwise and temporal power spectrum of the periodic solution in Figure 6.7 at $y \approx -0.86$ in panel (a) and $y \approx 0$ in panel (b). Only a slice of the spectrum is shown, showing only the lower spanwise and positive temporal modes.

solutions. The period was initialised by performing a spectral analysis of the solution from the DNS solver. The spectral analysis was a simple Welch periodogram, from which the fundamental mode frequency was used to determine the period of the flow. This analysis yielded a initial period of $T = 24.5$. It was observed that the permitted perturbation to the original field had to be notably smaller than for the optimisation of equilibrium solutions. If the perturbation of the DNS field was too large then the optimiser would converge to a periodic orbit that is not particularly close to the stable periodic solution observed from the DNS at the given Reynolds number. It is a feature of the variational optimiser that it is guaranteed to converge to some minimum after enough iterations, not accounting for possible numerical errors. This can either be a global minimum, corresponding to an exact solution of the Navier-Stokes equations, or a local minimum with a non-zero residual. Local minimum could have no physical significance, or they could represent so-called ghost solutions discussed in Zheng et al. (2024). These are solutions that have undergone a saddle-node bifurcation and so are no longer solutions to the Navier-Stokes equations, but nonetheless have an impact on the local dynamics. The bifurcation structure of RPCF at the Reynolds numbers shown is not investigated in any detail here, and it is not known if saddle-node bifurcations populate the state-space and have large effects on the behaviour of the optimiser.

Shown in Figure 6.7 are a set of snapshots for the periodic solution obtained at $Re = 450$, sampled at points along its trajectory. Note that for the sake consistency the domain has been extended back to $L_z = 8$ for plotting Figure 6.7. This has the effect of shifting the dominant spanwise frequencies. For EQ1, which had $L_z = 8$, every other

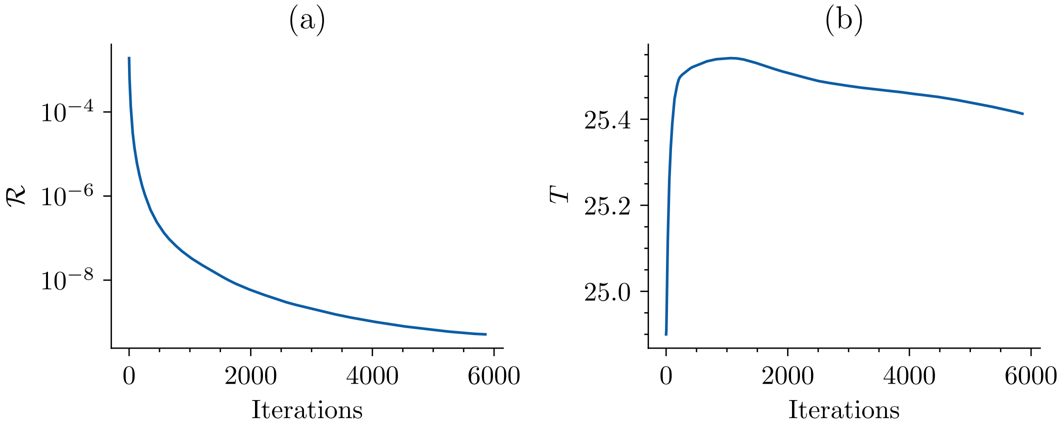

FIGURE 6.9: Traces of the global residual in panel (a), and the solution period in panel (b), of the periodic solution in Figure 6.7 over the duration of the optimisation.

the spanwise frequency sampled in the discretisation has a very small proportion of the energy due to the repeating nature of the simulated structure. Restricting the spanwise length to $L_z = 4$ removes these very small frequencies and retains only the more dominant structures, as a result of the domain size now matching size of the dominant modes of the solution. The primary streamwise rolling structures are clearly present, now evolving in a wavy motion as consecutive vortices contract and expand. Figure 6.8 shows the spectrum of the periodic solution in Figure 6.7 sampled at two wall-normal positions: $y \approx= -0.86$ and $y \approx 0$. The spectrum shown is a slice of the total spectrum, only showing the lower spanwise modes and the positive temporal modes. The higher frequency modes were cut-off due to them contributing an extremely small portion of the flows total energy, and the negative temporal modes are ignored due to them being symmetrical with the positive temporal modes (up to numerical discrepancies). If there was an imbalance in the positive and negative temporal frequencies this would be represented in the solution as apparent travelling waves moving in either direction. Since there is no mean energy input into the flow in the spanwise directions any solution must display this balance between the positive and negative temporal frequencies. A chequerboard pattern is observed in the spectrum near the centreline of the flow, which represent the presence of the oscillating “tails” on either side of the vortices in Figure 6.7. The most energetic mode is located at $(k_z, k_t) = (1, 0)$ which is mode that best fits the streamwise rolls that do not vary significantly with time. The spectrum at the location nearer the wall has a more continuous decay.

As mentioned earlier, in obtaining this solution, the optimiser was found to be rather sensitive to the initial guess for the flow. Only a relatively small perturbation from the original DNS data, compared to the equilibrium solutions, was permitted to allow the optimiser to converge to the desired periodic solution. If the perturbation was too large then the optimiser would begin to converge to a different solution. The trace of the global residual and flow period are shown in Figure 6.9(a-b), respectively. The

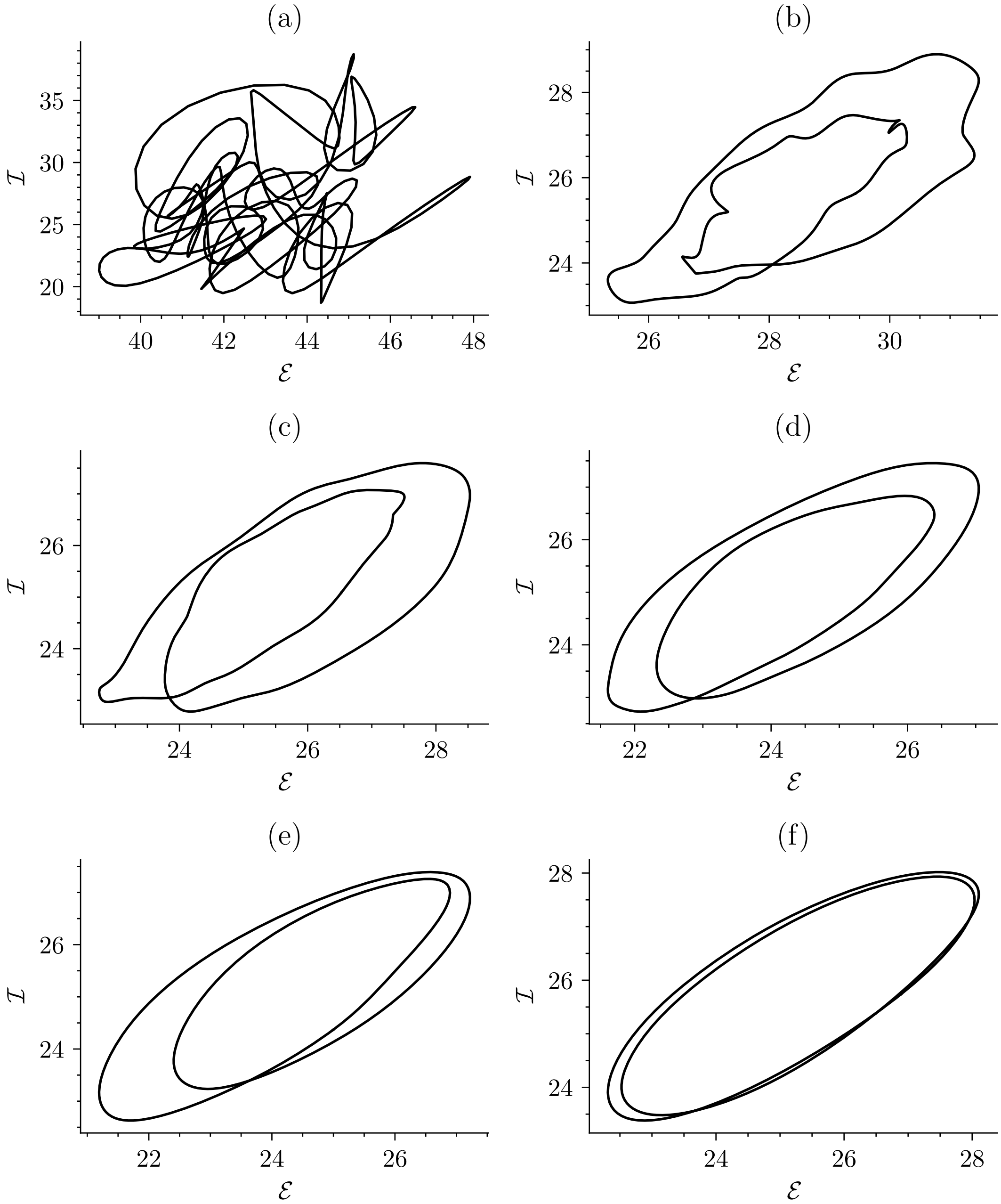

FIGURE 6.10: Energy dissipation and production of the solution shown in Figure 6.7 shown over the course of the optimisation, showing iterations 0, 100, 200, 500, 1000, 5800 in panels (a-f), respectively.

residual of this solution is $\mathcal{R} \approx 5 \times 10^{-10}$, slightly above the convergence threshold used for the equilibrium solutions in the previous section. The initial rapid decrease in the residual is observed, with the convergence rate decreasing gradually as the optimisation continues, with the addition that the lowest residual that can be achieved is not as small as for the simpler equilibrium solutions. An obvious first justification for the degraded performance compared to the equilibria shown earlier, is the possibility of the periodic solution being sought is only marginally stable. Although no in-depth analysis was performed to establish this, it was found through analysis of the DNS data that the solution is as stable as the equilibrium, with a characteristic decay time on the order of thousands of time units. This could be a result of the solution shown in Figure 6.7 representing a ghost solution, a state-space featured commented on in Zheng et al. (2024). It is also possible that the difficulty in the convergence for periodic solutions is a result of the modes being used either not completely spanning the required space or carrying some numerical defects that introduce small errors that manifest near the global residual minimum. It was observed that the modes generated for the low to moderate temporal and spanwise frequencies for the periodic case had large numerically induced oscillations in their second derivatives. This is possibly a result of the base flow used, the specific grid discretisation used, or a near singularly issue when computing the SVD of the resolvent operator. This property should be investigated further to determine their effect on the convergence rate and accuracy of the final solution. Further evidence that the solution has not completely converged to the minimum is that the period in Figure 6.9(b) is not displaying convergence towards a particular value. Figure 6.10 shows the energy dissipation and production of the periodic solution found at $Re = 450$ over the duration of the optimisation. Shown specifically are iterations 0, 100, 200, 500, 1000, 5800 in Figure 6.10(a-f), respectively. The optimisation is initialised with a noisy signal which has a significant amount of small scale perturbations, which explains the large dissipation in the initial field shown in Figure 6.10(a). The optimisation initially drastically decreases the dissipation and brings the energy production from the walls into the same range. The rest of the optimisation time is spent gradually smoothing out the trajectory modifying it into a double loop. This means the first 100 or so iterations are primarily spent balancing the integral energies of the flow and damping out the small scale noise. A large amount of time after this is dedicated to making smaller modifications to the trajectory as it approaches the desired global minimum. Figure 6.10(f) shows the final energy trajectory obtained by the optimiser. It can be seen that the double loop is not perfectly repeated as would be expected by the symmetry of the solution in time. This further implies that the final solution obtained by the optimiser is not completely converged.

Several attempts were made to improve convergence and reduce the residual in the optimisation of periodic flows. These are not detailed here, as none yielded a meaningful improvement in performance. One approach involved modifying the period gradient: it was excluded from the optimisation for the first few thousand iterations, allowing the flow to settle before the large changes in the predicted period—such as those seen in Figure 6.9(b)—could dominate. When the period gradient was later introduced, it was scaled by a relaxation factor in an attempt to dampen these fluctuations. An additional trial involved removing the period gradient entirely. While damping the gradient led to a slightly smaller residual, the improvement was marginal and did not significantly mitigate the stagnating convergence, especially when compared to the optimisation of equilibria. A separate

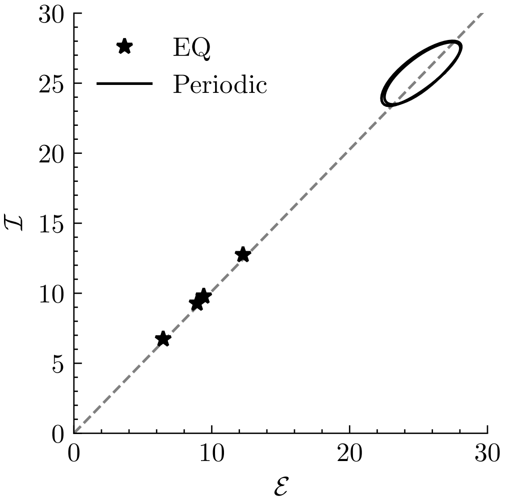

FIGURE 6.11: Energy dissipation and production of the all the solutions shown in preceding section, with the stars ($\star$) representing the equilibrium solutions at $Re = 50$, the solid line displaying the periodic solution of Figure 6.7, and the dashed line representing $\mathcal{E} = \mathcal{I}$.

stable periodic solution was also identified at a lower Reynolds number, $Re = 120$, with the expectation that a coarser grid and simpler dynamics might improve optimisation performance. However, similar trends were observed: the residual plateaued, and the period changes substantially without converging to a fixed value before termination. The primary obstacle to further investigation of these issues is the high computational cost of the optimisation process, as discussed at the end of Chapter 3, along with limited time and resources. In future work, a more efficient implementation would enable a more comprehensive investigation into the difficulties associated with optimising periodic flows.

To conclude this section, Figure 6.11 displays all the equilibria and periodic solutions showcased in this work, projected onto dissipation energy and energy input from the boundary. The equilibria, represented with stars, are located on the equilibrium line $\mathcal{E} = \mathcal{I}$. The periodic solution of Figure 6.7 is displayed as the line that oscillates around the equilibrium line. The solution actually loops over the same trajectory in energy dissipation-production space twice, with the second loop representing the same solution to the first loop reflected along the spanwise direction. So, in a sense the periodic solution, and generally the underlying periodic motion of this periodic solution to RPCF are described by only half the period of the solution, with the other half prescribed by a symmetry transformation. This is called a Pre-Periodic Orbit (PPO) and is type of solution that could be found if the discrete and continuous symmetries of the system are taken into account. Relative Periodic Orbits (RPOs) are another example of a type of solution that can only be found if these symmetries are incorporated into the optimisation. In its current implementation it is not possible to find these types of solutions since the optimiser does not explicitly take into account

Solution	Re	L_z	T	M	N_y	N_z	N_t	$\overline{\mathcal{E}}$	Stable?
EQ1	50	8	-	64	64	32	-	12.267	Yes
EQ2	50	8	-	64	64	32	-	9.4185	No
EQ3	50	8	-	64	64	32	-	8.9345	No
EQ4	50	8	-	64	64	32	-	6.4772	No
PO	450	8	~ 25.4	64	64	32	51	25.747	Yes

TABLE 6.1: Summarised properties of the equilibrium and periodic solutions obtained in Section 6.2.

any extra symmetries of the flow. It is possible to find travelling wave solutions (also known as relative equilibrium), however none were found for this flow in practice. It is not especially difficult to include this, however, as it simply includes an extra set of variables representing the permutation of the flow under the investigated symmetries. This is particularly important to include for certain flows, such as the 2D Kolmogorov flow, since the vast majority of the solutions that appear to populate the state-space are RPOs (Chandler and Kerswell, 2013). To flow properties and simulation parameters for each of the solutions shown in this section are given in Table 6.1. Note that the final period quoted in Table 6.1 is included as rough estimate as a result of the final output of the optimiser not being completely converged.

6.3 Effect of Mode Truncation

The results discussed up to this point have utilised a full set of basis modes; the number of modes used has been equal to the number of points used to discretise the wall-normal direction. As discussed in Section 3.5 the projection onto the set of modes $\boldsymbol{\psi}_{ki}$ does not have to include a set that spans the entire function space. By rejecting the resolvent modes associated with the smaller singular values of the resolvent operator a low-order model is constructed. If the remaining modes are particularly effective, in the sense that they point mostly in the same direction as the given solution, then an accurate reconstruction can be obtained using only a small subset of the total number of available resolvent modes. This idea is supported by the analysis in Section 4.3.2 which showed at the Reynolds numbers considered here that most of the dynamical information is contained in the higher-ranked resolvent modes. In this analysis the number of spanwise Fourier modes are not changed from the solution obtained in Section 6.2.1.

The application of this methodology is shown in Figure 6.12, where the EQ2 solution was perturbed by adding some random noise to the coefficients a_{ki}. The solution was perturbed enough to move it off the minimum, increasing the residual to a much larger value than the convergence criterion used here of $\mathcal{R} < 10^{-12}$, but not so much as to prevent the optimiser from converging towards the same solution. This perturbed EQ2 flow was then optimised retaining a truncated set of the resolvent modes for all frequencies, denoted as M. Here, as before, 64 resolvent modes represent a complete basis, without any dimensionality reduction taking place in the state-space. The results are shown in Figure 6.12.

Figure 6.12(a) shows the global residual traces for the perturbed field using 8, 16, 32, and 64 resolvent modes. The residuals for each case reduce initially at a relatively large rate, indicating the power of the variational optimiser to quickly seek out the solution primarily by modifying the large scale structures. This initially fast decrease is followed by a slower convergence rate, as is typically observed in the literature. The primary point to note from Figure 6.12(a) is that the degree to which the convergence rate decreases, and after how many iterations is strongly linked to the number of modes used for the Galerkin projection. The smaller the number of modes used, the faster the overall convergence rate is, achieving the minimum residual orders of magnitude faster than when more modes are retained. Specifically, the case of $M = 64$ resolvent modes achieved its final residual after roughly 10^5 iterations, whereas the $M = 8$ case shows the same residual after only hundreds of iterations. It should be noted that an immediate result of truncating the resolvent modes is to reduce the global residual of the initial field. This is a result of the noise introduced in the perturbation of EQ2 being truncated in the projection, reducing the smaller scale noise present in the starting flow. Any relative effects on the residual, i.e. normalised with respect to the norm of the velocity field, is similar to that shown. This can be understood by the fact that the truncation restricts the dynamics to a low-dimensional state for the larger scales of the flow. These scales are the energy containing scales of the flow and so the norm of the velocity field in this restricted subspace is only changed by a small amount relative to its total magnitude. The residual, however, is

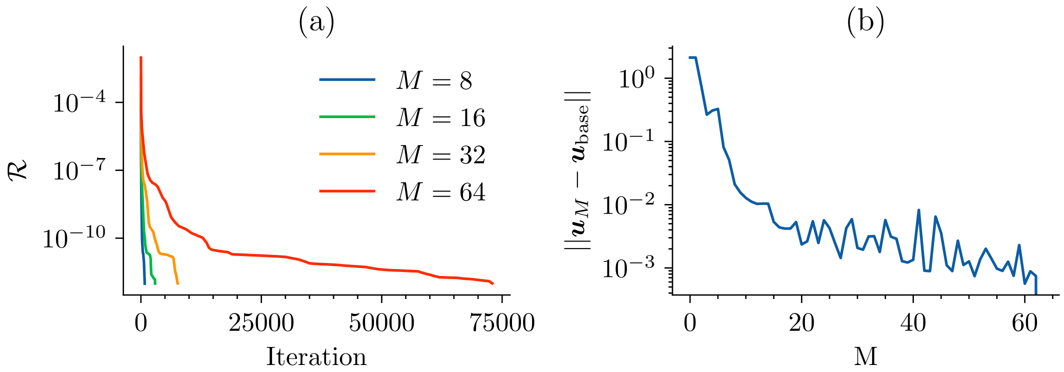

FIGURE 6.12: Panel (a): global residual traces for the optimisation of a perturbed EQ2 solution, performed using $M = 8$, 16, 32, and 64 resolvent modes, all starting from the same initial flow, using the L-BFGS algorithm. Panel (b): Accuracy of the resulting solutions found by the optimiser relative to the “base” case obtained for 64 resolvent modes, plotted against the number of modes used for the projection, each solution being converged such that $\mathcal{R} < 10^{-12}$.

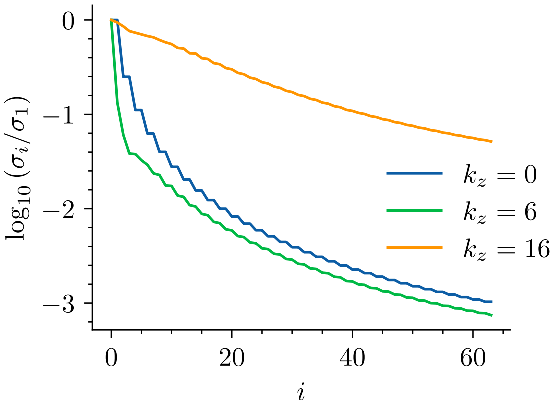

FIGURE 6.13: Singular values of the resolvent operator with a laminar base flow for a select number of spanwise frequencies at $Re = 50$ and $Ro = 0.5$.

far more sensitive to the small scale structures that are represented by the modes that are being truncated. This means that the relative effect on the residual from truncating these modes is large, removing a large number of directions from the optimisation space where the residual can grow or shrink rapidly. This is ultimately the argument that is made for why the convergence rate improves as the number of modes used decreases, discussed further at the end of this section.

Figure 6.12(b) shows the accuracy of the resulting solutions obtained from the projected optimisations plotted against the number of modes used for the Galerkin projection. The accuracy was computed as the norm of the difference between the field obtained from the projected optimisation, denoted as $\|\boldsymbol{u}_M\|_\Omega$, and a base solution, denoted as $\|\boldsymbol{u}_{\text{base}}\|_\Omega$, which is the solution obtained using the full set of resolvent modes, i.e. $M = 64$. As the number of modes used for the projection is increased, the error between the obtained solution and the base case reduces quite quickly initially, when the number of modes used is small, but then reducing more slowly and stagnating at around $\|\boldsymbol{u}_M - \boldsymbol{u}_{\text{base}}\|_\Omega \approx 10^{-3}$ at roughly $M = 30$. The initial decrease in the error is a result of the added modes having a relatively large contribution to the solution EQ2. After roughly 30 resolvent modes are being used, however, the accuracy cannot be improved further as the rest of the modes that could be used contain an extremely small component of the overall energy of the solution. To be specific, the first 30 resolvent modes contain a little over 99.9% of the total solution's energy. In fact, by only retaining the first 4 resolvent modes, over 90% of the solution's energy is retained, implying an aggressive reduced order model can be used to construct a physically significant solution while sacrificing some of the total accuracy.

The reason the error between the projected solution and the base case using the full set of modes does not decrease monotonically to zero is primarily a result of the complicated route taken by the L-BFGS algorithm over the duration of the optimisation. The truncation slightly alters the initial condition, which leads L-BFGS

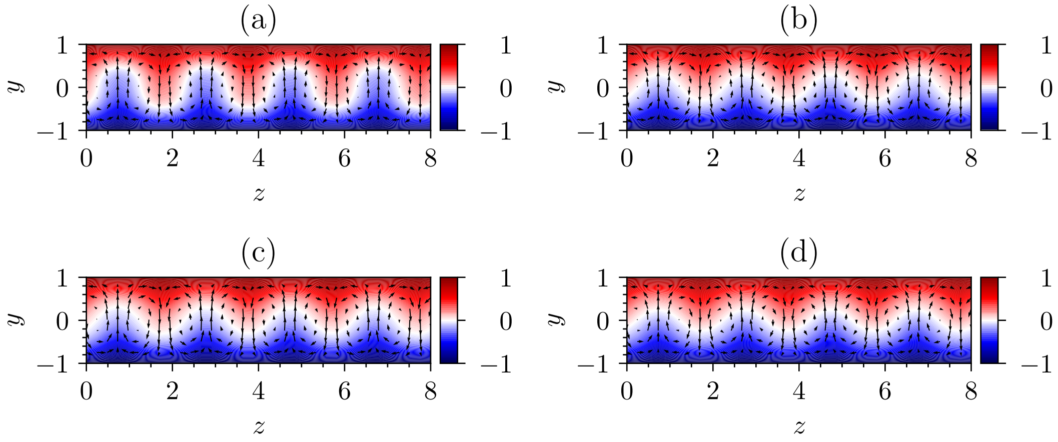

FIGURE 6.14: Snapshots of the solutions obtained from the projected optimisation of the perturbed EQ2 solution, for $M = 3, 4, 5, 64$ in panels (a-d), respectively.

to take different routes to the minimum representing the solution EQ2. Thus, although the solutions obtained using the higher number of modes are all very similar, the only way to decrease the error is to use a smaller residual as the criterion for convergence. This conclusion is supported with Figure 6.13, where the singular values of the resolvent operator used to generate the modes used for these optimisations are shown for a select set of spanwise frequencies. The spanwise frequency $k_z = 0$ correspond to the spanwise mean, with the other non-zero frequencies being the unsteady spanwise motions of progressively smaller wavelength. It can be seen that a large decay of over two orders of magnitude takes place for $k_z = 0$ and $k_z = 7$ within the first 30 singular values. For the largest frequency shown, corresponding to the largest spanwise frequency used in the optimisation, has a much slower decay rate. This, however, does not have a large effect on the accuracy of the solution obtained from the optimisation since the small scale structures that would be represented with these structures play a very small role in the solution to EQ2. Thus, by truncating roughly half the modes in the SVD of the resolvent sacrifices only a small amount of the structure of the resolvent and thus allows for accurate reconstructions of the desired solution.

This view of the error of each projected solution is reinforced by Figure 6.14, where the snapshots of the solutions obtained using $M = 3$, $M = 4$, $M = 5$, and the base case $M = 64$ are shown in panels (a-d), respectively. Each solution displays the desired streamwise rolls with the correct spanwise wavelength. The solution obtained for $M = 3$ has noticeable qualitative differences from the base solution, which is expected from the error shown in Figure 6.12(b) being $\mathcal{O}(1)$. However, the solutions obtained for $M = 4$ and $M = 5$ are far more similar to the base solution, despite the error shown in Figure 6.12 still being rather large. Taking the results of Figure 6.12 and 6.14 together, as long as a sufficiently small number of modes are retained for the projected optimisation the solution obtained will be able to reconstruct the structures of the desired solution rather faithfully, at the cost of the true accuracy of the final output, but with a significantly improved convergence rate. This allows for a trade-off, if only the very large scale structures of a solution are sought, without having to worry too much about the ultimate accuracy of the solution, then by aggressively truncating the number of modes used this solution could be obtained far faster than otherwise available. This could be used as a method to initialise searches for ECS, using a truncated set of modes to quickly reduce the residual. Once the largest structures are resolved, the number of modes could be increased to better capture the smaller scale structures once the largest ones are resolved, similar to the iterative methods described in Rosenberg and Mckeon (2019) used to construct approximations to ECSs based on the leading resolvent modes. This could achieve the best of both worlds, exploiting the improved convergence rate of the truncated set of modes at first while still being able to resolve the finer structures as required later on in the optimisation. The output could also be passed to the Newton-GMRES-Hookstep method to quickly finish the convergence following more closely to the procedure in Farazmand (2016).

The primary reason for this large difference in convergence rates related to the number of modes used for the projection is a result of the modes working similar to a preconditioner for the optimisation, improving the conditioning of the Hessian matrix. The higher order modes, $\boldsymbol{\psi}_{ki}$ for larger i, are associated with larger oscillations in the wall-normal directions and are thus generally associated with higher frequency and smaller scale motions in the flow. By removing these modes from the projection the flow is effectively restricted to building the best possible solution using only larger scale structures, typically the structures that have the largest share of the kinetic energy of a given flow. In addition, the higher frequency variations in the flow have a disproportionally large effect on the residual, where increases in coefficients a_{ki} results in a larger increase in the residual for larger $\boldsymbol{k}$ and i. This ultimately is a consequence of the Laplacian/diffusion terms in Equation 3.6 and Equation 3.43. It is well known the spectra of the Laplacian results in large effects for high frequency inputs, which physically is a consequence of more localised disturbances diffusing into the surrounding fluid at a faster rate. This effect becomes dominant for the higher order modes, and so the resulting residual function can be relatively poorly conditioned; the Hessian at the minimum will have a large condition number as a result of the vastly different growth rates of the residual in lower and higher frequency directions, respectively. Truncating the number of modes used, therefore, removes the directions with larger growth rates from the residual, improving the conditioning of the optimisation problem and increasing the convergence rates. The effect of modal truncation can be summarised as follows. By removing modes that correspond to structures with a disproportionately large effect on the residual, both the optimisation and the underlying dynamics are confined to a smaller subspace. This reduced subspace is typically better conditioned, while still retaining the majority of the energy-containing structures from the full system. As a result, the optimiser can converge more rapidly to a local minimum that often lies close to the global minimum of the full-dimensional problem. The accuracy of this result ultimately depends on how well the resolvent modes represent the true solution within the full state space.

6.3.1 Cost of Computing Solutions

The algorithm as depicted in Figure 3.4 transforms the velocity and residual fields between full and reduced space. Therefore, when it comes to computing invariant solutions this methodology does not provide a speed-up for each iteration as extra time is required to perform the projection and expansion computations. It is possible to formulate the optimisation problem completely in reduced space. This approach would omit the requirement for expanding the modal coefficients back into the full field. There are a couple of downsides to this approach. The first is due to the modes not being known a priori requiring the projected operators to be pre-computed, trading the speed gained in not transforming between spaces for the extra memory requirements of storing the projected operators, which for high-dimensional systems can be very expensive. The second problem stems from nonlinear terms, which when computed in reduced space resemble a nested set of convolutions over the resolvent and Fourier modes. This computation scales poorly with the number of modes in all directions, which means for any application of the method to even moderate Reynolds numbers would be much slower than the corresponding “fast convolution” approach utilising the transformations between spaces. These reasons outlined are the primary reasons why the algorithm is designed as it is. As shown in the previous section, even if the time per iteration is not any faster for the resolvent-based optimisation the total optimisation time can be greatly reduced through the improved conditioning afforded through the projection.

The scaling behaviour of the time required to perform the variational optimisation is discussed in Section 5.4.2. As previously noted, the efficiency of the methodology outlined in Chapter 3 is only fully realised when substantial dimensionality reduction is achieved. This reduction not only lowers the computational cost of the projection and expansion steps but also significantly decreases the number of iterations required to reach convergence—potentially by orders of magnitude. For example, the optimisations used to produce the results in Figure 6.12 took approximately one hour to complete for the base case with $M = 64$ modes, but only a few minutes when reduced to $M = 8$ modes. Storing the modes is the dominant factor in terms of the memory cost of the algorithm. Holding all the modes in memory for manipulation can become very costly for high Reynolds number problems where all the spatial and temporal discretisation become finer and the number of modes required for each frequency generally increases as well. With each element of the modes being a 128 bit complex number the total cost of storing the modes used for the periodic case in memory is already nearly on the order of gigabits. For turbulent problems the required memory can grow very quickly, severely limiting the maximum number of modes that can be used to represent the flow. Alternatively the modes could be read directly from the disk as they are needed which comes at a clear penalty for the speed of execution. The best solution here would not be to not have to use the modes at all during the optimisation, instead performing all the computations in the reduced space directly on the coefficients a_{ki}. A more in depth of a discussion on this alternative implementation can be found in Chapter 7.

6.4 Summary

In this chapter, a number of exact solutions to RPCF are generated using the resolvent-based variational optimisation methodology described in Chapter 3. The method is shown to be robust to initial guesses, retaining this desirable property from the general adjoint solver methodology (Farazmand, 2016). In addition, it was shown that by seeding the initial guess for the flow with energies in select modes corresponding to certain structures, the optimiser can be guided to converge to solutions with particular features. The methodology is demonstrated for equilibrium solutions and a periodic solution. It was found to be more difficult to converge the periodic solutions, with the optimisation terminating before the residual has converged, and not displaying the same linear convergence observed for the optimisation of equilibrium solutions. The reason for the difficulties with periodic solutions are postulated to be from a few possible sources. The first reason for the weaker convergence could be a direct result of the optimisation problem being larger. The extra temporal dimension that does not have to be considered for equilibria, increasing the size of the problem by many orders of magnitude, in addition to the finer discretisation required to resolve the flow at the higher Reynolds number. The second is the periodic solution presented may be better understood as a ghost of a periodic solution that exists at a different Reynolds number (Zheng et al., 2024). The final possible source of error is the choice of modal basis, by either not providing the necessary basis to completely describe the solution in the limiting infinite-dimensional state-space, or from numerical errors stemming from its computation and the choice of grid. Further work is required to properly understand the source of these difficulties.

A particular equilibrium solution found earlier was then projected onto a truncated set of resolvent modes to demonstrate the effect that the low-order model has on the accuracy of the resulting solution and to see if it modifies the convergence rates of the optimisation. It was shown that truncating the resolvent modes leads to a significantly improved convergence rate, reducing the number of iterations required to achieve convergence by over an order of magnitude. The improved convergence is a result of a pre-conditioning effect rejecting the modes has, reducing the condition number of the Hessian matrix of the residual by damping the large growth rates of rapidly varying modes associated primarily with the Laplace operator. The accuracy of the resulting low-order solutions compared to the base case (using the full basis set) is shown to be very accurate with the total energy of the flow being recovered up to three decimal places for ~ 30 resolvent modes. Additionally, it was shown that the qualitative resemblance of the very low-order solutions was very good, displaying the ability for the method to be used as a way to accelerate the search of invariant solutions through a coupled approach akin the method used in by Farazmand (2016), or through a type of multigrid method that gradually includes more modes building up flow complexity and accuracy as the residual decreases.

Chapter 7

Conclusions

This chapter is dedicated to a summary of the work presented in this thesis and how well it satisfies the main aims discussed in Chapter 1. In addition, there are added discussions on the main limitations of the methods used, where the presented results indicated difficulties in obtaining accurate solutions, and a list of future work that can be performed based on the foundation laid out in this work.

The thesis focused on a novel application of the variational optimisation solver developed by Farazmand (2016) and Azimi et al. (2022) coupled with a Galerkin projection onto a basis defined by a set of modes obtained from resolvent analysis. The method described in Chapter 3 is a novel approach to solve the problem that arises due to the coupling of the incompressibility condition (pressure) and the no-slip boundary condition. Ashtari and Schneider (2023) described another possible solution to the problem, using the influence matrix method to update velocity to be compatible with the pressure boundary conditions. The method as shown in Ashtari and Schneider (2023) only applied to equilibrium solutions, whereas the method described in this thesis is applicable to periodic solutions with any complex wall-bounded geometry, while allowing direct utilisation of the compression abilities of modal analysis techniques as discussed in Section 2.2. Using this projected variational optimisation methodology, the thesis aims as given in Chapter 1 were as follows.

1. Assess the efficacy of resolvent modes for constructing low-order models of RPCF.
2. Demonstrate the ability for the resolvent-based variational optimisation methodology to find exact solutions to dynamical systems.
3. Investigate the effect low-order modelling has on the performance of the optimiser.
4. Construct long periodic trajectories, called quasi-trajectories, that obtain useful ergodic statistics without exactly satisfying the governing equations.

After the main optimisation methodology was explained in Chapter 3 for the case of fluid dynamics problems, Chapter 4 takes some time characterise RPCF, the prime flow studied in this work. The velocity statistics and spectra are discussed, along with the optimal basis for select Reynolds numbers using the dominant SPOD modes. The first major objective is then addressed, analysing the resolvent modes for those same flow regimes in their capability to represent the given flow in as few modes as possible. It is shown that for the main Reynolds numbers considered in this work a much smaller proportion of resolvent modes are required to retain the majority of the flow's kinetic energy.

In Chapter 5 a smaller version of the same problem is setup and analysed for the Lorenz system (Lorenz, 1963) as an initial validating case, looking to satisfy the second and especially the fourth objective above. The variational optimisation and resolvent analysis formulations are specialised for the Lorenz system, and it is shown how to achieve an (exact) dimensionality reduction by exploiting the partial linearity in the governing equations for the Lorenz system. This projection takes the system from a 3-dimensional space down to a 2-dimensional space without any loss in dynamic information. It is first demonstrated that the optimiser can generate known UPOs. Then, the concept of quasi-trajectories introduced in Chapter 1 are then investigated. It is successfully shown that these quasi-trajectories can provide useful statistical information even when system residuals are large, $\mathcal{O}(1)$. The convergence of the statistics compared to the period of the quasi-trajectory, as well as the number of iterations taken for the optimisation. Both of these demonstrate that there is a saturation in the accuracy obtained by the quasi-trajectories, after which increases in the period and number of iterations does not produce any significant increases in accuracy of the prediction compared to the chaotic statistics.

Chapter 6 features the direct application of the optimisation methodology in Chapter 3 with the modes analysed in Chapter 4. This chapter focuses purely on the exact solutions that can be obtained using the projected optimisation, and the effect the number of resolvent modes used for said projection has on the optimisation performance. It is demonstrated that the optimiser is able to recover both stable and unstable equilibrium and periodic solutions to the Navier-Stokes equations, using a complete basis. The magnitude of the stability, or equivalently how far away a solution is from neutral stability, dictates how fast the optimiser can converge towards it. The closer the solution is to neutrally stable the slower the optimiser converges. This process continues to the limit of neutral stability where the optimiser effectively stalls some distance from the solution. It is shown that truncating the number of modes used can improve the convergence rate of the optimiser by orders of magnitude. This improvement is justified by arguing that the Hessian matrix, the operator that governs local convergence properties, is better conditioned as a result of truncating resolvent modes associated with small singular values.

7.1 Summary of the Analysis and Limitations

The analysis of Chapter 4 focused on characterising the main spectral features of RPCF, the dominant features of the flow, and most importantly the efficacy of resolvent modes in reconstructing the flow. This was done to motivate their use and understand how many modes would be required to construct efficient low-order models of the flow that can be exploited in finding invariant solutions. It was shown that the flow at all Reynolds numbers is dominated by a set of streamwise rolls with a well defined spectral content. The resolvent modes were shown to be able to accurately reconstruct the flow with over 99% of its original kinetic energy with roughly an order of magnitude fewer of modes than the spatial discretisation for $Re = 50$ and $Re = 450$. Individual inspection revealed particular modes that captured the streamwise roll structures which were identified as the significant dynamical feature of the flow.

Chapter 5 successfully demonstrated that the optimiser could construct large period quasi-trajectories that approximated statistics of chaotic trajectories, displaying both qualitative and quantitative convergence for only a modest number of iterations, between 1000 and 10000 well before the global residual has reached any local or global minimum. The effect of unique state-space structures, specifically an unstable fixed point at the origin, is observed to somewhat pollute the quasi-trajectory, as a result of it being transformed into an attracting point under the variational dynamics. In high-dimensional flows the effect of potentially many unstable, and rarely observed, fixed points/equilibria is not known, although for quasi-trajectories it is possible that they do not pose a significant issue as the solution would simply be much more attracted to countably infinite unstable solutions embedded within the attractor that are observed more commonly. The convergence of a few statistical moments of some observables against the period of the quasi-trajectory and the number of iterations was provided. A weak dependence on the number of iterations required to converge the statistics of the observables was observed, with improved results for more iterations as expected. The more dominant trend is that of the period of the quasi-trajectory. As expected the larger the period the better the estimation of the statistics, as a larger neighbourhood of the strange attractor is explored leading to more shadowing events which better represents a true chaotic trajectory. In addition to improved accuracy of the statistical estimation, the precision is also improved for larger periods, with the spread of the predictions obtained from different quasi-trajectories of the same period decrease in line with the central limit theorem.

The equilibrium solutions obtained in Chapter 6 displayed a large robustness to the initial conditions chosen, and an ability to converge to both the stable solution (at the given Reynolds number of $Re = 50$) and some more unorthodox unstable solution not observed in the DNS. The use of the L-BFGS optimisation algorithm provided a very noticeable improvement in performance of the optimiser compared to the standard choice of gradient descent for the optimisation algorithm. The effect of the number of modes used was demonstrated on one of the unstable equilibrium solutions found earlier in the chapter. Orders of magnitude improvements in the convergence rate were observed for a low number of modes, with the accuracy (norm difference) of the resulting solution showing only a modest drop-off. However, this accuracy decrease is also shown to have little effect on the qualitative resemblance of the solution, implying the modes exist in a dynamically very significant subspace and are able to effectively compress the information in the flow. The optimiser is also demonstrated for a periodic solution, using a continuation approach to generate a solution at a higher Reynolds number. Specifically, the optimiser was initialised with a solution obtained from DNS at a particular Reynolds number polluted with some noise, and then sought out a solution at a higher Reynolds number. It was shown that the optimiser is able to recover such a solution from a rather corrupted starting point. However, the convergence rate observed for the time varying case was significantly worse than for the equilibria. In the time varying case the convergence rate continues to monotonically decrease as the optimisation continues, as opposed to the equilibria optimisations where the average convergence rates essentially remain the same over the duration of the optimisation. It was also observed that the period of the solution was still changing when the optimisation terminated, implying that a true minimum had not been reached. The worse performance of the optimiser was postulated to be from a few possible sources. The first is the solution being close to bifurcation, where it is known that convergence is degraded as solutions approach neutral stability. The second is the possibility that periodic flow shown is not, in fact, an exact solution, but is instead some sort of state-space ghost as discussed in (Zheng et al., 2024), which means the desired periodic orbit does not correspond to a global minimum but instead a local minimum, which may have unexpected effects on the convergence properties of the optimiser once it is close. The second postulated source of performance loss is some kind of numerical errors populating the resolvent modes. It was observed that the modes generated for the low to moderate temporal and spanwise frequencies for the periodic case had large numerically induced oscillations in their second derivatives, which should be investigated further to determine their effect on the convergence rate and accuracy of the final solution.

The current work did not demonstrate the use of quasi-trajectories on any high-dimensional chaotic systems. Using quasi-trajectories necessarily requires one to hold a very large dimensional object in memory, due primarily to the large number of temporal modes required to properly resolve the evolution of a large period flow. The current implementation of the resolvent-based optimisation is mostly optimised for iteration time over the memory consumption, utilising pseudo-spectral methods to avoid computing convolutions that scale poorly with the dimension of the problem. This requires a number of intermediate objects that exist within the full, unprojected, state-space. Along the with the cost of holding the set of modes in memory for all the required spanwise and temporal frequencies considered, the memory footprint of the algorithm grows quickly. An implementation of the framework that performs the optimisation completely within the reduced space defined by the relatively small number of resolvent modes would be able to better exploit the memory savings that could achieved from the dimensionality reduction from the modal projection. In terms of implementation, this framework differs primarily in how the residual variables are computed. Specifically, instead of an expand-transform-project procedure using pseudo-spectral methods to treat the nonlinear terms, these terms would all be computed directly in the reduced space by projecting the operators. These projected operators could either be pre-computed and stored for use during the optimisation, or computed each time they are needed by taking the necessary derivatives of the provided modes. The primary downside of such an implementation would be the requirements to compute the nonlinear terms with explicit convolutions. This is only be comparable in speed only if the dimensionality reduction is significant, both in terms of the number if modes used for the inhomogeneous directions of the flow as well as the number of required frequencies in the homogeneous directions and time. Such choices depend strongly on the size of the problem as well as the performance of the compute resources available.

7.2 Further Work

The work in this thesis provides a conceptual framework upon which much work can be based. Although the basic qualities of the resolvent-based optimiser have been demonstrated in some relatively simple cases, there is a large body of possible work in refining and applying the framework to more complex cases. Each of the possible extensions of this work are given in each subsection below.

7.2.1 Pre-Conditioning Due to Low-Order Models

The discussion near the end of Chapter 6 justifies the improved convergence rates of the optimiser when rejecting a large number of the resolvent modes for the Galerkin projection as a form of Hessian pre-conditioning. The Hessian of the global residual is in general poorly conditioned due to the effect of the Laplace operator, which has eigenvalues that grow unbounded (in a continuous setting). It is argued that by rejecting higher-order resolvent modes, the directions in the optimisation space that correspond to the rapidly growing eigendirections of the Laplace operator are projected away, improving the condition number of the Hessian and hence the convergence rate. However, it is not shown here analytically. A proof of this would constitute a rigorous argument for using the resolvent modes, or other appropriately chosen modes such as the eigenvectors of the Laplace operator themselves. This would then be applied in more general cases to be able to improve convergence rates and the general practicality of optimisation for finding invariant solutions to the Navier-Stokes equations via generally pre-conditioned methods.

7.2.2 Quasi-Trajectories of Chaotic Flows

The arguably most pressing future application of this work is directly related to the second aim of this thesis: demonstrating the usefulness of large period quasi-trajectories in being able to estimate the statistics of turbulent flows. The demonstration in this thesis is on the smaller case of 3-dimensional case, with only a modest dimensionality reduction to 2 dimensions, which does not neglect any of the dynamical information as would be the case for fluid problems.

The likely best route to this end would be to tackle the RPCF with this approach, or some other flow with a single inhomogeneous spatial direction. The goal would then be to demonstrate that statistical measurable/physical observables of the resulting high-dimensional quasi-trajectory with a sufficiently large period have probability distributions that resemble those achieved from a DNS simulation. This could be achieved through comparison of energy plots (dissipations vs. energy production), velocity statistics such as mean profile or Reynolds stress, or simply the kinetic energy evolution of the flow. There is also the open question of whether extreme events and intermittence observed in turbulent flows could be accurately captured, and if they can, how large a period is required for the quasi-trajectory to do so.

There are some additional technical questions that could be answered as well. In this work, the mean profile of the candidate solution is not fixed over the duration of the optimisation. This was done to facilitate the search for exact solutions to the Navier-Stokes equations in Chapter 6. However, resolvent analysis requires the user to prescribe a given base profile, which in the literature is conventionally the turbulent mean profile. If the mean profile is known a-priori and fixed for the optimisation once the resolvent modes have been generated, then the effects of the accuracy of the given mean profile could be studied. The aim in that case would be answer questions such as: how accurate does the mean profile need to be for a quasi-trajectory to produce accurate statistics, or could a profile obtained from RANS simulation (without Reynolds stresses and a closure model) be sufficient for certain configurations to be able to produce statistically useful quasi-trajectories?

7.2.3 Sensitivity Analysis of Quasi-Trajectories

Quasi-trajectories have been proposed here as a possible method to estimate the statistics of chaotic systems without having to accurately simulate them. As discussed in the introduction, long UPOs of chaotic systems could be used to estimate the sensitivities of ergodic statistics as shown in Lasagna (2018, 2020) for the Lorenz system. Quasi-trajectories shadow orbits in the much the same way as any long trajectory obtained through a time-stepping/integration algorithm, and so could be used as a proxy to estimate the same sensitivities.

Using quasi-trajectories would have a couple of major benefits over using either chaotic simulations or long UPOs. Compared to chaotic simulations, quasi-trajectories are periodic orbits and thus the least squares shadowing methods Wang (2014); Lasagna et al. (2019) would be directly applicable, with the adjoint formulation being better conditioned due to the periodicity of the problem. Compared to long UPOs, quasi-trajectories are simply easier to find, requiring a much smaller number of iterations, with larger residuals. In addition, if a well-chosen basis is used, then an efficient low-order model can be constructed reducing the memory and time costs of obtaining the quasi-trajectory further. This would provide a lower bar to being able to perform sensitivity analyses, impacting the flow of engineering designs and the implementation of control schemes.

7.2.4 Hybrid-Solver

Farazmand (2016) originally developed the variational optimisation methodology, referred the adjoint solver in the manuscript. The primary use of the method is not to

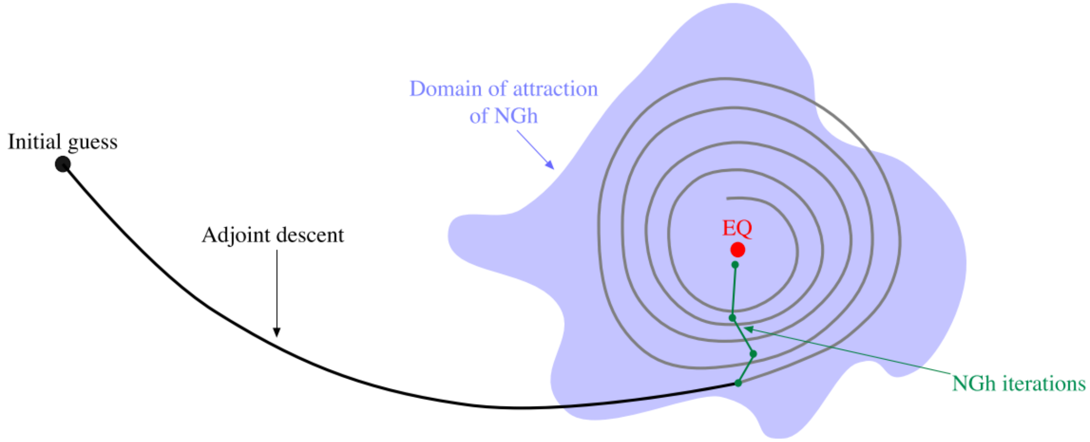

FIGURE 7.1: Hybrid solver approach, using variational optimisation (adjoint decent) as an initialiser with a large radius of convergence that moves a solution to within the much smaller radius of convergence for the faster converging Newton-GMRES-Hookstep (NGh) solver. Obtained from Farazmand (2016)

converge a solution to its minimum, but instead to exploit the optimiser's large radius of convergence and fast initial convergence rates to take solutions that otherwise wouldn't converge to within the radius of convergence for the faster converging Newton-GMRES-Hookstep method. This hybrid approach achieves the best of both worlds between robustness and total convergence iterations. This hybrid approach is depicted in Figure 7.1.

As shown in Section 6.3, rejecting a significant set of the resolvent modes used in the Galerkin projection can greatly improve the convergence rate of the optimiser without completely sacrificing the accuracy of the solution obtained. The robustness of the variational optimiser to initial guesses remains unaltered since the Galerkin projection is a least-squares projection onto a linear subspace. In Farazmand (2016), the optimisation was used to create a hybrid solver method; an initial high residual guess was converged towards a minimum using the variational optimiser, and once the trajectory is sufficiently close to the minimum the solver is swapped for Newton-GMRES-Hookstep. This hybrid approach balances the large radius of convergence of the optimisation and rapid convergence rates of the Newton-GMRES-Hookstep to get the best of both worlds. Adding the Galerkin projection to this hybrid methodology with an aggressive low-order model has the potential to make this approach even more appealing. The aggressive low-order model would generally further improve the convergence rate of the optimisation phase of the hybrid solver, and still get the solution sufficiently close to the minimum such that the Newton iterations would successfully converge. Referring back to Figure 7.1, this "Adjoint descent" step of the solver can be replaced with the projected optimisation which could reduce the number of iterations taken to converge to within the "domain of attraction of NGh" by orders of magnitude. This would be another step towards invariant solvers becoming more practical to use for research and engineering design applications, as more and longer solutions could be found just as fast and reliably with as little human input as possible.

References

L. I. Abreu, A. V. Cavalieri, and W. Wolf. Coherent Hydrodynamic Waves and Trailing-edge Noise. In *23rd AIAA/CEAS Aeroacoustics Conference*, AIAA AVIATION Forum. American Institute of Aeronautics and Astronautics, 2017.

R. L. Adler, A. G. Konheim, and M. H. McAndrew. Topological Entropy. *Transactions of the American Mathematical Society*, 1965.

L. Agostini. Exploration and prediction of fluid dynamical systems using auto-encoder technology. *Physics of Fluids*, 2020.

M. A. Ahmed and A. S. Sharma. Basis for finding exact coherent states. *Physical Review E*, 2020.

D. J. Albers and J. C. Sprott. Structural stability and hyperbolicity violation in high-dimensional dynamical systems. *Nonlinearity*, 2006.

P. L. Andrews and R. E. Waltz. Direct solution for the power spectrum of the Lorenz attractor. *The Physics of Fluids*, 1988.

D. B. Araya, T. Colonius, and J. O. Dabiri. Transition to bluff-body dynamics in the wake of vertical-axis wind turbines. *Journal of Fluid Mechanics*, 2017.

R. Artuso, E. Aurell, and P. Cvitanovic. Recycling of strange sets: I. Cycle expansions. *Nonlinearity*, 1990.

O. Ashtari and T. M. Schneider. Identifying invariant solutions of wall-bounded three-dimensional shear flows using robust adjoint-based variational techniques. *Journal of Fluid Mechanics*, 2023.

N. Aubry, P. Holmes, J. L. Lumley, and E. Stone. The dynamics of coherent structures in the wall region of a turbulent boundary layer. *Journal of Fluid Mechanics*, 1988.

D. Auerbach, P. Cvitanovic, J. P. Eckmann, G. Gunaratne, and I. Procaccia. Exploring chaotic motion through periodic orbits. *Phys. Rev. Lett.*, jun 1987.

D. Ayala and B. Protas. On maximum enstrophy growth in a hydrodynamic system. *Physica D: Nonlinear Phenomena*, 2011.

S. Azimi, O. Ashtari, and T. M. Schneider. Constructing periodic orbits of high-dimensional chaotic systems by an adjoint-based variational method. *Phys. Rev. E*, 2022.

G. Bachman and L. Narici. *Functional analysis*. Courier Corporation, 2000.

B. Barthel, X. Zhu, and B. J. McKeon. Closing the loop: nonlinear Taylor vortex flow through the lens of resolvent analysis. *Journal of Fluid Mechanics*, 2021.

G. K. Batchelor, A. A. Townsend, and H. Jeffreys. The nature of turbulent motion at large wave-numbers. *Proceedings of the Royal Society of London. Series A. Mathematical and Physical Sciences*, 1949.

S. Beneddine, R. Yegavian, D. Sipp, and B. Leclaire. Unsteady flow dynamics reconstruction from mean flow and point sensors: An experimental study. *Journal of Fluid Mechanics*, 2017.

E. Berger, S. Mark, V. David, J. Bernhard, and H. B. Amor. Estimation of perturbations in robotic behavior using dynamic mode decomposition. *Advanced Robotics*, 2015.

J. Boussinesq. *Essai sur la théorie des eaux courantes*. Imprimerie nationale, 1877.

B. W. Brunton, L. A. Johnson, J. G. Ojemann, and J. N. Kutz. Extracting spatial–temporal coherent patterns in large-scale neural recordings using dynamic mode decomposition. *Journal of Neuroscience Methods*, 2016.

N. B. Budanur, K. Y. Short, M. Farazmand, A. P. Willis, and P. Cvitanović. Relative periodic orbits form the backbone of turbulent pipe flow. *Journal of Fluid Mechanics*, 2017.

T. Burton, S. Symon, A. S. Sharma, and D. Lasagna. Resolvent-based optimization for approximating the statistics of a chaotic Lorenz system. *Physical Review E*, 2025.

C. Canuto, M. Y. Hussaini, A. Quarteroni, and T. A. Zang. Some Algorithms for Unsteady Navier—Stokes Equations. In Claudio Canuto, M Yousuff Hussaini, Alfio Quarteroni, and Thomas A Zang, editors, *Spectral Methods in Fluid Dynamics*, chapter 7. Springer Berlin Heidelberg, Berlin, Heidelberg, 1988.

G. J. Chandler and R. R. Kerswell. Invariant recurrent solutions embedded in a turbulent two-dimensional Kolmogorov flow. *Journal of Fluid Mechanics*, 2013.

N. Chandramoorthy and Q. Wang. On the probability of finding nonphysical solutions through shadowing. *Journal of Computational Physics*, 2021.

S. Chandrasekhar. *Hydrodynamic and Hydromagnetic Stability*. Oxford University Press, 1961.

S. J. Chapman. Subcritical transition in channel flows. *Journal of Fluid Mechanics*, 2002.

Y. Chen and T. Jiang. The pressure boundary conditions for the incompressible Navier-Stokes equations computation. *Communications in Nonlinear Science and Numerical Simulation*, 1996.

S. Cherubini, P. De Palma, J.-C. Robinet, and A. Bottaro. Rapid path to transition via nonlinear localized optimal perturbations in a boundary-layer flow. *Physical Review E*, 2010.

S. Cherubini, P. De Palma, J.-C. Robinet, and A. Bottaro. The minimal seed of turbulent transition in the boundary layer. *Journal of Fluid Mechanics*, 2011.

S. Cherubini, J.-C. Robinet, and P. De Palma. Nonlinear control of unsteady finite-amplitude perturbations in the Blasius boundary-layer flow. *Journal of Fluid Mechanics*, 2013.

F Christiansen, P Cvitanović, and V Putkaradze. Spatiotemporal chaos in terms of unstable recurrent patterns. *Nonlinearity*, 1997.

C. J. Crowley, J. L. Pughe-Sanford, W. Toler, M. C. Krygier, R. O. Grigoriev, and M. F. Schatz. Turbulence tracks recurrent solutions. *Proceedings of the National Academy of Sciences*, 2022.

P. Cvitanović. Invariant Measurement of Strange Sets in Terms of Cycles. *Physical Review Letters*, 1988.

P. Cvitanović. Dynamical averaging in terms of periodic orbits. *Physica D: Nonlinear Phenomena*, 1995.

P. Cvitanović and J. F. Gibson. Geometry of the turbulence in wall-bounded shear flows: periodic orbits. *Physica Scripta*, 2010.

P. Cvitanović, R. Artuso, R. Mainieri, G. Tanner, and G. Vattay. *Chaos: Classical and Quantum*. Niels Bohr Institute, Copenhagen, 2020. URL `http://chaosbook.org/`.

G. Dahlquist and Å. Björck. *Numerical Methods in Scientific Computing, Volume I*. Society for Industrial and Applied Mathematics, 2008.

C. A. Daly, T. M. Schneider, P. Schlatter, and N. Peake. Secondary instability and tertiary states in rotating plane Couette flow. *Journal of Fluid Mechanics*, 2014.

C. Dong. Topological classification of periodic orbits in Lorenz system. *Chinese Physics B*, 2018.

J. R. Dormand and P. J. Prince. A family of embedded Runge-Kutta formulae. *Journal of Computational and Applied Mathematics*, 1980.

B. Dubrulle, O. Dauchot, F. Daviaud, P.-Y. Longaretti, D. Richard, and J.-P. Zahn. Stability and turbulent transport in Taylor–Couette flow from analysis of experimental data. *Physics of Fluids*, 2005.

B. Eckhardt, S. Grossmann, and D. Lohse. Torque scaling in turbulent Taylor–Couette flow between independently rotating cylinders. *Journal of Fluid Mechanics*, 2007.

B. Eckhardt, C. R. Doering, and J. P. Whitehead. Exact relations between Rayleigh–Bénard and rotating plane Couette flow in two dimensions. *Journal of Fluid Mechanics*, 2020.

H Eivazi, S. Le Clainche, S. Hoyas, and R. Vinuesa. Towards extraction of orthogonal and parsimonious non-linear modes from turbulent flows. *Expert Systems with Applications*, 2022.

H. Faisst and B. Eckhardt. Traveling Waves in Pipe Flow. *Phys. Rev. Lett.*, 2003.

M. Farazmand. An adjoint-based approach for finding invariant solutions of Navier–Stokes equations. *Journal of Fluid Mechanics*, 2016.

B. F. Farrell, D. F. Gayme, P. A. Ioannou, B. K. Lieu, and M. R. Jovanović. Dynamics of the roll and streak structure in transition and turbulence. In *Center for Turbulence Research Proceedings of the Summer Program*, 2012.

L. Fazendeiro, B. M. Boghosian, P. V. Coveney, and J. Lätt. Unstable periodic orbits in weak turbulence. *Journal of Computational Science*, 2010.

M. J. Feigenbaum. The universal metric properties of nonlinear transformations. *Journal of Statistical Physics*, 1979.

R. Fletcher. Structure of Methods. In *Practical Methods of Optimization*, chapter 2. John Wiley & Sons, Ltd, 2000.

M. Frigo and S. G. Johnson. The Design and Implementation of FFTW3. *Proceedings of the IEEE*, 2005.

K. Fukami, T. Nakamura, and K. Fukagata. Convolutional neural network based hierarchical autoencoder for nonlinear mode decomposition of fluid field data. *Physics of Fluids*, 2020.

G. Gallavotti and E. G. D. Cohen. Dynamical ensembles in stationary states. *Journal of Statistical Physics*, 1995.

X. Garnaud, L. Lesshafft, P. J. Schmid, and P. Huerre. The preferred mode of incompressible jets: linear frequency response analysis. *Journal of Fluid Mechanics*, 2013.

D. Gayme. *A robust control approach to understanding nonlinear mechanisms in shear flow turbulence*. PhD thesis, California Institute of Technology, 2010.

D. F. Gayme and B. A. Minnick. Coherent structure-based approach to modeling wall turbulence. *Phys. Rev. Fluids*, nov 2019.

F. Giannetti, S. Camarri, and P. Luchini. Structural sensitivity of the secondary instability in the wake of a circular cylinder. *Journal of Fluid Mechanics*, 2010.

F. Giannetti, S. Camarri, and V. Citro. Sensitivity analysis and passive control of the secondary instability in the wake of a cylinder. *Journal of Fluid Mechanics*, 2019.

F. Gómez, H. M. Blackburn, M. Rudman, A. S. Sharma, and B. J. McKeon. A reduced-order model of three-dimensional unsteady flow in a cavity based on the resolvent operator. *Journal of Fluid Mechanics*, 2016.

M. D. Graham and D. Floryan. Exact Coherent States and the Nonlinear Dynamics of Wall-Bounded Turbulent Flows. *Annual Review of Fluid Mechanics*, 2021.

P. M. Gresho. Incompressible Fluid Dynamics: Some Fundamental Formulation Issues. *Annual Review of Fluid Mechanics*, 1991.

P. M. Gresho and R. L. Sani. On pressure boundary conditions for the incompressible Navier-Stokes equations. *International Journal for Numerical Methods in Fluids*, 1987.

G. Haçat, A. Çıbık, F. Yılmaz, and S. Kaya. Optimal Control problems of NS-α and NS-ω turbulence models: analysis and numerical tests. *Numerical Algorithms*, 2025.

W. W. Hager and H. Zhang. A New Conjugate Gradient Method with Guaranteed Descent and an Efficient Line Search. *SIAM Journal on Optimization*, 2005.

E. Hairer, S. Norsett, and G. Wanner. *Solving Ordinary Differential Equations I: Nonstiff Problems*, volume 8. Springer Berlin, Heidelberg, 1993.

S. M. Hammel, J. A. Yorke, and C. Grebogi. Numerical orbits of chaotic processes represent true orbits. *Bulletin (New Series) of the American Mathematical Society*, 1988.

M. R. Head and P. Bandyopadhyay. New aspects of turbulent boundary-layer structure. *Journal of Fluid Mechanics*, 1981.

L. H. O. Hellström and A. J. Smits. The energetic motions in turbulent pipe flow. *Physics of Fluids*, 2014.

K. Hiwatashi, P. H. Alfredsson, N. Tillmark, and M. Nagata. Experimental observations of instabilities in rotating plane Couette flow. *Physics of Fluids*, 2007.

E. Hopf. Abzweigung einer periodischen Lösung von einer Stationären Lösung eines Differentialsystems. *Ber. Verh. Sächs. Akad. Wiss. Leipzig Math.-Nat. Kl.*, 1942.

E. Hopf. A mathematical example displaying features of turbulence. *Communications on Pure and Applied Mathematics*, 1948.

Y. Hwang and H. Choi. Sensitivity of global instability of spatially developing flow in weakly and fully nonlinear regimes. *Physics of Fluids*, 2008.

B. Jin, S. J. Illingworth, and R. D. Sandberg. Resolvent-based approach for H_2-optimal estimation and control: an application to the cylinder flow. *Theoretical and Computational Fluid Dynamics*, 2022.

J. P. Johnston, R. M. Halleent, and D. K. Lezius. Effects of spanwise rotation on the structure of two-dimensional fully developed turbulent channel flow. *Journal of Fluid Mechanics*, 1972.

W. P. Jones and B. E. Launder. The prediction of laminarization with a two-equation model of turbulence. *International Journal of Heat and Mass Transfer*, 1972.

M. R. Jovanović and B. Bamieh. Componentwise energy amplification in channel flows. *Journal of Fluid Mechanics*, 2005.

G. Kawahara and S. Kida. Periodic motion embedded in plane Couette turbulence: regeneration cycle and burst. *Journal of Fluid Mechanics*, 2001.

G. Kawahara, M. Uhlmann, and L. van Veen. The Significance of Simple Invariant Solutions in Turbulent Flows. *Annual Review of Fluid Mechanics*, 2012.

T. Kawata and P. H. Alfredsson. Experiments in rotating plane Couette flow – momentum transport by coherent roll-cell structure and zero-absolute-vorticity state. *Journal of Fluid Mechanics*, 2016.

L. Keefe, P. Moin, and J. Kim. The dimension of attractors underlying periodic turbulent Poiseuille flow. *Journal of Fluid Mechanics*, 1992.

R. R. Kerswell, C. C. T. Pringle, and A. P. Willis. An optimization approach for analysing nonlinear stability with transition to turbulence in fluids as an exemplar. *Reports on Progress in Physics*, 2014.

L. Kleiser and U. Schumann. Treatment of Incompressibility and Boundary Conditions in 3-D Numerical Spectral Simulations of Plane Channel Flows. In E H Hirschel, editor, *Proceedings of the Third GAMM — Conference on Numerical Methods in Fluid Mechanics*. Vieweg+Teubner Verlag, Wiesbaden, 1980.

S. J. Kline and S. K. Robinson. Quasi-coherent structures in the turbulent boundary layer. I - Status report on a community-wide summary of the data. In *Near-Wall Turbulence*. Hemisphere Pub. Corp., 1990.

S. J. Kline, W. C. Reynolds, F. A. Schraub, and P. W. Runstadler. The structure of turbulent boundary layers. *Journal of Fluid Mechanics*, 1967.

M. C. Krygier, J. L. Pughe-Sanford, and R. O. Grigoriev. Exact coherent structures and shadowing in turbulent Taylor–Couette flow. *Journal of Fluid Mechanics*, 2021.

A. Kushwaha, J. S. Park, and M. D. Graham. Temporal and spatial intermittencies within channel flow turbulence near transition. *Physical Review Fluids*, 2017.

Y. Lan and P. Cvitanović. Variational method for finding periodic orbits in a general flow. *Physical Review E - Statistical Physics, Plasmas, Fluids, and Related Interdisciplinary Topics*, 2004.

L. D. Landau and E. M. Lifshitz. Chapter III - Turbulence. In L. D. Landau and E. M. B. T. Fluid Mechanics (Second Edition) Lifshitz, editors, *Fluid Mechanics*. Pergamon, 1987.

D. Lasagna. Sensitivity Analysis of Chaotic Systems using Unstable Periodic Orbits. *SIAM Journal on Applied Dynamical Systems*, 2018.

D. Lasagna. Sensitivity of long periodic orbits of chaotic systems. *Phys. Rev. E*, 2020.

D. Lasagna, O. R. Tutty, and S. Chernyshenko. Flow regimes in a simplified Taylor–Couette-type flow model. *European Journal of Mechanics - B/Fluids*, 2016.

D. Lasagna, A. Sharma, and J. Meyers. Periodic shadowing sensitivity analysis of chaotic systems. *Journal of Computational Physics*, 2019.

D K. Lezius and J. P. Johnston. Roll-cell instabilities in rotating laminar and turbulent channel flows. *Journal of Fluid Mechanics*, 1976.

D. C. Liu and J. Nocedal. On the limited memory BFGS method for large scale optimization. *Mathematical Programming*, 1989.

E. N. Lorenz. Deterministic Nonperiodic Flow. *Journal of Atmospheric Sciences*, 1963.

E. N. Lorenz. The problem of deducing the climate from the governing equations. *Tellus*, 1964.

D. Lucas and R. R. Kerswell. Recurrent flow analysis in spatiotemporally chaotic 2-dimensional Kolmogorov flow. *Physics of Fluids*, 2015.

D. Lucas and T. Yasuda. Stabilization of exact coherent structures in two-dimensional turbulence using time-delayed feedback. *Physical Review Fluids*, 2022.

J. L. Lumley. The Structure of Inhomogeneous Turbulent Flows. *Atm ospheric Turblence and Radio Wave Propagation*, 1967.

J. L. Lumley. *Stochastic Tools in Turbulence*. Academic Press, 1970.

J. Mann and J. N. Kutz. Dynamic mode decomposition for financial trading strategies. *Quantitative Finance*, 2016.

R. M. May. Simple mathematical models with very complicated dynamics. *Nature*, 1976.

B. J. McKeon and A. S. Sharma. A critical-layer framework for turbulent pipe flow. *Journal of Fluid Mechanics*, 2010.

B. J. McKeon, A. S. Sharma, and I. Jacobi. Experimental manipulation of wall turbulence: A systems approach. *Physics of Fluids*, 2013.

P. Meliga, E. Boujo, and F. Gallaire. A self-consistent formulation for the sensitivity analysis of finite-amplitude vortex shedding in the cylinder wake. *Journal of Fluid Mechanics*, 2016.

I. Mezić. Analysis of Fluid Flows via Spectral Properties of the Koopman Operator. *Annual Review of Fluid Mechanics*, 2013.

P. K. Mogensen and A. N. Riseth. Optim: A mathematical optimization package for Julia. *Journal of Open Source Software*, 2018.

A. Monokrousos, A. Bottaro, L. Brandt, A. Di Vita, and D. S. Henningson. Nonequilibrium Thermodynamics and the Optimal Path to Turbulence in Shear Flows. *Physical Review Letters*, 2011.

J. L. Morales and J. Nocedal. Remark on "algorithm 778: L-BFGS-B: Fortran subroutines for large-scale bound constrained optimization". *ACM Trans. Math. Softw.*, 2011.

S. Nabi, P. Grover, and C. P. Caulfield. Nonlinear optimal control strategies for buoyancy-driven flows in the built environment. *Computers & Fluids*, 2019.

M. Nagata. Three-dimensional traveling-wave solutions in plane Couette flow. *Physical Review E*, 1997.

M. Nagata. A note on the mirror-symmetric coherent structure in plane Couette flow. *Journal of Fluid Mechanics*, 2013.

M. Nagata, B. Song, and D. P. Wall. Onset of vortex structures in rotating plane Couette flow. *Journal of Fluid Mechanics*, 2021.

J. Nocedal and S. Wright. *Numerical Optimization*. Springer-Verlag New York, 2 edition, 2006.

J. Page, J. Holey, M. P. Brenner, and R. R. Kerswell. Exact coherent structures in two-dimensional turbulence identified with convolutional autoencoders. *Journal of Fluid Mechanics*, 2024a.

J. Page, P. Norgaard, M. P. Brenner, and R. R. Kerswell. Recurrent flow patterns as a basis for two-dimensional turbulence: Predicting statistics from structures. *Proceedings of the National Academy of Sciences*, 2024b.

J. S. Park and M. D. Graham. Exact coherent states and connections to turbulent dynamics in minimal channel flow. *Journal of Fluid Mechanics*, 2015.

J. P. Parker and T. M. Schneider. Variational methods for finding periodic orbits in the incompressible Navier–Stokes equations. *Journal of Fluid Mechanics*, 2022.

P.-Y. Passaggia and U. Ehrenstein. Adjoint based optimization and control of a separated boundary-layer flow. *European Journal of Mechanics - B/Fluids*, 2013.

H. Poincaré. *The Three-Body Problem and the Equations of Dynamics*. Springer Cham, 1 edition, 2017.

L. Prandtl. Bericht über Untersuchungen zur ausgebildeten Turbulenz. *ZAMM - Journal of Applied Mathematics and Mechanics / Zeitschrift für Angewandte Mathematik und Mechanik*, 1925.

C. C. T. Pringle and R. R. Kerswell. Using Nonlinear Transient Growth to Construct the Minimal Seed for Shear Flow Turbulence. *Physical Review Letters*, 2010.

C. C. T. Pringle, A. P. Willis, and R. R. Kerswell. Minimal seeds for shear flow turbulence: using nonlinear transient growth to touch the edge of chaos. *Journal of Fluid Mechanics*, 2012.

S. M. E. Rabin, C. P. Caulfield, and R. R. Kerswell. Triggering turbulence efficiently in plane Couette flow. *Journal of Fluid Mechanics*, 2012.

E. M. Redfern, A. L. Lazer, and D. Lucas. Dynamically relevant recurrent flows obtained via a nonlinear recurrence function from two-dimensional turbulence. *arXiv preprint arXiv:2408.05079*, 2024.

S. K. Robinson. Coherent Motions in the Turbulent Boundary Layer. *Annual Review of Fluid Mechanics*, 1991.

K. Rosenberg and B. J. Mckeon. Computing exact coherent states in channels starting from the laminar profile : A resolvent-based approach. *Physical Review E*, 2019.

C. W. Rowley and S. T. M. Dawson. Model Reduction for Flow Analysis and Control. *Annual Review of Fluid Mechanics*, 2017.

C. W. Rowley, I. Mezic, S. Bagheri, P. Schlatter, and D. S. Henningson. Spectral analysis of nonlinear flows. *Journal of Fluid Mechanics*, 2009.

D. Ruelle and F. Takens. On the nature of turbulence. *Communications in Mathematical Physics*, 1971.

Y. Saad and M. H. Schultz. GMRES: A Generalized Minimal Residual Algorithm for Solving Nonsymmetric Linear Systems. *SIAM Journal on Scientific and Statistical Computing*, jul 1986.

Y. Saiki and M. Yamada. Time-averaged properties of unstable periodic orbits and chaotic orbits in ordinary differential equation systems. *Phys. Rev. E*, jan 2009.

J. Sánchez, M. Net, B. Garcia-Archilla, and C. Simó. Newton–Krylov continuation of periodic orbits for Navier–Stokes flows. *Journal of Computational Physics*, 2004.

H. Schlichting. Berechnung der Anfachung kleiner Störungen bei der Plattenströmung. *ZAMM*, 1933.

P. Schmid and D. Henningson. *Stability and Transition in Shear Flows*. Springer New York, 2001.

P. J. Schmid. Dynamic mode decomposition of numerical and experimental data. *Journal of Fluid Mechanics*, 2010.

O. T. Schmidt, A. Towne, G. Rigas, T. Colonius, and G. A. Brès. Spectral analysis of jet turbulence. *Journal of Fluid Mechanics*, 2018.

G. B. Schubauer and H. K. Skramstad. Laminar-boundary-layer oscillations and transition on a flat plate. *Journal of research of the National Bureau of Standards*, 1947.

O. Semeraro, V. Jaunet, P. Jordan, A. V. Cavalieri, and L. Lesshafft. Stochastic and harmonic optimal forcing in subsonic jets. In *22nd AIAA/CEAS Aeroacoustics Conference*, Aeroacoustics Conferences. American Institute of Aeronautics and Astronautics, 2016.

A. S. Sharma. Elements of resolvent methods in fluid mechanics: notes for an introductory short course v0.3. *arXiv*, 2019.

A. S. Sharma, I. Mezić, and B. J. McKeon. Correspondence between Koopman mode decomposition, resolvent mode decomposition, and invariant solutions of the Navier-Stokes equations. *Physical Review Fluids*, 2016a.

A. S. Sharma, R. Moarref, B. J. McKeon, J. S. Park, M. D. Graham, and A. P. Willis. Low-dimensional representations of exact coherent states of the Navier-Stokes equations from the resolvent model of wall turbulence. *Phys. Rev. E*, 2016b.

J. Sierra, P. Jolivet, F. Giannetti, and V. Citro. Adjoint-based sensitivity analysis of periodic orbits by the Fourier – Galerkin method. *Journal of Computational Physics*, 2021.

Y. G. Sinai. Gibbs Measures in Ergodic Theory. *Russian Mathematical Surveys*, 1972.

A. Sinha, D. Rodríguez, G. A. Brès, and T. Colonius. Wavepacket models for supersonic jet noise. *Journal of Fluid Mechanics*, 2014.

L. Sirovich. Turbulence and the Dynamics of Coherent Structures Part I: Coherent Structures. *Quarterly of Applied Mathematics*, 1987.

L. Skowronek and P. Gora. Chaos in Newtonian iterations: Searching for zeros which are not there. *Acta Physica Polonica Series B*, 2007.

S. Smale. Differentiable Dynamical Systems. *Bulletin of the American Mathematical Society*, 1967.

A. Solera-Rico, C. Sanmiguel Vila, M. Gómez-López, Y. Wang, A. Almashjary, S. T. M. Dawson, and Ricardo Vinuesa. β-Variational autoencoders and transformers for reduced-order modelling of fluid flows. *Nature Communications*, 2024.

P. Spalart and S. Allmaras. A one-equation turbulence model for aerodynamic flows. In *30th Aerospace Sciences Meeting and Exhibit*. American Institute of Aeronautics and Astronautics, 1992.

K. R. Sreenivasan and R. A. Antonia. The Phenomenology of Small-Scale Turbulence. *Annual Review of Fluid Mechanics*, 1997.

B. Suri, L. Kageorge, R. O. Grigoriev, and M. F. Schatz. Capturing Turbulent Dynamics and Statistics in Experiments with Unstable Periodic Orbits. *Physical Review Letters*, 2020.

S. Symon, K. Rosenberg, S. T. M. Dawson, and B. J. McKeon. Non-normality and classification of amplification mechanisms in stability and resolvent analysis. *Physical Review Fluids*, 2018.

K. Taira, S. L. Brunton, S. T. M. Dawson, C. W. Rowley, T. Colonius, B. J. McKeon, O. T. Schmidt, S. Gordeyev, V. Theofilis, and L. S. Ukeiley. Modal analysis of fluid flows: An overview. *AIAA Journal*, 2017.

K. Taira, M. S. Hemati, S. L. Brunton, Y. Sun, K. Duraisamy, S. Bagheri, S. T. M. Dawson, and C. Yeh. Modal Analysis of Fluid Flows: Applications and Outlook. *AIAA Journal*, 2020.

F. Takens. Detecting strange attractors in turbulence. In David Rand and Lai-Sang Young, editors, *Dynamical Systems and Turbulence*, Berlin, Heidelberg, 1981. Springer Berlin Heidelberg.

W. Tollmien. Über die Entstehung der Turbulenz. 1. Mitteilung. *Nachrichten von der Gesellschaft der Wissenschaften zu Göttingen, Mathematisch-Physikalische Klasse*, 1928.

I. Tomoaki and T. Sadayoshi. The Dynamics of Bursting Process in Wall Turbulence. *Journal of the Physical Society of Japan*, 2001.

A. Towne, T. Colonius, P. Jordan, A. V. Cavalieri, and G. A. Brès. Stochastic and nonlinear forcing of wavepackets in a Mach 0.9 jet. In *21st AIAA/CEAS Aeroacoustics Conference*, AIAA AVIATION Forum. American Institute of Aeronautics and Astronautics, 2015.

A. Towne, O. T. Schmidt, and T. Colonius. Spectral proper orthogonal decomposition and its relationship to dynamic mode decomposition and resolvent analysis. *Journal of Fluid Mechanics*, 2018.

L. N. Trefethen, A. E. Trefethen, S. C. Reddy, and T A. Driscoll. Hydrodynamic Stability Without Eigenvalues. *Science*, 1993.

T. Tsukahara. Structures and turbulent statistics in a rotating plane Couette flow. *Journal of Physics: Conference Series*, 2011.

T. Tsukahara, N. Tillmark, and P. H. Alfredsson. Flow regimes in a plane Couette flow with system rotation. *Journal of Fluid Mechanics*, 2010.

J. H. Tu, C. W. Rowley, D. M. Luchtenburg, S. L. Brunton, and J. N. Kutz. On dynamic mode decomposition: Theory and applications. *Journal of Computational Dynamics*, 2014.

M. Tutkun and W. K. George. Lumley decomposition of turbulent boundary layer at high Reynolds numbers. *Physics of Fluids*, 2017.

M. Tutkun, P. B. V. Johansson, and William K George. Three-Component Vectorial Proper Orthogonal Decomposition of Axisymmetric Wake Behind a Disk. *AIAA Journal*, 2008.

L. van Veen, S. Kida, and G. Kawahara. Periodic motion representing isotropic turbulence. *Fluid Dynamics Research*, 2006.

L. Van Veen, A. Vela-Martín, and G. Kawahara. Time-Periodic Inertial Range Dynamics. *Physical Review Letters*, 2019.

J. Vanneste and I. Yavneh. Unbalanced instabilities of rapidly rotating stratified shear flows. *Journal of Fluid Mechanics*, 2007.

M. Viana. What's new on Lorenz strange attractors? *Mathematical Intelligencer*, 2000.

D. Viswanath. Symbolic dynamics and periodic orbits of the Lorenz attractor. *Nonlinearity*, 2003.

D. Viswanath. Recurrent motions within plane Couette turbulence. *Journal of Fluid Mechanics*, 2007.

D. Viswanath. The Dynamics of Transition to Turbulence in Plane Couette Flow. In Hans Munthe-Kaas and Brynjulf Owren, editors, *Mathematics and Computation, a Contemporary View*, Berlin, Heidelberg, 2008. Springer Berlin Heidelberg.

Th. von Kármán. Ueber den Mechanismus des Widerstandes, den ein bewegter Körper in einer Flüssigkeit erfährt. *Nachrichten von der Gesellschaft der Wissenschaften zu Göttingen, Mathematisch-Physikalische Klasse*, 1911.

F. Waleffe. Three-Dimensional Coherent States in Plane Shear Flows. *Phys. Rev. Lett.*, 1998.

F. Waleffe. Exact coherent structures in channel flow. *Journal of Fluid Mechanics*, 2001.

J. Wang, J. Gibson, and F. Waleffe. Lower Branch Coherent States in Shear Flows: Transition and Control. *Physical Review Letters*, 2007.

Q. Wang. Convergence of the Least Squares Shadowing Method for Computing Derivative of Ergodic Averages. *SIAM Journal on Numerical Analysis*, 2014.

H. Wedin and R. R. Kerswell. Exact coherent structures in pipe flow: travelling wave solutions. *Journal of Fluid Mechanics*, 2004.

R. D. Whalley, D. J. C. Dennis, M. D. Graham, and R. J. Poole. An experimental investigation into spatiotemporal intermittencies in turbulent channel flow close to transition. *Experiments in Fluids*, 2019.

M. O. Williams, I. G. Kevrekidis, and C. W. Rowley. A Data–Driven Approximation of the Koopman Operator: Extending Dynamic Mode Decomposition. *Journal of Nonlinear Science*, 2015.

P. Wolfe. Convergence Conditions for Ascent Methods. *SIAM Review*, 1969.

P. Wolfe. Convergence Conditions for Ascent Methods. II: Some Corrections. *SIAM Review*, 1971.

C. S. Yih. *Dynamics of Nonhomogeneous Fluids*. Macmillan, 1965.

B. Zhang. Airfoil-based convolutional autoencoder and long short-term memory neural network for predicting coherent structures evolution around an airfoil. *Computers & Fluids*, 2023.

Z. Zheng, P. Beck, T. Yang, O. Ashtari, J. P. Parker, and T. M. Schneider. Ghost states underlying spatial and temporal patterns: how non-existing invariant solutions control nonlinear dynamics. *arXiv preprint arXiv:2411.10320*, 2024.

S. M. Zoldi. Unstable Periodic Orbit Analysis of Histograms of Chaotic Time Series. *Phys. Rev. Lett.*, 1998.